POLITECNICO DI MILANO

DEPARTMENT MECHANICAL ENGINEERING

DOCTORAL PROGRAMME IN MECHANICAL ENGINEERING

PARTICLE FILTER-BASED DAMAGE PROGNOSIS IN ENGINEERING STRUCTURES SUBJECTED TO FATIGUE LOADING

DOCTORAL DISSERTATION OF:
Tianzhi Li

SUPERVISOR:
Prof. Claudio Sbarufatti
Prof. Francesco Cadini
Ir. David Dumas

TUTOR:
Prof. Federico Cheli

THE CHAIR OF THE DOCTORAL PROGRAM:
Prof. Daniele Rocchi

Year 2023 – Cycle XXXV

SUMMARY

Fatigue degradation is an inevitable phenomenon in engineering structures, where the damage can evolve with time or the number of load cycles, and, eventually, safety may no longer be guaranteed when the damage state reaches a limit. Regular inspections should be carried out for functionality evaluation but require high financial expenses and unwanted system shutdowns. One desirable scenario for ensuring structural integrity while keeping maintenance costs at a minimum is to schedule the maintenance just before the damage reaches a critical limit. To this end, an advanced damage prognosis technology is required to anticipate the future damage state through a proper damage evolution model.

Provided with the uncertainties arising from many sources like complex fatigue degradation and environmental factors, a probabilistic damage evolution model has to be built to take care of those factors. Then, the damage state is quantified through a direct or indirect measurement system, and adopted for model updating through a proper state estimation technique. Finally, the future state and RUL are predicted by the updated model. Therefore, this thesis proceeds with the development of a robust prognostic method towards three paths, i.e., *damage evolution modeling*, *damage quantification*, and *model updating algorithm*.

The thesis has three contributions to *damage evolution modeling*. First, a method for predicting the delamination shape growth is proposed and validated by the composite fatigue test with ultrasonic C-scan monitoring. Then, a dataset containing sufficiently enough delamination images is obtained from some numerical simulation of composite fatigue delamination growth, and then adopted for training the delamination shape evolution models. Finally, a method by fusing multiple physics-based and data-driven damage evolution models is proposed to enhance the prognostic performance, and then validated by an aluminum fatigue test with Lamb wave monitoring.

As to *damage quantification*. Aiming to address the measurement uncertainties arising from various sources such as temperature variation, the author developed a bias-based prognostic model accounting for those uncertainties. Additionally, a dataset of some numerically simulated Lamb waves is used to build the damage quantification model, avoiding the need to collect experimental data for modeling. Finally, as the selection of a proper damage-sensitive statistical feature is crucial to the performance of the prognostic model, an online bias-based feature fusion and selection method is proposed to fuse multiple features and select the best one. All three contributions are tested by the same aluminum fatigue test with Lamb wave monitoring.

Targeting high-dimensional model updating, a new *particle filter* method is proposed to simplify the identification of one high-dimensional system into that of multiple lower-dimensional systems, and consequently, to allow for more efficient state and parameter estimation. This is validated by a numerical simulation of a twenty-story Bouc-wen frame structure under seismic excitation.

In conclusion, this thesis has provided the solutions to open problems in current

prognostic practices from three paths, which may serve as a solid base for further extensions toward a more robust prognostic method.

CONTENT

SUMMARY ..... **I**

CONTENT ..... **III**

INTRODUCTION **1**

1.1 BACKGROUND 1

1.2 RESEARCH GOAL AND SCOPES 2

1.3 THESIS OUTLINE 4

LITERATURE REVIEW **5**

2.1 INTRODUCTION 5

2.2 DAMAGE EVOLUTION MODELING 5

2.3 DAMAGE QUANTIFICATION 10

2.4 PARTICLE FILTER-BASED MODEL UPDATING 11

REFERENCES 14

DAMAGE EVOLUTION MODELING **17**

DAMAGE QUANTIFICATION **99**

HIGH-DIMENSIONAL PARTICLE FILTER **166**

CONCLUSIONS AND FUTURE WORKS **197**

6.1 CONCLUSIONS 197

6.2 FUTURE WORKS 198

PUBLICATIONS **200**

BIOGRAPHY **201**

ACKNOWLEDGEMENTS **202**

CHAPTER 1

INTRODUCTION

1.1 Background

Engineering structures and mechanical systems are critical components of modern society, used in a wide range of applications including aerospace vehicles and civil infrastructure. Over time, these structures can experience degradation in their material properties due to harsh operating conditions and loading, which can ultimately result in a loss of structural integrity or functionality. With many structures nearing the end of their design life, ensuring their ongoing safety and functionality has become an increasingly pressing issue in recent years.

Structural health monitoring (SHM) is a process that seeks to address these concerns by combining physical knowledge, reliable measurement systems, and advanced signal processing algorithms. By providing early detection, localization, and quantification of structural damage. timely alerts can be triggered for necessary inspections and maintenance, preventing potential catastrophic structural failures.

On the other hand, too early interventions can be wasteful, mainly due to the unnecessary replacement of still-functioning components and system shutdowns. To address these challenges, predictive maintenance is being developed to schedule maintenance just before the damage state reaches a critical limit. This requires the ability to forecast the propagation of fatigue damage under a specific mode, from its initial stages to the point of structural failure, and to calculate the remaining useful life (RUL) of a structure.

To achieve this, a reliable and accurate prognostic technique must be developed that incorporates uncertainties arising from the sources like complex fatigue degradation, environmental factors, loading conditions, and material properties. The development of a typical damage prognosis method involves four main steps, as shown in Figure 1. First, a deterministic damage evolution model is developed to describe the evolution of fatigue damage with time or the number of load cycles. Next, its probabilistic form is proposed to include uncertainties arising from the degradation process. The third step involves quantifying the damage state through a direct or indirect measurement system and updating the damage evolution model using a suitable state estimation technique. Finally, the updated model is used to predict the future state and RUL of the structure. To improve the robustness of the prognostic method, three potential paths are being explored: *damage evolution modeling*, *damage quantification*, and *model updating algorithm*. These developments will enable the creation of a more reliable and accurate RUL prediction for engineering structures and mechanical systems, ultimately contributing to their ongoing safety and functionality.

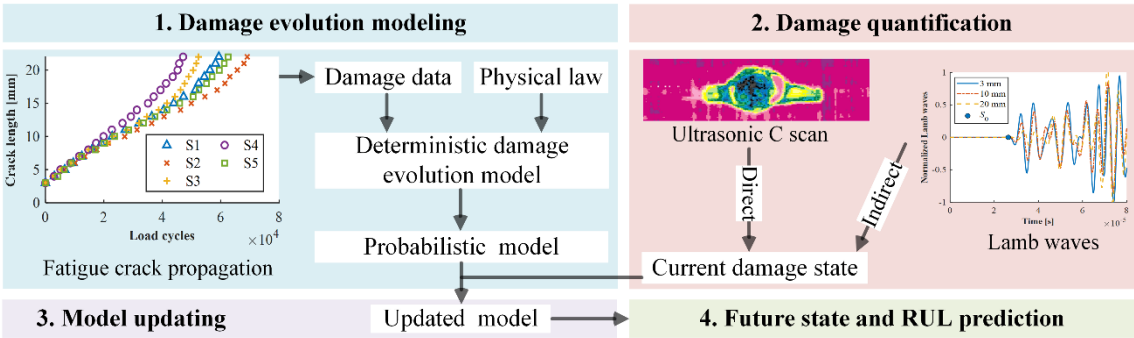

Figure 1 Four main steps in a typical prognostic method

1.2 Research goal and scopes

The goal of this research is to develop a robust particle filter-based damage prognosis method, from the perspectives of *damage evolution modeling*, *damage quantification*, and *model updating algorithm*. The scope of this thesis is restricted to the seven issues listed in Table 1.

Table 1 Seven issues to be addressed in this thesis.

Damage evolution modeling	I1: Selection of a proper damage state for damage prognosis I2: No available experimental data for training a data-driven damage evolution model I3: Fusion of multiple degradation models
Damage quantification	I4: Uncertainties in damage quantification model I5: No available experimental data for training a data-driven damage quantification model I6: Fusion of multiple damage-sensitive statistical features or damage quantification models
Model updating algorithm	I7: Curse of dimensionality

The first fundamental question arising from *damage evolution modeling*, or more generally, damage prognosis investigation, is the selection of an appropriate damage state to be predicted. Such a state should be predictable and contains lots of information for safety evaluation. Provided that many damage evolution models are derived from experimental fatigue damage growth data, the second question would be how to build such a model under no availability of experimental data. Finally, as there is no universally best model, the fusion of multiple models may be one of the possibilities to enhance the prognostic performance.

One of the most significant issues in *damage quantification* is how to take care of the uncertainties arising from multiple sources like sensor error and service conditions. A proper damage quantification model accounting for those uncertainties is always highly desirable. Then, As most damage quantification investigations would resort to a data-driven model linking the damage and measurement (or mostly some sort of damage-sensitive statistical feature), a typical issue is how to build such a model in case of no available experimental data from one or some

replications of the same structure. Finally, we will explore the potential of fusing multiple damage-sensitive features or damage quantification models to improve the overall accuracy.

As to the *model updating algorithm*, particle filter is a nonlinear and non-Gaussian state estimation algorithm. By sequentially providing the estimates of the damage state and its growth parameters, it has been widely adopted in the prognostic investigation. One critical problem arising is that the computational effort will increase with the state dimension, which is also defined as the curse of dimensionality. As the problem with high dimensionality arises in real-world applications where tens or even hundreds of unknown variables need to be estimated, such an issue deserves investigation.

Targeting the seven issues, this thesis proposes seven contributions, all of which are depicted within the solid line rectangle in Figure 2. The conclusion section will present two ideas (Dash line rectangle box) that relate to these contributions. The arrow line connecting the contributions signifies that the succeeding work takes advantage of the previous one by sharing the same model, model updating algorithm, or experimental studies.

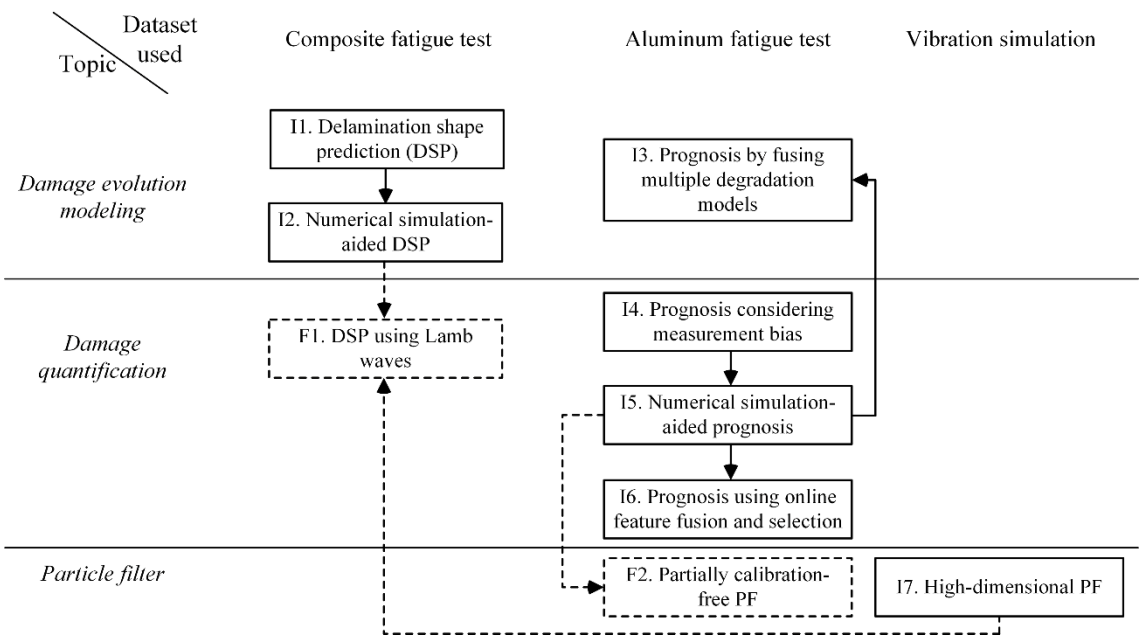

Figure 2 Summary of the contributions of this thesis

The first contribution to *damage evolution modeling* considers the delamination shape in composites as a damage state to be predicted. A method for predicting the delamination shape growth is proposed and validated by the composite fatigue test with ultrasonic C-scan monitoring. Then, in order to avoid the need to collect experimental data for modeling, a dataset containing sufficiently enough delamination images is created by some numerical simulation of fatigue delamination growth in composites, and then adopted for training the delamination shape evolution models. Finally, a method by fusing multiple physics-based and data-driven damage evolution models is proposed to enhance the prognostic performance, and then validated by an aluminum fatigue test with Lamb wave monitoring.

As to *damage quantification*, aiming to address the measurement uncertainties arising from various sources such as temperature variation, the author developed a bias-based prognostic model accounting for those uncertainties. Additionally, a dataset of some numerically simulated Lamb waves is used to build the damage quantification model, avoiding the need to collect experimental data for modeling. Finally, as the selection of a proper damage-sensitive statistical feature is crucial to the performance of the prognostic model, an online bias-based feature fusion and selection method is proposed to fuse multiple features and select the best one. All three contributions are tested by the aluminum fatigue test with Lamb wave monitoring mentioned above.

Targeting high-dimensional system identification, the author developed a new *particle filter* method of simplifying the identification of one high-dimensional system into that of multiple lower-dimensional systems, allowing for more efficient state and parameter estimation. This is validated by a numerical simulation of a twenty-story Bouc-wen frame structure under seismic excitation.

The discussions presented in this thesis are anticipated to enhance the robustness of damage prognosis for metal or composites undergoing fatigue degradation by introducing and implementing some improvements towards the three paths. Although the ultimate goal, beyond the scope of this thesis, is that the SHM community should strive to provide benefits that outweigh the costs and accelerate the adoption of SHM as a transformative engineering methodology.

1.3 Thesis outline

This thesis is composed of 6 chapters:

- Chapter 2 reviews the available literature on the field of damage prognosis from the perspectives of damage evolution modeling, damage quantification, and model updating, and summarizes some of the open problems.

- Chapters 3, 4, and 5 present the contributions to damage evolution modeling, damage quantification, and model updating algorithm, respectively.

- Finally, Chapter 6 summarizes the results of the thesis, draw some conclusions, and provides some perspectives for future research in this field.

CHAPTER 2

LITERATURE REVIEW

2.1 Introduction

This chapter aims to summarize the literature related to the three topics of damage prognosis:

- Damage evolution modeling
- Damage quantification
- Model updating (mainly related to the particle filter method)

and to provide some perspectives on those issues being or to be studied in current practices. It is organized as follows: Section 2.2 discusses the use of a physics-based damage state or data-driven health indicator to characterize the damage level in the structure, and the corresponding damage evolution modeling. Section 2.3 presents the available work on damage quantification within the scope of prognostic studies. Section 2.4 introduces the strategies for updating the damage evolution models. Note that some open problems are provided at the end of each section.

2.2 Damage evolution modeling

The organization of this section follows the schematic diagram depicted in Figure 3. Initially, the author introduces the application of physics-based damage state or data-driven health indicators (HI) in prognostic investigations. Subsequently, three types of degradation models (or damage evolution models) and the probabilistic modeling are reviewed. Finally, the author presents a summary of open problems in this field that warrant further exploration.

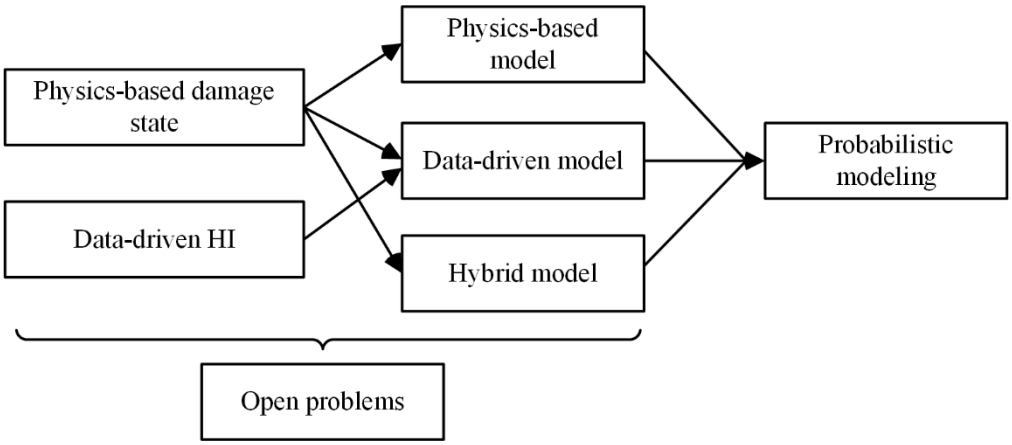

Figure 3 Summary of this section

Current studies on damage prognosis typically involve the description of damage occurring during the degradation process as a physics-based damage state [1-3] or a data-driven health indicator (HI) [4-7]. For such a damage state or HI to be effective, it must be predictable,

exhibiting a specific pattern under fatigue loading. Additionally, there should be a direct relationship between the state or HI and structural failure, such that the structure fails when the state or HI reaches a predefined threshold. In particular, the damage state should provide sufficient information for calculating the threshold through physical laws or numerical simulations, while the development of a robust HI under service conditions filled with uncertainties usually requires the implementation of advanced machine learning algorithms.

The former includes crack length [8], matrix cracking density [9, 10], delamination area or length [11], stiffness reduction [9, 10] in composites, and crack length [1-3] or shape [12] in metals. A significant advantage of this approach is its capacity to directly incorporate existing knowledge of physical mechanisms, which can contribute to fatigue degradation modeling and also the design of a proper threshold of structural failure. Furthermore, a more comprehensive understanding of the physical system can lead to further improvements in this regard [13]. HI can be viewed as an advanced statistical feature obtained from the SHM data like guided waves, fiber Bragg grating, or acoustic emission, and it shows the health (or damage) status of the structure or system under monitoring [4, 7]. Despite it can hardly be interpreted and realized in terms of an understandable connection to the physical implications, it has the potential to be designed and optimized based on the intended purposes, such as a HI evolution function considering the monotonicity, trendability and prognosability [5].

Since the evolution of either the damage state or HI under a particular service condition can exhibit a specific pattern, a proper model describing this pattern can predict future damage conditions. Depending on whether a physical law, fatigue damage data, or SHM data is used for modeling, damage evolution models can be classified as physics-based, data-driven, or hybrid, as detailed in Table 2. It is worth noting that the physical damage state can be used to develop all three types of models, while the HI for data-driven model only.

Table 2 Classification for fatigue damage evolution models.

Criteria	*Physics-based* model	*Data-driven* model (using damage state)	*Data-driven* model (using HI)	*Hybrid* model
Is a physical law directly used in the model?	Yes	No	NO	Yes
Is fatigue damage data or SHM data from a (or some) replication of testing structure mandatory for modeling?	No. But the damage data can be used for initialization.	Yes. Damage data	Yes. SHM data	Yes. Damage data

Note: (i) damage data refers to the direct measurement of physics-based damage state, e.g., fatigue crack lengths observed by the microscope, fatigue delamination measured by the ultrasonic C-scan; (ii) SHM data is taken as the data from any online SHM measurements system like guided waves, fiber Bragg grating, or acoustic emission that can indirectly quantify the damage state.

The physics-based model typically falls within the scope of Paris' law or its extensions, where the rate of damage evolution is considered as the stress intensity factor (SIF) for metal or the strain energy release rate (SERR) for composites. For a simple-shaped structure under a

specific loading condition, both the SIF [3, 14] and SERR [9, 10] can be calculated using an analytical law including the crack shape function, crack length, and applied fatigue stress. However, when dealing with more complex geometries or loading conditions in real-world applications, numerical methods like the finite element method are often used for calculation. Successful applications are mainly related to SIF calculation in metal, where, for computational efficiency, a surrogating model linking the SIF and damage level (mostly crack length) is usually built using polynomial fitting [1, 2], support vector regression [12], Gaussian process [8, 15], or neural networks [16]. Additionally, the degradation parameters like C and m in Paris' law can be obtained from literature or some standard tests, as illustrated in [14]. To produce a more accurate distribution of these parameters, one may also use fatigue damage data during the actual degradation process [2], although this is not always necessary.

When physical knowledge is insufficient to describe the evolution of damage, due to factors such as complex fatigue degradation or unknown loading conditions, an alternative is to build a data-driven model through a dataset of sufficient fatigue damage data [3, 17, 18] or structural health monitoring (SHM) data [4-6, 19]. The former [3, 17, 18] typically involves the direct measure of the physical damage state from one or more replications of the testing structure, which can then be used for data-driven modeling, such as crack growth [3] and stiffness reduction [18] depicted by neural networks, or delamination shape growth modeled by polynomial fitting functions [17]. It is important to note that this dataset can be derived from numerical simulations or experiments, meaning experimental fatigue damage data is not always necessary for data-driven modeling. This will be further elaborated on in Chapter 3.

In contrast, the latter approach [4-6, 19] involves extracting data-sensitive statistical features from SHM measurements, such as acoustic emission, strain, or acceleration. These features can be used directly as health indicators (HIs) or processed through machine learning algorithms to provide a HI, resulting in a database of HIs during the entire run-to-failure process for training an HI evolution model.

Hybrid modeling is often required when coupling well-understood and hard-to-model physics in fatigue damage propagation, such as in the case of corrosion-induced fatigue crack growth [20, 21]. In such cases, the authors have proposed a cumulative damage model that uses a physical law and a data-driven function to model the effect of external loading and corrosion on crack propagation, respectively.

Since hybrid modeling is still a relatively under-researched area, Table 3 provides a summary of the physics-based and data-driven damage evolution models discussed above. The table serves to briefly conclude the previous discussions and highlight the key features of each model.

Table 3 Summary of physics-based and data-driven damage evolution models used in current practices.

Is that used for modeling?	*Physics-based model*	*Data-driven model* (Damage state)	*Data-driven model* (Health indicator)
Damage state or health indicator	• Crack length [1-3, 14-16, 22, 23] and shape [12] in metal • Crack length [8], matrix cracking density [9, 10], delamination area or length [11], or stiffness reduction [9, 10] in composites.	• Crack length [3], crack depth [24] in metal • Matrix cracking density [25], delamination shape [17], or stiffness reduction [18, 25] in composites.	• HI can be taken as an advanced feature obtained from the SHM data, and it shows the health (or damage) status of the structure or system under monitoring [4, 7].
Physical law (Mainly Paris' law or its extension)	Yes	No	No
Another physical knowledge	Optional. Some studies [1, 2, 8, 12, 15, 16, 22, 23] resort to numerical simulations to calculate the SIF.	Optional. Numerical simulation of fatigue damage growth can be used for modeling (See Chapter 3).	No
Fatigue damage data	Optional. Some studies [1, 2] resort to those data for initializing the degradation parameters like C and m in Paris' law.	Yes. Either experimental or numerical data	No
SHM data	No. But this is required for indirect damage quantification and model updating.	No. But this is required for model updating.	Yes. Such as acoustic emission [4, 5], acceleration [6], or strain [7].
Data-driven algorithm	Optional. For example, a data-driven surrogating model is usually built through the numerically simulated SIFs at different crack lengths.	Yes. Such as polynomial fitting [17], Gaussian process, and neural network [3, 18, 25]	Yes. Such as Gaussian process [7] and neural network [4].

Note: (i) damage data refers to the direct measurement of physics-based damage state, e.g., fatigue crack lengths observed by the microscope, fatigue delamination measured by the ultrasonic C-scan; (ii) SHM data is taken as the data from any online SHM measurements system like guided waves, fiber Bragg grating, or acoustic emission that can indirectly quantify the damage state.

It is widely recognized that even under the same fatigue test, different specimens of the same structure can exhibit similar fatigue degradation behavior, but with different growth rates due to uncertainties arising from complex structural degradations and environmental effects [26, 27]. Therefore, the deterministic form of the model described above is unlikely to provide an accurate prognostic result. To improve their prognostic performance, a well-established strategy is to develop a probabilistic model with the model parameters set as unknown variables. These parameters can then be updated with the latest damage data through a state estimation technique such as the particle filter (PF).

The above discussions describe the procedure of transitioning from a damage state (or HI)-based deterministic model to a probabilistic model. The open problems arising from this process can be classified into four types, (i) selection of a suitable damage state or HI, (ii) insufficient physical knowledge, (iii) insufficient experimental data, and (iv) model fusion.

The first and foremost question is always selecting a proper damage state or HI. Regarding the former, the threshold of structural failure is usually predetermined in RUL calculation. To ensure safety, this threshold must be less than or at least equal to the smallest damage level leading to such failure among repeated tests. Little attention is paid to the uncertainties relating to the physics-based threshold. As to the latter, the performance of pure data-driven HI may be subjected to the quality of the SHM data. One possibility to enhance its performance may be to develop a hybrid HI combining both the damage and SHM data, which has yet to be explored.

The second problem relates to the insufficiency of physical knowledge to depict the degradation behavior, such as the coupling of multiple cracks in metal, coupling of multiple damage modes in composites, and fatigue growth accelerated by corrosion. One possible approach is to explore underlying physical knowledge or utilize a data-driven or hybrid model. The latter leads to the third issue of limited or no available experimental damage and SHM data. While advanced numerical tools may offer a solution, their potential remains largely untapped in prognostic investigations.

Finally, there is no universally best model, as each type of model has its pros and cons [28]. Even the same model can yield different prognostic performances when applied to different specimens of the same structure under the same fatigue test due to the uncertainties mentioned above. Therefore, the future of damage evolution modeling lies in an efficient fusion scheme containing a sufficient number of damage evolution models, which has received only limited attention in prognostic investigations [29, 30].

In summary, this section first discusses the use of physics-based damage states and data-driven health indicators in prognostic studies, then explains the three types of degradation models, namely physics-based, data-driven, and hybrid. Finally, the section concludes by presenting some open problems that require further investigation.

2.3 Damage quantification

Damage quantification involves measuring the severity of a physics-based damage state, such as crack length in metal or stiffness reduction in composites, through direct or indirect measurement systems. Note that the HI will not be discussed in this section. While many damage quantification methods have been proposed in SHM, this section will only review those only used for prognostic studies. Furthermore, the author will highlight three critical issues in current practices of indirect damage quantification, namely uncertainties, limited availability of experimental data, and feature fusion and selection.

Direct damage quantification involves a direct measure of the damage state. For example, the crack length in a metallic structure can be acquired by a caliper [3, 14], and the matrix cracking density and delamination length in composites can be measured by X-rays [9, 10, 31]. The corresponding damage quantification model (or measurement model) is usually a straightforward formulation where the measurement equals the damage state, with the possibility of additional measurement noise. It is also possible that the measurement system may have some deterministic errors. By including a bias parameter in that model, the error can be online estimated by a state estimation technique, having little effect on the estimation of other state components [32].

In many cases, damage cannot be directly measured and therefore, a damage quantification process is implemented through structural health monitoring (SHM) online measurement, which may include techniques such as fiber Bragg grating strain sensors [11, 22] or Lamb wave-based monitoring systems [23, 33, 34]. The collected data is then processed to extract one or more damage-sensitive statistical features, which are used to build a data-driven model that describes the relationship between the damage state and the extracted features. This approach has been successfully applied using various methods such as neural networks [11, 22], polynomial functions [34], the leave-one-out method [33], or Gaussian process regression [23]. However, there are still some open problems relating to indirect damage quantification to be explored.

Firstly, accounting for uncertainties arising from the sources like environmental effects and sensor errors is essential in building a reliable measurement model. A bias can occur between the measurements from a test specimen and those predicted by the model, leading to inaccurate damage estimation and prognosis. Such a problem is investigated only in a few prognostic studies [23, 35, 36], where the measurement model is either offline updated by a few direct measures of damage state [23] or online updated by the SHM measurement [2, 36].

Secondly, the limited availability of experimental data presents a significant challenge to data-driven damage quantification. An accurate mapping between the damage state and the features extracted from SHM measurements requires a large database of damage states and measurements collected during the run-to-failure process. However, due to high costs, such a database is rarely available. Only a few studies [1, 22] have explored the use of numerically simulated SHM measurements at different damage levels to construct a dataset.

Finally, the selection of a proper statistical feature is critical to the prognostic performance of the measurement model. Identifying the best feature among multiple features may vary in different replications of the same structure or even at different time instants during damage progression on the same structure or specimen. Therefore, an integrated framework that fuses multiple features (feature fusion) and online selects the best ones (feature selection) for identifying the current damage state is necessary. However, this issue has received little attention in pure damage quantification studies [37, 38].

In summary, while direct damage quantification is relatively straightforward, indirect damage quantification presents several challenges that need to be addressed to build a reliable measurement model for SHM and prognostic studies. Addressing issues such as uncertainties, limited availability of experimental data, and feature selection and fusion will be crucial in developing accurate and reliable damage quantification schemes in the prognostic study.

2.4 Particle filter-based model updating

This section presents an overview of the state space modeling in the prognostic application, as well as an introduction to the particle filter (PF) and its limitations. Additionally, the section discusses the improvements made to the PF algorithm.

Let us consider that a discrete form of damage evolution model can be described as

$$x_k = f(x_{k-1}, \boldsymbol{\theta}) \tag{1}$$

where x is the damage state, $\boldsymbol{\theta}$ is a vector including the parameters governing the damage evolution, the subscript k is the discrete time step, and the function $f(\cdot)$ can be a physics-based or data-driven function. The parameters $\boldsymbol{\theta}$ can vary in different specimens of the same structure due to the uncertainties in the damage evolution process, a deterministic evolution model may hardly provide accurate prognosis results.

To overcome this problem, according to the common practices in PF-based prognosis, the parameters $\boldsymbol{\theta}$ should also be taken as unknown variables to be online updated. If a direct damage quantification is pursued, the prognostic model can be built in state space as [14]

$$\begin{cases} \begin{bmatrix} \boldsymbol{\theta}_k \\ x_k \end{bmatrix} = \begin{bmatrix} \boldsymbol{\theta}_{k-1} + \boldsymbol{\omega}_{\theta,k} \\ f(x_{k-1}, \boldsymbol{\theta}_k, \omega_k) \end{bmatrix} \\ y_k = x_k + \nu_k \end{cases} \tag{2}$$

where the measurement y denotes a direct measure of damage state, ω and $\boldsymbol{\omega}_\theta$ are the process noises for the damage state and the parameters, respectively, and ν represents the measurement noise. Eq. (2) also has another version [3, 17], i.e.,

$$\begin{cases} \boldsymbol{\theta}_k = \boldsymbol{\theta}_{k-1} + \boldsymbol{\omega}_{\theta,k} \\ x_k = f(x_{k-1}, \boldsymbol{\theta}_k) + \nu_k \end{cases} \tag{3}$$

The prognostic model in case of indirect damage measurement is usually built as [1, 2, 36]

$$\begin{cases} \boldsymbol{z}_k = \begin{bmatrix} \boldsymbol{\theta}_k \\ x_k \\ \boldsymbol{\gamma}_k \end{bmatrix} = \begin{bmatrix} \boldsymbol{\theta}_{k-1} + \boldsymbol{\omega}_{\theta,k} \\ f(x_{k-1}, \boldsymbol{\theta}_k, \omega_k) \\ \boldsymbol{\gamma}_{k-1} + \boldsymbol{\omega}_{\gamma,k} \end{bmatrix} \\ y_k = g(x_k, \boldsymbol{\gamma}_k) + v_k \end{cases} \tag{4}$$

where the function g (·) describes the relationship between the damage state and the measurement, $\boldsymbol{\gamma}$ is a vector of its function parameters, $\boldsymbol{\omega}_\gamma$ is its process noise, and $\boldsymbol{z}$ is the state vector with both the damage state and the model parameters included.

Let us take Eq. (4) as a reference example. In a Bayesian framework, the unknown state vector at k-th step $\boldsymbol{z}_k$ is inferred based on a sequence of sensor observations as

$$p(\boldsymbol{z}_k|\boldsymbol{y}_{1:k-1}) = \int p(\boldsymbol{z}_k|\boldsymbol{z}_{k-1}) p(\boldsymbol{z}_{k-1}|\boldsymbol{y}_{1:k-1}) d\boldsymbol{z}_{k-1} \tag{5}$$

$$p(\boldsymbol{z}_k|\boldsymbol{y}_{1:k}) \propto p(y_k|\boldsymbol{z}_k) p(\boldsymbol{z}_k|\boldsymbol{y}_{1:k-1}) \tag{6}$$

where $\boldsymbol{y}_{1:k}$ are the measurements collected from time step 1 to k, the transition distribution $p(\boldsymbol{z}_k|\boldsymbol{z}_{k-1})$ and the likelihood function $p(y_k|\boldsymbol{z}_k)$ are obtained from the process and measurement equations, respectively, $p(\boldsymbol{z}_k|\boldsymbol{y}_{1:k-1})$ and $p(\boldsymbol{z}_k|\boldsymbol{y}_{1:k})$ are the prior and the posterior probability distribution functions (PDF) of the variables in the state vector, respectively, and $\propto$ denotes the proportionality.

Eqs. (5) and (6) form the basis for the optimal Bayesian solution, which is however difficult to be analytically calculated in a nonlinear and non-Gaussian system as it happens in many problems of practical interest. Therefore, the sampling importance resampling (SIR) PF [39] is usually used in the prognostic investigation to provide an approximated solution for $p(\boldsymbol{z}_k|\boldsymbol{y}_{1:k})$, as showed in Figure 4 and Table 4.

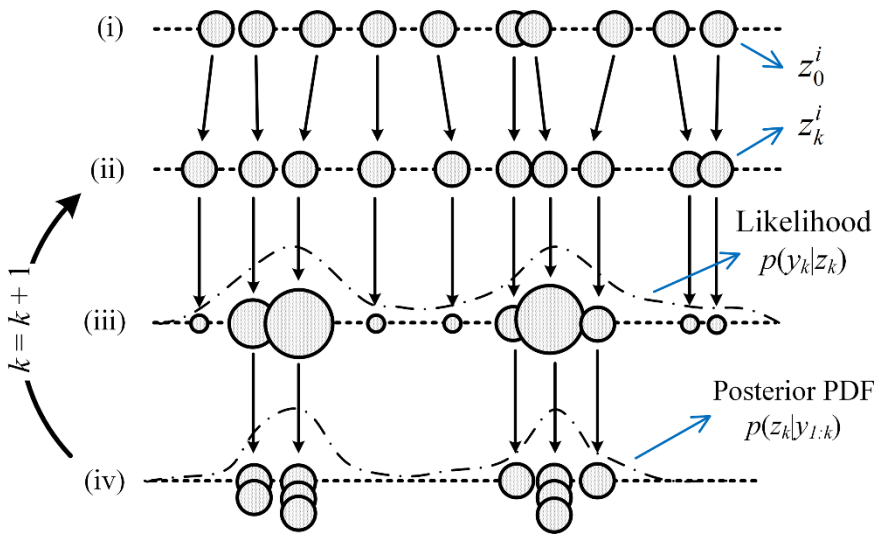

Figure 4 Sampling importance resampling (SIR) particle filter [40]

Table 4 Sampling importance resampling particle filter

(i) **Initialization**: draw N_p particles $\{\boldsymbol{z}_{l,0}^i: i = 1,2,\dots,N_p\}$ from the distribution $p(\boldsymbol{z}_{l,0})$

For *k*=1, 2, …,

(ii) **Prediction** in PF: draw N_p particles $\{\boldsymbol{z}_{l,k}^i: i = 1,2,\dots,N_p\}$ by $\boldsymbol{z}_k^i \sim p(\boldsymbol{z}_{l,k}|\boldsymbol{z}_{l,k-1}^i)$

(iii) **Weight update**: calculate the particle weight w_k^i through $w_k^i \propto p(\boldsymbol{y}_k|\boldsymbol{z}_{l,k}^i)$, and assign its normalized form $\widetilde{w}_k^i$ to each particle $\boldsymbol{z}_{l,k}^i$

(iv) **Resample** for those particles based on the normalized weights

End

Despite many successful applications of PF in prognostic practices, PF still suffers from many drawbacks, as outlined in Table 5. There are very few prognostic studies are dedicated to those issues, such as [41] for particle impoverishment and [14] for process noise definition.

Table 5 A list of drawbacks of PF in current SHM practices

Drawback	**Quote**
Large computational cost	• A significant drawback is the fact that depending on the problem, a large number of samples may be required, thus making the PF analysis computationally expensive [40]. • A disadvantage of the PF technique is that it is computationally expensive [42]. • The relatively high computational cost of PF is sometimes the major concern [43].
Curse of dimensionality	• PF is known to behave poorly in high dimensional spaces, especially when static parameters are added to the state vector [44]. • Number of particles needs to have an acceptable approximation explodes with the dimension of the state which makes the standard particle filter inefficient for high dimensional systems [45].
Particle impoverishment	• This method is faced with what is referred to as the sample impoverishment problem, which essentially refers to the loss of diversity among particles as the analysis progresses [40].
Difficulty in calibration for process noise	• Additional uncertainties are artificially added to model parameters, which ultimately influences the precision of the state estimation [10]. • Some process noise formulations might cause inefficiency in the algorithm [14].

References

[1] T. Li, L. Lomazzi, F. Cadini, C. Sbarufatti, J. Chen, S. Yuan, Numerical simulation-aided particle filter-based damage prognosis using Lamb waves, Mechanical Systems and Signal Processing, 178 (2022) 109326.

[2] T. Li, C. Sbarufatti, F. Cadini, J. Chen, S. Yuan, Particle filter-based hybrid damage prognosis considering measurement bias, Structural Control and Health Monitoring, n/a (2021) e2914.

[3] F. Cadini, C. Sbarufatti, M. Corbetta, F. Cancelliere, M. Giglio, Particle filtering-based adaptive training of neural networks for real-time structural damage diagnosis and prognosis, Structural Control and Health Monitoring, 26 (2019).

[4] M. Moradi, A. Broer, J. Chiachío, R. Benedictus, T.H. Loutas, D. Zarouchas, Intelligent health indicator construction for prognostics of composite structures utilizing a semi-supervised deep neural network and SHM data, Engineering Applications of Artificial Intelligence, 117 (2023) 105502.

[5] N. Eleftheroglou, D. Zarouchas, R. Benedictus, An adaptive probabilistic data-driven methodology for prognosis of the fatigue life of composite structures, Composite Structures, 245 (2020) 112386.

[6] X. Liu, Y. Lei, N. Li, X. Si, X. Li, RUL prediction of machinery using convolutional-vector fusion network through multi-feature dynamic weighting, Mechanical Systems and Signal Processing, 185 (2023) 109788.

[7] G. Galanopoulos, N. Eleftheroglou, D. Milanoski, A. Broer, D. Zarouchas, T. Loutas, A novel strain-based health indicator for the remaining useful life estimation of degrading composite structures, Composite Structures, 306 (2023) 116579.

[8] S. Datta, R.K. Neerukatti, A. Chattopadhyay, Buckypaper embedded self-sensing composite for real-time fatigue damage diagnosis and prognosis, Carbon, 139 (2018) 353-360.

[9] M. Chiachío, J. Chiachío, S. Sankararaman, K. Goebel, J. Andrews, A new algorithm for prognostics using Subset Simulation, Reliability Engineering & System Safety, 168 (2017) 189-199.

[10] J. Chiachío, M. Chiachío, S. Sankararaman, A. Saxena, K. Goebel, Condition-based prediction of time-dependent reliability in composites, Reliability Engineering & System Safety, 142 (2015) 134-147.

[11] D. Cristiani, C. Sbarufatti, M. Giglio, Damage diagnosis and prognosis in composite double cantilever beam coupons by particle filtering and surrogate modelling, Structural Health Monitoring, (2020) 1475921720960067.

[12] X. Zhou, S. He, L. Dong, S.N. Atluri, Real-Time Prediction of Probabilistic Crack Growth with a Helicopter Component Digital Twin, AIAA Journal, 60 (2022) 2555-2567.

[13] J.Z. Sikorska, M. Hodkiewicz, L. Ma, Prognostic modelling options for remaining useful life estimation by industry, Mechanical Systems and Signal Processing, 25 (2011) 1803-1836.

[14] M. Corbetta, C. Sbarufatti, M. Giglio, M.D. Todd, Optimization of nonlinear, non-Gaussian Bayesian filtering for diagnosis and prognosis of monotonic degradation processes, Mechanical Systems and Signal Processing, 104 (2018) 305-322.

[15] R.K. Neerukatti, A. Chattopadhyay, N. Iyyer, N. Phan, A hybrid prognosis model for predicting fatigue crack propagation under biaxial in-phase and out-of-phase loading, Structural Health Monitoring, 17 (2017) 888-901.

[16] F. Zhao, X. Zhou, C. Wang, L. Dong, S.N. Atluri, Setting Adaptive Inspection Intervals in Helicopter Components, Based on a Digital Twin, AIAA Journal, (2023) 1-14.

[17] T. Li, F. Cadini, M. Chiachío, J. Chiachío, C. Sbarufatti, Particle filter-based delamination shape prediction in composites subjected to fatigue loading, Structural Health Monitoring, (2022) 14759217221116041.

[18] C. Tao, C. Zhang, H. Ji, J. Qiu, Application of neural network to model stiffness degradation for composite laminates under cyclic loadings, Composites Science and Technology, 203 (2021) 108573.

[19] S. Buchaiah, P. Shakya, Bearing fault diagnosis and prognosis using data fusion based feature extraction and feature selection, Measurement, 188 (2022) 110506.

[20] A. Dourado, F. Viana, Ensemble of hybrid neural networks to compensate for epistemic uncertainties: a case study in system prognosis, Soft Computing, 26 (2022) 6157-6173.

[21] A. Dourado, F.A.C. Viana, Physics-Informed Neural Networks for Missing Physics Estimation in Cumulative Damage Models: A Case Study in Corrosion Fatigue, Journal of Computing and Information Science in Engineering, 20 (2020).

[22] D. Cristiani, C. Sbarufatti, F. Cadini, M. Giglio, Fatigue damage diagnosis and prognosis of an aeronautical structure based on surrogate modelling and particle filter, Structural Health Monitoring, 0 1475921720971551.
[23] J. Chen, S. Yuan, H. Wang, On-line updating Gaussian process measurement model for crack prognosis using the particle filter, Mechanical Systems and Signal Processing, 140 (2020) 106646.
[24] P. Baraldi, M. Compare, S. Sauco, E. Zio, Ensemble neural network-based particle filtering for prognostics, Mechanical Systems and Signal Processing, 41 (2013) 288-300.
[25] J. Fernández, M. Chiachío, J. Chiachío, R. Muñoz, F. Herrera, Uncertainty quantification in Neural Networks by Approximate Bayesian Computation: Application to fatigue in composite materials, Engineering Applications of Artificial Intelligence, 107 (2022) 104511.
[26] I. Lopez, N. Sarigul-Klijn, A review of uncertainty in flight vehicle structural damage monitoring, diagnosis and control: Challenges and opportunities, Progress in Aerospace Sciences, 46 (2010) 247-273.
[27] P. Baraldi, F. Mangili, E. Zio, Investigation of uncertainty treatment capability of model-based and data-driven prognostic methods using simulated data, Reliability Engineering & System Safety, 112 (2013) 94-108.
[28] Y. Lei, N. Li, L. Guo, N. Li, T. Yan, J. Lin, Machinery health prognostics: A systematic review from data acquisition to RUL prediction, Mechanical Systems and Signal Processing, 104 (2018) 799-834.
[29] J. Chiachío, M. Chiachío, A. Saxena, S. Sankararaman, G. Rus, K. Goebel, Bayesian model selection and parameter estimation for fatigue damage progression models in composites, International Journal of Fatigue, 70 (2015) 361-373.
[30] X. Guan, R. Jha, Y. Liu, Model selection, updating, and averaging for probabilistic fatigue damage prognosis, Structural Safety, 33 (2011) 242-249.
[31] M. Corbetta, C. Sbarufatti, M. Giglio, A. Saxena, K. Goebel, A Bayesian framework for fatigue life prediction of composite laminates under co-existing matrix cracks and delamination, Composite Structures, 187 (2018) 58-70.
[32] D. An, J.-H. Choi, N.H. Kim, Identification of correlated damage parameters under noise and bias using Bayesian inference, Structural Health Monitoring, 11 (2011) 293-303.
[33] J. Chen, S. Yuan, X. Jin, On-line prognosis of fatigue cracking via a regularized particle filter and guided wave monitoring, Mechanical Systems and Signal Processing, 131 (2019) 1-17.
[34] T. Li, C. Sbarufatti, F. Cadini, J. Chen, S. Yuan, Particle filter-based hybrid damage prognosis considering measurement bias, Strctural Control and Health Monitoring, (2nd-Round Under Review).
[35] M.E. Orchard, G.J. Vachtsevanos, A particle-filtering approach for on-line fault diagnosis and failure prognosis, Transactions of the Institute of Measurement and Control, 31 (2009) 221-246.
[36] E. Rabiei, E.L. Droguett, M. Modarres, Fully Adaptive Particle Filtering Algorithm for Damage Diagnosis and Prognosis, Entropy, 20 (2018).
[37] D. Song, F. Xu, T. Ma, Crack damage monitoring for compressor blades based on acoustic emission with novel feature and hybridized feature selection, Structural Health Monitoring, (2022) 14759217211068107.
[38] A. Broer, G. Galanopoulos, R. Benedictus, T. Loutas, D. Zarouchas, Fusion-based damage diagnostics for stiffened composite panels, Structural Health Monitoring, 21 (2021) 613-639.
[39] M.S. Arulampalam, S. Maskell, N. Gordon, T. Clapp, A tutorial on particle filters for online nonlinear/non-Gaussian Bayesian tracking, IEEE Transactions on Signal Processing, 50 (2002) 174-188.
[40] E.N. Chatzi, A.W. Smyth, Particle filter scheme with mutation for the estimation of time-invariant parameters in structural health monitoring applications, Structural Control & Health Monitoring, 20 (2013) 1081–1095.
[41] J. Chen, S. Yuan, C. Sbarufatti, X. Jin, Dual crack growth prognosis by using a mixture proposal particle filter and on-line crack monitoring, Reliability Engineering & System Safety, 215 (2021) 107758.
[42] J. Ching, J.L. Beck, K.A. Porter, Bayesian state and parameter estimation of uncertain dynamical systems, Probabilistic Engineering Mechanics, 21 (2006) 81-96.
[43] S. Sen, A. Crinière, L. Mevel, F. Cérou, J. Dumoulin, Seismic-induced damage detection through parallel force and parameter estimation using an improved interacting Particle-Kalman filter, Mechanical Systems and Signal Processing, 110 (2018) 231-247.

[44] A. Olivier, A.W. Smyth, Particle filtering and marginalization for parameter identification in structural systems, Structural Control and Health Monitoring, 24 (2017) e1874.
[45] M. Zghal, L. Mevel, P. Del Moral, Modal parameter estimation using interacting Kalman filter, Mechanical Systems and Signal Processing, 47 (2014) 139-150.

CHAPTER 3

DAMAGE EVOLUTION MODELING

Chapter 3 illustrates how the author proceeds with robust damage prognosis from the perspective of *damage evolution modeling*. Targeting the three fundamental questions, namely the selection of proper damage state, insufficient experimental damage data, and model fusion, this chapter has three corresponding contributions.

Firstly, a method for predicting the delamination shape growth is proposed and validated by the composite fatigue test with ultrasonic C-scan monitoring. Then, a dataset containing sufficiently enough delamination images is created by some numerical simulation of fatigue delamination growth in composites. Finally, a method by fusing multiple physics-based or data-driven damage evolution models is proposed to enhance the prognostic performance, and validated by an aluminum fatigue test with Lamb wave monitoring.

Check for updates

Original Article

Structural Health Monitoring
1–19
© The Author(s) 2022
Article reuse guidelines:
sagepub.com/journals-permissions
DOI: 10.1177/14759217221116041
journals.sagepub.com/home/shm
SAGE

Particle filter-based delamination shape prediction in composites subjected to fatigue loading

Tianzhi Li[1], Francesco Cadini[1], Manuel Chiachío[2,3], Juan Chiachío[2,3] and Claudio Sbarufatti[1]

Abstract

Modeling generic size features of delamination, such as area or length, has long been considered in the literature for damage prognosis in composites through specific models describing damage state evolution with load cycles or time. However, the delamination shape has never been considered, despite that it holds important information for damage diagnosis and prognosis, including the delamination area, its center, and perimeter, useful for structural safety evaluation. In this context, this paper develops a novel particle filter (PF)-based framework for delamination shape prediction. To this end, the delamination image is discretized by a mesh, where control points are defined as intersections between the grid lines and the perimeter of the delamination. A parametric data-driven function maps each point position as a function of the load cycles and is initially fitted on a sample test. Then, a PF is independently implemented for each node whereby to predict their future positions along the mesh lines, thus allowing delamination shape progression estimates. The new framework is demonstrated with reference to experimental tests of fatigue delamination growth in composite panels with ultrasonics C-scan monitoring.

Keywords

Composite, damage prognosis, particle filter, fatigue delamination, shape prediction

Introduction

Composites have been widely used in numerous industries due to their striking benefits such as high strength-to-weight ratio and corrosion resistance, yet they suffer from multiple damage processes, among which fatigue degradation is one of the most common. The degradation initially results in internal damages such as matrix cracking and delamination and eventually brings to fiber, yet catastrophic, failure. To timely avoid this issue, inspections are usually required for evaluating the damage state in composites, often resulting in service disruption and therefore high maintenance costs. One desirable scenario for ensuring structural integrity while keeping maintenance costs at a minimum is to schedule the maintenance just before the damage reaches a critical limit. To this end, an advanced damage prognosis technology is required to provide an anticipated and accurate picture of the future state of damage.

Current damage prognosis practices in composites usually have considered several physics-based damage modes observed during the degradation process, including matrix crack density,[1] delamination length or area,[2,3] crack length,[4] and stiffness reduction,[1,2,5,6] or damage-sensitive statistical features extracted from measured signals, such as normalized cumulative energy[7] and cumulative risetime and amplitude.[8] They are based on the fact that damage evolution with load cycles or time under a certain service condition follows a specific pattern; thus, the future condition can be calculated by the current state through a proper model depicting such a pattern. From the perspective of the type of information used for modeling the degradation behavior in composites, namely physical knowledge or experimental and in-field data, damage evolution

[1]Dipartimento di Meccanica, Politecnico di Milano, Milan, Italy
[2]Department of Structural Mechanics and Hydraulic Engineering, University of Granada, Granada, Spain
[3]Andalusian Research Institute in Data Science and Computational Intelligence, Granada, Spain

Corresponding author:
Claudio Sbarufatti, Dipartimento di Meccanica, Politecnico di Milano, via La Masa, 1, Milan 20156, Italy.
Email: claudio.sbarufatti@polimi.it

models can be classified either as physics based[1–5] or data driven.[6–8] The former ones generally lie within the scope of Paris' law or its extensions, where the rate of damage evolution (e.g., strain energy release rate or stress intensity factor) is analytically calculated[1–3,5] or fitted from numerical simulations through a data-driven modeling strategy such as Gaussian process.[4] On the other hand, the data-driven approaches, for example, using neural networks[6] or Markov models,[7,8] resort to sufficient damage data or statistical features extracted from measured signals during the actual degradation process for describing the above relationship.

In practice, the efficiency of any damage evolution model is case specific, and in general, they provide good results under a number of assumptions.[9–11] However, their capability to account for the uncertainties arising from complex structural degradations, environmental effects, and sensor health conditions is limited.[12,13] A well-acknowledged strategy to improve their prognostic performance with consideration of the uncertainty is to set the model parameters as unknown state variables to be updated using data by a state estimation technique, such as the particle filter (PF), given its versatility for nonlinear and non-Gaussian problems[14–16] and also its demonstrated performance for damage prognosis.[2,3,17] The latter implies quantifying the current damage state through a direct or indirect measurement system, depending on whether the damage state can be directly measured or not. More specifically, if a direct measure of the damage is pursued, for example, by observing the matrix crack density and delamination area through X-ray[1,2] or the stiffness reduction by strain observations,[1,2] the measurement model will be a simple formulation with the observation equal to the damage state, possibly corrupted by measurement noise. In the case of indirect damage observation, an analytical[4] or data-driven function[3] is required to describe the relationship between the internal damage state and the external observations, for example, relating any local strain[3] or distributed scatter[15] feature to the damage.

Within the referred approaches, delamination prognosis has attracted the attention of the research community due to its threats to structural integrity with invisible warnings.[2,3] However, delamination shape has never been considered, although it holds important information for damage diagnosis and prognosis, including the delamination area, its center, and perimeter, useful for damage growth rate prediction, and finally, structural safety evaluation. Similar to other damage state variables, the progress of delamination shape under a certain loading condition also follows a specific pattern,[18] which can be directly observed by X-ray[5] and ultrasonic C-scan[19,20] or indirectly reconstructed from digital image correlation[20] and guided waves.[19,21]

This paper, therefore, develops a novel PF-based delamination shape prediction framework, where C-scan is adopted for delamination imaging. The delamination shape, rather than its area or a specific length, serves as the damage state to be predicted, thus limiting the loss of useful information for prognosis. More specifically, considering the delamination shape is described by some artificially defined control points (CPs), that is, the intersections between some grid mesh lines and the perimeter of the delamination, the motion of each CP can be modeled with a data-driven parametric function, whose parameters are online updated by a PF. The future position of each CP can be located through the updated models and then adopted to reconstruct the future delamination shape. This method is demonstrated with reference to experimental tests of fatigue delamination growth in composite panels with ultrasonics C-scan monitoring.

The rest of this paper is organized as follows: section "Delamination shape prediction" gives the methodological details of the proposed framework, including the mesh discretization, the evolution model, and the PF framework for damage shape prediction. The validation of the proposed method by an experiment is given in section "Application." Finally, section "Conclusion" concludes this paper with some topics for future work.

Delamination shape prediction

The proposed framework consists of four main steps, namely, (i) defining the mesh nodes and lines for discretizing the delamination shape, (ii) modeling the evolution for each node, (iii) independently updating the evolution parameters of each model through PF, and (iv) calculating the future delamination shape.

Delamination shape discretization

This study assumes that a delamination image is available through a C-scan monitoring system, or similar technique, as presented in Figure 1(a). Figure 1(b) shows the image segmented by some grid lines, whose layout, that is, the locations of the 18 cross-markers, is kept constant during delamination evolution. Note that a number of CPs are located where the grid lines intersect the delamination perimeter, whereas one control length (CL) is taken as the distance between one CP and one corresponding cross marker, for example, CP4, CP14, CL4, and CL14 in Figure 1(c).

Since the delamination shape in composites under fatigue loading can grow with a specific pattern,[18] the motion of each CP along its corresponding grid line, namely the evolution of each CL, is assumed to follow

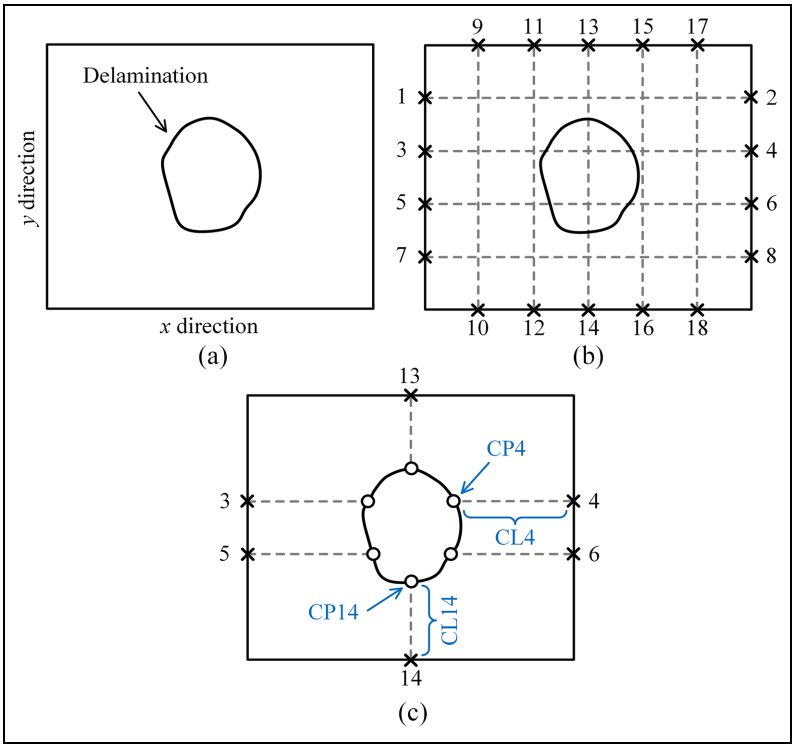

Figure 1. Definition of CPs and CLs in a delamination image: (a) delamination image, (b) grid lines, and (c) CPs and CLs.
CP: control point; CL: control length.

a certain law, as will be validated in section "Image processing." In this context, the delamination shape prediction problem is reduced to the predictions of these CLs, thus requiring a proper model to describe the evolution of each CL, as well as a state estimation technique to update the model parameters for predicting the future states. Note that, during damage progression, the delamination perimeter will intersect more and more mesh lines, thus increasing the number of CLs and, thus, their relative evolution models. Note that, in this preliminary application, each model is independently updated, under the assumption of the independent evolution of each CL. However, the method could be extended to consider the correlation among CLs' evolutions, which is a matter of future research by the authors.

Definition of evolution models

Let us assume the evolution of the lth CL can be modeled as

$$z_{l,k} = f_l(N_k, \boldsymbol{\theta}_l) \tag{1}$$

where the subscript k means the kth time step, z_l is the CL, N_k is the difference in the number of load cycles between the step of the CL occurrence (zero for all CLs in this study) and the time step k, $f_l(\cdot)$ is a data-driven function governing the length evolution with the number of load cycles, and $\boldsymbol{\theta}_l$ is a vector of model parameters.

Given the uncertainties in the delamination growth, the parameters $\boldsymbol{\theta}_l$ are assumed to vary in different specimens of the same structure, and they should be taken as uncertain components to be added in the state vector for online updating, based on a state-space model including the process and measurement equations, as follows:

$$\begin{cases} \boldsymbol{\theta}_{l,k} = \boldsymbol{\theta}_{l,k-1} + \boldsymbol{\omega}_{l,k} \\ z_{l,k} = f_l(N_k, \boldsymbol{\theta}_{l,k}) + \nu_{l,k} \end{cases} \tag{2}$$

In the last equations, $\boldsymbol{\omega}$ and ν are the process and measurement noises, respectively. Note that the state-space model for other CL is the same formulated as above; thus, the amount of models utilized for shape prediction at kth step equals that of CLs that are active at that step. Each model will be embedded into an online PF-based scheme due to the assumption of the independent evolution for each CL.

This choice of the state-space, which, as already stated, is also driven by the lack of reliable physics-based descriptions of the delamination shape evolution in composite materials, intuitively allows estimating

Table 1. SIR PF for one CL.

Initialization: draw N_p particles $\{\boldsymbol{\theta}_{l,0}^i: i=1,2,\ldots,N_p\}$ from the initial distribution $p(\boldsymbol{\theta}_{l,0})$
For k = 1, 2,…,
  Prediction in PF: draw N_p particles $\{\boldsymbol{\theta}_{l,k}^i: i=1,2,\ldots,N_p\}$ by $\boldsymbol{\theta}_{l,k}^i \sim p(\boldsymbol{\theta}_{l,k}|\boldsymbol{\theta}_{l,k-1}^i)$
  Weight update: calculate the weight w_k^i by $w_k^i \propto p(z_{l,k}|\boldsymbol{\theta}_{l,k}^i)$, and assign its normalized form $\tilde{w}_k^i$ to each particle $\boldsymbol{\theta}_{l,k}^i$
  Resample for $\{\boldsymbol{\theta}_{l,k}^i: i=1,2,\ldots,N_p\}$ using the particle weights $\{\tilde{w}_k^i: i=1,2,\ldots,N_p\}$
  Approximate the estimate $\hat{\boldsymbol{\theta}}_{l,k}$ as $\hat{\boldsymbol{\theta}}_{i,k} = \frac{1}{N_p}\sum_{i=1}^{N_p} \boldsymbol{\theta}_{l,k}^i$
End

CL: control length; PF: particle filter; SIR: sampling importance resampling.

the parameters of a fitting curve describing the progression of the shape with the number of load cycles. Then, at a given load cycle, the most updated estimates of those parameters (in the form of a particle swarm) are used to project the future CLs, and finally to reconstruct the future delamination shape. The use of a PF allows casting this problem into a sequential Bayesian parameter estimation framework, very convenient for online, real-time applications. At the same time, the use of a zero-mean random walk as artificial dynamics for the augmented states representing the possibly constant parameters allows for a certain degree of adaptability of the filter with respect to both training on delamination dynamics different from the current one and sudden changes in the progression behavior, as shown, for example, in some works by some of the same authors.[22,23]

To be a little more specific, uncertainties (or unknowns) from multiple sources such as undetected flaws and environmental effects usually result in different fatigue delamination growths (or more generally, different state evolutions), as shown by the three specimens later. Most uncertainties can hardly be directly embedded into a model, for example, we can hardly find a model with a parameter describing an undetected flaw included. As also described above, the effects of uncertainties on damage growth (or state evolution) are then addressed automatically in the PF framework by online updating the parameters of the damage growth (or state evolution) model, as validated in many other damage prognosis investigations, for example, in Cadini et al.[22] and Sbarufatti et al.[23]

PF-based model updating

Following a Bayesian approach, the unknown state vector at kth step $\boldsymbol{\theta}_{l,k}$ can be inferred from the measurement, as follows:

$$p(\boldsymbol{\theta}_{l,k}|z_{l,1:k-1}) = \int p(\boldsymbol{\theta}_{l,k}|\boldsymbol{\theta}_{l,k-1}) p(\boldsymbol{\theta}_{l,k-1}|z_{l,1:k-1}) d\boldsymbol{\theta}_{l,k-1} \tag{3}$$

$$p(\boldsymbol{\theta}_{l,k}|z_{l,1:k}) \propto p(z_{l,k}|\boldsymbol{\theta}_{l,k}) p(\boldsymbol{\theta}_{l,k}|z_{l,1:k-1}) \tag{4}$$

Table 2. Calculation of future lth CL.

For i = 1: N_p
  For j = 1, 2, 3, …
  Calculate future $z_{l,k}^{i,j}$ as $z_{l,k}^{i,j} = f_l(N_{k+j}, \boldsymbol{\theta}_{l,k}^i)$
  End
End

CL: control length.

where $z_{l:k}$ are the measurements collected from time step 1 to k, the terms $p(\boldsymbol{\theta}_{l,k}|\boldsymbol{\theta}_{l,k-1})$ and $p(z_{l,k}|\boldsymbol{\theta}_{l,k})$ stand for the transition distribution and the likelihood function, which are driven by the process and measurement equations, respectively, and finally $p(\boldsymbol{\theta}_{l,k}|z_{l:k-1})$ and $p(\boldsymbol{\theta}_{l,k}|z_{l:k})$ are the prior and posterior probability distribution functions, respectively.

Equations (3) and (4) form the basis for the optimal Bayesian solution, which is rarely possible to be analytically calculated in a nonlinear and non-Gaussian system. Therefore, the sampling importance resampling (SIR) PF[24,25] is used in this study as an efficient and general state estimation technique. Table 1 lists a pseudo-code implementation of the SIR PF for one CL. Note that, at each time step, a number of PFs equal to the number of active CLs are running in parallel and independently.

Future delamination shape prediction

The target of this structural health monitoring (SHM) application is that of predicting the future CLs based on the updated PF estimates, then locating the future CPs, and finally constructing the future delamination shapes. Thus, by combining the evolution model by Equation (1) and the kth posterior distribution of its parameters $p(\boldsymbol{\theta}_{l,k}|z_{l,1:k})$, the jth step ahead of the lth CL $z_{l,k}^j$ can be calculated as in Table 2.

Figure 2 reveals how this method works for one future step, while the same procedure also applies to all the other future steps. Figure 2(a) shows the means and 95% confidence boundaries (CBs) of the predicted CLs

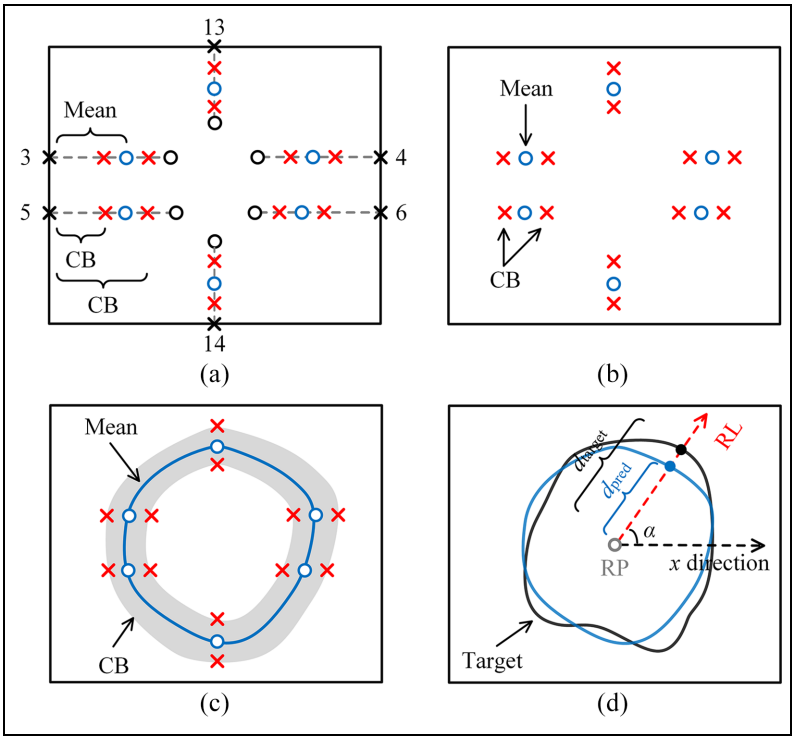

Figure 2. Future shape prediction procedure and performance evaluation: (a) predicted CLs, (b) predicted CPs, (c) predicted shape, and (d) performance metric.
"CL," "CP," "CB," "RP," and "RL" mean "control length," "control point," "confidence boundary," "reference point," and "reference line," respectively.

after one step, which can then be used for locating the corresponding CPs, as plotted in Figure 2(b). By resorting to a curve fitting strategy, that is, the MATLAB® function "cscvn," the delamination shape can be constructed by these discrete CPs, as shown in Figure 2(c). Note that a simple rule will be used to merge these discrete CBs into a global CB for delamination shape: those lying within the mean delamination shape will be adopted for building the lower global CB of delamination shape, while those outside the mean shape are used for upper global CB.

Finally, inspired by the cumulative relative accuracy (CRA) in Saxena et al.,[26] a new CRA is developed in this study to evaluate the accuracy of the shape predicted at jth ahead step based on the estimates at kth step as,

$$\mathrm{CRA}_{k,j} = \frac{1}{N_r}\sum_{q=1}^{N_r}\left(1 - \frac{\left|d_{\mathrm{target}}^{k,j,q} - d_{\mathrm{pred}}^{k,j,q}\right|}{d_{\mathrm{target}}^{k,j,q}}\right) \tag{5}$$

where N_r means the number of reference lines (RLs), each of which is a ray starting at the reference point (RP, simply defined as the center of the image in this study) with a certain angle α to the x-direction, d_{target} is the distance between the RP and the target shape perimeter along with a specific RL, whereas d_{pred} is the distance between the RP and the predicted shape perimeter, as shown in Figure 2(d). Note that the CRA indicator should lie in the $[-\infty,1]$ interval, where a higher CRA means a more accurate prediction, and vice versa.

Application

The context of the engineering application of this manuscript is given in this subsection, along with information on the source of the data used and how they have been processed for reproducibility.

Experimental setup

The proposed framework is applied to fatigue cycling data obtained from a set of run-to-failure fatigue experiments in cross-ply carbon–epoxy laminates. The tests were conducted using a servo-hydraulic *Instron/Schenk*® 100 kN tension–tension test machine with hydraulic clamps (see Figure 3(a)). Cycom 977-2-35-12 k HTS (Solvay, Germany) pre-impregnated (commonly known as *prepreg*) material was used for

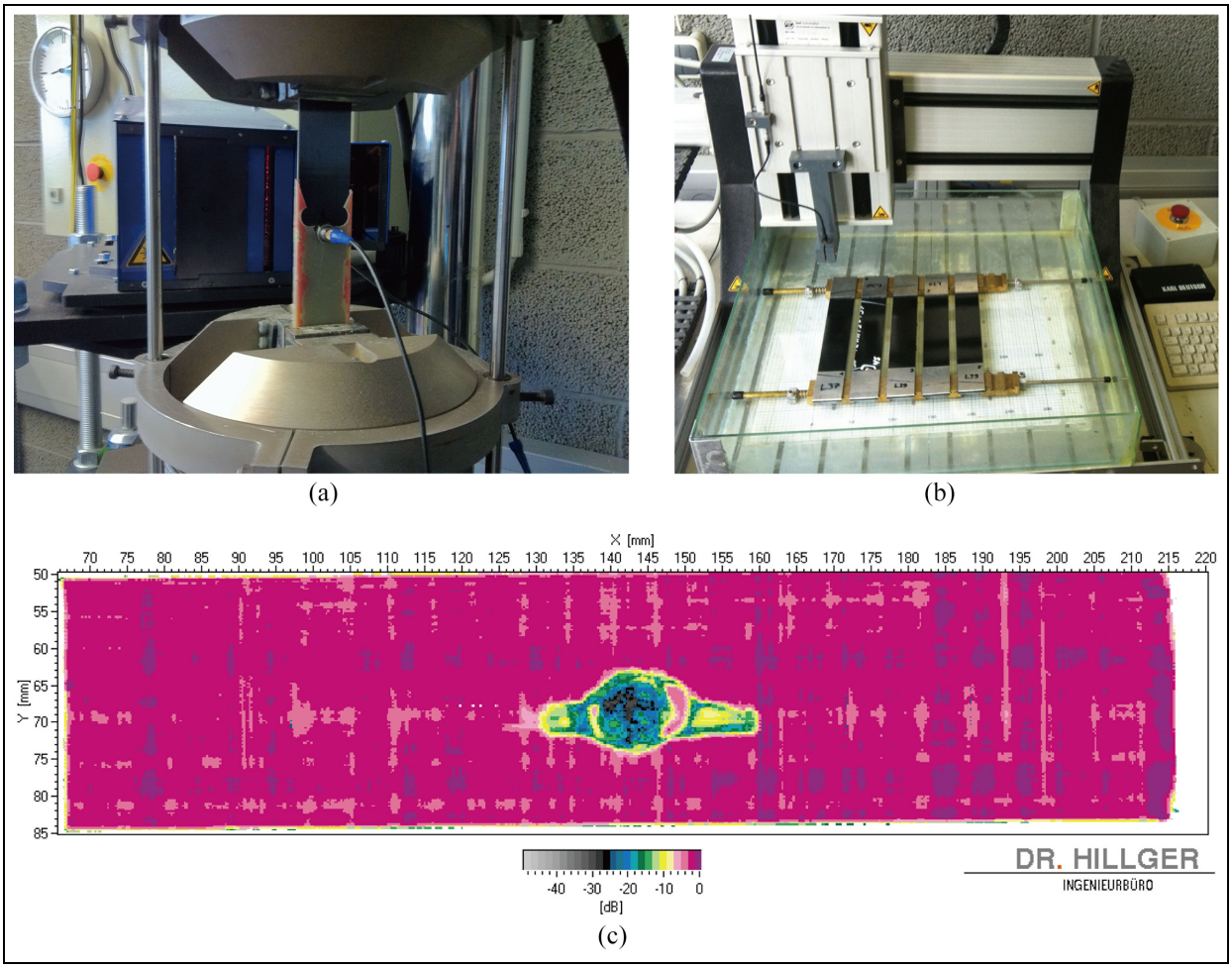

Figure 3. Fatigue test for composite panel with ultrasonic C-scan monitoring system: (a) fatigue test, (b) ultrasonic C-scan system, and (c) sample delamination image at 10,000 load cycles for specimen S1.

Table 3. Mechanical and manufacturing parameters of the coupon.

Type	Parameter	Value	Units	Description
Mechanical	E_m	3.52	GPa	Matrix stiffness
	ν_m	0.35	—	Poisson's ratio of the matrix
	E_{fx}	240	GPa	*X*-axis laminate stiffness
	E_{fy}	28	GPa	*Y*-axis laminate stiffness
	σ_{fx}	1160	MPa	*X*-axis failure tension
Manufacturing	v_f	0.65	—	Fiber volume fraction
	ρ_f	1770	kg/m^3	Fiber density

rectangular 250 × 35 mm coupons with 2 mm thickness and $[0/90]_{4S}$ stacking sequence. The coupons were cured in an autoclave at 177°C for 3 hours using a pressure of 7 bar. To induce an initial local state of matrix-cracks and delamination, impact damage was introduced using a semi-spherical striker drop weight tower, which produced 3.8 Joule impact energy. The fatigue tests were carried out at a maximum applied load of 49 kN, a frequency $f = 6$ Hz, and a stress ratio $R = 0.1$. Further details about the material properties along with the fatigue test data are given in Table 3.

Monitoring data were collected from laser extensometer for online strain measurements, and infrared thermography and C-scan for offline delamination monitoring, although in this work, only the C-scan data are used for demonstration purposes. C-scan

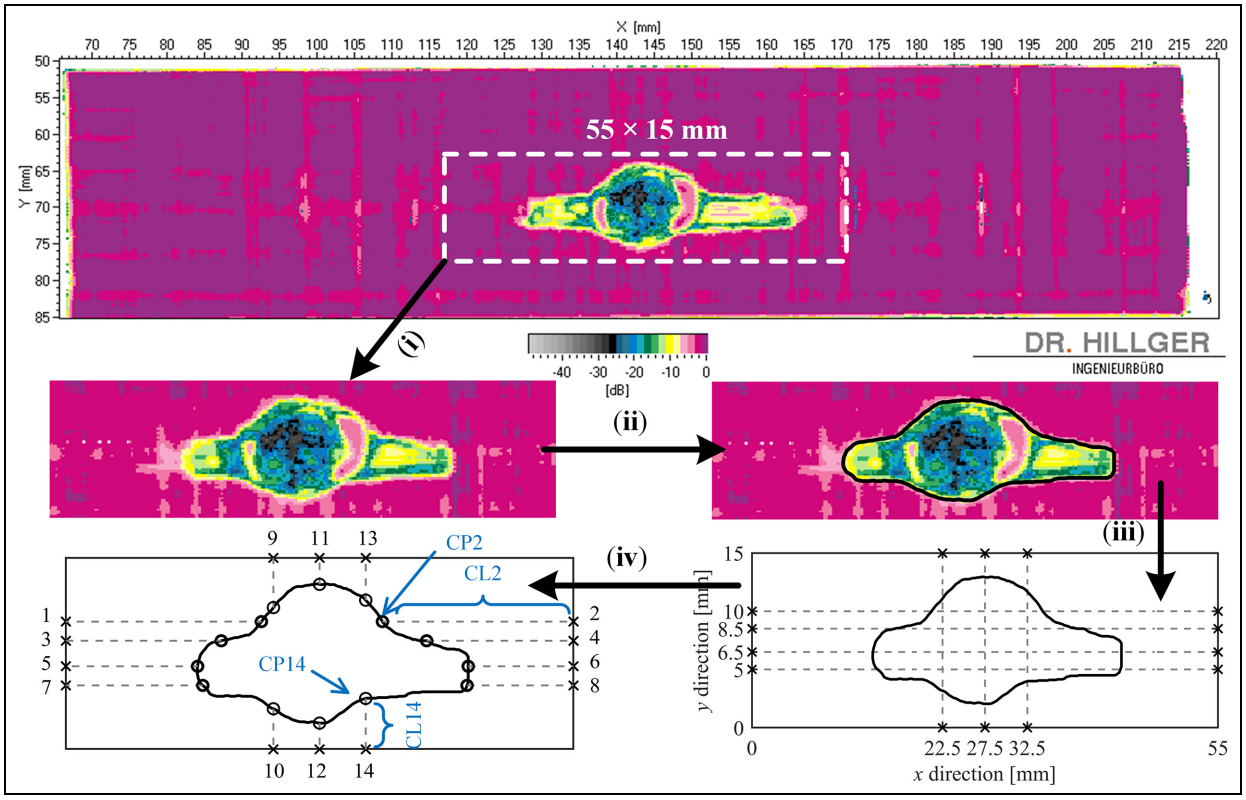

Figure 4. Image processing procedure.

measurements were carried out using a USPC 3040 DAC from Ingenieurbüro Dr. Hillger® system (Braunschweig, Germany) (see Figure 3(b)), with a resolution of 20 MHz and amplification of up to 106 dB in 0.5 dB steps. Figure 3(c) shows a sample C-scan image obtained during the experiments.

Image processing

Figure 4 shows the four steps for processing the raw ultrasonic C-scan delamination image to identify the CPs and CLs. They can be taken as a sequence of actions triggered after an alarm is drawn by a damage detection and localization strategy:

(i) Image cropping: a 55 × 15 mm rectangle sub-image, centered on the delamination, is extracted from the raw image at each load cycle step. Though specific for the case under analysis, in the most general case, the rectangle dimension can be tuned according to limits on damage sizes imposed by certification authorities or airworthiness.

(ii) Extraction of delamination contour. The dB unit provides a measure of the depth of delamination such that a lower amplitude means deeper delamination within the laminate thickness. As a generic rule of thumb specific to this application, the contour is selected as the area limit where the signal amplitude is less than −6 dB. Though a visual check is adopted here for better control of the target delamination perimeter, automatic delamination contour identification is possible, leaving the PF the assignment to filter the additional unavoidable uncertainty.

(iii) Definition of grid lines, using seven grid lines to segment the image, located at the following x-y coordinates: x = 22.5, 27.5, 32.5, and y = 5, 6.5, 8.5, 10, where the units are expressed in millimeter.

(iv) Definition of CPs and CLs: the CPs can be defined as the intersections between the grid lines and the delamination contour, whereas the CLs are taken as the distance between the CPs and the corresponding cross-markers.

The delamination shapes at different load cycles for three specimens S1, S2, and S3 are extracted by Steps (i) and (ii), and they are given in Appendix A1. Note that for each specimen, the delamination grows under a similar pattern, that is, it propagates along the x-direction (the load direction) but not along the y-direction. To better understand the damage evolution pattern, Figure 5 shows the growths of four selected

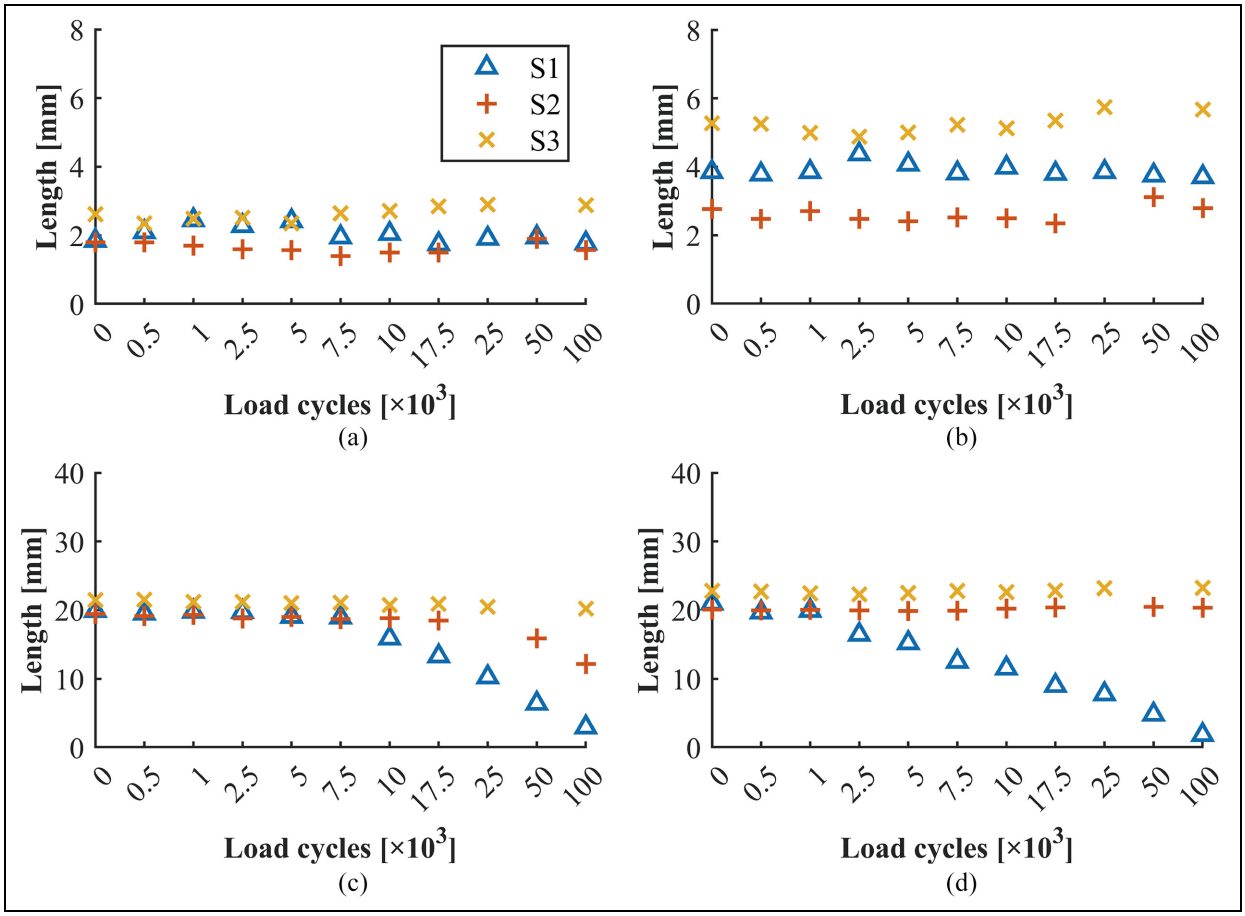

Figure 5. Growths of selected CLs from specimens S1–S3: (a) *y* direction, CL12; (b) *y* direction, CL14; (c) *x* direction, CL4; and (d) *x* direction, CL8.
CL: control length.

CLs from three specimens, where can be observed that both CL12 and CL14 remain stable during the fatigue test, while CL4 decreases with load cycles but at different rates. These observations demonstrate that CLs from different specimens can evolve under a similar pattern, and also that a deterministic evolution model can hardly provide an accurate prediction, as already mentioned in Chen et al.,[14] Li et al.,[15] and Corbetta et al.[16] The latter is even more evident in Figure 5(d), where CL8 from specimens S2 and S3 remain stable with load cycle steps, while those from S1 strictly decrease over fatigue cycles.

Modeling and PF parameters

Given the demonstrated performance of polynomial fitting for depicting fatigue degradation,[27,28] a second-order polynomial function is adopted to map the lth CL and the number of load cycles, as follows

$$z_{l,k} = p_{1,l,k}N_k^2 + p_{2,l,k}N_k + p_{3,l,k} \tag{6}$$

where the polynomial coefficients $p_{1,l}$, $p_{2,l}$, and $p_{3,l}$ are taken as the evolution parameters for the lth CL.

Thus, the state-space model for the lth CL can then be formulated as

$$\begin{cases} \begin{bmatrix} p_{1,l,k} \\ p_{2,l,k} \\ p_{3,l,k} \end{bmatrix} = \begin{bmatrix} p_{1,l,k-1} \\ p_{2,l,k-1} \\ p_{3,l,k-1} \end{bmatrix} + \begin{bmatrix} \omega_{1,l,k} \\ \omega_{2,l,k} \\ \omega_{3,l,k} \end{bmatrix} \\ z_{l,k} = p_{1,l,k}N_k^2 + p_{2,l,k}N_k + p_{3,l,k} + \nu_{l,k} \end{cases} \tag{7}$$

where $\omega_{1,l}$, $\omega_{2,l}$, and $\omega_{3,l}$ are the process noise, and ν_l is the measurement noise. Additionally, kernel smoothing[29] is adopted to improve the estimation performance for the parameters $p_{1,l}$, $p_{2,l}$, and $p_{3,l}$, as already used in Cristiani et al.[3] and Corbetta et al.[16] Taking the parameter $p_{1,l}$ as one reference example, kernel smoothing can be presented as:

$$p_{1,l,k} = \sqrt{1-h^2}\,p_{1,l,k-1} + (1-\sqrt{1-h^2})\hat{p}_{1,l,k-1} + \omega_{1,l,k} \tag{8}$$

Table 4. PF parameters for the lth CL.

Number of particles N_p	STD in likelihood function	Kernel smoothing parameter h
6000	0.4	0.2
	Initial ranges for $\{p_{1,l}, p_{2,l}, p_{3,l}\}$	
$p_{1,l} \sim \mathrm{U}(m_{1,l} - r_{1,l}, m_{1,l} + r_{1,l})$	$p_{2,l} \sim \mathrm{U}(m_{2,l} - r_{2,l}, m_{2,l} + r_{2,l})$	$p_{3,l} \sim \mathrm{U}(m_{3,l} - r_{3,l}, m_{3,l} + r_{3,l})$
	Distributions of process noises $\{\omega_{1,l}, \omega_{2,l}, \omega_{3,l}\}$ for $\{p_{1,l}, p_{2,l}, p_{3,l}\}$	
$\omega_{1,l} \sim \mathcal{N}(0, (1\times10^{-12})^2)$	$\omega_{2,l} \sim \mathcal{N}(0, (1\times10^{-7})^2)$	$\omega_{3,l} \sim \mathcal{N}(0, 1^2)$

Note: (a) $\{m_1, m_2, m_3\}$ and $\{r_1, r_2, r_3\}$ are the PF parameters for defining the initial ranges; (b) the terms $\mathrm{U}(\cdot)$ and $\mathcal{N}(\cdot)$ indicate uniform distribution and Gaussian probability density function, respectively.
CL: control length; PF: particle filter.

where $\hat{p}_{1,l,k-1}$ is the estimate of $p_{1,l,k-1}$, and h is the kernel smoothing parameter. The same procedure applies to the other two parameters $p_{2,l}$ and $p_{3,l}$.

Next, the model for each CL is updated within an independent PF whose hyperparameters have been selected through a trial-and-error procedure, as reported in Table 4. More details on the effects of these parameters on the estimate and CB can be found in literature, as for the number of particles,[30] the standard deviation in the likelihood function,[3] the kernel smoothing parameter,[3] the initial ranges,[30] and the process noise,[3,30] while some comments are provided hereafter as for the selection of the initial ranges of model parameters.

Though one can expect algorithm convergence without informative priors on model parameters, in order to limit the number of particles and to facilitate convergence to target parameters, we tested a scenario in which all the delamination images from two specimens are used to "train" the initial ranges of state parameters, while those from a third specimen are taken as the testing case. More specifically, results for training with S2 and S3 and testing on S1 are shown in section "Shape prediction results," while discussion on other combinations is provided in section "Predictions for other specimens."

A general belief for this kind of problem is that "the predictions will be more accurate with an increasing number of images (or CLs) used for initialization until the number of images becomes large enough." For different applications (or different specimens in the same application, or even different numbers of load cycles for the same specimen), the definition of "enough" should probably be different, and it can hardly be calculated online. Thus, a general recommendation could be to use the images as much as possible.

To use more CLs for "training" the initial ranges of the parameters of each CL evolution model, the 14 CLs have been classified into four groups based on their expected similarity, as listed in Table 5. For each group, the centers $\{m_1, m_2, m_3\}$ for the initialization ranges are defined as the mean parameters providing the best fitting on the initialization sets, while $\{r_1, r_2, r_3\}$ (related to the parameter prior uncertainty) are defined through a trial-and-error procedure.

Shape prediction results

Results for prediction of S1 degradation, based on prior knowledge within S2 and S3 degradations, are reported hereafter. Figure 6(a) and (b) shows the parameter estimation results for two CLs along the y-direction, that is, CL12 and CL14, respectively, while Figure 6(c) and (d) shows those for two CLs along the x-direction, CL4 and CL8, respectively. In each plot, particles representing samples of the three evolution parameters in Equation (6), namely p_1, p_2, and p_3, gradually reduce their spread during the estimation process and finally accumulate within certain ranges, demonstrating that PF can provide satisfactory filtering. Noticeably, parameters of the two x-direction CLs exhibit larger shifts than those of the two y-direction CLs, due to the larger delamination growth along the x-direction, as shown in Appendix A1.

Figure 7(a) to (f) shows the predictions for the two y-direction CLs based on their PF parameter estimates at 1000, 10,000, and 25,000 load cycles, respectively. Note the means of the predictions remain close to the target, and their 95% CBs embrace the target values, proving that the evolution models of the two selected CLs are correctly updated by the PF within a few measurement steps.

Figure 8(a) to (f) shows the predictions for the two x-direction CLs based on their PF parameter estimates at 1000, 10,000, and 25,000 load cycles, respectively. Predictions overestimate the target lengths at lower cycles, due to the shape bias between specimens S2 and S3 (used for setting the initialization ranges for

Table 5. Four groups of CLs.

Group	Direction	CL	$\{m_1, m_2, m_3\}$	$\{r_1, r_2, r_3\}$
1	x	1, 2, 7,8	$\{1.54\times10^{-10},\ -4.42\times10^{-5},\ 20.9\}$	$\{4\times10^{-10}, 4\times10^{-5},\ 4\}$
2	x	3, 4, 5, 6	$\{0.44\times10^{-10},\ -1.93\times10^{-5},\ 20.2\}$	$\{4\times10^{-10}, 4\times10^{-5},\ 4\}$
3	y	9, 10, 13, 14	$\{-0.82\times10^{-10}, 0.12\times10^{-5},\ 3.67\}$	$\{1\times10^{-10}, 1\times10^{-5},\ 2\}$
4	y	11, 12	$\{-1.29\times10^{-10}, 1.57\times10^{-5},\ 1.87\}$	$\{1\times10^{-10}, 1\times10^{-5},\ 2\}$

CL: control length

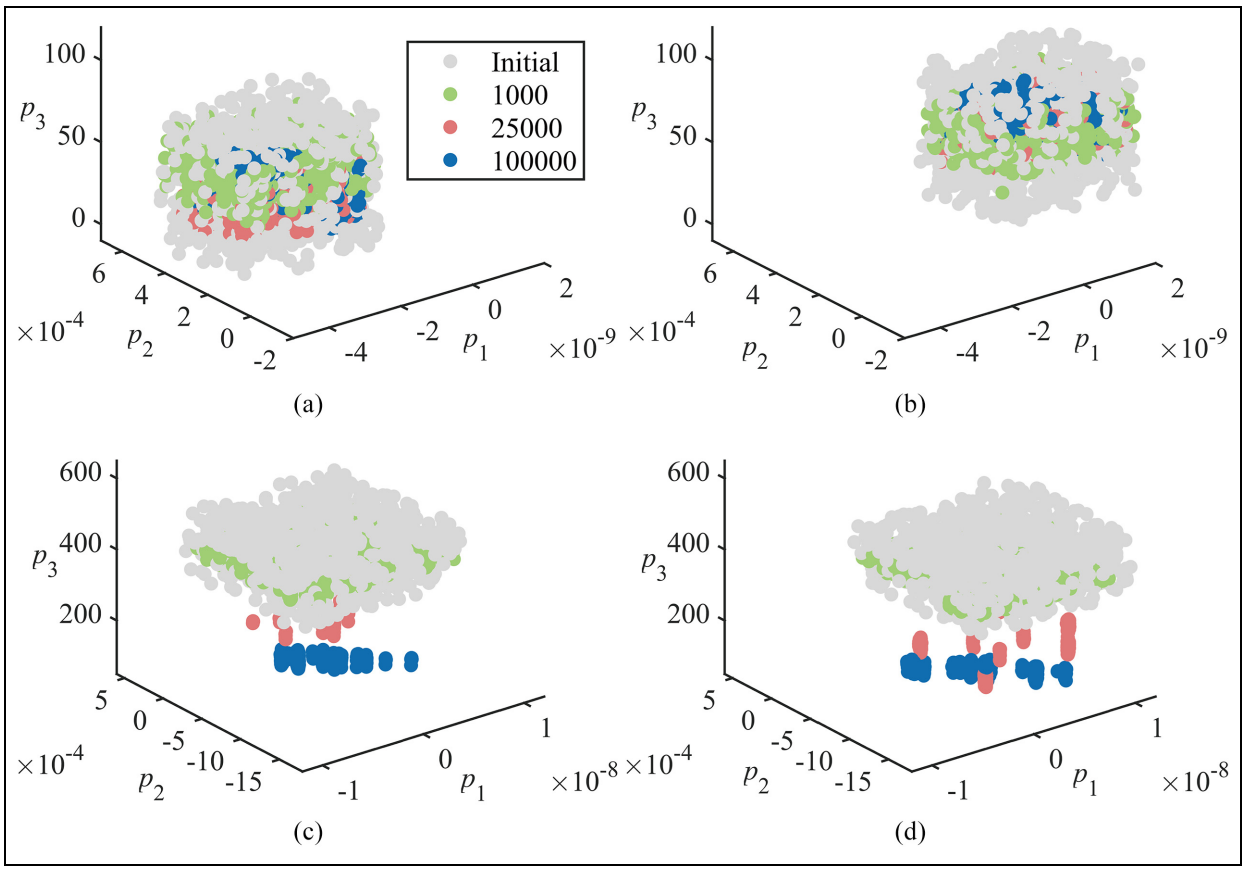

Figure 6. Parameter estimation results for four CLs for specimen S1: (a) y direction, CL12; (b) y direction, CL14; (c) x direction, CL4; and (d) x direction, CL8.
CL: control length.

parameters) and specimen S1 (used for testing). However, the predictions of the two x-direction CLs become more accurate as more delamination images are processed.

The difference in the prediction performances of the CLs along the x- and y-directions is actually due to the adaptation speed of the filter, rather than to the fact that the artificial dynamics are used for the polynomial form coefficients. In turn, the adaptation speed is related to the number of available measurements (the more, the faster the filter) and also to the CL evolutions available for the initialization. It can be seen, in fact, that the evolutions of the x-direction CLs for specimens S2 and S3 are much slower than those of specimen S1 so that the filter initially "expects" (and coherently predicts) a slower evolution: unfortunately, the number of observations available is not sufficiently high for the filter to capture the faster dynamics, at least not until the last observations, when it seems to finally converge.

In general, it can be concluded from Figures 6 to 8 that the proposed methodology can provide satisfactory estimates of the evolution model parameters and accurately anticipate the future CL, and thus the delamination shape, after a sufficient number of delamination images is processed for parameter updating.

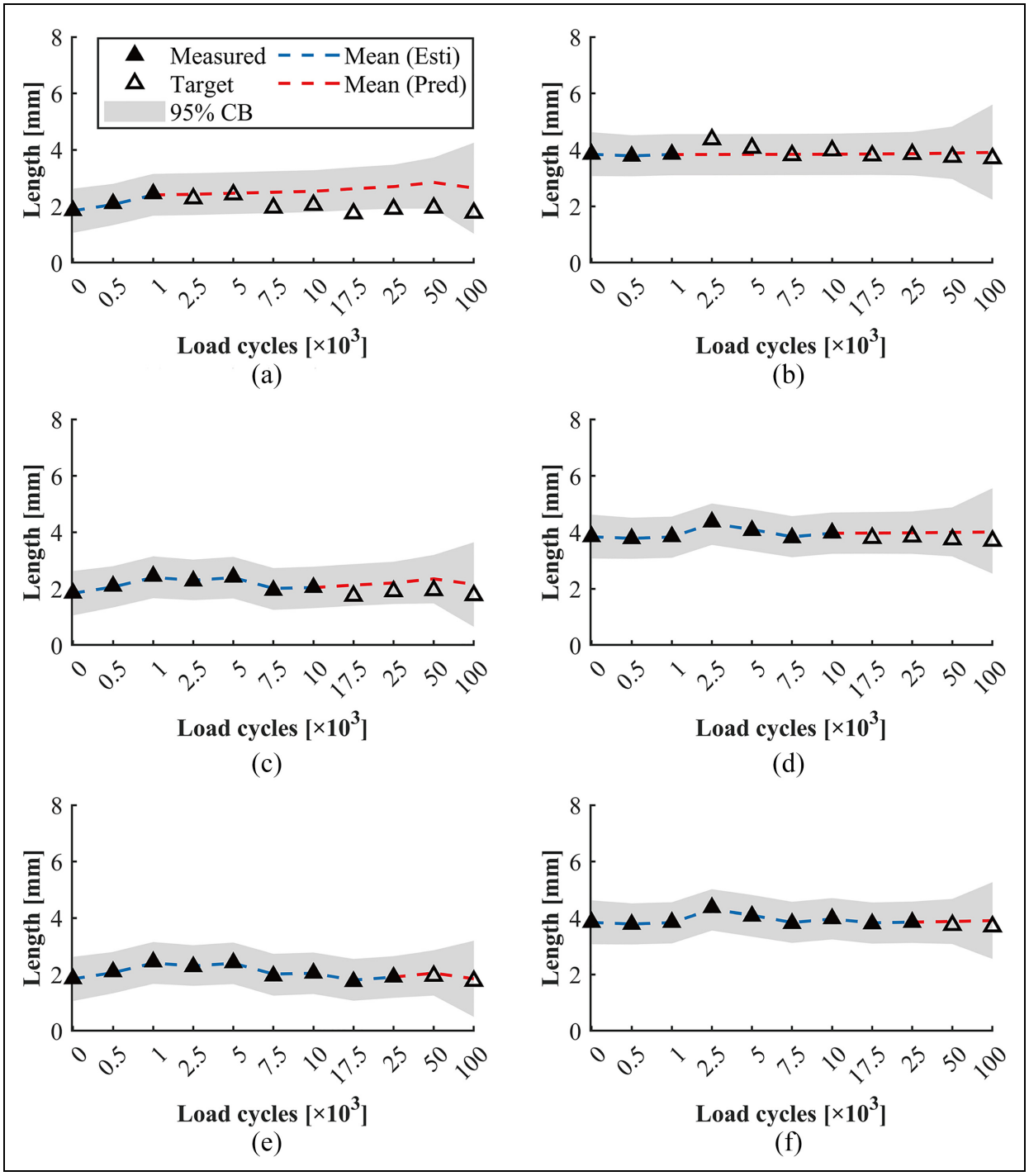

Figure 7. Predictions for two *y*-direction CLs with the estimates at three selected load cycles for specimen S1: (a) 1000 load cycles, CL12; (b) 1000 load cycles, CL14; (c) 10,000 load cycles, CL12; (d) 10,000 load cycles, CL14; (e) 25,000 load cycles, CL12; and (f) 25,000 load cycles, CL14.
CB: confidence boundary; CL: control length.

After acquiring the future CLs, the CPs and their CBs can be located and then used to shape the future delamination, as performed in section "Future delamination shape prediction." For simplicity, only the delamination shape predicted with the estimates at 1000, 10,000, and 25,000 load cycles are given in Figure 9(a) to (c), respectively. It can be observed that the shape prediction becomes less accurate while increasing the steps ahead for prediction, as the uncertainties of delamination growth also increase ahead in the future. On the

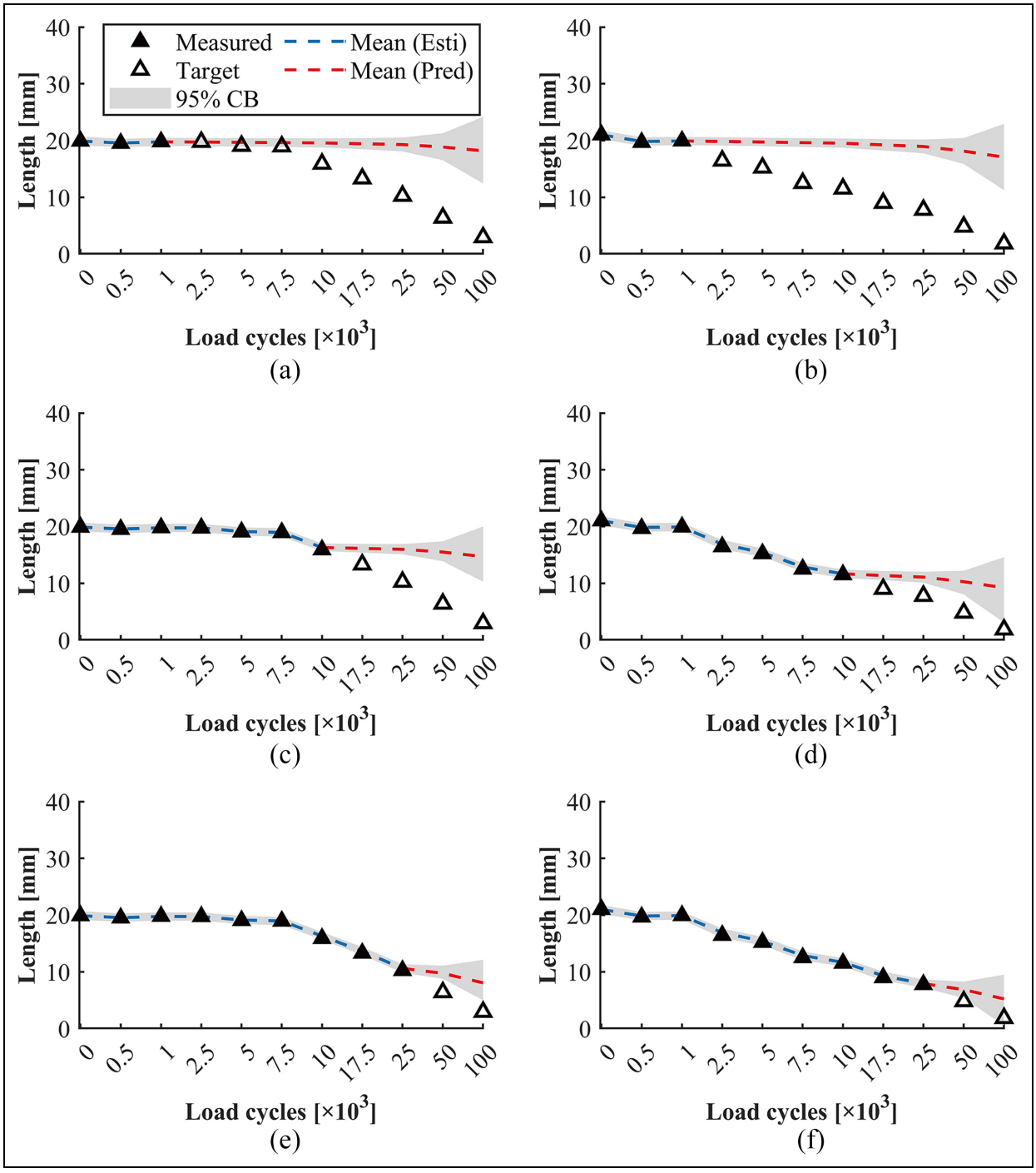

Figure 8. Predictions for two *x*-direction CLs with the estimates at three selected load cycles for specimen S1: (a) 1000 load cycles, CL4; (b) 1000 load cycles, CL8; (c) 10,000 load cycles, CL4; (d) 10,000 load cycles, CL8; (e) 25,000 load cycles, CL4; and (f) 25,000 load cycles, CL8.
CB: confidence boundary; CL: control length.

other hand, the prediction at one specific future step gets more accurate if more delamination images are adopted for model updating, due to the convergence of the evolution parameters as shown in Figure 6.

After defining RF as the center of the delamination image, that is (27.5 mm, 7.5 mm) based on the reference system of the s-scan images in Figure 9, and $\boldsymbol{\alpha}$ = [0, 5, 10, 15, 45, 90, 135, 165, 170, 175, 180,

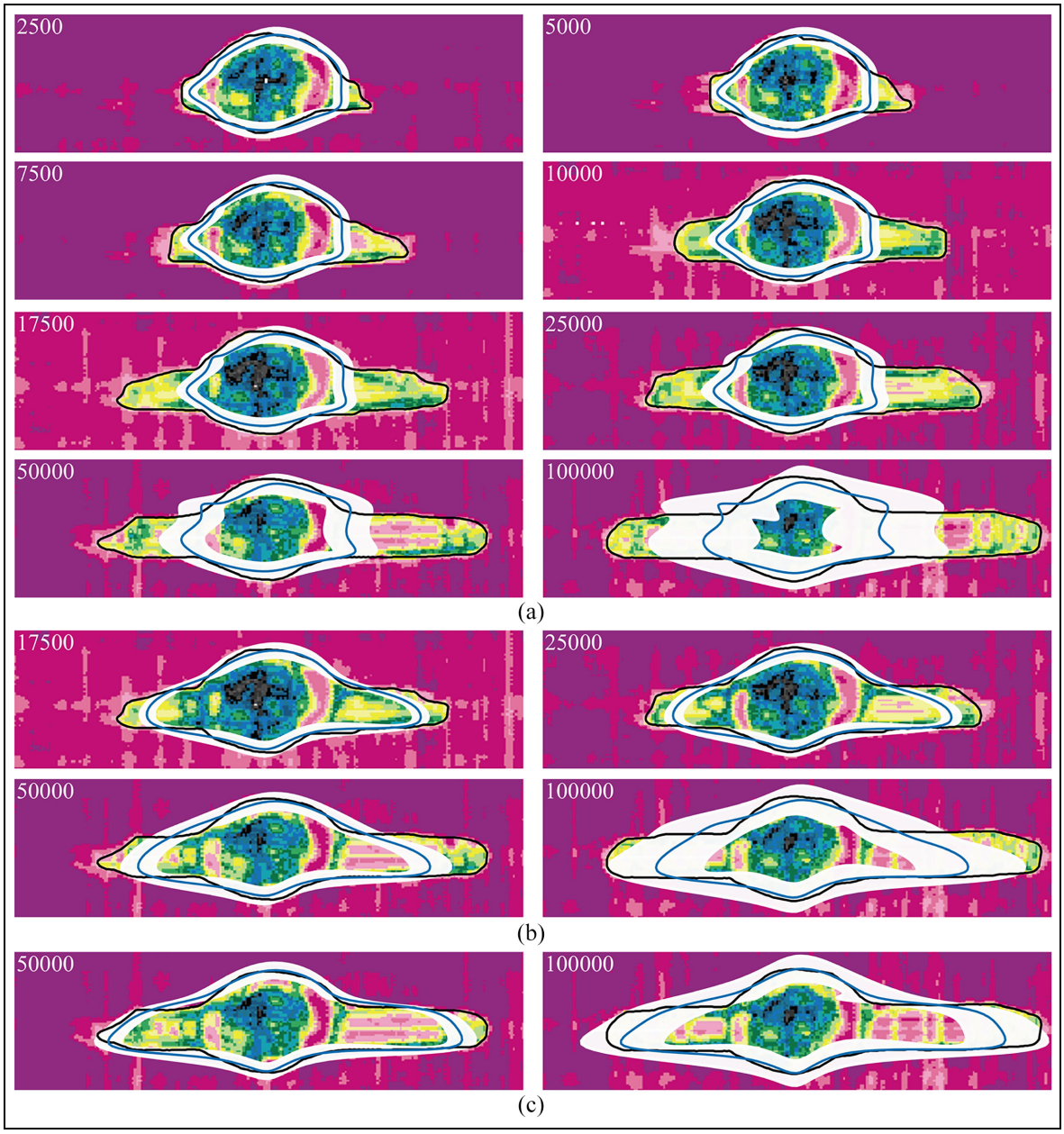

Figure 9. Shapes predicted at future load cycles based on the estimates at three selected load cycles for specimen S1: (a) prediction based on the parameter estimates at 1000 load cycles; (b) prediction based on the parameter estimates at 10,000 load cycles; and (c) prediction based on the parameter estimates at 25,000 load cycles.
The load cycles at which the future shape is predicted are in the left-top corner. The black curve, blue curve, and white area are the target shape, the predicted shape, and its 95% CBs, respectively.
CB: confidence boundary.

185, 190, 195, 235, 270, 315, 345, 350, 355] degrees with respect to the x-direction, the CRA prognostic performance metric is shown in Figure 10 for different future load cycles based on the parameter estimates at different steps of delamination growth. The same conclusions drawn after Figure 9 are valid, as highlighted by the red and green arrows.

Note that our case study is based on a series of laboratory tests, not focused on studying the effects of variable loading. However, according to our previous experience and the results obtained in some previous works by some of the same authors,[22,23] we can expect that the filters, even if initialized on the basis of different load amplitude, should be able to adapt to the new,

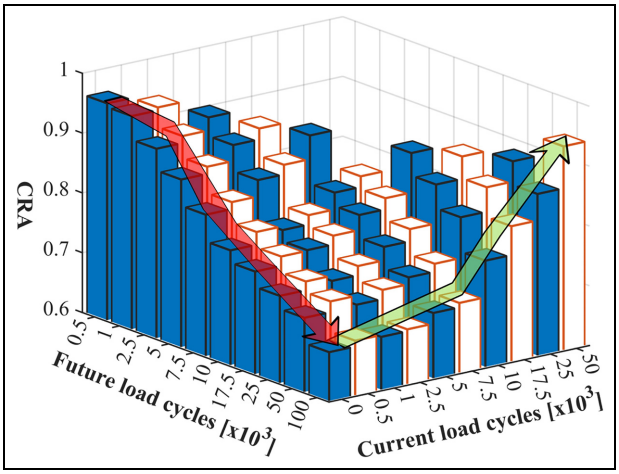

Figure 10. CRAs of shape predictions for specimen S1.
CRAs: cumulative relative accuracies.

changed conditions (provided they are not too different from the initial ones), albeit at the expense of some convergence delays.

Predictions for other specimens

The proposed framework is also tested for specimens S2 (with parameter initialization based on S1 and S3) and S3 (with parameter initialization based on S1 and S2), while the same procedure as in section "Modeling and PF parameters" is used for the definition of $\{m_1, m_2, m_3\}$. Also, the other PF hyperparameters are the same as those in section "Modeling and PF parameters."

The CL predictions for specimens S2 and S3 are presented in Figures 11 and 12, respectively, and shape predictions and CRAs are presented in Figures 13 and 14, respectively, yielding the same conclusions drawn from Figures 7 to 10, demonstrating the robustness of

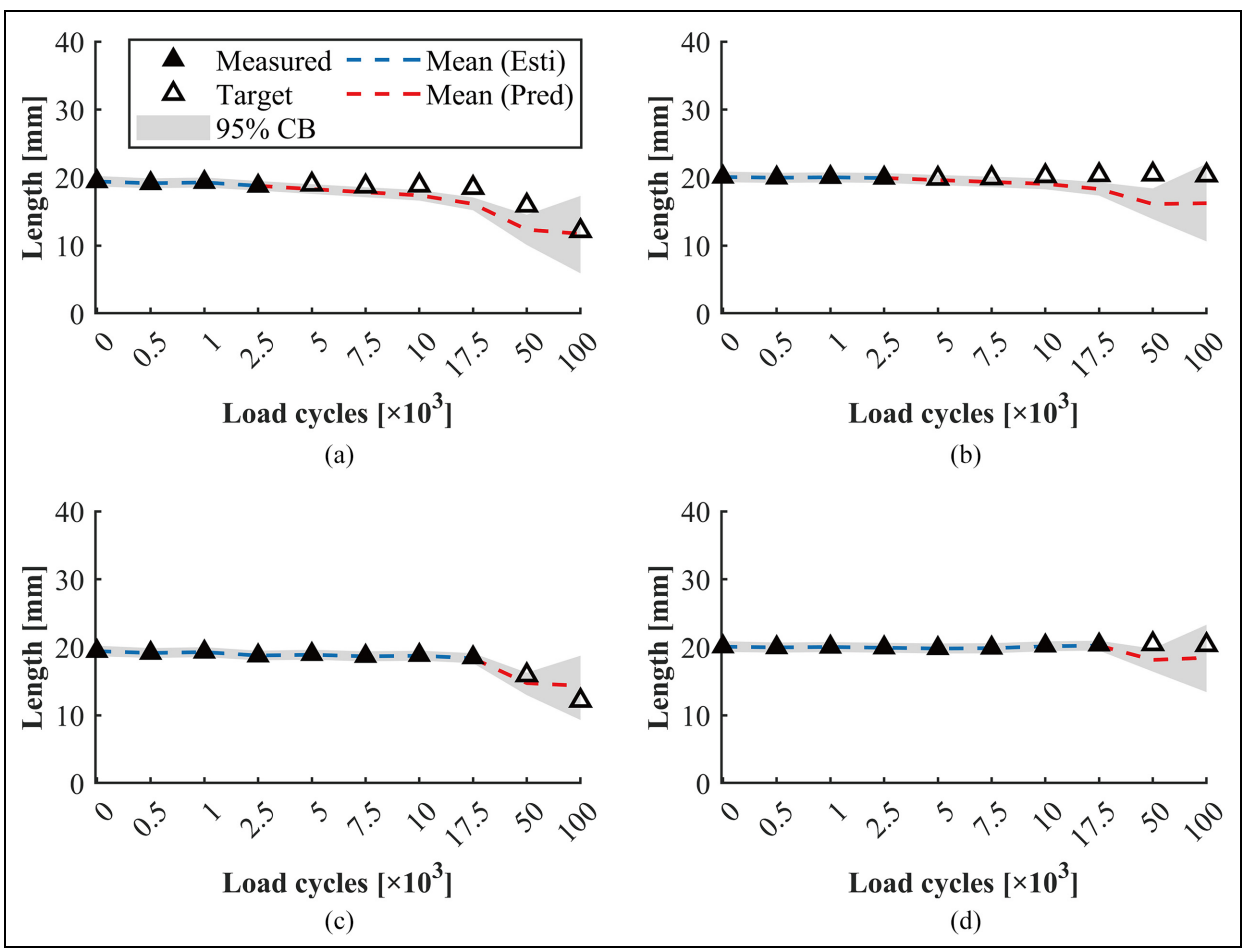

Figure 11. Predictions for two *x*-direction CLs with the estimates at two selected load cycles for specimen S2: (a) 2500 load cycles, CL4; (b) 2500 load cycles, CL8; (c) 17,500 load cycles, CL4; and (d) 17,500 load cycles, CL8.
CB: confidence boundary; CL: control length.

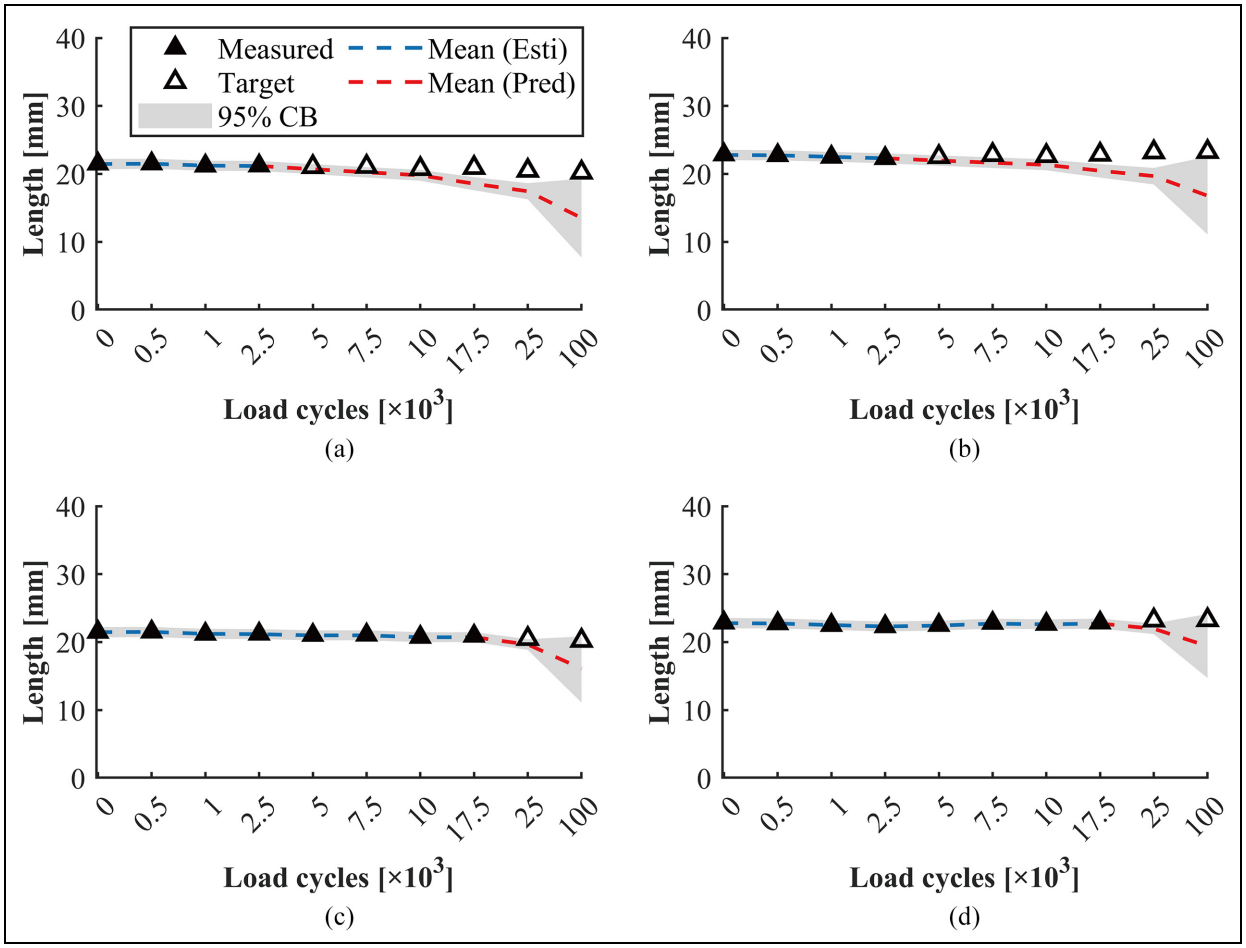

Figure 12. Predictions for two *x*-direction CLs with the estimates at two selected load cycles for specimen S3: (a) 2500 load cycles, CL4; (b) 2500 load cycles, CL8; (c) 17,500 load cycles, CL4; and (d) 17,500 load cycles, CL8.
CB: confidence boundary; CL: control length.

the proposed method over different specimens. Though the performance of the method for each specimen is noted slightly different, due to the stochasticity of delamination growth and also the initial ranges for those CL parameters, the method could cope with these uncertainties by online updating the CL model parameters.

Conclusions

This paper has developed a novel PF-based delamination shape prediction method for composites by taking the delamination shape as a damage state for damage prognosis. By artificially defining a number of CLs to discretize the delamination contour, the shape prediction problem can be simplified into the predictions of these CLs, whose efficiency has been demonstrated with reference to experimental tests of fatigue delamination growth in composite panels with ultrasonics C-scan monitoring during the entire run-to-failure process. This method has been proven robust over different specimens, as it can consider the uncertainties of damage evolution by online updating the CL model parameters.

To move toward a more practical application for delamination shape prediction, one may consider four potential development paths for this research.

- Sufficient experimental or in-field delamination images during the run-to-failure process are required in this study to train the initial ranges in PF, which, however, may not always be feasible due to unconceivable costs. Thus, one may resort to simulated data, for example, from a finite element model, for the definition of the initial ranges. The uncertainties arising from the difference between the numerical and experimental delamination growths can then be automatically taken care of by the adaptation capabilities of PF.

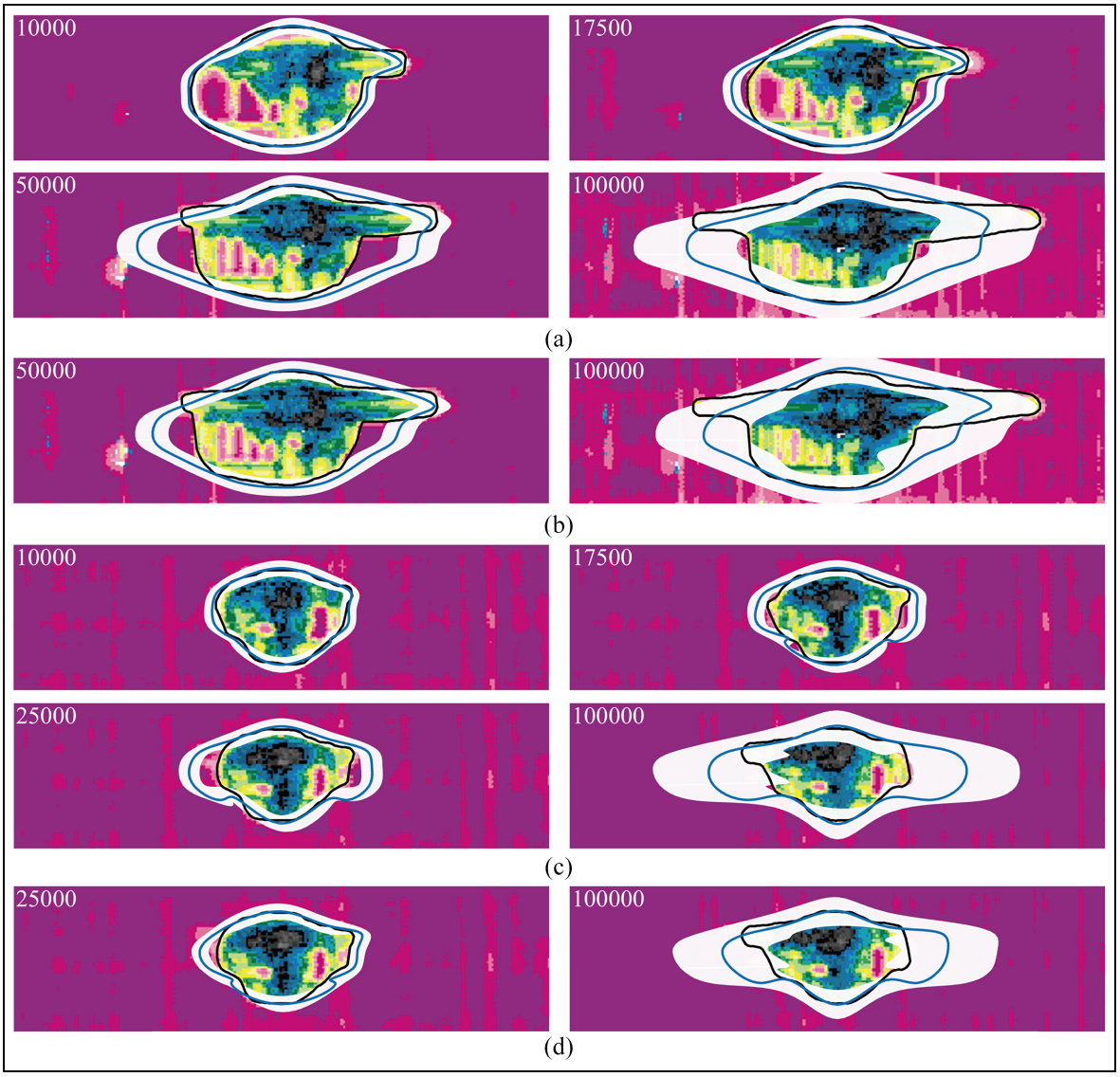

Figure 13. Shape predictions for specimens S2 and S3: (a) prediction based on the parameter estimates at 2500 load cycles, specimen S2; (b) prediction based on the parameter estimates at 17,500 load cycles, specimen S2; (c) prediction based on the parameter estimates at 2500 load cycles, specimen S3; and (d) prediction based on the parameter estimates at 17,500 load cycles, specimen S3.

The load cycles at which the future shape is predicted are in the left-top corner. The black curve, blue curve, and white area are the target shape, the predicted shape, and its 95% CBs, respectively.

CB: confidence boundary.

- In case even numerically generated data are not available, one may, for example, fit the model parameters by assuming no delamination growth during the fatigue test and then create sufficiently wide initial ranges for the parameters in PF implementation, probably at the expense of slower convergence and larger uncertainty intervals at early steps, thus calling for some PF modifications for fast convergence.
- Provided that the adaptability of a quadratic function may not be sufficient for other practical cases with too large uncertainties, involving, for example, more complex delamination shapes, delamination depth, etc., a more sophisticated surrogate model like Gaussian process or neural network could be implemented for building a more detailed damage evolution model.
- Given the difficulty of the online implementation of the ultrasonic C-scan monitoring system, an online measurement system, for example, guided wave, can be adopted for inferring the delamination shapes through a data-driven function

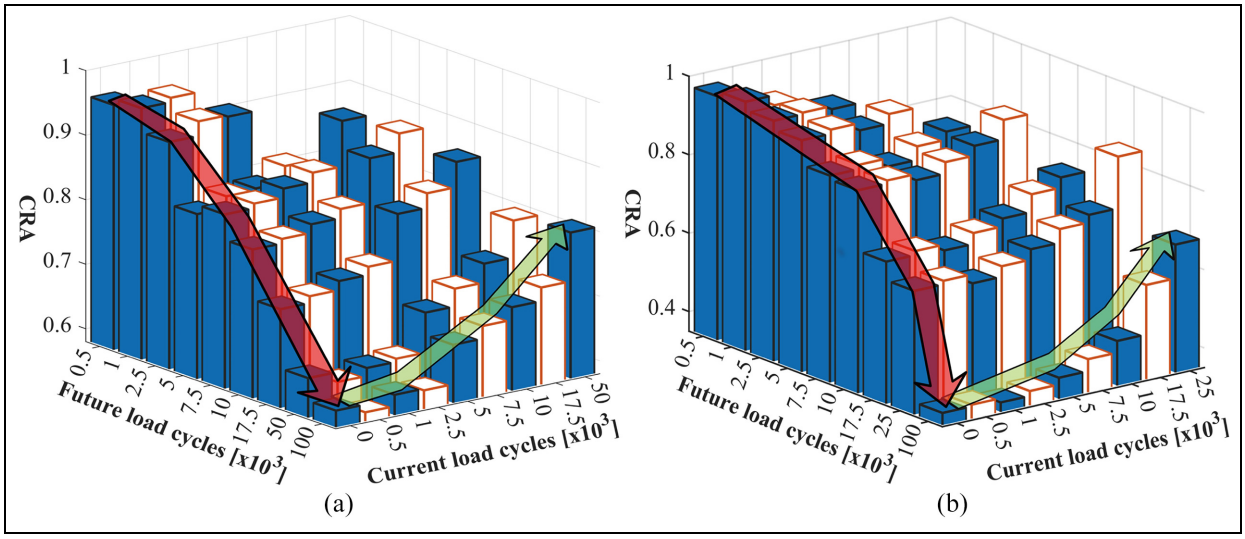

Figure 14. CRAs of shape predictions for specimens S2 and S3: (a) specimen S2 and (b) specimen S3.
CRAs: cumulative relative accuracies.

mapping between the shape and measurements, finally yielding an online damage prognosis framework for industrial application.

Finally, the general idea discussed in this work, that is, the simplification of a two-dimensional prediction problem into the predictions of some CPs, can potentially contribute to the other applications, for example, for the deformation estimate during the service life of a structure, which is left for the interested readers.

Acknowledgements

The authors would like to thank the Institute of Polymers and Composites at Hamburg University of Technology (TUHH), for their collaborative support regarding the production of samples and the collection of monitoring data.

Declaration of conflicting interests

The authors declared no potential conflicts of interest with respect to the research, authorship, and/or publication of this article.

Funding

The authors disclosed receipt of the following financial support for the research, authorship, and/or publication of this article: This project has received funding from the European Union's Horizon 2020 research and innovation program under the Marie Skłodowska-Curie grant agreement No. 859957.

ORCID iD

Tianzhi Li https://orcid.org/0000-0001-6196-9948

References

1. Chiachío M, Chiachío J, Sankararaman S, et al. A new algorithm for prognostics using subset simulation. *Reliab Eng Syst Saf* 2017; 168: 189–199.
2. Corbetta M, Sbarufatti C, Giglio M, et al. A Bayesian framework for fatigue life prediction of composite laminates under co-existing matrix cracks and delamination. *Compos Struct* 2018; 187: 58–70.
3. Cristiani D, Sbarufatti C and Giglio M. Damage diagnosis and prognosis in composite double cantilever beam coupons by particle filtering and surrogate modelling. *Struct Health Monit* 2020; 20: 1475921720960067.
4. Datta S, Neerukatti RK and Chattopadhyay A. Buckypaper embedded self-sensing composite for real-time fatigue damage diagnosis and prognosis. *Carbon* 2018; 139: 353–360.
5. Chiachío J, Chiachío M, Sankararaman S, et al. Condition-based prediction of time-dependent reliability in composites. *Reliab Eng Syst Saf* 2015; 142: 134–147.
6. Tao C, Zhang C, Ji H, et al. Application of neural network to model stiffness degradation for composite laminates under cyclic loadings. *Compos Sci Technol* 2021; 203: 108573.
7. Eleftheroglou N, Zarouchas D and Benedictus R. An adaptive probabilistic data-driven methodology for prognosis of the fatigue life of composite structures. *Compos Struct* 2020; 245: 112386.
8. Loutas T, Eleftheroglou N and Zarouchas D. A data-driven probabilistic framework towards the in-situ prognostics of fatigue life of composites based on acoustic emission data. *Compos Struct* 2017; 161: 522–529.
9. Peng Y, Dong M and Zuo MJ. Current status of machine prognostics in condition-based maintenance: a review. *Int J Adv Manuf Technol* 2010; 50: 297–313.
10. Liao L and Köttig F. Review of hybrid prognostics approaches for remaining useful life prediction of engineered systems, and an application to battery life prediction. *IEEE Trans Reliab* 2014; 63: 191–207.

11. Lei Y, Li N, Guo L, et al. Machinery health prognostics: a systematic review from data acquisition to RUL prediction. *Mech Syst Sig Process* 2018; 104: 799–834.
12. Lopez I and Sarigul-Klijn N. A review of uncertainty in flight vehicle structural damage monitoring, diagnosis and control: challenges and opportunities. *Prog Aerosp Sci* 2010; 46: 247–273.
13. Baraldi P, Mangili F and Zio E. Investigation of uncertainty treatment capability of model-based and data-driven prognostic methods using simulated data. *Reliab Eng Syst Saf* 2013; 112: 94–108.
14. Chen J, Yuan S and Wang H. On-line updating Gaussian process measurement model for crack prognosis using the particle filter. *Mech Syst Sig Process* 2020; 140: 106646.
15. Li T, Sbarufatti C, Cadini F, et al. Particle filter-based hybrid damage prognosis considering measurement bias. *Struct Control Health Monit* 2021; 29: e2914.
16. Corbetta M, Sbarufatti C, Giglio M, et al. Optimization of nonlinear, non-Gaussian Bayesian filtering for diagnosis and prognosis of monotonic degradation processes. *Mech Syst Sig Process* 2018; 104: 305–322.
17. Jouin M, Gouriveau R, Hissel D, et al. Particle filter-based prognostics: review, discussion and perspectives. *Mech Syst Sig Process* 2016; 72–73: 2–31.
18. Abhinav Saxena KG, Larrosa CC, et al. *CFRP composites data set*. Moffett Field, CA: NASA Ames Prognostics Data Repository, NASA Ames Research Center. http://ti.arc.nasa.gov/project/prognostic-data-repository (2021).
19. Tian Z, Lingyu Y, Leckey C, et al. Guided wave imaging for detection and evaluation of impact-induced delamination in composites. *Smart Mater Struct* 2015; 24: 105019.
20. Li X, Kupski J, Teixeira De, Freitas S, et al. Unfolding the early fatigue damage process for CFRP cross-ply laminates. *Int J Fatig* 2020; 140: 105820.
21. Tibaduiza DA, Torres-Arredondo MA, Mujica LE, et al. A study of two unsupervised data driven statistical methodologies for detecting and classifying damages in structural health monitoring. *Mech Syst Sig Process* 2013; 41: 467–484.
22. Cadini F, Sbarufatti C, Corbetta M, et al. Particle filtering-based adaptive training of neural networks for real-time structural damage diagnosis and prognosis. *Struct Control Health Monit* 2019; 26: e2451.
23. Sbarufatti C, Corbetta M, Giglio M, et al. Adaptive prognosis of lithium-ion batteries based on the combination of particle filters and radial basis function neural networks. *J Power Sources* 2017; 344: 128–140.
24. Arulampalam MS, Maskell S, Gordon N, et al. A tutorial on particle filters for online nonlinear/non-Gaussian Bayesian tracking. *IEEE Trans Signal Process* 2002; 50: 174–188.
25. Chen Z. Bayesian filtering: from Kalman filters to particle filters, and beyond. *Statistics* 2003; 1–69: 182.
26. Saxena A, Celaya J, Balaban E, et al. Metrics for evaluating performance of prognostic techniques. In: *2008 international conference on prognostics and health management*, Denver, Colorado, USA, 6–9 October 2008, pp. 1–17.
27. Davies KB and Feddersen CE. Evaluation of fatigue-crack growth rates by polynomial curve fitting. *Int J Fatigue* 1973; 9: 116–118.
28. Zhang Y, Vassilopoulos AP and Keller T. Fracture of adhesively-bonded pultruded GFRP joints under constant amplitude fatigue loading. *Int J Fatigue* 2010; 32: 979–987.
29. Liu J and West M. Combined parameter and state estimation in simulation-based filtering. In: Doucet A, Freitas JFGD and Gordon NJ (eds.) *Sequential Monte Carlo methods in practice*. New York: Springer, 2001, pp. 197–223.
30. Chatzi EN and Smyth AW. The unscented Kalman filter and particle filter methods for nonlinear structural system identification with non-collocated heterogeneous sensing. *Struct Control Health Monit* 2009; 16: 99–123.

Appendix A1

Figures A.1 to A.3 present the images of the delamination and its contour at different load cycles from specimens S1, S2, and S3, respectively.

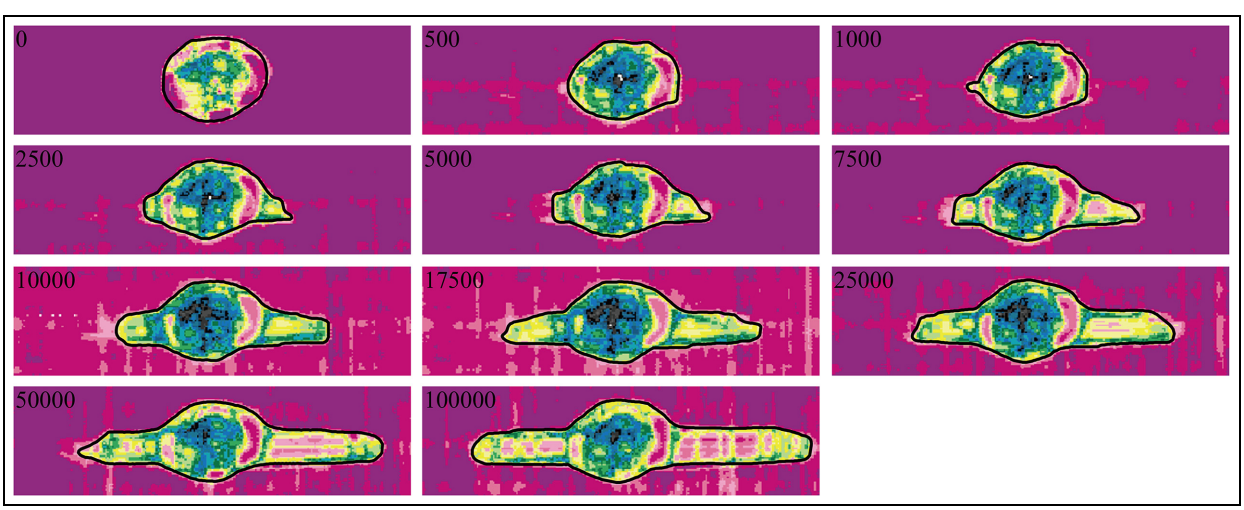

Figure A.1. Ultrasonic C-scan delamination images at different load cycles from specimen S1.

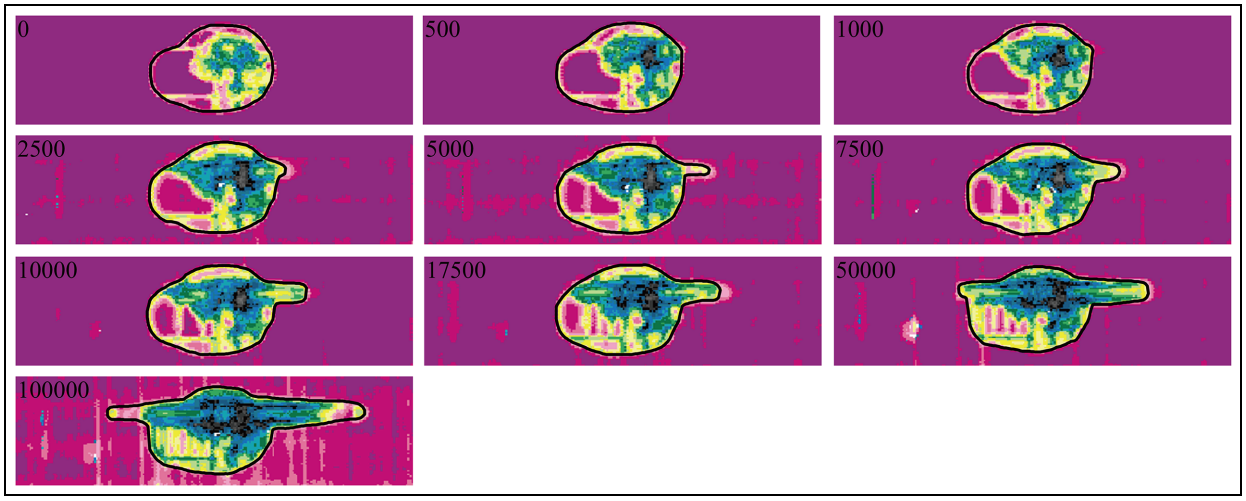

Figure A.2. Ultrasonic C-scan delamination images at different load cycles from specimen S2.

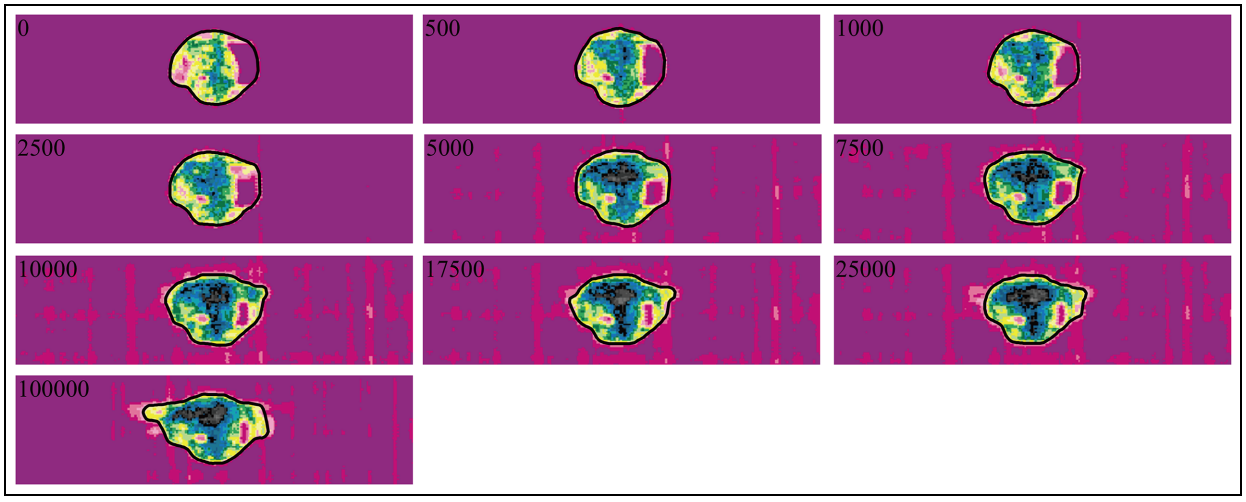

Figure A.3. Ultrasonic C-scan delamination images at different load cycles from specimen S3.

View publication stats

Numerical simulation-aided particle filter-based fatigue delamination shape prediction in composites

Tianzhi Li [1], David Dumas [2], Olivier Pierard [2], Manuel Chiachío [3,4], Claudio Sbarufatti [1], Francesco Cadini [1]

[1]*Dipartimento di Meccanica, Politecnico di Milano, Milan, Italy*

[2]*Methods for Structural Applications and Processes, Cenaero, Belgium*

[3]*Department of Structural Mechanics and Hydraulic Engineering, University of Granada, Spain*

[4]*Andalusian Research Institute in Data Science and Computational Intelligence, Granada, Spain*

[*]Corresponding author: *francesco.cadini@polimi.it*

Abstract

Given that the delamination shape holds useful information for structural safety evaluation, such as the delamination area, its center, and perimeter, the prediction of its evolution has recently gained increasing consideration in the literature dealing with damage prognosis in composites, where usually the shape prediction is simplified into the prediction of the motion of properly defined control points (CPs) along a line crossing the shape of interest. First, the CPs are defined as the intersections between some pre-defined grid lines and the delamination contour. Then, by (i) resorting to some data-driven models describing the dynamics of the above motions with respect to the load cycles or time and (ii) adopting particle filter (PF) for model parameter updating, the future positions of the CPs can be estimated and adopted for future shape reconstruction. This approach, however, requires some experimental or in-field tests to provide a sufficiently large dataset of delamination shape images for both training the data-driven models above and identifying some hyperparameters for PF initialization. In order to save the costs and efforts in conducting such tests, this paper proposes a new numerical simulation-aided approach for feeding the particle filter-based framework, where the shape discretization and reconstruction are based on the same idea illustrated above, whereas numerically simulated delamination growths are generated for the training and initialization processes. The new framework is demonstrated with reference to experimental tests of fatigue delamination growth in composite panels with ultrasonics C-scan monitoring.

Keywords: composite, damage prognosis, particle filter, fatigue delamination, numerical simulation, shape prediction

1. Introduction

Degradation in composites may lead to the occurrence of matrix cracking and delamination, and then fiber failure, or even more severely, structural failure if not properly dealt with. Regular inspection and maintenance should be carried out during the service life of a structure to ensure its safety, however often incurring frequent system shutdowns and high operative costs. In order to guarantee safety at a lower cost, maintenance should be scheduled just before the structural damage reaches a critical level, which requires advanced prognostic techniques to provide an accurate picture of the future damage level of the structure.

Current damage prognosis investigations usually consider the damage level in composites during the complex degradation process depicted by either a physics-based damage state or a data-driven health indicator. The former includes matrix crack density [1], delamination length or area [2, 3], delamination shape [4], crack length [5], and stiffness reduction [1, 2, 6, 7], whilst the latter can be taken as some sort of damage-sensitive statistical feature extracted from SHM signals [8-10]. As the evolution of the damage state or health indicator under a certain service condition should probably follow a specific rule, the future condition can be anticipated by the current one through a proper model describing such a pattern.

Depending on the type of information used for modeling the degradation behavior in composites, namely physical knowledge and experimental or in-field data, the degradation models can be classified into physics-based [1-3, 5, 6] and data-driven [4, 7-9]. The former ones generally fall into the scope of Paris' law or its extensions, where the rate of damage evolution such as strain energy release rate is either analytically calculated [1-3, 6] or fitted from some numerical simulations with a data-driven modeling strategy such as Gaussian process [5]. On the other hand, the data-driven approaches resort to the damage data or health indicators collected during the actual degradation process for building the above relationship through some sort of data-driven modeling strategy, e.g., polynomial fitting functions [4], neural networks [7], Markov models [8], or support vector regression [9]. Note that, when either a physics-based or data-driven model is applied to damage prognosis, its deterministic form can hardly provide accurate prognostic results, due to the uncertainties arising from complex structural degradations, environmental effects, and sensor health conditions [11, 12]. A successful strategy is to set their model parameters as uncertain variables being updated through a state estimation technique, such as the particle filter (PF), given its demonstrated performance in prognostic investigations [13-15].

Among those damage states mentioned above, the delamination shape has been taken as one of the most promising, since it holds important information for the composite health evaluation, such as the delamination area, its center, and perimeter. Given the difficulty of depicting the shape evolution with a physics-based analytical model, current practices usually consider the fatigue delamination shape predicted

by either numerical or surrogate model. The former usually considers a deterministic numerical model built through the virtual crack closure technique (VCCT) [16, 17], or cohesive zone models (CZMs) [18-20], but only for the fatigue delamination growth in composites during double cantilever beam (DCB) tests [17, 18]. Few research is devoted to simulating the other complex scenarios, where the experimental delamination growth is subjected to much more uncertainties, leading to the different shape evolutions of different specimens of the same structure under the same fatigue test [4, 21]. A deterministic numerical model that fails to capture those uncertainties has limited usage for accurately predicting the shape evolution, thus requiring some sort of updating by the collected measurement.

As to the latter, some data-driven surrogate models can be built through a database of delamination images during the run-to-failure process, then online updated by the latest measurement, and finally adopted for the prediction. This method has been recently shown feasible for predicting the complex fatigue delamination growth [4], but requiring a sufficiently large experimental database for training, which may not be always available in practice, mainly due to the unaffordable costs in experimental activities or in-field data collection. An alternative is to use numerical models of fatigue delamination to simulate delamination growth patterns and apply the simulation results for the training of a surrogate model mentioned above, which, however, has never been investigated in practice.

This paper proposes such a numerical simulation-aided framework for predicting the fatigue delamination shape growth by combining delamination growth simulations with the shape prediction method proposed in [4]. The resulting method only requires a few numerical simulations rather than some experiments to provide a training dataset for surrogate modeling at little cost of prognostic accuracy, thus avoiding the cost and effort of conducting any experimental test for training. The delamination shape is discretized by a mesh which produces a number of the control points (CPs) as intersections between the grid lines and the perimeter of the delamination. Then, the data-driven functions describing the CP evolution with the load cycles or time are trained by some simulations and afterward updated by the latest collected data through the particle filtering (PF) method [4]. The resulting sequential approach of prediction is finally used for delamination shape prognostics. The method is demonstrated with reference to experimental tests of fatigue delamination growth in composite panels where delamination detection and evolution are measured through ultrasonics C-scan monitoring.

The rest of this paper is organized as follows: the proposed framework is given in Section 2. Section 3 compares the experimental and numerical delamination growths, and Section 4 provides the validation of the proposed method. Finally, Section 5 concludes this paper with some topics for future work.

2. Delamination shape prediction

The framework in this paper, which is schematically illustrated in Figure 1 for clarity, consists of five main steps, namely: (i) numerical simulation of the delamination growth with respect to the actual test, (ii) definition of mesh nodes and lines for discretizing the delamination shape, (iii) modeling the evolution of the meshed delamination shape depending on some uncertain model parameters, (iv) using the collected experimental delamination image to update those model parameters through PF, and (v) prediction of the future delamination shape. Here, the combination of the two types of models for shape prediction, i.e., the numerical model [17, 18] and the surrogate one [4], allows us to account for the uncertainties within the fatigue delamination growth whilst saving costs and efforts in building experimental datasets for model training.

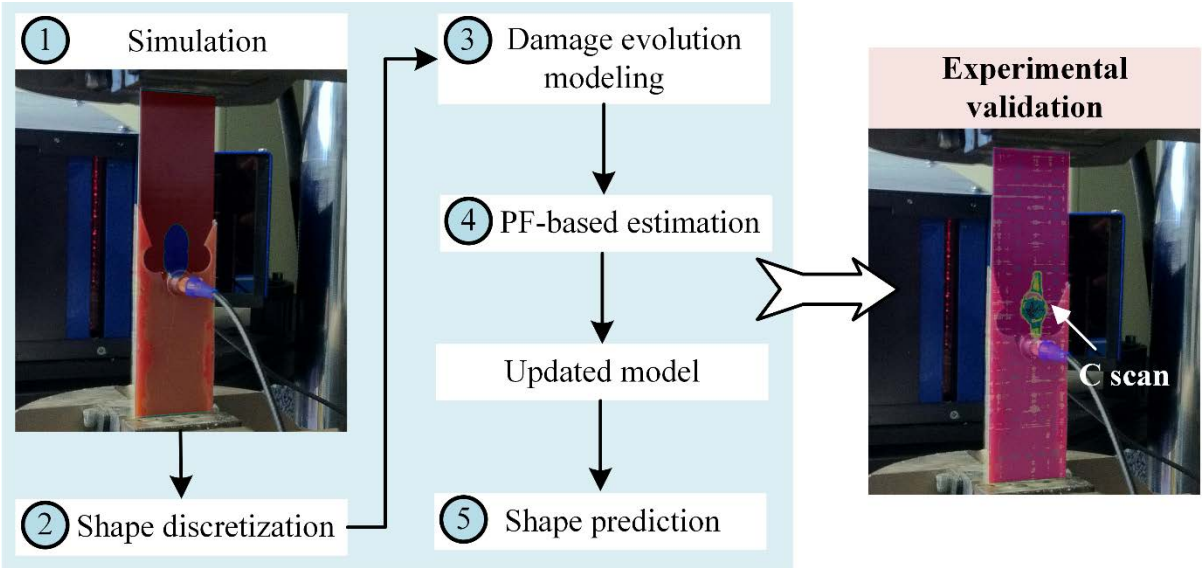

Figure 1 Proposed delamination shape prediction framework

2.1 Delamination growth simulation

The finite element method has long been adopted for numerically simulating the fatigue delamination propagation, including the virtual crack closure technique (VCCT) [16, 17] and cohesive zone models (CZMs) [18-20]. The ability of these techniques to capture the experimental delamination growth has been well demonstrated in the above literature, but mainly for simple double cantilever beam configurations with the delamination growth starting from one edge of the specimen. As larger uncertainties will arise in a more complex scenario like the delamination growth of multidirectional laminate or that under in-plane loading, the shape evolutions are subject to higher uncertainty which limits their accuracy [4, 21]. The corresponding numerical model itself cannot have all the uncertainties considered in such cases, thus probably providing a similar growth pattern with those tests but a less accurate shape contour at each load cycle step, as will be

validated in Section 3.4. This, on the other hand, enables the possibility of adopting those numerical simulations for training some data-driven shape evolution models and then having those model to be updated by the latest measurement.

In this context, we propose that, rather than resorting to the experimental or in-field data for training the shape evolution models and for effectively identifying the hyperparameters for the PF-based algorithm initialization [4], one or more numerical delamination growth simulations can be conducted before (or at least simultaneously) any experimental or in-field test to provide such a dataset, thus saving the cost and effort in conducting those experiments. Here, the VCCT is used, as will be described in Section 3.3.

2.2 Delamination shape discretization

The discretization of the delamination shape is depicted in Figure 2, which shows how the delamination image is processed into some control lengths (CL) and control points (CPs). The method has been recently published in [4] by some of the authors, hence the reader is referred to this publication for further details. First, the image is segmented by some grid lines with their layout (i.e., the locations of the six cross markers) kept unchanged for all the other images. Then, some control points (CPs) can be determined at which the grid lines intersect the delamination contour, and one control length (CL) is taken as the distance between one CP and its corresponding cross marker. As demonstrated in [4], the CL evolution follows a certain pattern during fatigue loading, thus it can be predicted through a model describing such a pattern and further be adopted for shape reconstruction. Note that, in this study, the evolution model of each CL is independently updated, under the assumption of the independency of variation of each CL. However, the method might consider correlation among CLs' evolutions, e.g., by adding some selected or all the CLs into each evolution model, which can be left for future research.

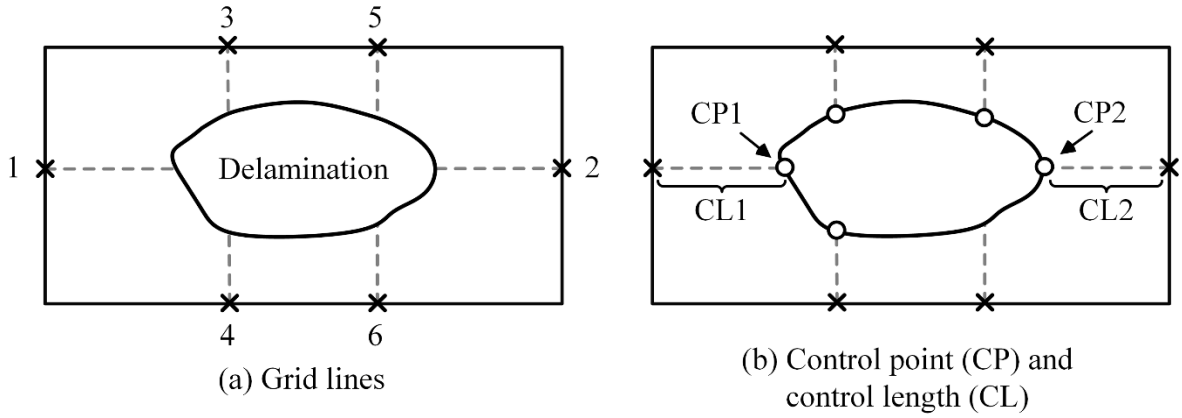

Figure 2 Definition of control points (CPs) and control lengths (CLs) in a delamination image

2.3 Damage evolution modeling and particle filter

The evolution model of the *l*-th CL z_l is assumed as

$$z_{l,k} = f_l(N_k, \boldsymbol{\theta}_l) \tag{1}$$

where the subscript *k* means the *k*-th time step, N_k is the number of load cycles at time step *k*, $f_l(\cdot)$ is a data-driven function describing the length evolution with the number of load cycles, and $\boldsymbol{\theta}_l$ is a vector of model parameters within the function above. A particle filter (PF)-based model updating scheme [22-24] is adopted to improve the prognostic performance in presence of uncertainties. The PF state-space model proposed can be defined using the following recurrence:

$$\begin{cases} \boldsymbol{\theta}_{l,k} = \boldsymbol{\theta}_{l,k-1} + \boldsymbol{\omega}_{l,k} \\ z_{l,k} = f_l\left(N_k, \boldsymbol{\theta}_{l,k}\right) + \nu_{l,k} \end{cases} \tag{2}$$

where $\boldsymbol{\omega}$ and ν are the process and measurement noises, respectively. The state space models for the other CLs take the same form of Eq. (2) and will be embedded into an online PF-based scheme under the assumption of the independent CL evolution.

Following a Bayesian PF approach, the posterior probability of the unknown state vector at *k*-th step $\boldsymbol{\theta}_k$ can be sequentially updated from the measurements as:

$$p\left(\boldsymbol{\theta}_{l,k} \middle| \boldsymbol{z}_{l,1:k-1}\right) = \int p(\boldsymbol{\theta}_{l,k} | \boldsymbol{\theta}_{l,k-1}) p(\boldsymbol{\theta}_{l,k-1} | \boldsymbol{z}_{l,1:k-1}) d\boldsymbol{\theta}_{l,k-1} \tag{3}$$

$$p\left(\boldsymbol{\theta}_{l,k} \middle| \boldsymbol{z}_{l,1:k}\right) \propto p\left(z_{l,k} \middle| \boldsymbol{\theta}_{l,k}\right) p\left(\boldsymbol{\theta}_{l,k} \middle| \boldsymbol{z}_{l,1:k-1}\right) \tag{4}$$

where $\boldsymbol{z}_{l,1:k}$ are the measurements collected from time step 1 to *k*, $p(\boldsymbol{\theta}_{l,k} | \boldsymbol{\theta}_{l,k-1})$ and $p\left(z_{l,k} \middle| \boldsymbol{\theta}_{l,k}\right)$ are the transition distribution and the likelihood function, governed by the process and measurement equations, respectively, and finally $p\left(\boldsymbol{\theta}_{l,k} \middle| \boldsymbol{z}_{l,1:k-1}\right)$ and $p\left(\boldsymbol{\theta}_{l,k} \middle| \boldsymbol{z}_{l,1:k}\right)$ are the prior and posterior probability distribution functions, respectively. Equations (3) and (4) form the basis for the optimal Bayesian solution, which can hardly be analytically calculated in most cases like those in the nonlinear or non-Gaussian system. Therefore, the sampling importance resampling (SIR) PF [25, 26] is chosen in this study for the state estimation. Note that, at each time step, the number of running PFs is equal to that of active CLs.

2.4 Delamination shape prognostics

As a natural step forward after the Bayesian PF approach, a prediction of future CLs at future load cycle steps is made for locating the future CPs, whereby an envelope of the future delamination shape can be obtained. By combining the evolution model Eq. (1) and the *k*-th posterior distribution of its parameters $p(\boldsymbol{\theta}_{l,k}|\boldsymbol{z}_{l,1:k})$, the *j*-th step ahead of the *l*-th CL $z_{l,k}^{j}$ can be calculated by the following Algorithm 1 [4].

Algorithm 1: calculation of future *l*-th control length

For $i = 1 : N_p$

  For $j = 1, 2, 3, \ldots$

    Calculate future $z_{l,k}^{i,j}$ as $z_{l,k}^{i,j} = f_l(N_{k+j}, \boldsymbol{\theta}_{l,k}^{i})$

  End

End

Figure 3(a) utilizes one representative example to illustrate how the shape is reconstructed for one future step through the predicted CLs, while the same procedure also applies to all the other future steps. First, the means and confidence boundaries (CBs) of the future CL are used for locating the corresponding CPs (the blue and red dots). Then, the latter can be adopted for reconstructing the future shapes through a cubic spline interpolation, due to its demonstrated performance in [4]. Note that those CBs of the discrete CPs lying within the average shape are adopted for building the lower CB of the delamination shape, while those outside the average are sued for the upper CB.

Figure 3 (b) shows the cumulative relative accuracy (CRA) proposed in [4] for evaluating the shape prediction accuracy at each load cycle step. Provided with multiple reference line (RL), each of which is a ray arising from a reference point (RP, simply defined as the center of the image in this study) along a certain angle α, the CRA can be written as:

$$CRA_{k,j} = \frac{1}{N_r}\sum_{q=1}^{N_r}\left(1 - \frac{\left|d_{target}^{k,j,q} - d_{pred}^{k,j,q}\right|}{d_{target}^{k,j,q}}\right) \tag{5}$$

where N_r means the number of RLs, d_{target} is the distance between the RP and the target shape along with one RL, whereas d_{pred} is the distance between the RP and the predicted shape. The CRA indicator should be a number within the range of $[-\infty, 1]$, where a higher CRA represents a more accurate prediction.

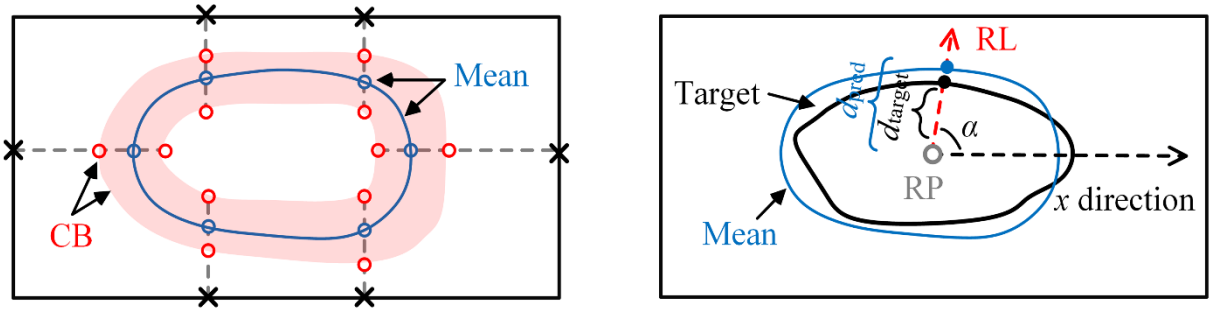

(a) Future shape reconstruction (b) Performance metric: CRA

Figure 3 Future shape prediction procedure and performance evaluation
Note: (i) the blue and red dots denote the mean and the confidence boundaries (CBs) of the predicted control points (CPs), respectively; (ii) the blue curve and the red part denote the mean and the confidence boundaries (CBs) of predicted shape, respectively; and (iii) 'RP' and 'RL' mean 'reference point', and 'reference line', respectively.

3. Experimental and numerical delamination growths

The experimental setup and the delamination growths of three specimens for validating the proposed framework are briefly introduced in Sections 3.1 and 3.2, respectively. The numerical models generated within the experimental specimen are developed in Section 3.3. Section 3.4 compares the delamination propagation from the two studies, which are then adopted to extract the control lengths, as given in Section 3.5.

3.1 Experimental setup

Figure 4 (a) shows that the run-to-failure fatigue experiments of three cross-ply carbon-epoxy laminate specimens were conducted with a servo-hydraulic *Instron/Schenk*® 100 kN tension-tension test machine. The laminate has a size of $250 \times 35 \times 2$ mm. It was manufactured by Cycom 977-2-35-12 k HTS *prepreg* material with the stacking sequence of $[0/90]_{4S}$, resulting in 18 plies in total. An impact with 3.8 Joule impact energy was produced by a semi-spherical striker drop weight tower and then applied to the panel center, leading to initial damage like delamination and modulus reduction. The fatigue tests were then carried out at a maximum applied load of 49 kN, a loading frequency of 6 Hz, and a stress ratio of 0.1. Note that the bottom and top of the laminate are covered by aluminum protection plates with a length of 50 mm for avoiding global bucking during the fatigue test.

Figure 4 (b) shows that the *USPC 3040 DAC* from Ingenieurbüro Dr. Hillger® C-scan system was adopted for offline monitoring. A sample C-scan image obtained during these tests is given in Figure 4 (c), where the *x*-direction is the load direction.

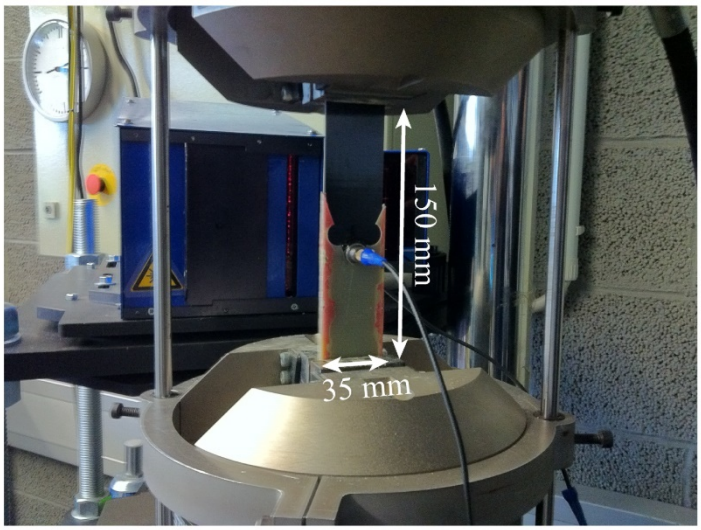

(a) Fatigue test

(b) Ultrasonic C-scan system

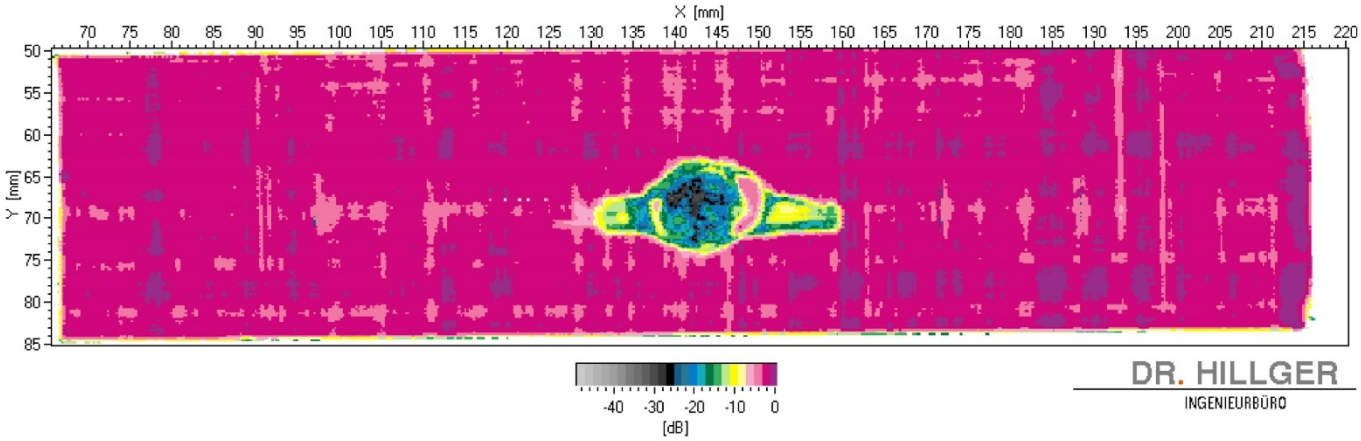

(c) Sample delamination image at 10000 load cycles for specimen S1

Figure 4 Fatigue test for composite panel with ultrasonic C-scan monitoring system.

3.2 Delamination image processing

Figure 5 shows the two steps for extracting the 'true' delamination shape from the raw ultrasonic C-scan image for validation. First, a 55×15 mm rectangle sub-image, centered on the delamination, is extracted from the raw image at each load cycle step. Then, provided that the unit of dB stands for the depth of delamination, the delamination contour is selected as the area limit where the signal amplitude is less than -6 dB, by which we ensure that the delamination is considered deep enough within the laminate thickness. A visual check is adopted here for better control of the target delamination perimeter, possibly resulting in some additional uncertainties, which, however, can be automatically taken care of within the PF framework.

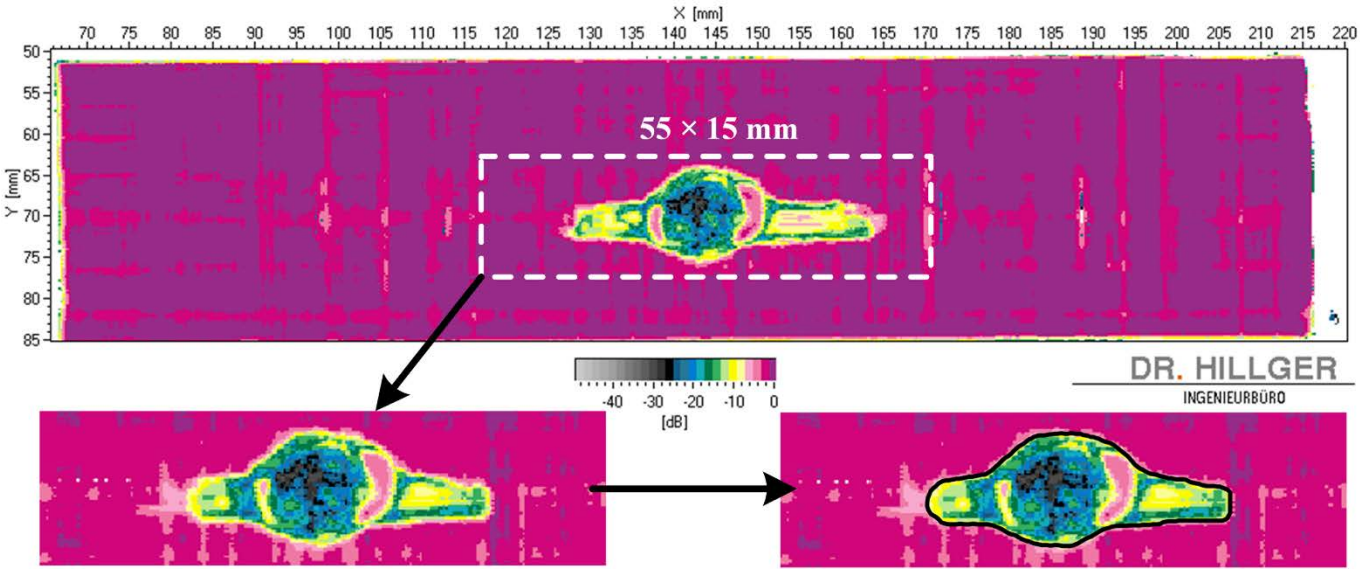

Figure 5 Image processing procedure

The delamination shapes extracted at different load cycles for the three specimens S1, S2, and S3 are given in Appendix A.1. For each specimen, the delamination shape always grows under a similar pattern, i.e., it propagates along the loading direction only, thus enabling the possibility of its prediction. On the other hand, the shape evolutions of the three specimens under the same test are at different rates, mainly because of larger uncertainties arising in such a case. This means that a numerical model that may accurately describe the shape evolution of one specimen cannot deal with another specimen, thus requiring an online model updating scheme.

3.3 Mechanical simulations

This section introduces the numerical fatigue delamination growth using Abaqus with the respect to the experiment. Six simulations are conducted as listed in Table 1, where the usage of different initial damaged shapes, percentages of modulus reduction, locations of delamination growth, and *C* and *m* in Paris' law accounts for the uncertainties arising from the experimental or in-field delamination growth. The reasons for considering these settings are explained below. Note that each of the last five simulations only has one different setting from the first simulation for comparing the effect of such selection.

Table 1 Six fatigue delamination growth simulations

Simulation	Geometry of initial damage	Location of delamination position	Modulus reduction	*C* and *m* in Paris' law
i	10 mm diameter round	Between 2nd and 3rd plies	Reduced to 30 % of healthy values	0.396, 4.14 [18]
ii	10 mm diameter round	Between 2nd and 3rd plies	50 %	0.396, 4.14

iii	10 mm diameter round	Between 2nd and 3rd plies	30 %	0.0306, 4.14 [27]
iv	10 mm diameter round	Between 1st and 2nd plies	30 %	0.396, 4.14
v	10 mm diameter round	Between 3rd and 4th plies	30 %	0.396, 4.14
vi	10 × 10 mm rectangle	Between 2nd and 3rd plies	30 %	0.396, 4.14 [18]

In current practices of simulating double cantilever beam test, the two adjacent plies between which the fatigue delamination grows are usually pre-defined [16, 17]. Thus, the delamination growth in this study is also simulated between two plies. Despite that multiple delamination growths, each between two plies, can happen in the experiment, only one delamination growth is simulated in this study for saving the computation time. Three locations of delamination growth, i.e., the 1st and 2nd plies, the 2nd and 3rd plies, or the 3rd and 4th plies, are considered to investigate the effect of this setting on the delamination growth. Relevant discussions will be made in Section 3.4. based on the results from simulations (i), (iv), and (v). For each simulation, the composite panel is divided into the upper and lower parts, as shown in Figures 6 (a) and (b), respectively, whose numbers of plies and dimensions are listed in Table 2. The delamination growth between the two parts is, therefore, taken as that between the two plies.

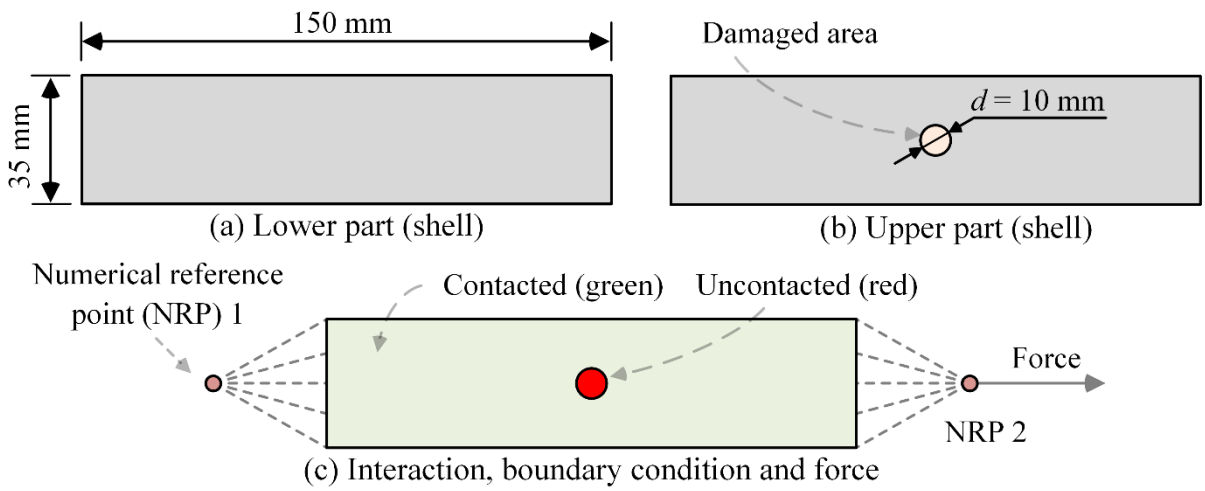

Figure 6 Upper and lower parts of the composite panel.

Table 2 Dimensions of the upper and lower parts in each simulation.

Simulation	Part	Number of plies	Dimension [mm]
i, ii, iii, vi	Upper	2	150 × 35 × 0.250
	Lower	16	150 × 35 × 1.750
iv	Upper	1	150 × 35 × 0.125
	Lower	17	150 × 35 × 1.875

v	Upper	3	150 × 35 × 0.375
	Lower	15	150 × 35 × 1.625

Table 3 lists Young's modulus, shear modulus, and Poisson's ratio for each ply under no damage as well as the mode I, mode II, and mode III fracture toughness for delamination [28]. The impact can result in damages like modulus reduction [29] and initial delamination. The former is simulated by reducing the moduli of the $10\ \mathrm{mm}$ diameter round (or the $10 \times 10\ \mathrm{mm}$ rectangle) to 30% or 50% of their healthy values [29]. The size and shape of the simulated initial damage area are similar with those of the actual one. Note that the exact level of such reduction can hardly be quantified in actual test, thus the two different percentages are adopted for evaluating the delamination growth under different modulus reductions, and those comparison will be made based on the results from simulations (i) and (ii). The use of different initial damage shapes represents the realistic situation in which the same impact can result in different damage shapes, as already shown in [4]. The effect of different initial shapes on the delamination growth simulation will be discussed using the results from simulations (i) and (vi).

As to the latter, the lower part is contacted with the upper one except for the damaged area, as shown in Figure 6 (c). Meanwhile, the left and right sides of the panel are coupling with their corresponding numerical reference points (NRPs), respectively, which are set as fixed but only with the transverse direction motion of NRP 2 allowed. The concentrated force applied to NRP 2 is the same as the experimental cyclic load.

Table 3 Ply properties and fracture toughness [28].

Young's modulus for each ply $[\mathrm{GPa}]$	E_1, E_2, E_3	153, 10.3, 10.3
Shear modulus for each ply $[\mathrm{GPa}]$	G_{12}, G_{13}, G_{23}	6, 6, 3.7
Poisson's ratio for each ply	$\nu_{12}, \nu_{13}, \nu_{23}$	0.3, 0.3, 0.4
Mode I, II, and III fracture toughness $[\mathrm{N/m}]$	$G_{\mathrm{I}C}, G_{\mathrm{II}C}, G_{\mathrm{III}C}$	0.28, 079, 0.79

The mesh size of the area far from the initial delamination is set as $1\ \mathrm{mm}$ [17], while that close to the delamination is set as $0.5\ \mathrm{mm}$ to improve the accuracy. Convergence studies with regard to the element size have not been included, since this probably would not be transferable to another application scenario [20], and also the uncertainties with the respect to the mesh size should probably be taken care of by the proposed framework.

The numerical delamination growth is conducted with the virtual crack closure technique (VCCT)

through the 'direct cyclic' analysis in Abaqus. Paris' law is adopted for calculating the delamination growth as

$$\frac{da}{dN} = C(\Delta G)^m \tag{6}$$

where the parameters *C* and *m* used in this study are taken from [18, 27], as listed in Table 3. Note that two sets of those parameters are adopted for evaluating their effect on the simulation, as will be discussed based on the results from simulations (i) and (iii). The relative strain energy release rate (SERR) ΔG is the difference between the maximum and minimum SERRs ($namely\ G_{max}$ and $G_{min,}respectively$). The former is calculated by the SERRs of the three modes under the maximum load, as follows:

$$G_{max} = G_{\mathrm{I},max} + G_{\mathrm{II},max} + G_{\mathrm{III},max} \tag{7}$$

where the subscripts I, II, and III correspond with mode I, II, and III delaminations, respectively. The above equation also applies for the minimum SERR G_{min}.

The fatigue delamination will occur when $c_1 G_c < G_{max} < c_2 G_c$, where c_1 and c_2 are set as 0.01 and 0.85, respectively, as recommended by the Abaqus user manual. The critical SERR G_c is calculated through the VCCT Benzeggagh-Kenane (BK) criterion as

$$G_c = G_{\mathrm{I}C} + (G_{\mathrm{II}C} - G_{\mathrm{I}C})\left(\frac{G_{\mathrm{II}}+G_{\mathrm{III}}}{G_{\mathrm{I}}+G_{\mathrm{II}}+G_{\mathrm{III}}}\right)^{\eta} \tag{8}$$

where the factor of $\eta = 1.45$ is taken from [28].

3.4 Numerical delamination growths

Figure 7 presents the processed 55×15 mm delamination images at 1×10^5 load cycles (last load cycle step) of each simulation. Note that only simulations (i) and (ii) have the same numerical setup except the magnitude of modulus reduction, while the latter has not delamination growth occurring, possibly because that the use of relatively larger damaged modulus results in the lower-level relative SERR. The use of different initial shapes and different locations do not show a significant effect on the simulated growth, as the last delamination shapes from simulations (i), (iv), (v), and (vi) are quite similar. Moreover, the delamination from simulation (iii) is with a smaller area than that from simulation (i), proving that the growth parameters *C* and

m are directly related to the growth rate.

At the meantime, the last shape from each simulation shows that, similar with what happened in experiment, the numerically simulated delamination also grows along the loading direction. This phenomenon is also apparent in the delamination images at each load cycle step from simulations (i) and (vi), as plotted in Figures 8 and 9. These are also observed in the fatigue delamination growths of the three experimental specimens, as given in the Appendix A1 and also in the work from some of the same author [4].

On the other hand, the simulation that can provide an approximate shape prediction for one specimen may not be feasible for the accurate prediction for another specimen, mainly because the uncertainties arising in the experiment can hardly be fully extrapolated for another simulation. For example, the last delamination shape from simulation (iii) is similar with that from the experimental specimen S3, while not with that from the specimen S1 or S2. Moreover, the numerical and experimental delamination growths can share a similar pattern but with different rate, e.g., both the delamination shapes from the specimen S1 and simulation (i) propagate along the loading direction, but obviously with different contours at each load cycle step.

These implies that (i) the simulation can represent the actual test to a certain level, thus it can be used for the surrogate model, but (ii) it can hardly guarantee an accurate prediction at each load cycle step or among different specimens, thus requiring an online updating scheme at each step when applied to each specimen. Note that the five simulations with the occurrence of delamination growth will be adopted for extracting the CLs, as illustrated in Section 3.5.

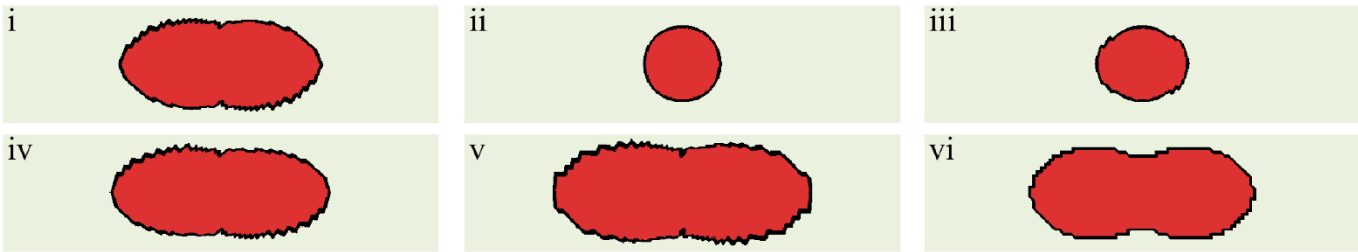

Figure 7 Delamination at 1×10^5 load cycles of each simulation.
Note: (i) the light green, red, and black parts mean ‘healthy’, ‘delamination’, and ‘delamination front’, respectively; (ii) the number at the left-top corner is the serial number of the simulation.

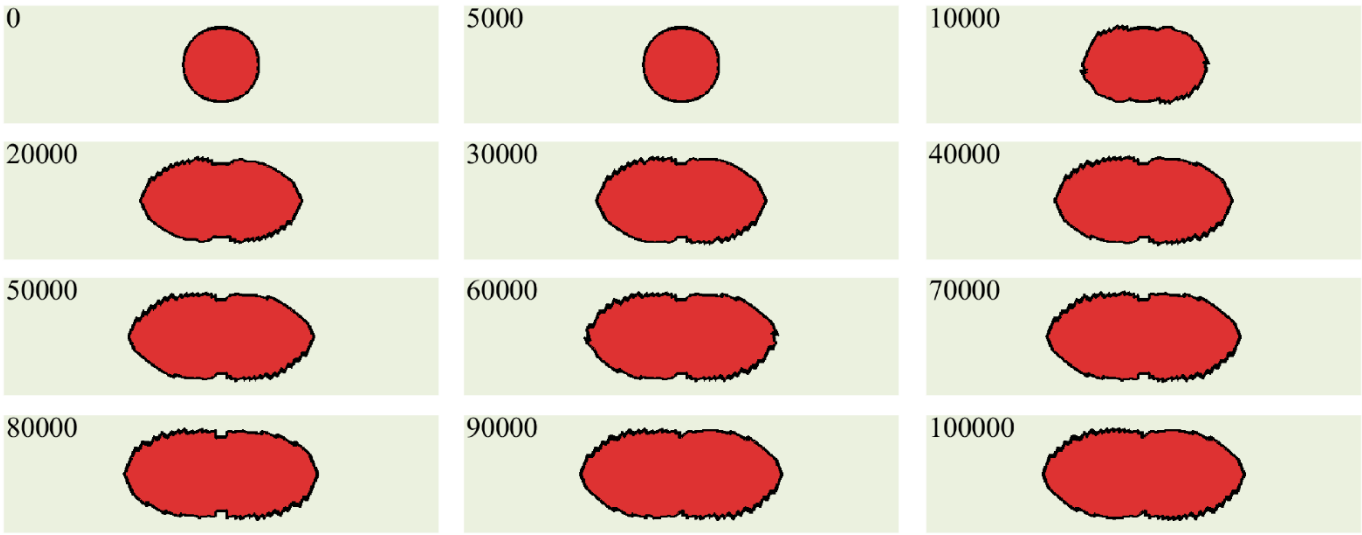

Figure 8 Delamination growth of Simulation (i).
Note: (i) the light green, red, and black parts mean ‘healthy’, ‘delamination’, and ‘delamination front’, respectively; (ii) the number at the left-top corner is the number of load cycles.

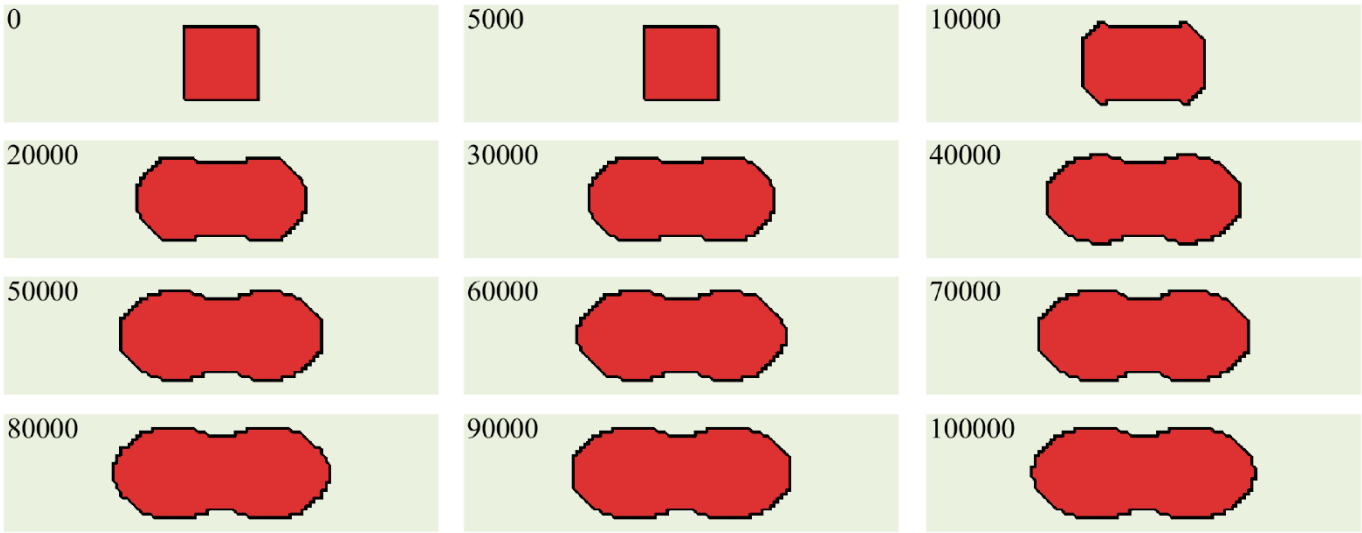

Figure 9 Delamination growth of Simulation (vi)
Note: (i) the light green, red, and black parts mean ‘healthy’, ‘delamination’, and ‘delamination front’, respectively; (ii) the number at the left-top corner is the number of load cycles.

3.5 Numerical and experimental control lengths

The numerical (i, iii, iv, v, vi) and experimental (S1, S2, S3) CLs are extracted through the two steps explained above, and the results are shown in Figure 10. First, seven grid lines, located at the following x - y coordinates (unit: mm): x = 23, 27.5, 32, and y = 5, 6.5, 8.5, 10, are adopted for segmenting the processed delamination images. The control points (CPs) are then defined as the intersections between the grid lines and the delamination contour, whereas the control lengths (CLs) are taken as the distance between the CPs and the corresponding cross-markers. Note that the layout of the lines may not have a significant effect on the prediction performance, once the number of those lines has been chosen to be sufficiently large, as verified by the authors, but not shown here for brevity’s sake.

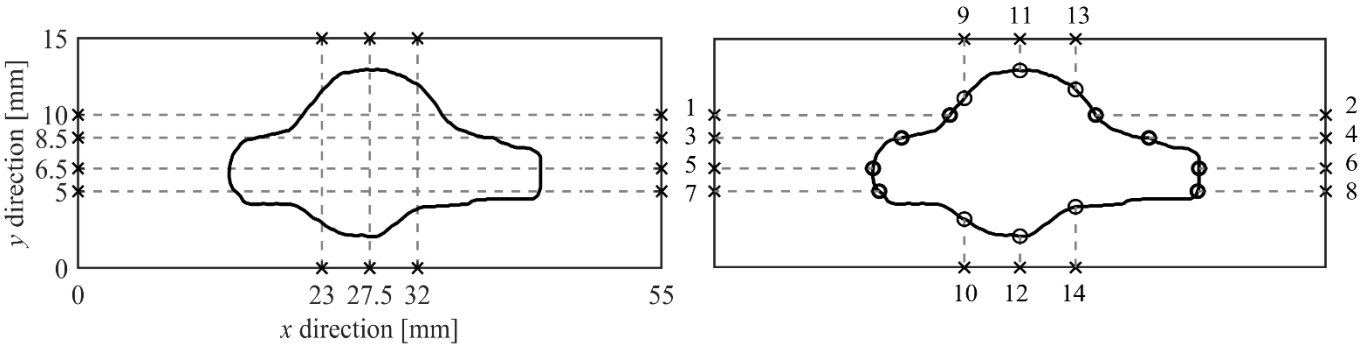

(a) Seven grid lines (b) Control points (CPs) and control lengths (CLs)

Figure 10 Definition of control points (CPs) and control lengths (CLs) in the numerical and experimental studies.

Four selected CL evolutions of simulations (i) and (vi) and the three experimental specimens are given in Figure 11, where the *y*-direction CL12 always remains stable during the experimental or numerical delamination growth, whilst the *x*-direction CLs, e.g., CL2, CL4, and CL8, decrease with load cycles but at different rates. The CL evolutions from the two simulations and the experiments share a similar pattern, so that the former can be adopted for modeling the CL evolution, but they have different CLs at each load cycle step, thus still requiring a model updating scheme for accurate prediction. Note that the CLs from the five simulations above will be adopted for modeling the CL evolution, as will be detailed in Section 4.1.

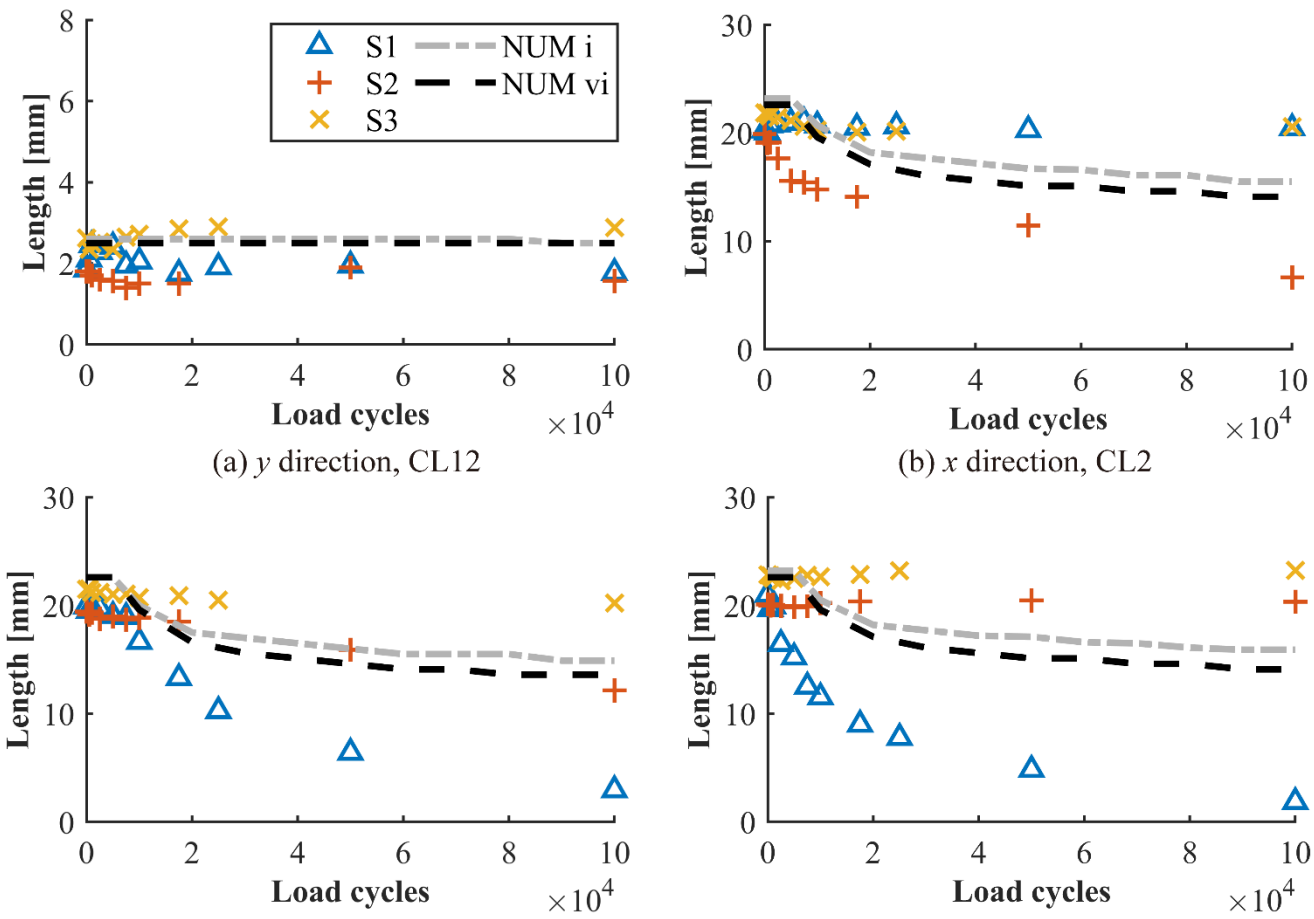

(a) *y* direction, CL12 (b) *x* direction, CL2

(c) *x* direction, CL4 (d) *x* direction, CL8

Figure 11 Four selected control lengths of the numerical and experimental studies

4. Validation of the proposed framework

4.1 Modeling and PF hyperparameters

Given the demonstrated performance of the second-order polynomial fitting for depicting fatigue degradation [4], it is adopted here to build the *l*-th CL as a function of the number of load cycles according to the following formulation:

$$z_{l,k} = \theta_{1,l,k} N_k^2 + \theta_{2,l,k} N_k + \theta_{3,l,k} \tag{6}$$

where the polynomial coefficients $\theta_{1,l}$, $\theta_{2,l}$ and $\theta_{3,l}$ are taken as the three evolution parameters $\boldsymbol{\theta}_k = \{\theta_{1,\mathrm{k}}, \theta_{2,\mathrm{k}}, \theta_{3,\mathrm{k}}\}$ for the *l*-th CL. Then, the state space model for the *l*-th CL can then be formulated as

$$\begin{cases} \begin{bmatrix} \theta_{1,l,k} \\ \theta_{2,l,k} \\ \theta_{3,l,k} \end{bmatrix} = \begin{bmatrix} \theta_{1,l,k-1} \\ \theta_{2,l,k-1} \\ \theta_{3,l,k-1} \end{bmatrix} + \begin{bmatrix} \omega_{1,l,k} \\ \omega_{2,l,k} \\ \omega_{3,l,k} \end{bmatrix} \\ z_{l,k} = \theta_{1,l,k} N_k^2 + \theta_{2,l,k} N_k + \theta_{3,l,k} + \nu_{l,k} \end{cases} \tag{7}$$

where $\omega_{1,l}$, $\omega_{2,l}$ and $\omega_{3,l}$ are the process noise, and ν_l is the measurement noise. Additionally, kernel smoothing [30] is adopted to improve the estimation performance for the parameters $\theta_{1,l}$, $\theta_{2,l}$, and $\theta_{3,l}$, as already used in [3, 31]. Taking the parameter $\theta_{1,l}$ as one reference example, kernel smoothing can be presented as:

$$\theta_{1,l,k} = \sqrt{1-h^2}\,\theta_{1,l,k-1} + \left(1 - \sqrt{1-h^2}\right)\hat{\theta}_{1,l,k-1} + \omega_{1,l,k} \tag{8}$$

where $\hat{\theta}_{1,l,k-1}$ is the estimate of $\theta_{1,l,k-1}$, and h is the kernel smoothing parameter. The same procedure applies to the other two parameters $\theta_{2,l}$ and $\theta_{3,l}$.

Then, the model for each *l*-th CL is updated within an independent PF whose hyperparameters have been selected through the work from some of the same authors [4] and a trial-and-error procedure, as reported in Table 4. More details on sensitivity analyses can be found in the literature, as for the number of particles [32], the standard deviation (STD) in likelihood function [3], the kernel smoothing parameter [3], and the process noise [32], while some comments are provided hereafter as for the selection of the initial ranges of model parameters.

Table 4 Particle filter hyperparameters for the *l*-th control length

Number of particles (N_p)	STD in likelihood function	Kernel smoothing parameter (h)
6000	0.3	0.2
Initial ranges for $\{\theta_{1,l}, \theta_{2,l}, \theta_{3,l}\}$		
$\theta_{1,l} \sim \mathrm{U}(0.6m_{1,l}, 1.4m_{1,l})$	$\theta_{2,l} \sim \mathrm{U}(0.6m_{2,l}, 1.4m_{2,l})$	$\theta_{3,l} \sim \mathrm{U}(0.6m_{3,l}, 1.4m_{3,l})$
Distributions of process noises $\{\omega_{1,l}, \omega_{2,l}, \omega_{3,l}\}$ for $\{\theta_{1,l}, \theta_{2,l}, \theta_{3,l}\}$		
$\omega_{1,l} \sim \mathcal{N}\left(0, (0.015m_{1,l})^2\right)$	$\omega_{2,l} \sim \mathcal{N}\left(0, (0.015m_{2,l})^2\right)$	$\omega_{3,l} \sim \mathcal{N}\left(0, (0.05m_{3,l})^2\right)$

Note: (a) $\{m_1, m_2, m_3\}$ are the PF hyperparameters for defining the initial ranges and the magnitude of process noise; (b) the terms $\mathrm{U}(\cdot)$ and $\mathcal{N}(\cdot)$ indicate uniform distribution and Gaussian probability density function, respectively.

In general, the predictions will be more accurate with an increasing number of images (or CLs) used for initialization until the number of images becomes large enough. For different applications, the number of sufficient images should probably be different, and it can hardly be calculated in advance. Thus, a general recommendation could be to use the images as much as possible. To use more CLs for training the initial ranges of the parameters of each CL evolution model, the 14 CLs have been classified into four groups based on the fourteen CLs have been classified into four groups based on their expected similarity [4], as listed in Table 5. The PF hyperparameters $\{m_1, m_2, m_3\}$ for all the CLs in the same one group are the same, and they are created as follows: for each group, the CL (highlighted in red in Table 5) from each of the five simulations is used to provide one set of polynomial coefficients, finally resulting in five sets of coefficients, whose means are taken as $\{m_1, m_2, m_3\}$.

Table 5 Groups of control lengths. The values of the right-most column are obtained from simulations

Group	Direction	Control length	$\{m_1, m_2, m_3\}$
1	*x*	1, 2, 7 ,8	$\{1.06 \times 10^{-9}, -1.74 \times 10^{-4}, 22.90\}$
2	*x*	3, 4, 5, 6	$\{1.17 \times 10^{-9}, -1.85 \times 10^{-4}, 22.47\}$
3	*y*	9, 10, 13, 14	$\{-0.43 \times 10^{-9}, -0.67 \times 10^{-4}, 4.71\}$
4	*y*	11, 12	$\{-4.91 \times 10^{-12}, -6.17 \times 10^{-8}, 2.56\}$

Note: the number highlighted in red denotes the serial number of numerical CL for training and initialization.

4.2 Shape prediction results for specimen S1

The validation using specimen S1 is reported hereafter. Figures 12 (a) and (b) show the parameter estimation results for the two CLs, i.e., CL12 and CL4, respectively. The distributions of the three evolution parameters, namely θ_1, θ_2 and θ_3, gradually shrink during the estimation process, thus proving a good convergence.

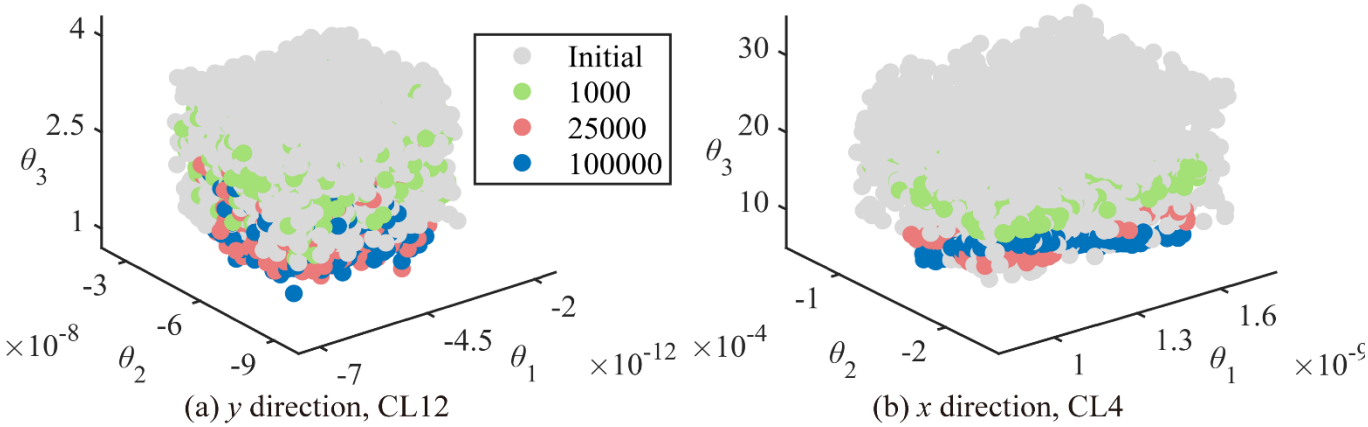

(a) *y* direction, CL12 (b) *x* direction, CL4

Figure 12 Parameter estimation results for two control lengths for specimen S1

Note that 'initial', '1000', '25000', and '100000' within the legend represent the samples of the three parameters at initial, 1000, 25000, and 100000 load cycles, respectively.

Figures 13 (a)(b), (c)(d), and (e)(f) show the predictions for the two CLs based on their PF parameter estimates at 1000, 10000, and 25000 load cycles, respectively. The predictions of the posterior pdfs have their averages approaching the target with the increasing load cycle step, and the 90% confidence boundaries (CBs) including the target, while those made by the second-order polynomial function fitting the collected measurements up to the last step remain unstable and inaccurate, proving the value of numerical simulation of the training and also the superior performance of the PF-based model updating for CL prediction. On the other hand, it takes longer for the updated evolution model of the *x*-direction CL (i.e., CL4) to correctly track the future state than that of the *y*-direction CL (i.e., CL12), mainly due to the larger uncertainties of the *x*-direction CLs during fatigue delamination growth.

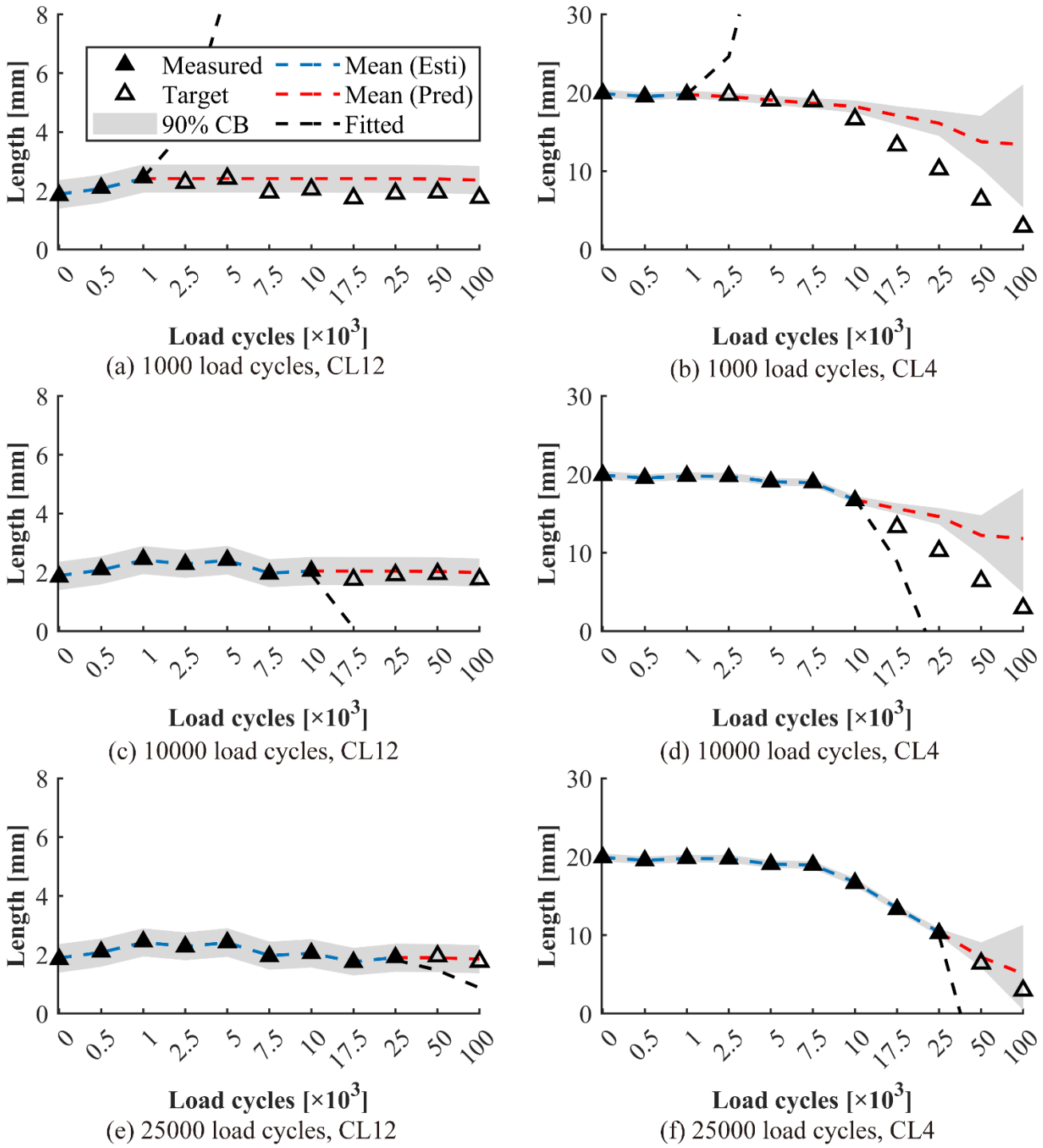

Figure 13 Predictions for two control lengths with the estimates at three selected load cycles for specimen S1

Following the strategy proposed in Section 2.4, the control points (CPs) and their CBs at those steps can be located by the future CLs, and then used for future delamination shaping. For simplicity, only the delamination shape predicted with the estimates at 1000, 10000, and 25000 load cycles are given in Figures 14 (a), (b), and (c), respectively. As expected, the shape prediction based on the estimates at one certain step seems less accurate as the prediction step horizon increases, because of the growing uncertainties of delamination growth ahead in the future. On the other hand, the prediction at one specific future step gets more accurate if more delamination images are adopted for model updating, due to the convergence of the evolution parameters as shown in Figure 12.

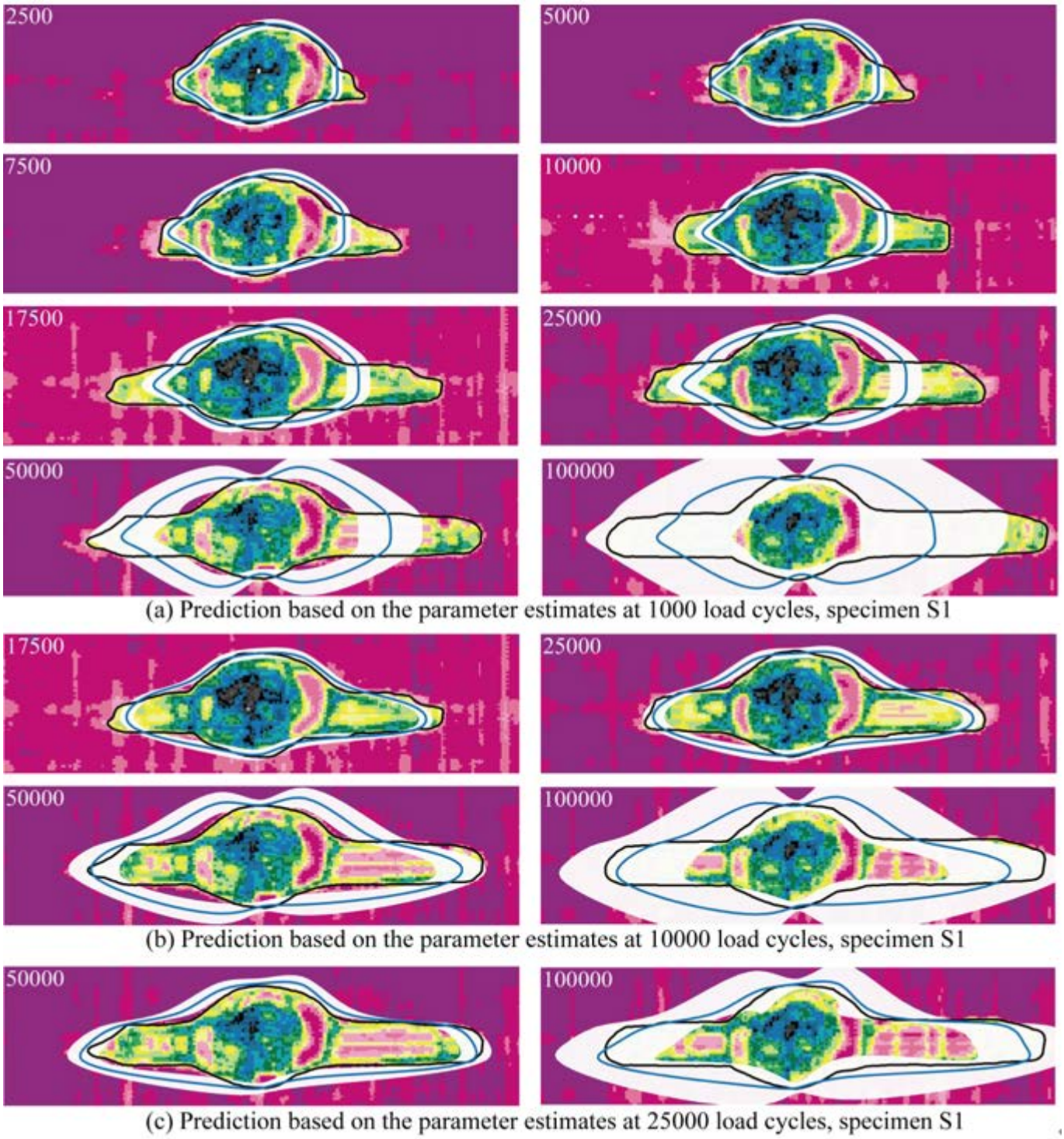

Figure 14 Shapes predicted at future load cycles based on the estimates at three selected load cycles for specimen S1

Note: the load cycles at which the future shape is predicted are in the left-top corner. The black curve, blue curve, and white area are the target shape, the predicted shape, and its 90% CBs, respectively.

By defining the center of the delamination image (i.e., $[27.5\text{ mm}, 7.5\text{ mm}]$) as the reference point (RP), and $\boldsymbol{\alpha} = [0, 5, 10, 15, 45, 90, 135, 165, 170, 175, 180, 185, 190, 195, 235, 270, 315, 345, 350, 355]$ degrees with respect to the *x*-direction, the CRA prognostic performance metric is shown in Figure 15 (a), where the parameter estimates at each step are adopted for shape prediction at the remaining future steps, drawing the same conclusion as Figure 14, as highlighted by the red and green arrows. Similar performances

have been observed in Figure 15 (b). The latter is taken from the work of some of the same authors [4], where the delamination images from specimens S2 and S3 are adopted for training the damage evolution model, and then initializing the PF. This, on the other hand, emphasizes the advantage of the proposed method, i.e., it requires no experimental or in-field data for training the model and then providing some PF initialization hyperparameters, at little cost of prediction accuracy.

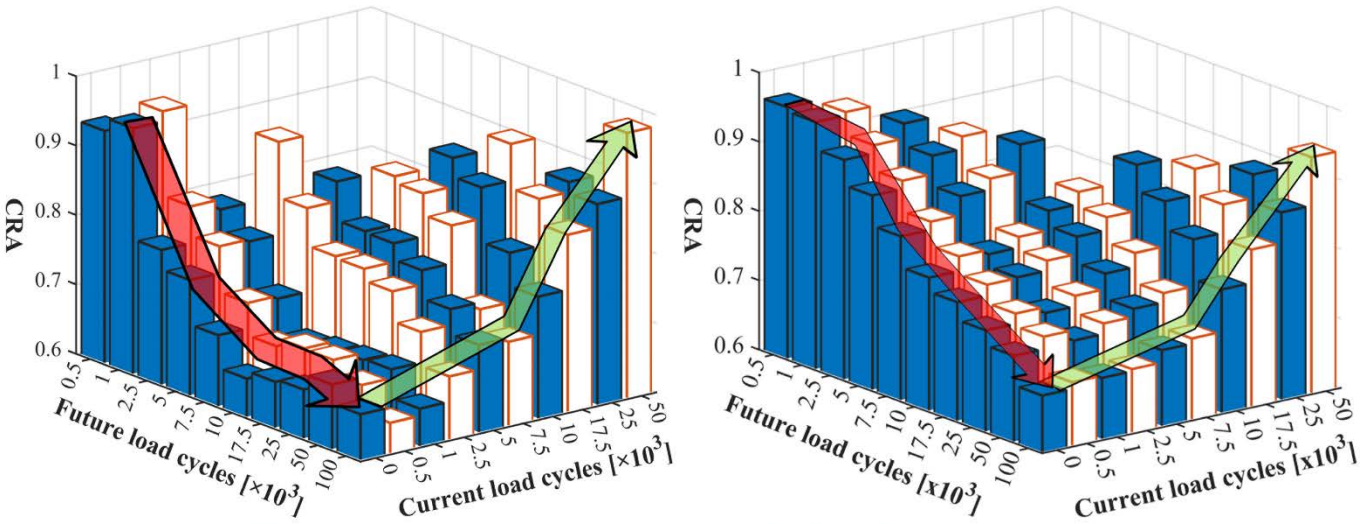

(a) NUM for PF initialization, this study (b) EXP for PF initialization, our previous work

Figure 15 Cumulative relative accuracies (CRAs) of shape predictions for specimen S1

4.3 Predictions extrapolation to other specimens

The proposed framework is also tested for specimens S2 and S3 with the same PF hyperparameters in Table 6. Parameter estimation results, CL predictions, shape predictions, and their CRAs are presented in Figures 16, 17 and 18, 19, and 20, respectively. Despite that the performance of the method for each specimen is noted as slightly different due to the stochasticity of delamination growth, the observations from Section 4.2 remain valid, again indicating that the method could cope with the uncertainties of damage evolution by online updating the CL model parameters and also demonstrating the robustness of the proposed method over different experimental specimens.

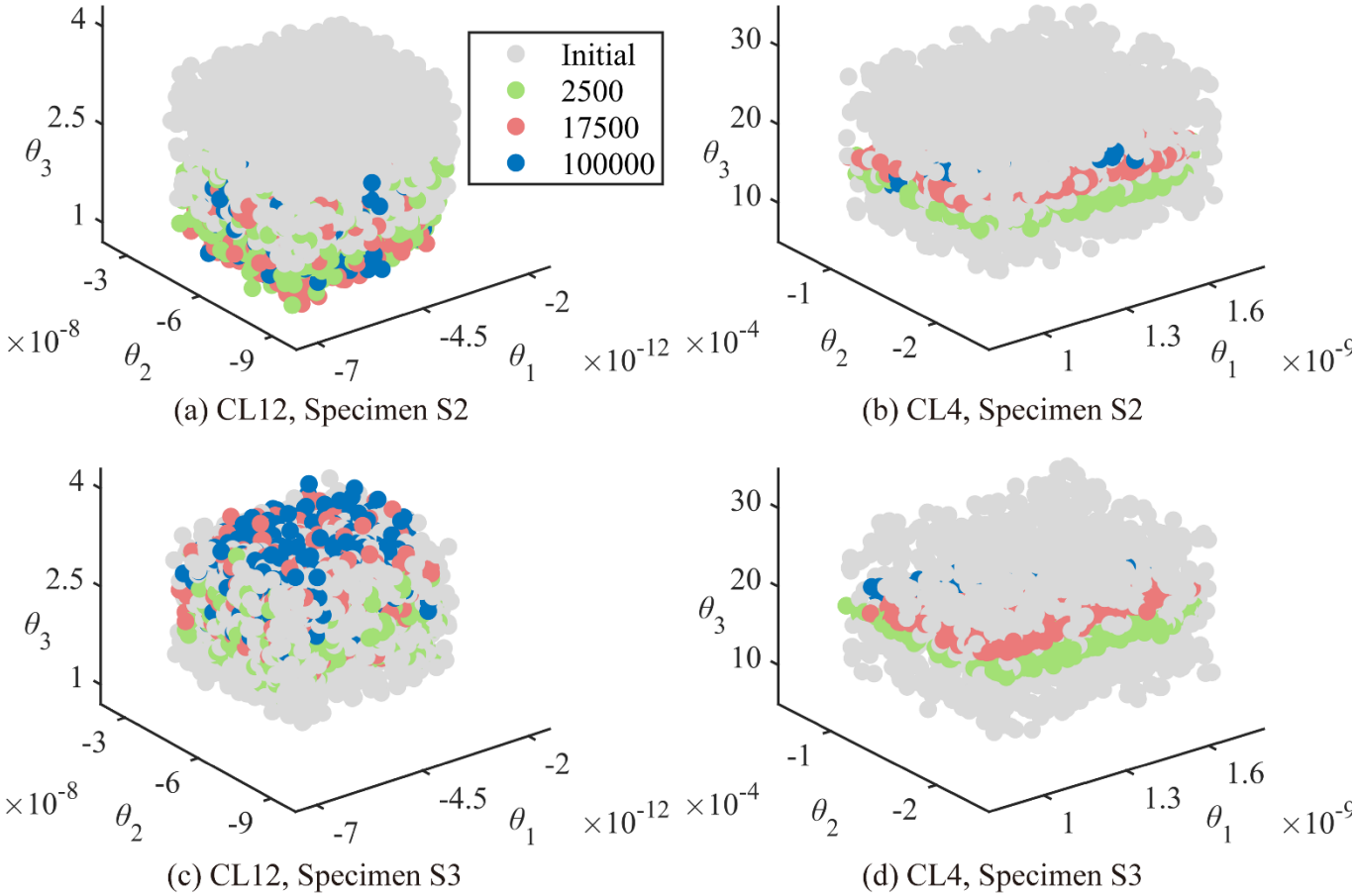

Figure 16 Parameter estimation results for two control lengths for specimens S2 and S3

Note that 'initial', '2500', '17500', and '100000' within the legend represent the samples of the three parameters at initial, 2500, 17500, and 100000 load cycles, respectively.

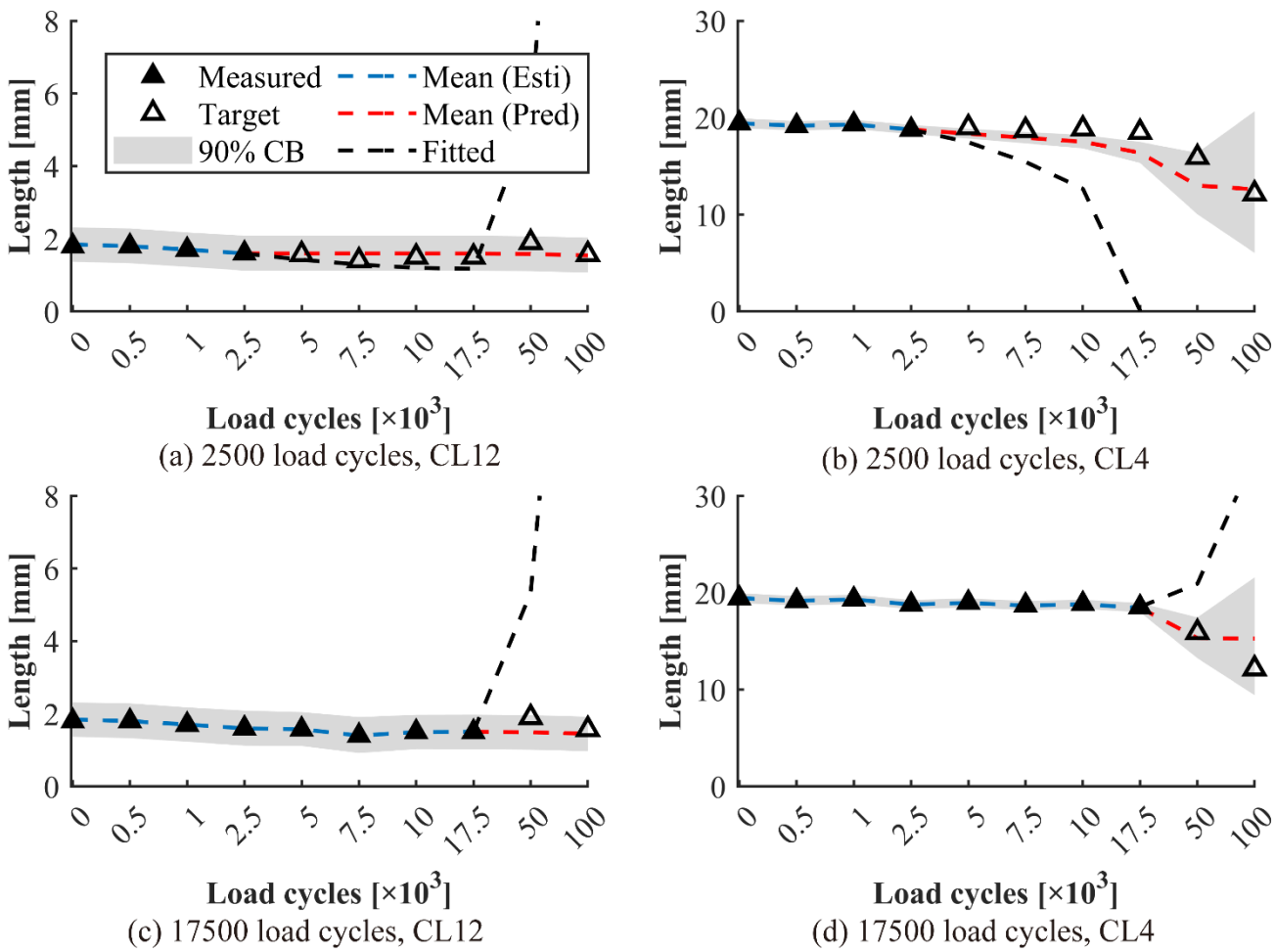

Figure 17 Predictions for two control lengths with the estimates at two selected load cycles for specimen S2

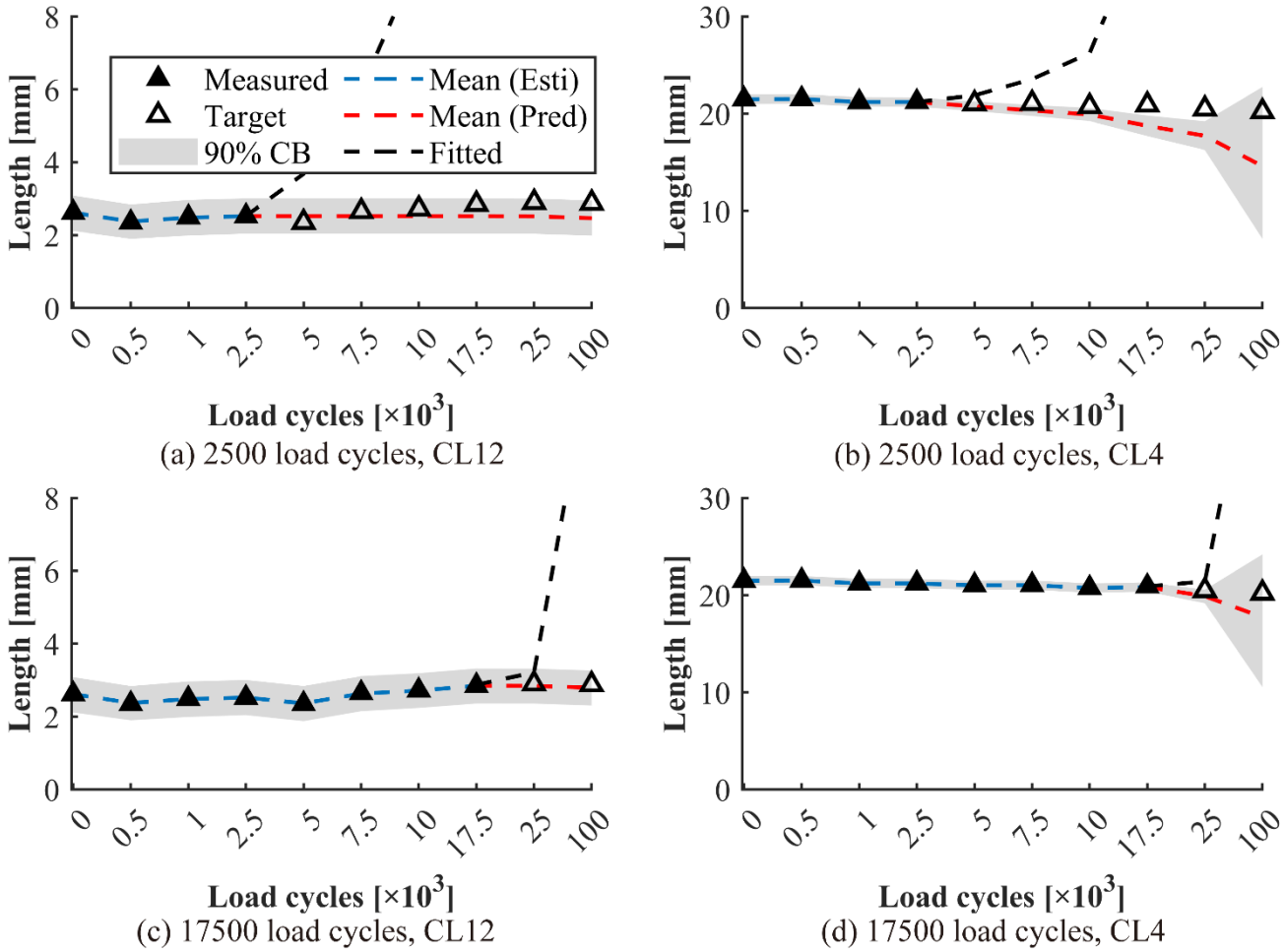

Figure 18 Predictions for two control lengths with the estimates at two selected load cycles for specimens S3

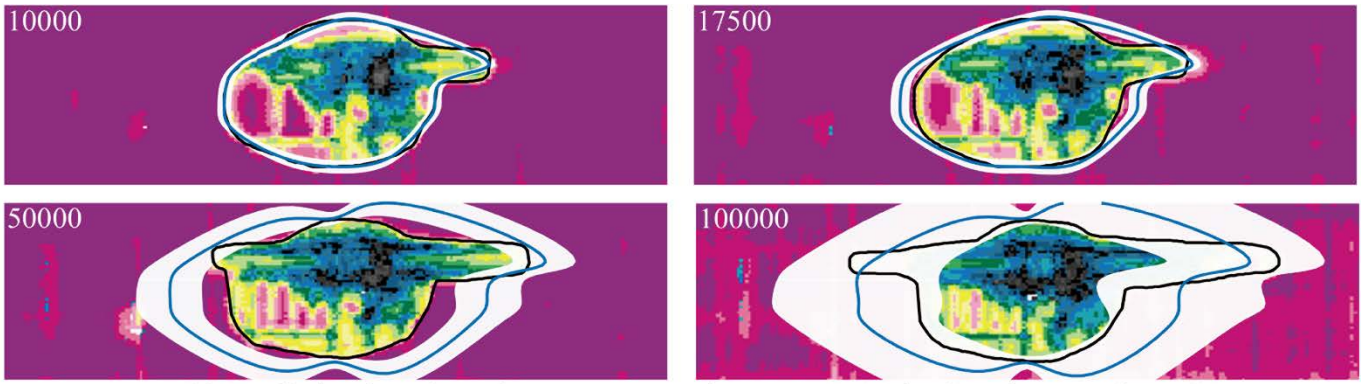

(a) Prediction based on the parameter estimates at 2500 load cycles, specimen S2

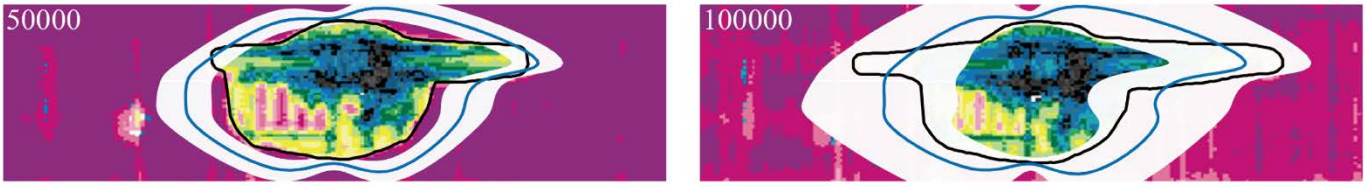

(b) Prediction based on the parameter estimates at 17500 load cycles, specimen S2

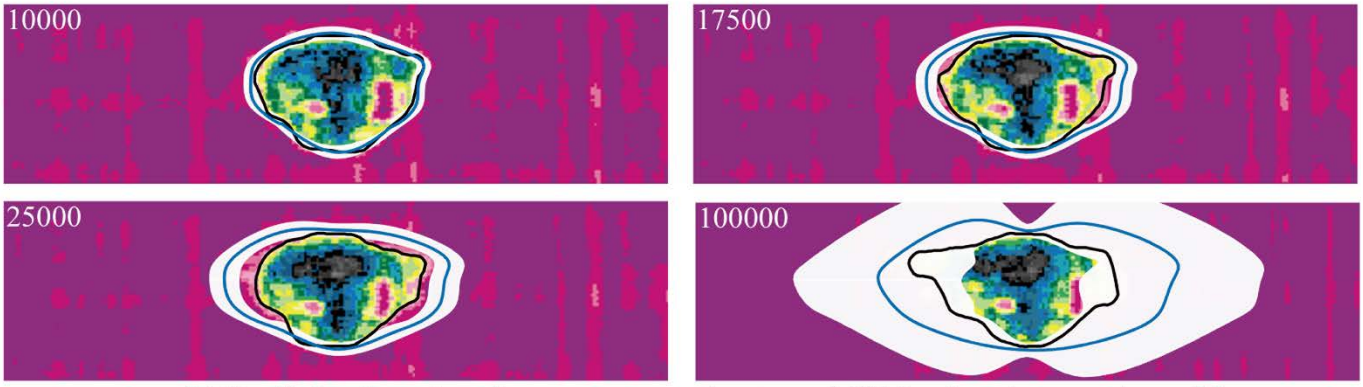

(c) Prediction based on the parameter estimates at 2500 load cycles, specimen S3

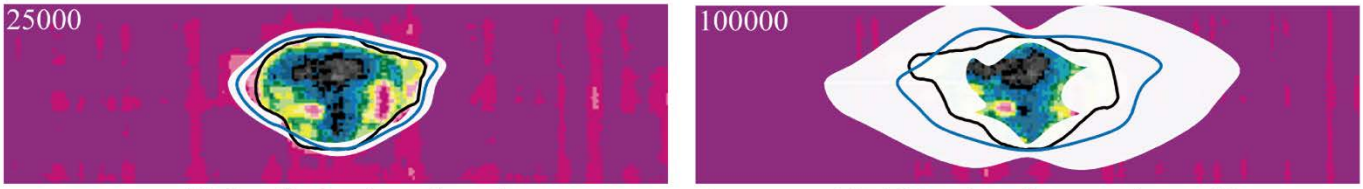

(d) Prediction based on the parameter estimates at 17500 load cycles, specimen S3

Figure 19 Shape predictions for specimens S2 and S3

Note: the load cycles at which the future shape is predicted are in the left-top corner. The black curve, blue curve, and white area are the target shape, the predicted shape, and its 90% CBs, respectively.

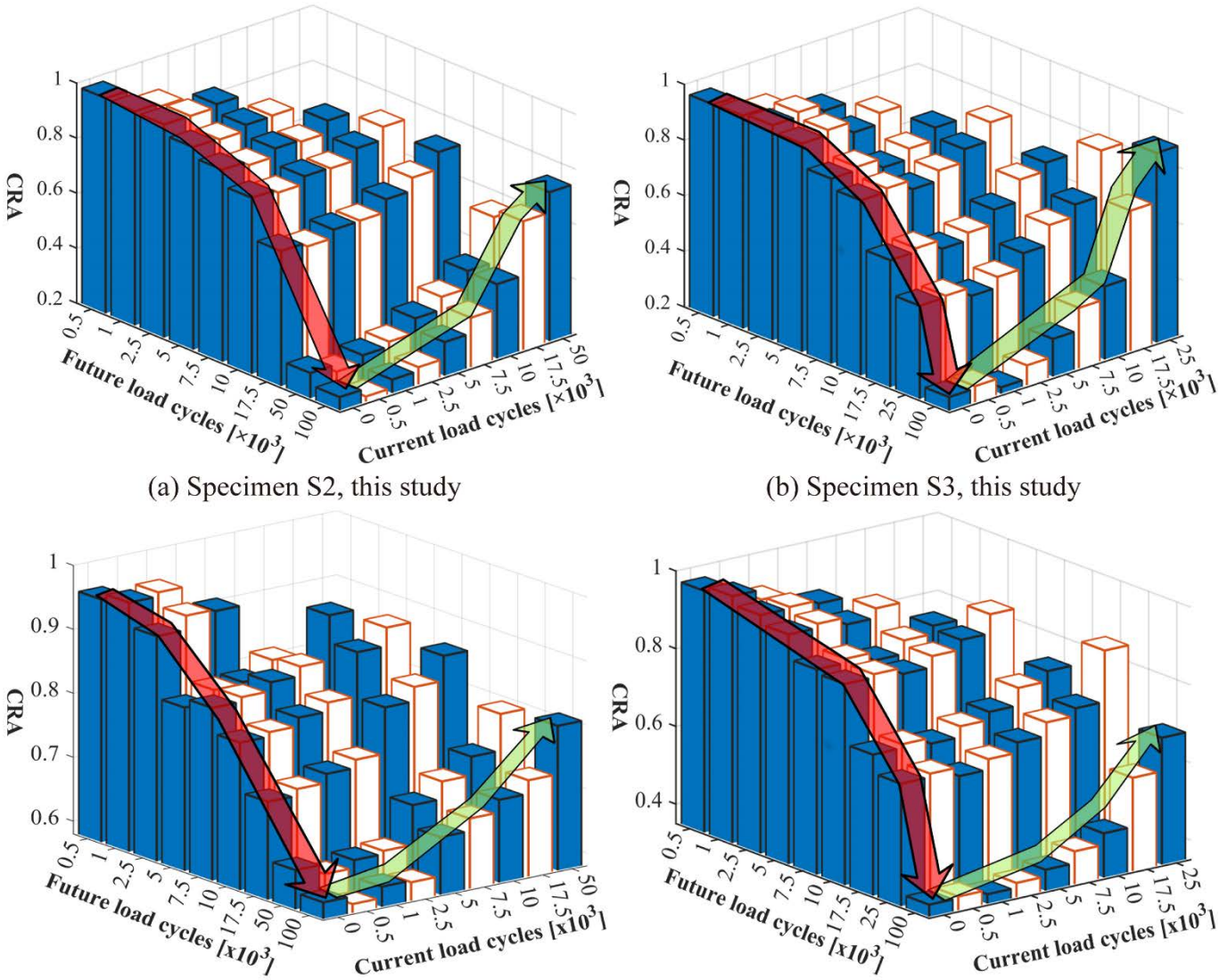

(a) Specimen S2, this study (b) Specimen S3, this study

(c) Specimen S2, our previous work (d) Specimen S3, our previous work

Figure 20 Cumulative relative accuracies (CRAs) of shape predictions for specimens S2 and S3

Note: the delamination images for training and initialization in Figure (c) originate from the experimental specimens S1 and S3, while those in Figure (d) are from specimens S1 and S2.

5. Conclusions

Current practices usually have the fatigue delamination shape predicted through either numerical or surrogate model. The former has been demonstrated accurate in simulating the double cantilever beam (DCB) test, but not capable for complex application scenarios due to the lack of consideration of multiple sources of uncertainties, while the latter is demonstrated feasible for predicting the complex fatigue delamination growth but requiring a sufficiently large experimental database for training.

By combining the two methods above, this work has proposed a new numerical simulation-aided particle filter-based shape prediction framework, which only requires numerically simulated delamination growth for building the above function and then providing the PF initialization hyperparameters. The proposed framework has three advantages, i.e.,

- The costs and efforts in conducting run-to-failure tests and collecting experimental or in-field

data for PF initialization can be avoided.

- The numerical database developed in this work only consists of five numerical simulations, which can be run in parallel on an AMD Ryzen 9 3950X 16-Core Processor, requiring about 48 hours in total.
- By taking takes the model uncertainties into account by online updating their parameters, the proposed method is robust among three specimens.

In a more realistic application scenario, where the delamination growth may occur in a more complex and larger structure, the numerical simulation might be more time-consuming and less accurate, still calling for advanced numerical methods for high-fidelity and computationally efficient simulation, and a more sophisticated state estimation algorithm for an accurate model updating. Moreover, to explore the possibility of the proposed method for online implementation, an online measurement system, e.g., guided wave, can be installed for monitoring and then inferring the delamination shapes through a data-driven function mapping between the shape and measurements.

Appendix A1

Figures A.1, A.2, and A.3 present the images of the delamination and its contour at different load cycles from experimental specimens S1, S2, and S3, respectively.

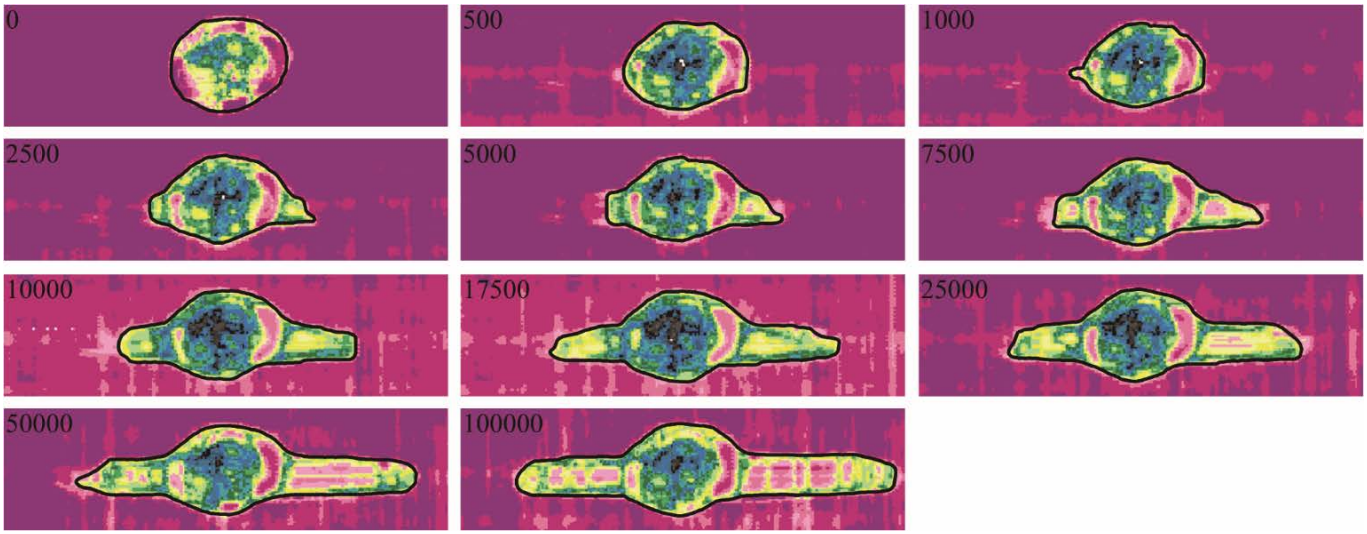

Figure A.1 Ultrasonic C-scan delamination images at different load cycles from specimen S1

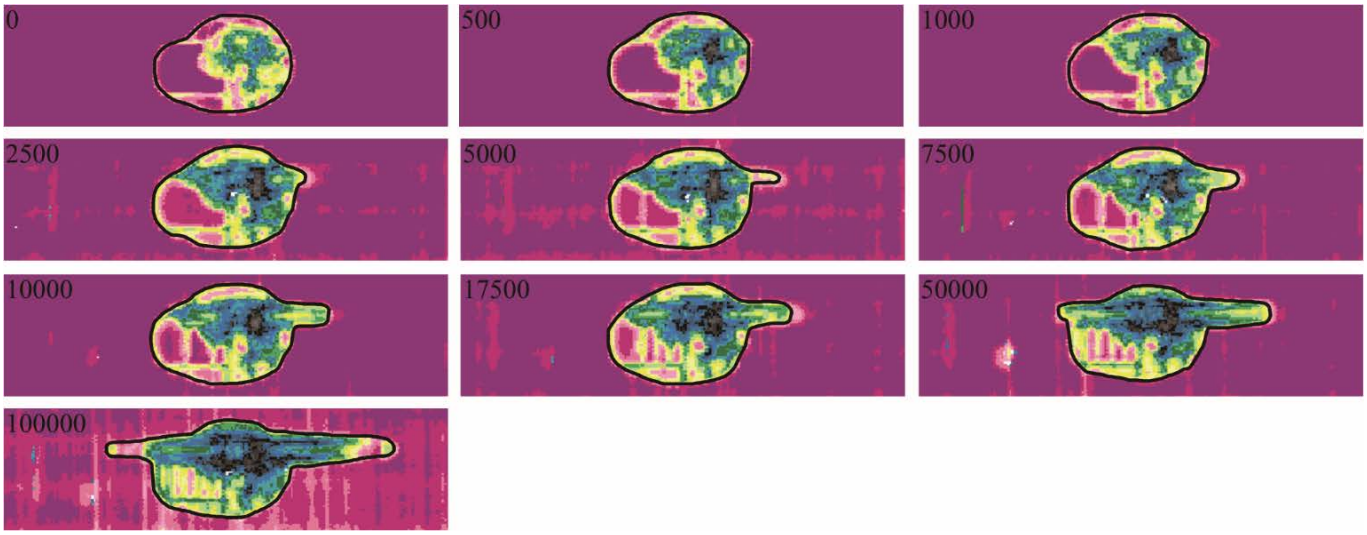

Figure A.2 Ultrasonic C-scan delamination images at different load cycles from specimen S2

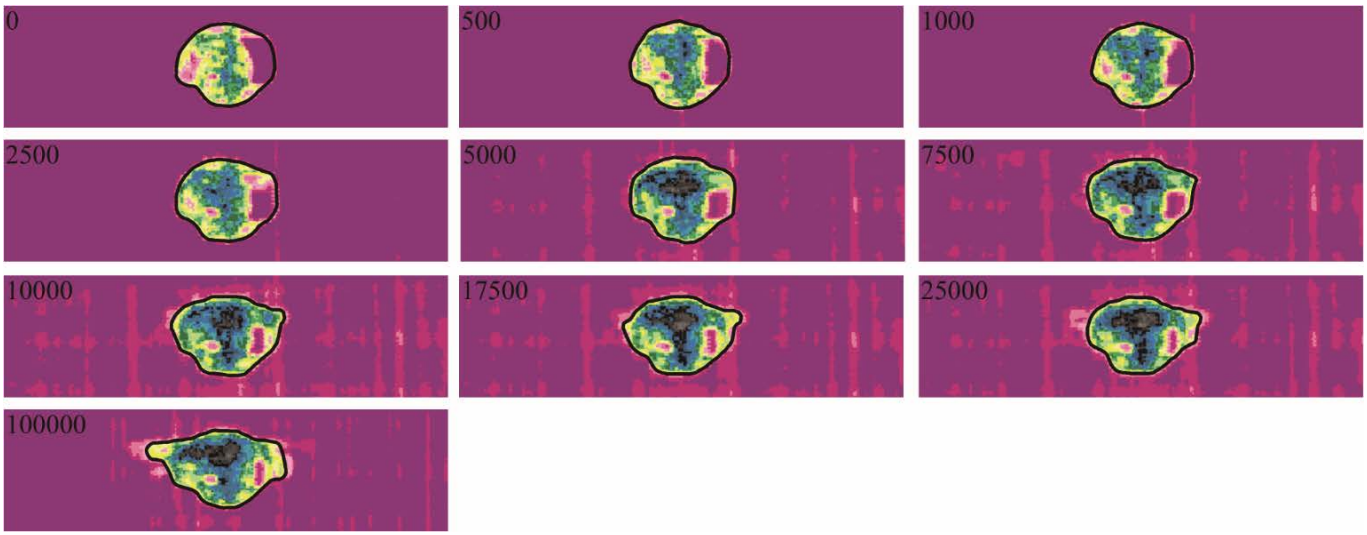

Figure A.3 Ultrasonic C-scan delamination images at different load cycles from specimen S3

Acknowledgments

This project has received funding from the European Union's Horizon 2020 research and innovation programme under the Marie Skłodowska-Curie grant agreement No. 859957. Also, the authors would like to thank the Institute of Polymers and Composites at Hamburg University of Technology (TUHH), for their collaborative support regarding the production of samples and the collection of monitoring data.

References

[1] M. Chiachío, J. Chiachío, S. Sankararaman, K. Goebel, J. Andrews, A new algorithm for prognostics using Subset Simulation, Reliability Engineering & System Safety, 168 (2017) 189-199.
[2] M. Corbetta, C. Sbarufatti, M. Giglio, A. Saxena, K. Goebel, A Bayesian framework for fatigue life prediction of composite laminates under co-existing matrix cracks and delamination, Composite Structures, 187 (2018) 58-70.
[3] D. Cristiani, C. Sbarufatti, M. Giglio, Damage diagnosis and prognosis in composite double cantilever beam coupons by particle filtering and surrogate modelling, Structural Health Monitoring, (2020)

1475921720960067.
[4] T. Li, F. Cadini, M. Chiachío, J. Chiachío, C. Sbarufatti, Particle filter-based delamination shape prediction in composites subjected to fatigue loading, Structural Health Monitoring, 0 14759217221116041.
[5] S. Datta, R.K. Neerukatti, A. Chattopadhyay, Buckypaper embedded self-sensing composite for real-time fatigue damage diagnosis and prognosis, Carbon, 139 (2018) 353-360.
[6] J. Chiachío, M. Chiachío, S. Sankararaman, A. Saxena, K. Goebel, Condition-based prediction of time-dependent reliability in composites, Reliability Engineering & System Safety, 142 (2015) 134-147.
[7] C. Tao, C. Zhang, H. Ji, J. Qiu, Application of neural network to model stiffness degradation for composite laminates under cyclic loadings, Composites Science and Technology, 203 (2021) 108573.
[8] N. Eleftheroglou, D. Zarouchas, R. Benedictus, An adaptive probabilistic data-driven methodology for prognosis of the fatigue life of composite structures, Composite Structures, 245 (2020) 112386.
[9] F. Jaramillo, J.M. Gutiérrez, M. Orchard, M. Guarini, R. Astroza, A Bayesian approach for fatigue damage diagnosis and prognosis of wind turbine blades, Mechanical Systems and Signal Processing, 174 (2022) 109067.
[10] M. Moradi, A. Broer, J. Chiachío, R. Benedictus, T.H. Loutas, D. Zarouchas, Intelligent health indicator construction for prognostics of composite structures utilizing a semi-supervised deep neural network and SHM data, Engineering Applications of Artificial Intelligence, 117 (2023) 105502.
[11] I. Lopez, N. Sarigul-Klijn, A review of uncertainty in flight vehicle structural damage monitoring, diagnosis and control: Challenges and opportunities, Progress in Aerospace Sciences, 46 (2010) 247-273.
[12] P. Baraldi, F. Mangili, E. Zio, Investigation of uncertainty treatment capability of model-based and data-driven prognostic methods using simulated data, Reliability Engineering & System Safety, 112 (2013) 94-108.
[13] J. Chen, S. Yuan, H. Wang, On-line updating Gaussian process measurement model for crack prognosis using the particle filter, Mechanical Systems and Signal Processing, 140 (2020) 106646.
[14] T. Li, C. Sbarufatti, F. Cadini, J. Chen, S. Yuan, Particle filter-based hybrid damage prognosis considering measurement bias, Structural Control and Health Monitoring, n/a (2021) e2914.
[15] T. Li, L. Lomazzi, F. Cadini, C. Sbarufatti, J. Chen, S. Yuan, Numerical simulation-aided particle filter-based damage prognosis using Lamb waves, Mechanical Systems and Signal Processing, 178 (2022) 109326.
[16] N.V. De Carvalho, G.E. Mabson, R. Krueger, L.R. Deobald, A new approach to model delamination growth in fatigue using the Virtual Crack Closure Technique without re-meshing, Engineering Fracture Mechanics, 222 (2019) 106614.
[17] F. Teimouri, M. Heidari-Rarani, F. Haji Aboutalebi, An XFEM-VCCT coupled approach for modeling mode I fatigue delamination in composite laminates under high cycle loading, Engineering Fracture Mechanics, 249 (2021) 107760.
[18] L. Carreras, A. Turon, B.L.V. Bak, E. Lindgaard, J. Renart, F. Martin de la Escalera, Y. Essa, A simulation method for fatigue-driven delamination in layered structures involving non-negligible fracture process zones and arbitrarily shaped crack fronts, Composites Part A: Applied Science and Manufacturing, 122 (2019) 107-119.
[19] C. Tao, J. Qiu, W. Yao, H. Ji, A novel method for fatigue delamination simulation in composite laminates, Composites Science and Technology, 128 (2016) 104-115.
[20] B.L.V. Bak, A. Turon, E. Lindgaard, E. Lund, A benchmark study of simulation methods for high-cycle fatigue-driven delamination based on cohesive zone models, Composite Structures, 164 (2017) 198-206.
[21] K.G. Abhinav Saxena, Cecilia C. Larrosa, and Fu-Kuo Chang, CFRP Composites Data Set, NASA Ames Prognostics Data Repository (http://ti.arc.nasa.gov/project/prognostic-data-repository), NASA Ames Research Center, Moffett Field, CA.
[22] F. Cadini, C. Sbarufatti, M. Corbetta, F. Cancelliere, M. Giglio, Particle filtering-based adaptive training of neural networks for real-time structural damage diagnosis and prognosis, Structural Control and Health Monitoring, 26 (2019).

[23] C. Sbarufatti, M. Corbetta, M. Giglio, F. Cadini, Adaptive prognosis of lithium-ion batteries based on the combination of particle filters and radial basis function neural networks, Journal of Power Sources, 344 (2017) 128-140.
[24] F. Cadini, C. Sbarufatti, M. Corbetta, M. Giglio, A particle filter-based model selection algorithm for fatigue damage identification on aeronautical structures, Structural Control & Health Monitoring, (2017) e2002.
[25] M.S. Arulampalam, S. Maskell, N. Gordon, T. Clapp, A tutorial on particle filters for online nonlinear/non-Gaussian Bayesian tracking, IEEE Transactions on Signal Processing, 50 (2002) 174-188.
[26] Z. Chen, Bayesian Filtering: From Kalman Filters to Particle Filters, and Beyond, Statistics, 182 (2003).
[27] L. Carreras, J. Renart, A. Turon, J. Costa, B.L.V. Bak, E. Lindgaard, F. Martin de la Escalera, Y. Essa, A benchmark test for validating 3D simulation methods for delamination growth under quasi-static and fatigue loading, Composite Structures, 210 (2019) 932-941.
[28] Y. Shi, C. Pinna, C. Soutis, Modelling impact damage in composite laminates: a simulation of intra-and inter-laminar cracking, Composite Structures, 114 (2014) 10-19.
[29] B.Z.G. Haque, A progressive composite damage model for unidirectional and woven fabric composites, MAT162 user manual, 10 (2015).
[30] J. Liu, M. West, Combined parameter and state estimation in simulation-based filtering, Sequential Monte Carlo methods in practice, Springer, 2001, pp. 197-223.
[31] M. Corbetta, C. Sbarufatti, M. Giglio, M.D. Todd, Optimization of nonlinear, non-Gaussian Bayesian filtering for diagnosis and prognosis of monotonic degradation processes, Mechanical Systems and Signal Processing, 104 (2018) 305-322.
[32] E.N. Chatzi, A.W. Smyth, The unscented Kalman filter and particle filter methods for nonlinear structural system identification with non-collocated heterogeneous sensing, Structural Control & Health Monitoring, 16 (2009) 99-123.

Particle filter-based damage prognosis by fusing multiple degradation models

Tianzhi Li[1], Jian Chen[3], Shenfang Yuan[3], Dimitrios Zarouchas[2], Claudio Sbarufatti[1], Francesco Cadini[1, *]

[1]*Dipartimento di Meccanica, Politecnico di Milano, Milan, Italy*

[2]*Center of Excellence in Artificial Intelligence for Structures, Prognostics & Health Management, Aerospace Engineering Faculty, Delft University of Technology, Delft, The Netherlands*

[3]*Research Center of Structural Health Monitoring and Prognosis, State Key Laboratory of Mechanics and Control of Mechanical Structures, Nanjing University of Aeronautics and Astronautics, Nanjing, China*

**francesco.cadini@polimi.it*

Abstract

Damage prognosis always requires a degradation model describing the damage evolution with time, thus the prognostic performance highly depends on the selection of such a model. The best model should probably be case-specific, calling for the fusion of multiple degradation models for a robust prognosis. In this context, this paper proposes a scheme of online fusing multiple models in a particle filter-based damage prognosis framework. First, each prognostic model has its process equation built through a physics-based or data-driven degradation model and has its measurement equation linking the damage state and the measurement. Second, one PF is used to estimate the damage state and the parameters within one model. Then, the estimates from all models are adopted for RUL prediction. Finally, the samples from each PF are fused with those from all the other PFs to improve their particle diversity, and consequently, to provide better estimation and prognostic performance. The feasibility and robustness of the proposed method are validated by an experimental study, where an aluminum lug structure subject to fatigue crack growth is monitored by a guided wave measurement system.

Keywords: structural health monitoring, damage prognosis, degradation model, fusion, particle filter, Lamb wave

1. Introduction

Degradation is an inevitable process that exists in engineering structures. Once a certain level of damage is

reached, the proper functionality of the structure can no longer be guaranteed. Necessary inspections should be regularly carried out for avoiding such failure, possibly resulting in high financial expenses and long system downtime. In order to simultaneously guarantee structural safety/reliable operation and reduce maintenance costs, the maintenance is desired to be scheduled just before the damage state reaches a critical level, calling for an advanced damage prognosis technique to provide the structure remaining useful life (RUL).

Current damage prognosis studies usually have the damage occurring during the degradation process described as a physics-based damage state, such as matrix crack [1], delamination [2], or stiffness reduction [3, 4] in composites, crack length [5-8] or shape [9] in metal, or a data-driven health indicator (HI) [10-13] extracted from online measured structural health monitoring (SHM) signals. As the structure degradation follows a specific pattern under a certain service condition, the future damage condition can be predicted by a proper model describing such a pattern. A large variety of both physics-based [1, 5, 6, 9] and data-driven [2, 3, 7, 10-12] degradation models have been proposed for such a task. The former resorts to a physics-based law like Paris' law or its extensions, where the degradation rate, e.g., strain energy release rate or stress intensity factor, is either analytically calculated [1] or fitted by a data-driven modeling strategy, such as polynomial fitting [5, 6], support vector regression [9], or neural networks [14], through numerically simulated data.

On the other hand, the data-driven models are usually built through sufficient physical damage data [2, 3, 7] or data-driven health indicators (HI) [10-13] collected during the actual degradation process. The former [2, 3, 7] typically considers a physical damage state to be measured for one or more specimens, and then it applies those data for model training, such as the crack growth [7] and stiffness reduction [3] depicted by neural networks, or the delamination shape growth modeled by polynomial fitting function [2]. As to the latter [10-13], at each time instant or load cycle step, some data-sensitive statistical features like mean value, standard deviation, and root-mean-square value are extracted from some online measurements like acoustic emission or acceleration. Those features can either be directly taken as the health indicator (HI) at that step [11], or further processed through a machine learning algorithm to create a more robust HI [10, 12, 13], finally producing a database of the HIs during the whole run-to-failure process for training a HI evolution model.

There is no universally best degradation model, as each type of model has its pros and cons [15]. Indeed, even the same model can yield different prognostic performances when applied to different specimens of the same structure under the same fatigue test, because of the uncertainties arising from several sources, such as, for example, very complex degradation mechanisms, not fully captured, or environmental

effects [16, 17]. One possibility to enhance the prognostic robustness is to properly fuse multiple degradation models as in [18], where two physics-based fatigue crack growth models are combined within a Monte Carlo framework for crack length prediction. On the other hand, some studies of battery RUL prediction [19, 20] have multiple data-driven capacity degradation models fused in a particle filter (PF)-based framework, generally yielding better performance than the use of one model. However, few study is dedicated to developing a framework for fusing both physics-based and data-driven degradation models.

In this context, this work proposes a scheme for fusing those degradation models within a PF-based prognostic framework. Each degradation model is adopted to formulate a different state space model and to provide one group of PF estimates. As all PF estimates share the same state component such as the damage state, each PF estimates can be fused with all the others to improve their diversity, and, consequently, to allow for more robust estimation and prognostic performance. The proposed method is demonstrated by an experimental study, where an aluminum lug structure subjected to fatigue crack growth (FCG) is monitored by an online measurement system of Lamb waves.

The rest of this paper is organized as follows: Section 2 introduces the four steps of the prognosis framework. The application setup is given in Section 3, while the results of the proposed method applied to the experimental case study are provided in Section 4. Finally, Section 5 concludes this paper.

2. Novel damage prognosis framework

Figure 1 presents the four main steps of the proposed damage prognosis framework. First, for each prognostic model, the process equation is formulated using either a physics-based or data-driven degradation model, and the measurement equation is built to describe the relationship between the damage state and the measurement. Note that the number of state space models is equal to the number of available degradation models. Second, one PF is used to estimate the damage state and the parameters of one model, thus resulting in multiple groups of particles. Then, for each time step, the damage state and RUL obtained from each group of particles are simply merged for damage quantification and RUL prediction, respectively. Finally, provided with multiple groups of PF estimates sharing the same state components, the samples of those components from one PF can be modified by those from the other PFs through either the mutation or crossover operator. Compared to the traditional method [5, 6], where PF is only applied to one prognostic model to provide one group of estimates for predicting the future state and RUL, the main novelty of the proposed method is that a fusion scheme is online implemented to fuse all PF estimates for improving the particle diversity of each PF, and consequently, the overall estimation and prognostic accuracy.

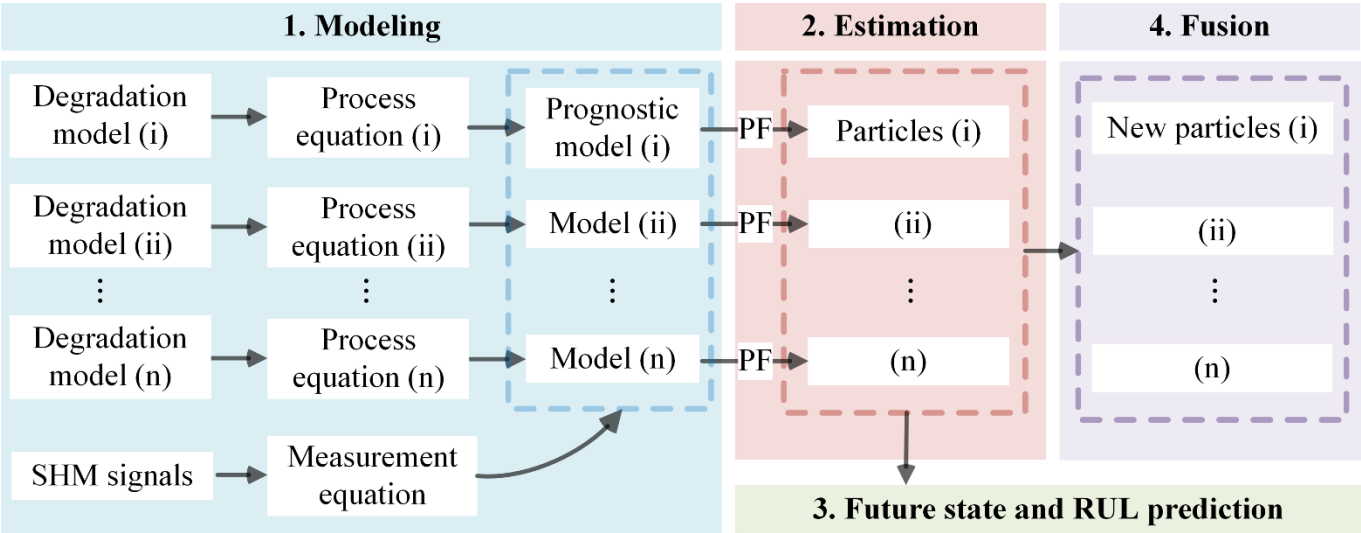

Figure 1 Schematics of the proposed framework.

2.1 State space modeling

The degradation behavior of a structure can be in general described as:

$$x_k = f_l(x_{k-1}, \boldsymbol{\theta}_l) \tag{1}$$

where x is the damage state, $f_l(\cdot)$ is the l-th degradation function, $\boldsymbol{\theta}_l$ is a vector of function coefficients, and the subscript k denotes the k-th time step. The parameters $\boldsymbol{\theta}_l$ usually vary in different specimens of the same structure due to the uncertainties arising from the degradation process, so they are taken as unknown variables to be estimated. To this aim, following a popular approach, they are added into an augmented state vector:

$$\begin{bmatrix} \boldsymbol{\theta}_{l,k} \\ x_k \end{bmatrix} = \begin{bmatrix} \boldsymbol{\theta}_{l,k-1} + \boldsymbol{\omega}_{\theta,l,k} \\ f_l\left(x_{k-1}, \boldsymbol{\theta}_{l,k}, \omega_k\right) \end{bmatrix} \tag{2}$$

where ω_k and $\boldsymbol{\omega}_{\theta,l}$ are the process noises for the damage state and the parameters, respectively.

With a proper measurement y (which, in most cases, is a damage-sensitive statistical feature extracted from measured signals) for inferring the unknown damage state, the measurement equation in a PF-based damage prognosis can be formulated as:

$$y_k = g(x_k) + v_k \tag{3}$$

where $g(\cdot)$ is usually a data-driven function describing the relationship between the damage state and the measurement, ν_k is the measurement noise. Due to the unavoidable bias between the sensor-based and predicted (from the function $g(\cdot)$) measurements, the prognostic model in current practices [5, 6] is usually formulated as

$$\begin{cases} \boldsymbol{z}_{l,k} = \begin{bmatrix} \boldsymbol{\theta}_{l,k} \\ x_k \\ b_k \end{bmatrix} = \begin{bmatrix} \boldsymbol{\theta}_{l,k-1} + \boldsymbol{\omega}_{\theta,l,k} \\ f_l(x_{k-1}, \boldsymbol{\theta}_{l,k}, \omega_k) \\ b_{k-1} + \omega_{b,k} \end{bmatrix} \\ y_k = g(x_k) + b_k + \nu_k \end{cases} \tag{4}$$

where b is the bias parameter and ω_b is its corresponding process noise, and $\boldsymbol{z}_{l,k}$ is the state vector including the model parameter, damage state, and bias.

Note that each degradation model has its version of Eq. (4). More specifically, each model has a different process equation from the others, thus the number of models built in this framework is equal to the number of available degradation models. On the other hand, in order to provide an accurate comparison between the performance of multiple degradation models and that of one model, this study has the same measurement equation shared by each prognostic model. Note that the use of the same measurement equation among different prognostic models is not mandatory, and one may in general resort to different measurement equations in this application.

2.2 Particle filter-based estimation

In a Bayesian approach, the k-th-step unknown state vector $\boldsymbol{z}_{l,k}$ can be inferred from the observation as:

$$p(\boldsymbol{z}_{l,k}|\boldsymbol{y}_{1:k-1}) = \int p(\boldsymbol{z}_{l,k}|\boldsymbol{z}_{l,k-1}) p(\boldsymbol{z}_{l,k-1}|\boldsymbol{y}_{1:k-1}) d\boldsymbol{z}_{l,k-1} \tag{5}$$

$$p(\boldsymbol{z}_{l,k}|\boldsymbol{y}_{1:k}) \propto p(y_k|\boldsymbol{z}_{l,k}) p(\boldsymbol{z}_{l,k}|\boldsymbol{y}_{1:k-1}) \tag{6}$$

where $\boldsymbol{y}_{1:k}$ is the measurement vector collected from time step 1 to k, the symbol $\propto$ means 'proportional to', the transition distribution $p(\boldsymbol{z}_{l,k}|\boldsymbol{z}_{l,k-1})$ and the likelihood function $p(y_k|\boldsymbol{z}_{l,k})$ are the process and measurement equations, respectively, $p(\boldsymbol{z}_{l,k}|\boldsymbol{y}_{1:k-1})$ and $p(\boldsymbol{z}_{l,k}|\boldsymbol{y}_{1:k})$ represent the prior and posterior probability distribution function (PDF), respectively.

Given that the analytical solution of Eqs. (5) and (6) can hardly be acquired in a nonlinear and non-Gaussian system like Eq. (4), an efficient state estimation, i.e., the sampling importance resampling (SIR) PF [21], is used in this study. Table 1 lists the pseudo-code of the SIR PF. Note the number of PFs

implemented at each step is equal to the number of models.

Table 1 Sampling importance resampling particle filter

Initialization: draw N_p particles $\{\boldsymbol{z}_{l,0}^i: i = 1,2,\dots,N_p\}$ from the distribution $p(\boldsymbol{z}_{l,0})$

For k=1, 2, …,

Prediction in PF: draw N_p particles $\{\boldsymbol{z}_{l,k}^i: i = 1,2,\dots,N_p\}$ by $\boldsymbol{z}_k^i \sim p(\boldsymbol{z}_{l,k}|\boldsymbol{z}_{l,k-1}^i)$

Weight update: calculate the particle weight w_k^i through $w_k^i \propto p(\boldsymbol{y}_k|\boldsymbol{z}_{l,k}^i)$, and assign its normalized form $\widetilde{w}_k^i$ to each particle $\boldsymbol{z}_{l,k}^i$

Resample for those particles based on the normalized weights

End

2.3 RUL prediction

The prognostic step enables the prediction of future damage state at any step ahead of the k-th one through the degradation model Eq. (1) and the posterior PDF of the damage state and its growth parameters. Once the predicted state reaches a pre-defined threshold of the damage state l_{th}, above which the structure fails, the RUL is taken as the multiplication of the number of prediction steps and the number of load cycles ΔN in one step. The pseudo-code of the above procedure for the l-th prognostic model is summarized in Table 2. Note that the RUL is independently predicted through each degradation model, and then multiple groups of RUL estimates are merged to produce the RUL distribution.

Table 2 Calculation of future state and RUL at time step k for the l-the model

Initialization: set $\{x_k^{i,0}: i = 1,2,\dots,N_p\}$ as $\{x_k^i: i = 1,2,\dots,N_p\}$

For i = 1 : N_p

j = 0

While $x_k^{i,j} < l_{th}$

Calculate the future state $x_k^{i,j+1}$ by $x_k^{i,j+1} = f_l\left(x_k^{i,j}, \boldsymbol{\theta}_{l,k}^i\right)$

$j = j + 1$

End

$\mathrm{RUL}_{l,k}^i = j \times \Delta N$

End

2.4 Fusion for improving particle diversity

In the SIR PF resampling procedure, the particles with large weights are duplicated and those with small weights are eliminated. As a result, the diversity of the particles tends to decrease over time, which can limit the performance of the PF. This phenomenon is commonly referred to as particle impoverishment. It has been well elaborated that the strategies for improving particle diversity can lead to more robust state and parameter estimation [22, 23].

The proposed method has multiple prognostic models providing multiple groups of PF estimates, among which they share some state components, i.e., the damage state and bias parameter of Eq. (4). The two components can be included into a vector as,

$$\boldsymbol{s}_k = \begin{bmatrix} x_k \\ b_k \end{bmatrix} \tag{7}$$

This enables the possibility of improving the sample diversity of those shared components for each PF by fusing all PF estimates.

The objective of this paper is to verify the applicability of the proposed method to diverse algorithms aimed at enhancing diversity. To achieve this goal, the paper employs the crossover and mutation operators, two widely used genetic operators for addressing such problems [22, 23], to the shared components mentioned earlier in a separate manner. For each time step and each PF, the crossover operator is implemented as follows,

$$\boldsymbol{s}_{k,l}^{i} = \alpha \boldsymbol{s}_{k,l}^{i} + (1-\alpha)\underbrace{\left(\boldsymbol{s}_{k,1}^{i} + \cdots + \boldsymbol{s}_{k,l-1}^{i} + \boldsymbol{s}_{k,l+1}^{i} + \cdots\right)} \tag{8}$$

where the *i*-th sample $\boldsymbol{s}_{k,l}^{i}$ contains a vector of the shared components from the *l*-th PF, while the samples from all the other PFs are included in the horizontal curly bracket, and α is a coefficient within a range of $[0 \quad 1]$. On the other hand, when the mutation operator is applied to the *l*-th PF, a certain percentage of samples of the shared components from that PF is replaced by some samples randomly selected from all the other PFs.

Notice that the proposed method is generic enough so that the other operators can be included. The fusion of multiple degradation models intends to provide multiple groups of well-distributed samples, while the algorithm for adopting all the samples to improve the diversity for each group can be user-defined. Interested readers may refer to [24, 25] for those algorithms, but not mentioned here for simplicity.

3. Application setup

This section includes the experimental and numerical studies, signal processing, state space modeling, and the creation of the target crack length and features. The experimental setup of the fatigue tests and Lamb wave monitoring is briefly introduced in Section 3.1. The Lamb wave simulations for modeling the measurement equation [5] are presented in Section 3.2. The Lamb waves from the experimental and numerical studies are adopted to provide the statistical feature for damage quantification in Section 3.3. Section 3.4 presents three typical degradation models used in practices, while Section 3.5 shows the state space modeling and the PF parameters. Section 3.6 illustrates the creation of the target crack growths and their corresponding features using all the experimental specimens.

3.1 Experimental study

Figures 2 (a) and (b) show the fatigue test of an aluminum lug structure and a Lamb wave-based monitoring system [26], respectively. The structure has a thickness of $5\ \mathrm{mm}$ and a through hole with a diameter of $5\ \mathrm{mm}$. The latter has a $2\ \mathrm{mm}$-long notch created on the edge for initiating the crack growth. The MTS810 electro-hydraulic servo material test system is used to provide the sinusoidal tensile fatigue load, with maximum value, minimum value, and frequency set as $18\ \mathrm{kN}$, 0.1, and $10\ \mathrm{Hz}$, respectively.

Figure 2 (c) shows an image collected by a digital microscope for observing the crack length. The scale lines are equally spaced by $1\ \mathrm{mm}$. A pre-cracking step is performed at the beginning of the fatigue test until the crack length reaches $3\ \mathrm{mm}$. The fatigue loading is occasionally paused during the test, and then a static tensile load of $18\ \mathrm{kN}$ is applied to the specimen for better visualization of the crack. The crack length is considered to increase by $1\ \mathrm{mm}$ once the crack tip reaches the next line. At each measured crack length, e.g., $3\ \mathrm{mm}$ or $4\ \mathrm{mm}$, one transducer serves as the actuator providing a 3-cycle Hanning-windowed sine burst with a central frequency of $160\ \mathrm{kHz}$, and another one is the sensor collecting the Lamb waves with a sampling frequency of $50\ \mathrm{MHz}$.

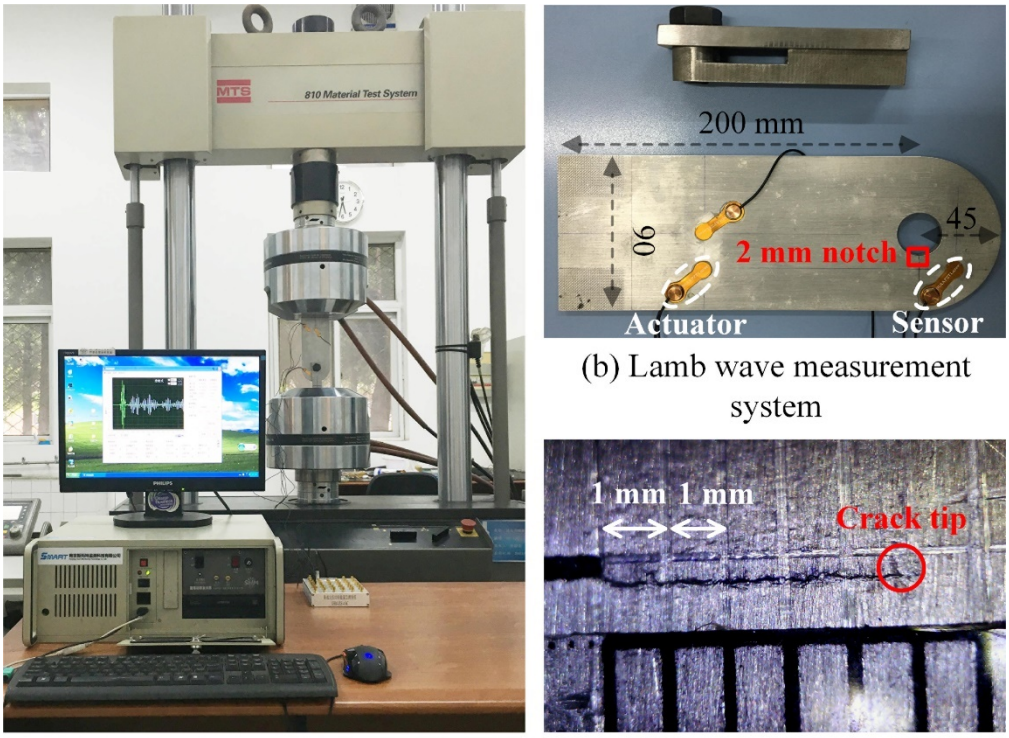

(a) Fatigue test (b) Lamb wave measurement system (c) Crack and scale lines

Figure 2 Experimental setup.

Figure 3(a) depicts the fatigue crack growth trajectories of six specimens, namely S1 to S6. These specimens exhibit variations that primarily result from uncertainties in the manufacturing process and specimen assembly, among other factors. The initial crack length and the threshold for RUL calculation are $3\ \mathrm{mm}$ and $22\ \mathrm{mm}$, respectively. It is noteworthy that the crack growth data of specimen S6 will be utilized to determine the coefficients of degradation models, as discussed in Sections 3.4 and 3.5. Conversely, the data from specimens S1 to S5 will serve for testing purposes.

Figure 3(b) illustrates the experimental Lamb waves, with a duration of 1.2×10^{-4} s, at three different crack lengths. The first wave package is a crosstalk, which arises from the electromagnetic induction between the actuator and sensor circuits. To account for this, the start of the crosstalk (SoC) is considered as the time when the actuator applies the excitation to the structure [27]. The analytical arrivals of the S_0 and A_0 waves are approximately equivalent to the summation of the SoC and the S_0 wave time-of-flight (ToF), and to that of the SoC and the A_0 ToF, respectively. Interested readers can refer to [5, 6] for further details on the calculation. Typically, increasing crack lengths result in amplitude reductions of the S_0 waves, which cause variations in the feature extracted from these waves.

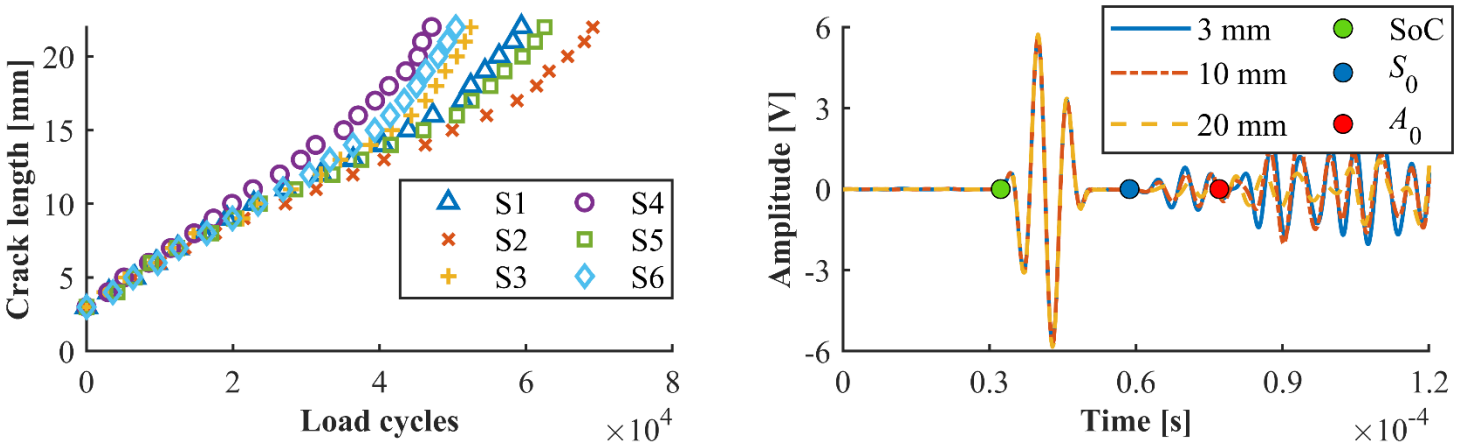

(a) Crack growths of specimens S1 ~ S6 (b) Lamb wave signals at three crack lengths from S1

Figure 3 Fatigue crack growths with Lamb wave monitoring

Note: 'SoC' means 'start of crosstalk'.

3.2 Numerical study

Figure 4 shows the Lamb wave numerical simulations under different crack lengths, which has been well detailed in [5], thus briefly introduced here. ABAQUS EXPLICIT is used to provide the numerical S_0 Lamb waves of the structure at nine crack lengths $\{3, 5, 8, 10, 12, 15, 18, 20, 22\ \text{mm}\}$. Two symmetric out-of-plane pressures, whose amplitudes are the same as the excitation used in the experiment, are applied within the circles (same as the actuator shape) on the two sides of the plate at each crack length. The out-of-plane displacements at the center of the sensor location are taken as the numerical Lamb wave.

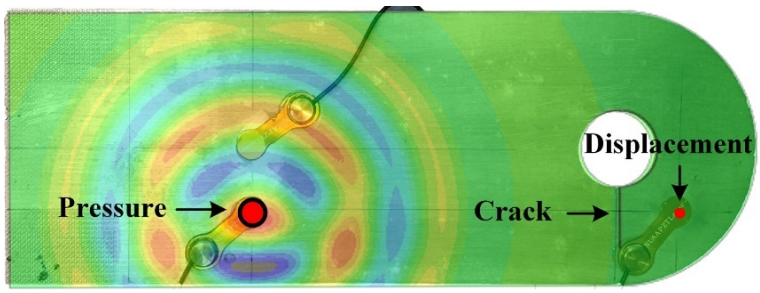

Figure 4 Numerical setup.

Figures 5 (a) and (b) show the comparisons of the numerical and experimental (specimen S1) Lamb waves at crack lengths of $3\ \text{mm}$ and $20\ \text{mm}$, respectively. The crosstalk of the experimental signal is replaced by zero values for simplicity. The numerical S_0 Lamb waves satisfactorily agree with the experimental ones before 4×10^{-5} s, thus can be adopted for modeling the measurement equation relating the crack length and some sort of Lamb wave-based statistical feature.

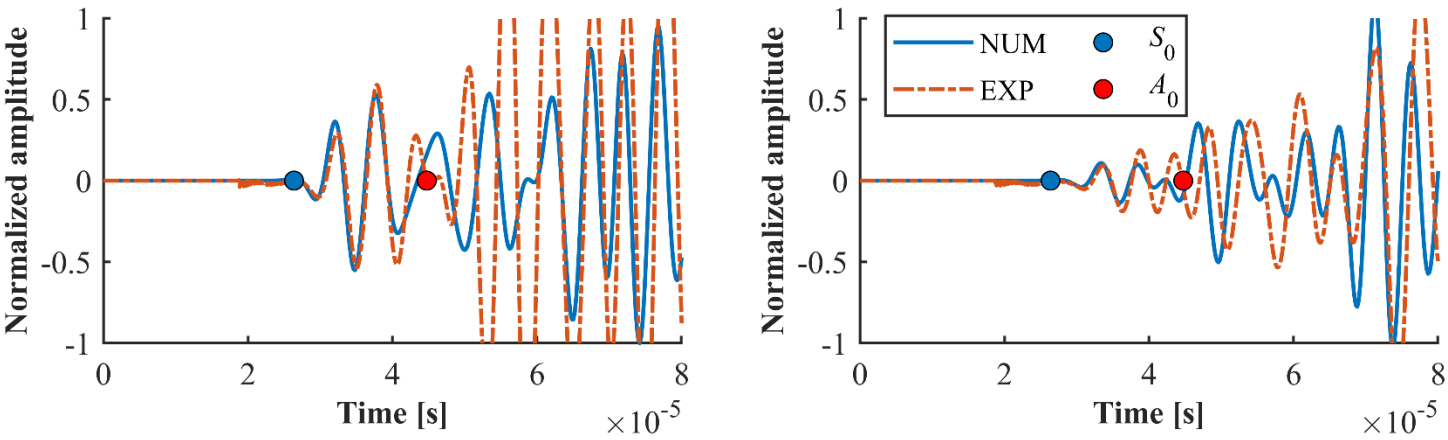

(a) 3 mm crack length (b) 20 mm crack length

Figure 5 Numerical and experimental (specimen S1) Lamb waves at two crack lengths.

3.3 Feature extraction

Same to the work [5] from the same authors, the feature is extracted from the Lamb wave signals within a properly selected time window, whose start and width are defined as the S_0 arrival and 10^{-5} s, respectively. Given the demonstrated performances of root-mean-square (RMS)-based feature in prognostic investigation [28], it is chosen in this study and defined as follows,

$$RMS_l = 1 - \frac{rms(f_l)}{rms(f_r)} \tag{9}$$

Note that f_r and f_l are the windowed Lamb waves at the initial crack length 3 mm and another crack length l mm, respectively, and the function '*rms*' is the root-mean-square value of an individual set of signals.

The above processing is implemented for the numerical Lamb waves and the experimental Lamb waves from each of the specimens S1 ~ S5, as shown in Figure 6. The satisfactory match between the numerical and experimental features enables the feasibility of adopting the numerical data for modeling the measurement equation. The features from experimental specimens S1 ~ S5 will be processed in Section 3.6 for testing the proposed method.

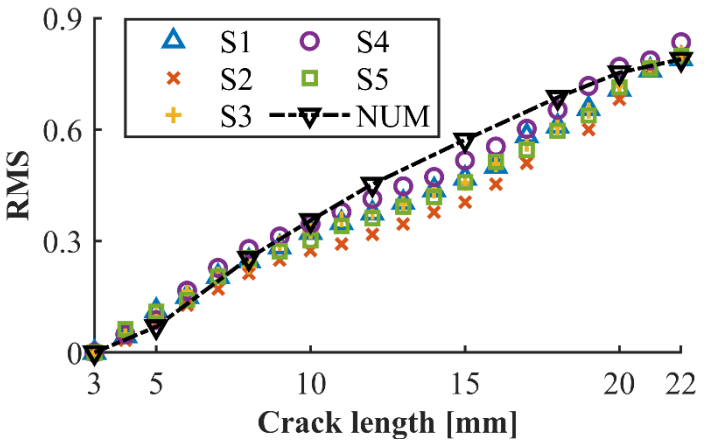

Figure 6 Root-mean-square (RMS) values at different crack lengths from numerical and experimental studies.

3.4 Typical degradation models

Table 3 lists three typical degradation models adopted in current prognostic practices. The rate of damage evolution in the first two models is characterized as a function of the current damage state, which can be determined from either theoretical knowledge or empirical data. The last model considers the damage state as a function of time or the number of load cycles, and it can only be built through some experimental data. This study adopts all three types of models, as detailed below.

Table 3 Three typical degradation models used in practices

Model	Literature	Which type of model	General expression	The model used in this study
1	[5, 6]	Physics-based	$x_k = x_{k-1} + \Delta N_k f_1(x_{k-1})$	$x_k = x_{k-1} + C\left(\Delta K(x_{k-1})\right)^m \Delta N_k$
2	[3]	Data-driven	$x_k = x_{k-1} + \Delta N_k f_2(x_{k-1})$	$x_k = x_{k-1} + \Delta N_k (p_1 {x_{k-1}}^3 + p_2 {x_{k-1}}^2 + p_3 x_{k-1} + p_4)$
3	[7]	Data-driven	$x_k = f_3(N_k)$ or $x_k = f_3(t_k)$	$x_k = q_1 {N_{k-1}}^3 + q_2 {N_{k-1}}^2 + q_3 N_{k-1} + q_4$

Note: (i) the function $f_1(\cdot)$ is derived from physical knowledge, while $f_2(\cdot)$ and $f_3(\cdot)$ from experimental data, (ii) N and t denote the number of load cycles and the time, respectively, and ΔN is the number of load cycles included at one time step; and (iii) the parameters C and m and the polynomial coefficients p_1, p_2, p_3, p_4, q_1, q_2, q_3, and q_4 will be fitted from the crack growth data of experimental specimen S6 for initializing the particle filter.

The first model used in this study adopts Paris's law to describe the crack growth. The two parameters C and m are the empirical values, and the calculation of stress intensity factor range ΔK is taken from the work of some of the same authors [6],

$$\Delta K(x) = 1.43 \times 10^{-3} x^3 + 5.63 \times 10^{-1} x^2 - 13.5x + 497.8 \tag{10}$$

The two data-driven functions $f_2(\cdot)$ and $f_3(\cdot)$ in the last two models used in this study are built by the third-order polynomial fitting function, due to its demonstrated performance in damage prognosis investigation [2], although other approaches, e.g. machine learning-based, can be used in principle. The parameters C and m and the polynomial coefficients p_1, p_2, p_3, p_4, q_1, q_2, q_3, and q_4 will be acquired through the experimental data of specimen S6 for initializing each PF.

3.5 State space modeling and PF parameters

The three degradation models lead to three prognostic models as below,

$$\begin{cases} \begin{bmatrix} \ln C_k \\ m_k \\ x_k \\ b_k \end{bmatrix} = \begin{bmatrix} \ln C_{k-1} + \omega_{c,k} \\ m_{k-1} + \omega_{m,k} \\ x_{k-1} + e^{\omega_{1,k}} C_k (\Delta K(x_{k-1}))^{m_k} \Delta N_k \\ b_{k-1} + \omega_{b,k} \end{bmatrix} \\ y_k = g(x_k) + b_k + v_k \end{cases} \tag{11}$$

$$\begin{cases} \begin{bmatrix} p_{1,k} \\ p_{2,k} \\ p_{3,k} \\ p_{4,k} \\ x_k \\ b_k \end{bmatrix} = \begin{bmatrix} p_{1,k-1} + \omega_{p,1,k} \\ p_{2,k-1} + \omega_{p,2,k} \\ p_{3,k-1} + \omega_{p,3,k} \\ p_{4,k-1} + \omega_{p,4,k} \\ x_{k-1} + e^{\omega_{1,k}} \left(p_{1,k} {x_{k-1}}^3 + p_{2,k} {x_{k-1}}^2 + p_{3,k} x_{k-1} + p_{4,k}\right) \Delta N_k \\ b_{k-1} + \omega_{b,k} \end{bmatrix} \\ y_k = g(x_k) + b_k + v_k \end{cases} \tag{12}$$

$$\begin{cases} \begin{bmatrix} q_{1,k} \\ q_{2,k} \\ q_{3,k} \\ q_{4,k} \\ x_k \\ b_k \end{bmatrix} = \begin{bmatrix} q_{1,k-1} + \omega_{q,1,k} \\ q_{2,k-1} + \omega_{q,2,k} \\ q_{3,k-1} + \omega_{q,3,k} \\ q_{4,k-1} + \omega_{q,4,k} \\ p_{1,k} {N_k}^3 + p_{2,k} {N_k}^2 + p_{3,k} N_k + p_{4,k} + e^{\omega_{2,k}} \\ b_{k-1} + \omega_{b,k} \end{bmatrix} \\ y_k = g(x_k) + b_k + v_k \end{cases} \tag{13}$$

where $\omega_1 \sim \mathcal{N}\left(-\frac{\sigma^2}{2}, \sigma^2\right)$ is the unbiased Gaussian process noise with the standard deviation σ [29], $\omega_{p,1}$, $\omega_{p,2}$, $\omega_{p,3}$, $\omega_{p,4}$, $\omega_{q,1}$, $\omega_{q,2}$, $\omega_{q,3}$, $\omega_{q,4}$, ω_2 and ω_b are zero-mean Gaussian process noises, the measurement y is the RMS feature, where the function $g(\cdot)$ is taken as one 4-th order polynomial fitting regression fitted through the numerical RMS features,

$$g(x) = 7.42 \times 10^{-6}x^4 + 4.20 \times 10^{-4}x^3 + 7.27 \times 10^{-3}x^2 + 4.43 \times 10^{-3}x + 7.37 \times 10^{-2} \quad (14)$$

Each prognostic model mentioned above is nonlinear and non-Gaussian, because of the non-linearities of the degradation model and the function $g(\cdot)$, and the non-Gaussian noise e^{ω}, respectively. Note that these models share two state components, i.e., the crack length *x*, and the bias parameter *b*. For each PF, the distribution of the samples of the two components will be modified with those from all the other PFs through either the mutation or the crossover operator.

Kernel smoothing [30] is adopted to improve the accuracy of estimating the time-invariant parameters ln *C*, *m*, p_1, p_2, p_3, p_4, q_1, q_2, q_3, and q_4. The parameter *m* is taken as an example for the illustration as follows,

$$m_k = \sqrt{1-h^2}m_{k-1} + \left(1-\sqrt{1-h^2}\right)\hat{m}_{k-1} + \omega_{m,k} \quad (15)$$

where *h* is the smoothing parameter selected within a range of $[0 \quad 1]$, and $\hat{m}$ are the mean of the samples for the parameter *m*.

Table 4 shows the values of the PF parameters used in this study, most of which are determined from the works of the same authors [2, 5, 6]. As to the model fusion, the coefficient α for the crossover operator is set to 0.1 [22], while the mutation percentage of the mutation operator to 10%.

Table 4 Particle filter parameters.

PF parameters used for all three models		
Number of particles N_p	*h* in kernel smoothing	Standard deviation in likelihood function
4000	0.1	0.02
Initial range for *x* [mm]	Initial value for *b* [-]	Distributions of process noise ω_b for *b*
$x_0 \sim \mathrm{U}(2.5, 3.5)$	$b_0 = 0$	$\omega_b \sim \mathcal{N}(0, 0.005^2)$
PF parameters used for Model 1 only		
Initial distributions for $\ln C$ $\left[\ln \frac{\mathrm{mm}}{\mathrm{cycle}(\mathrm{MPa}\sqrt{\mathrm{mm}})^{-m}}\right]$, *m* [-]	Distributions of process noises $\{\omega_1, \omega_c, \omega_m\}$ for *x*, $\ln C$, *m*	
$\begin{bmatrix}\ln C_0 \\ m_0\end{bmatrix} \sim \mathcal{N}\left(\begin{bmatrix}-45.01 \\ 6.117\end{bmatrix}, \begin{bmatrix}0.9966 & -0.1764 \\ -0.1764 & 0.0346\end{bmatrix}\right)$	$\omega_1 \sim \mathcal{N}\left(-\frac{0.01^2}{2}, 0.01^2\right)$ $\omega_c \sim \mathcal{N}(0, 0.01^2)$	$\omega_m \sim \mathcal{N}(0, 0.001^2)$
PF parameters used for Model 2 only		
Initial range for $\{p_{l,0}: l = 1,2,3,4\}$	Distributions of process noises $\{\omega_{p,l}: l = 1,2,3,4\}$ for $\{p_l: l = 1,2,3,4\}$	Distribution of process noise ω_1 for *x*

$p_{l,0} \sim \mathrm{U}(0.8p_{f,l}, 1.2p_{f,l})$	$\omega_{p,l} \sim \mathcal{N}\left(0, \left(0.00015p_{f,l}\right)^2\right)$	$\omega_1 \sim \mathcal{N}\left(-\frac{0.01^2}{2}, 0.01^2\right)$
PF parameters used for Model 3 only		
Initial range for $\{q_{l,0}: l = 1,2,3,4\}$	Distributions of process noises $\{\omega_{q,l}: l = 1,2,3,4\}$ for $\{q_l: l = 1,2,3,4\}$	Distributions of process noise ω_2 for x
$q_{l,0} \sim \mathrm{U}(0.8q_{f,l}, 1.2q_{f,l})$	$\omega_{q,l} \sim \mathcal{N}\left(0, \left(0.00015q_{f,l}\right)^2\right)$	$\omega_2 \sim \mathcal{N}(0, 0.01^2)$

Note: (i) the means of the distribution of $\begin{bmatrix} \ln C_0 \\ m_0 \end{bmatrix}$ are fitted from the crack growth data of specimen S6, and they are -45.01, and 6.117, respectively; and (ii) $p_{f,l}$ and $q_{f,l}$ are the l-th coefficient of the third polynomial fitting function of Models (2) and (3), respectively, and they are fitted from the crack growth data of specimen S6.

3.6 Target crack growth and features

The crack lengths and the Lamb waves in this experiment are collected every several thousand load cycles. For simulating a more realistic SHM case, where the Lamb waves can be collected over shorter load cycle intervals for crack length quantification, the crack growth and the features from each of the five experimental specimens (S1 ~ S5) are used to create the target crack lengths and the corresponding features at a shorter cycle interval through the procedure below [5].

(i) The target crack lengths for each specimen are created every 300 load cycles through linear interpolation by the crack data provided in Section 3.1, and then corrupted by white Gaussian noise with a signal-to-noise ratio (SNR) of 50 dB to introduce some uncertainties in the crack growth process, as shown in Figure 7 (a).

(ii) For each specimen, linear interpolation is applied to create the RMS-based feature at each target length, which is then corrupted by white Gaussian noise with a SNR of 30 dB to simulate the measurement noise, as given in Figure 7 (b).

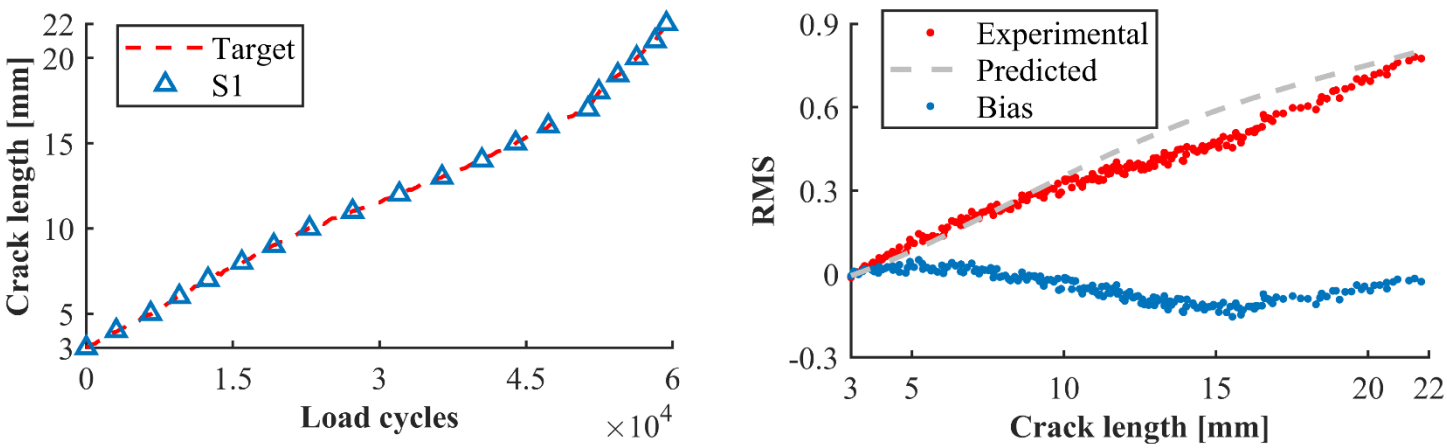

(a) Target crack growth (b) RMS features and bias

Figure 7 Target crack growth, RMS features, and bias.

4. Application results

This section provides a comprehensive comparison between the performances of traditional method resorting to each degradation model, and between those of traditional and new methods. Section 4.1 presents the estimation and prognostic results of specimen S1 from the traditional method resorting to each of the three degradation models, while Section 4.2 illustrates those from the new method by fusing all three models. The robustness of the proposed method among all the other specimens is validated in Section 4.3.

4.1 Traditional method for specimen S1

The traditional method applies one particle filter (PF) to one prognostic model to provide one group of estimates of the crack length and degradation parameters, which are then adopted for projecting the future state and RUL. Then, the estimates of crack length and RUL from the three models (or three PFs) are simply merged at each time step (called 'simple fusion') for comparison. Those results are plotted in Appendix A.1. Provided with satisfactory bias estimation, the samples of crack length from each model or simple fusion have the average values remaining close to the target values and their confidence boundaries (CBs) shrinking with load cycle step, and the samples of those degradation parameters reduce their spread over load cycle steps, indicating a successful convergence.

Figure A.4 shows the predicted future states at 3.6×10^4 load cycles using each model and simple fusion, where, in general, each group of future states is distributed around the true crack lengths. This is also observed in Figure A.5, where the average RUL is close to the target RUL, and the confidence boundaries shrink with the increasing load cycle steps. The above observations are the same as those in [5, 6], where the traditional method resorting to one prognostic model has been applied to the same experimental study.

On the other hand, the estimation and prognostic performances using each model are different, which are then quantified by three metrics, i.e., the root-mean-square error (RMSE) for the crack length estimation, the cumulative relative accuracy (CRA) for the RUL prediction, and the prognostic horizon (PH) for the RUL prediction, respectively. They are described as follows,

$$RMSE = \sqrt{\frac{1}{T}\sum_{k=1}^{T}\left(\bar{x}_k - x_{true,k}\right)^2} \tag{16}$$

$$CRA = \frac{1}{T-1}\sum_{k=1}^{T-1}\left(1 - \frac{\left|\overline{RUL}_k - RUL_{true,k}\right|}{RUL_{true,k}}\right) \tag{17}$$

where $\bar{x}$ and $\overline{RUL}$ denote the mean of posterior estimates of the crack length and that of the RUL, respectively, the subscript '$true$' means the true crack length or RUL, and T is the number of discrete load cycle steps required by the PF until failure is reached.

PH is usually taken as the difference between the load cycle step of the latest measurement and the failure threshold, provided the RUL prediction at that step meets a pre-defined specification [31]. Following the strategy proposed in [29], this study considers the PH as the number of load cycles when 60% of the RUL distribution first falls within a range of 'true RUL $\pm$ 10%N'. Lower RMSE, higher CRA, and larger PH represent better estimation and prognosis performances, respectively.

Table 5 presents the RMSEs, CRAs, and PHs for specimen S1, where, despite the parameters of each degradation model are online estimated for compensating the uncertainties, the three models still yield different performances for the same specimen. The performance of simple fusion does not show a significant improvement, because it is just a simple mixture of the three groups of estimates.

Table 5 Estimation and prognostic performances from traditional method resorting to one degradation model for specimen S1.

	Traditional method using one degradation model			Simple Fusion
Which model	1	2	3	-
RMSE [mm]	1.175	1.640	0.796	0.961
CRA	0.536	0.584	0.807	0.753
PH [Load cycles]	5400	30600	33600	5700

Note: the smallest RMSE, largest PH, or highest CRA means the 'best' performance, and those from the results of the traditional method are highlighted in green.

4.2 New method for specimen S1

The proposed method has each of the three prognostic models processed through one PF at each step, then applies all the estimates for crack length quantification and RUL prediction, and finally modifies the distribution of samples of the two shared components (i.e., crack length and bias) for each PF through either the crossover or mutation operator. Note that the two operators are separately inserted into the proposed method, providing two sets of results of crack length quantification and RUL prediction, and they are defined as 'Fusion 1' and 'Fusion 2', respectively.

Figures 8 and 9 show the crack length and bias estimation and the parameter estimation, respectively. The future state and RUL prediction are given in Figure 10. The general conclusions relating to those

performances are similar to those arising from Appendix A.1, thus not repeated here. On the other hand, the CB width of either crack length or bias from the new method is narrower than that from the traditional method resorting to any of the three models. This is because the proposed method has the samples from each model interacting with those from the other two models, bringing a narrower posterior PDF that can fit with the three models. One may argue that this method has improved the particle diversity and should produce larger CBs. Indeed, larger diversity means that there are fewer same particles for each PF, which is not directly associated with the width of CB.

Table 6 presents the comparison between the performances of the traditional and the new methods, where the new method using either the crossover or mutation operator always performs more accurate crack length quantification and RUL prediction over the simple fusion, which confirms that the fusion scheme for improving the particle diversity can yield better prognostic performance. Although the proposed method does not exhibit a significant improvement compared to the use of the traditional method with the third degradation model (which is the most effective among the three models), this does not reduce the significance of the proposed approach. This is because the prognostic model that delivers the best performance can vary among different specimens, and it is exceedingly challenging to predict beforehand, as detailed Section 4.3.

Table 6 Estimation and prognostic performances by adopting one degradation model (traditional method) and by fusing multiple models (new method) for specimen S1.

	Traditional method using one degradation model			Simple Fusion	Proposed method	
					Fusion 1 (Crossover)	Fusion 2 (Mutation)
Which model	1	2	3	-	-	-
RMSE [mm]	1.175	1.640	0.796	0.961	0.338	0.402
CRA	0.536	0.584	0.807	0.753	0.870	0.884
PH [Load cycles]	5400	30600	33600	5700	27300	27600

Note: (i) the smallest RMSE, largest PH, or highest CRA means the 'best' performance, and those from the results of traditional method are highlighted in green; and (ii) the result from new method is highlighted in blue if it is more accurate than that from simple fusion. Same below.

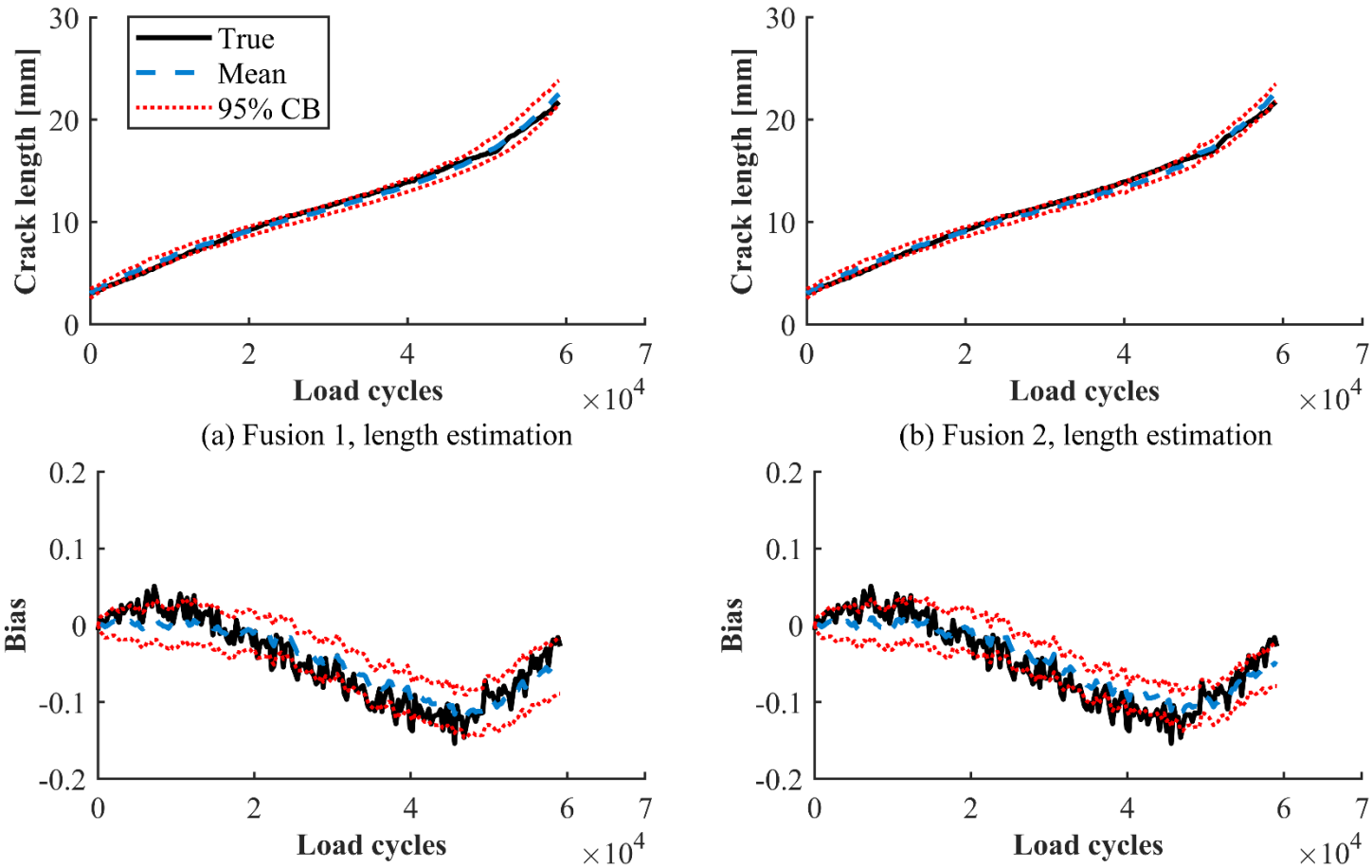

(a) Fusion 1, length estimation

(b) Fusion 2, length estimation

(c) Fusion 1, bias estimation

(d) Fusion 2, bias estimation

Figure 8 Estimation results of crack length and bias using new method for specimen S1.
Note: 'CB' means the confidence boundary. Same below.

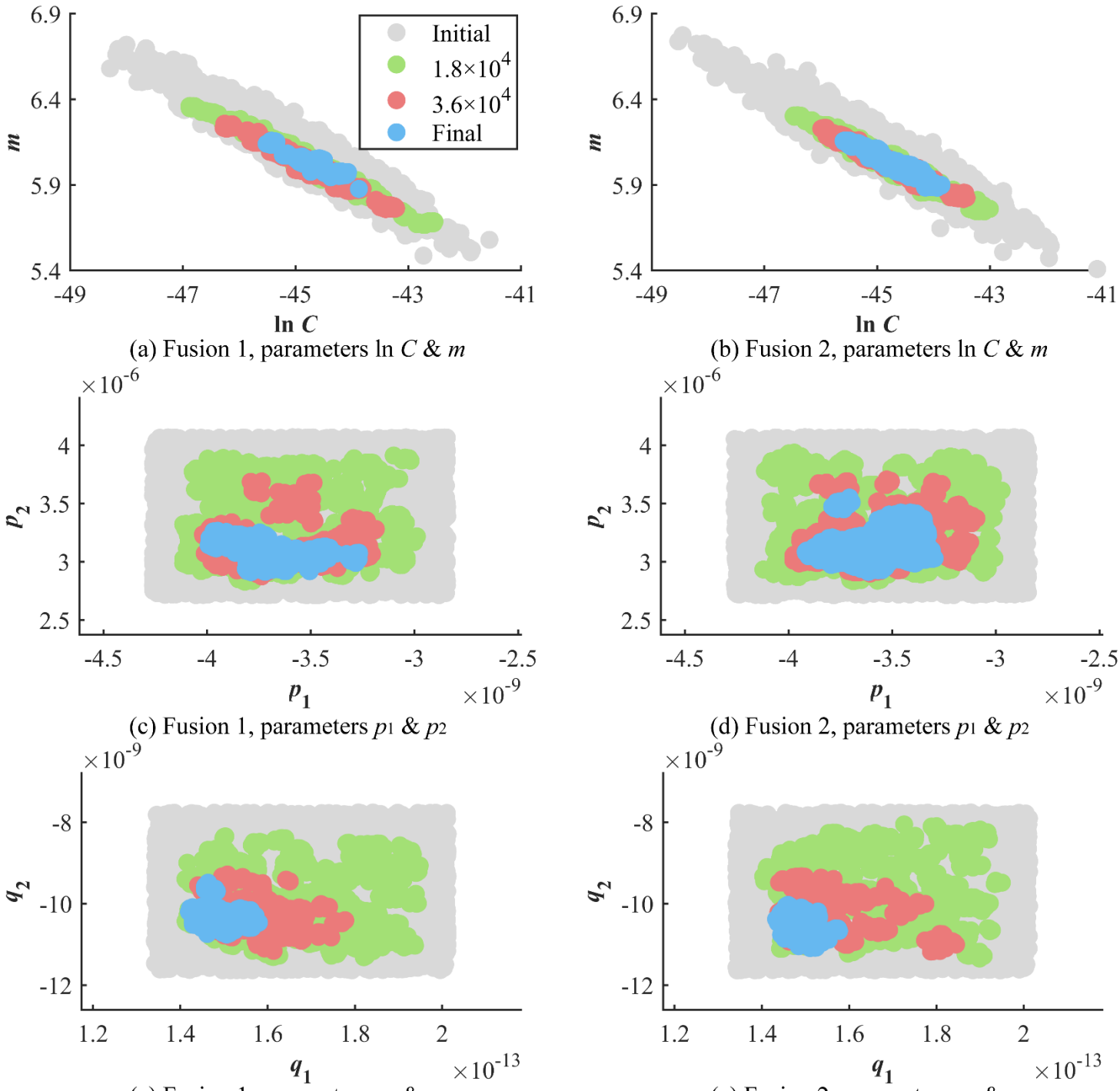

(a) Fusion 1, parameters ln C & m

(b) Fusion 2, parameters ln C & m

(c) Fusion 1, parameters p_1 & p_2

(d) Fusion 2, parameters p_1 & p_2

(e) Fusion 1, parameters q_1 & q_2

(e) Fusion 2, parameters q_1 & q_2

Figure 9 Estimation results of model parameters using new method for specimen S1.
Note that 'Initial', '1.8×10^4', '3.6×10^4', and 'Final' within the legend represent the samples of the three parameters at 0, 1.8×10^4, 3.6×10^4, and last load cycles, respectively.

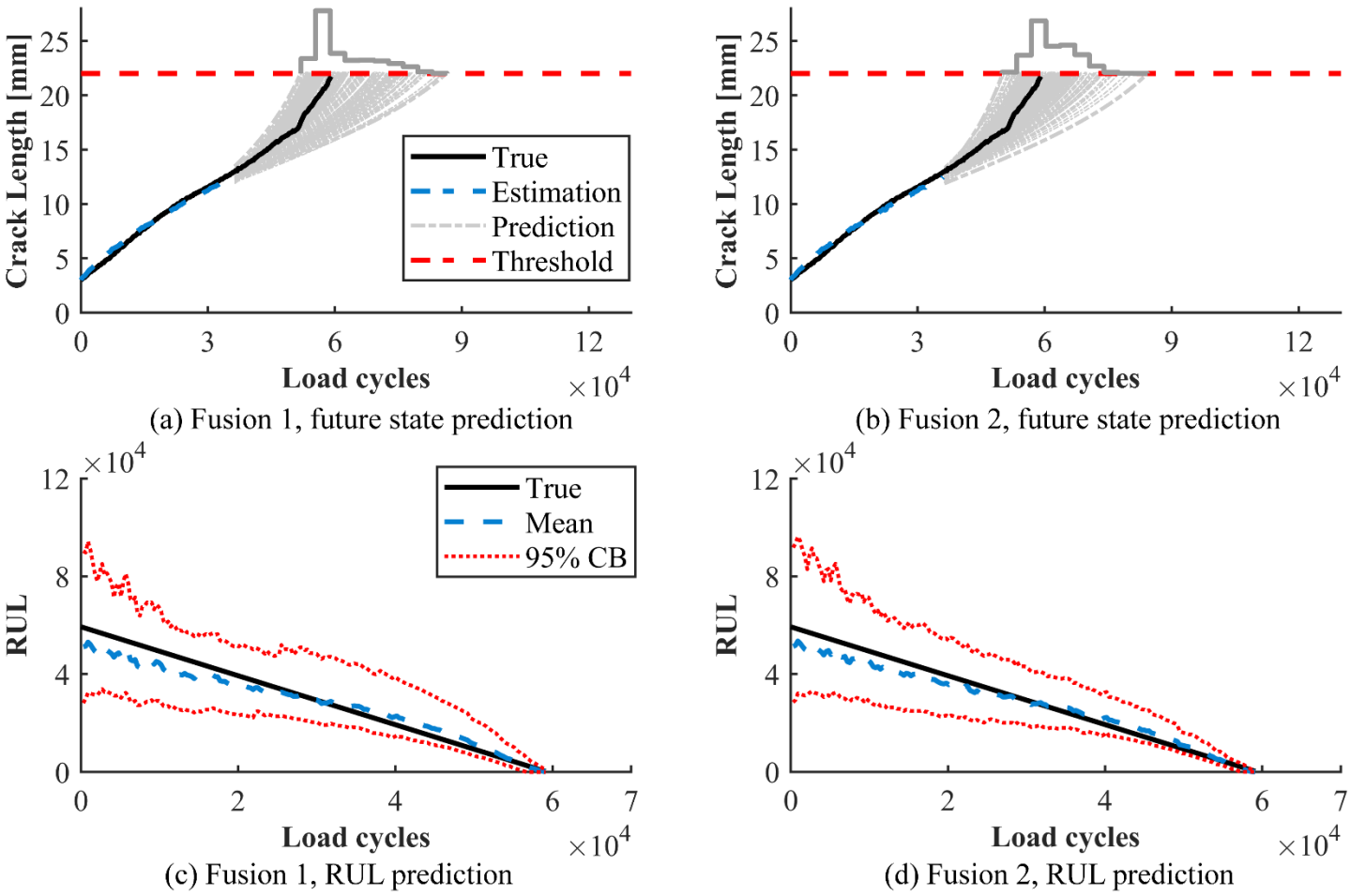

(a) Fusion 1, future state prediction

(b) Fusion 2, future state prediction

(c) Fusion 1, RUL prediction

(d) Fusion 2, RUL prediction

Figure 10 Future state prediction at 3.6×10^4 load cycles and RUL prediction using new method for specimen S1.

4.3 Results from all the other specimens

The robustness of the proposed framework is now tested with the specimens S2 ~ S5. The analyses in Sections 4.1 and 4.2 is repeated with the same PF parameters given in Section 3.5. The crack length estimation and RUL prediction results using the new method are presented in Figures 11 and 12, respectively, which lead to the same conclusions drawn from Figures 8 and 10, and then demonstrate the robustness of the proposed method over different specimens.

Tables 7 ~ 10 show the estimation and prognostic performances from specimens S2 ~ S5, respectively. When resorting to the traditional method, the model providing the best prognostic performance can be different among different specimens, or even, by using different performance metrics. For example, when the traditional method is applied to specimen S4, the results from Model (1) have the smallest RMSE and the largest CRA, while the results from Model (3) have the largest PH.

In general, the proposed method yields better performance than the use of simple fusion, demonstrating the robustness of this method, but it does not always guarantee superior performance over the traditional method resorting to the best model for each specimen. The latter, however, never degrades the

value of this method, as already discussed above.

Table 7 Estimation and prognostic performances by adopting one degradation model (traditional method) and by fusing multiple models (new method) for specimen S2.

	Traditional method using one degradation model			Simple Fusion	Proposed method	
					Fusion 1 (Crossover)	Fusion 2 (Mutation)
Which model	1	2	3	-	-	-
RMSE [mm]	1.250	1.381	2.050	1.109	0.829	1.290
CRA	0.382	0.801	0.588	0.784	0.831	0.814
PH [Load cycles]	4800	43200	6600	6600	20100	14400

Note: (i) the smallest RMSE, largest PH, or highest CRA means the 'best' performance, and those from the results of traditional method are highlighted in green; and (ii) the result from new method is highlighted in blue if it is more accurate than that from simple fusion.

Table 8 Estimation and prognostic performances by adopting one degradation model (traditional method) and by fusing multiple models (new method) for specimen S3.

	Traditional method using one degradation model			Simple Fusion	Proposed method	
					Fusion 1 (Crossover)	Fusion 2 (Mutation)
Which model	1	2	3	-	-	-
RMSE [mm]	1.206	1.694	0.996	0.884	0.716	0.256
CRA	0.423	0.175	0.561	0.429	0.470	0.730
PH [Load cycles]	40500	3600	39000	4200	28200	26400

Note: (i) the smallest RMSE, largest PH, or highest CRA means the 'best' performance, and those from the results of traditional method are highlighted in green; and (ii) the result from new method is highlighted in blue if it is more accurate than that from simple fusion.

Table 9 Estimation and prognostic performances by adopting one degradation model (traditional method) and by fusing multiple models (new method) for specimen S4.

	Traditional method using one degradation model			Simple Fusion	Proposed method	
					Fusion 1 (Crossover)	Fusion 2 (Mutation)
Which model	1	2	3	-	-	-
RMSE [mm]	0.685	1.584	1.072	1.006	0.665	0.670
CRA	0.592	0.582	0.477	0.580	0.688	0.670

PH [Load cycles]	29400	4200	38400	4200	25800	7200

Note: (i) the smallest RMSE, largest PH, or highest CRA means the 'best' performance, and those from the results of traditional method are highlighted in green; and (ii) the result from new method is highlighted in blue if it is more accurate than that from simple fusion.

Table 10 Estimation and prognostic performances by adopting one degradation model (traditional method) and by fusing multiple models (new method) for specimen S5.

	Traditional method using one degradation model			Simple Fusion	Proposed method	
					Fusion 1 (Crossover)	Fusion 2 (Mutation)
Which model	1	2	3	-	-	-
RMSE [mm]	1.059	0.951	1.533	0.962	0.446	0.713
CRA	0.548	0.762	0.659	0.830	0.868	0.834
PH [Load cycles]	4500	36900	28800	24600	28500	29400

Note: (i) the smallest RMSE, largest PH, or highest CRA means the 'best' performance, and those from the results of traditional method are highlighted in green; and (ii) the result from new method is highlighted in blue if it is more accurate than that from simple fusion.

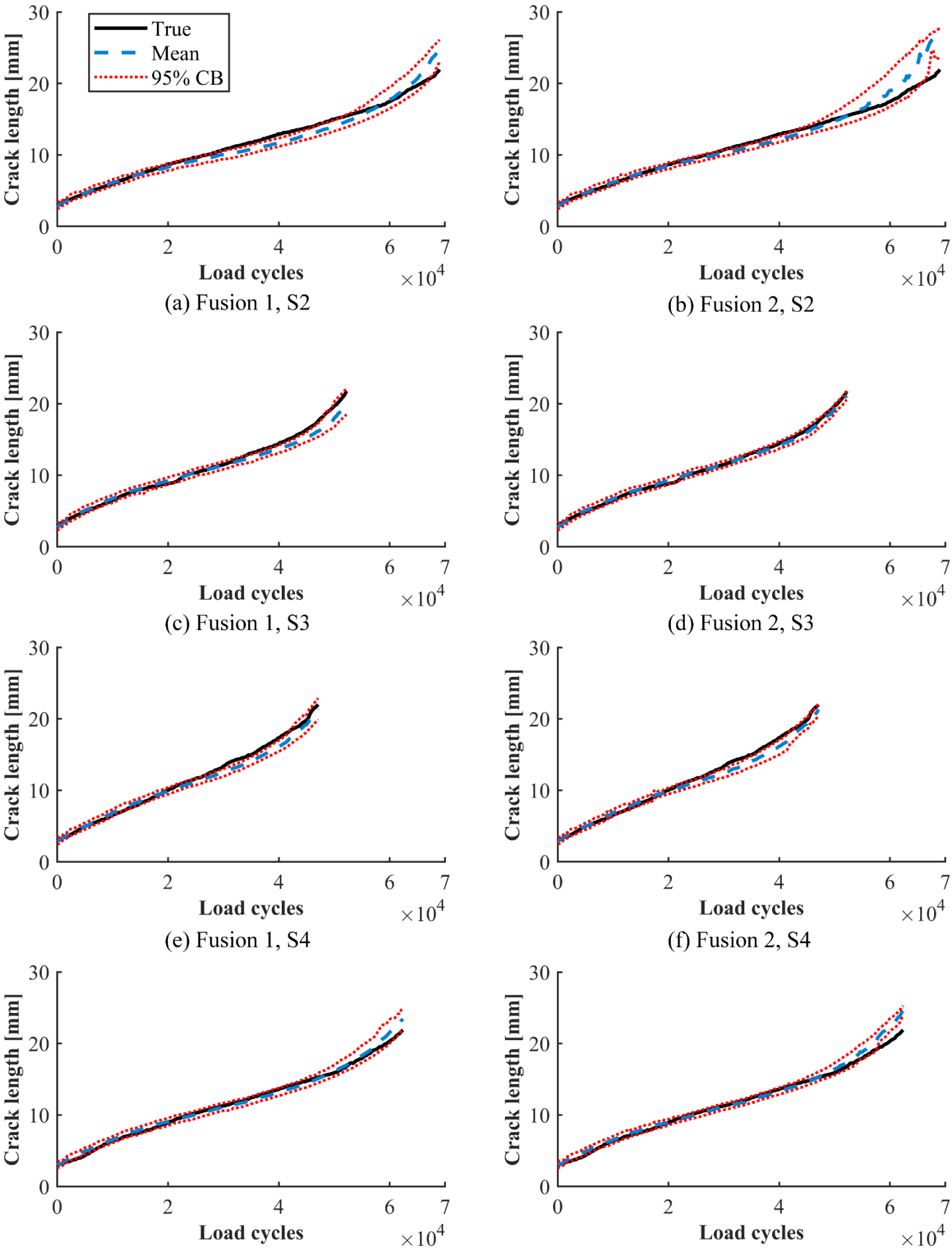

(a) Fusion 1, S2 (b) Fusion 2, S2

(c) Fusion 1, S3 (d) Fusion 2, S3

(e) Fusion 1, S4 (f) Fusion 2, S4

(g) Fusion 1, S5 (h) Fusion 2, S5

Figure 11 Crack length estimations from new method for specimens S2 ~ S5.
Note: 'CB' means the confidence boundary.

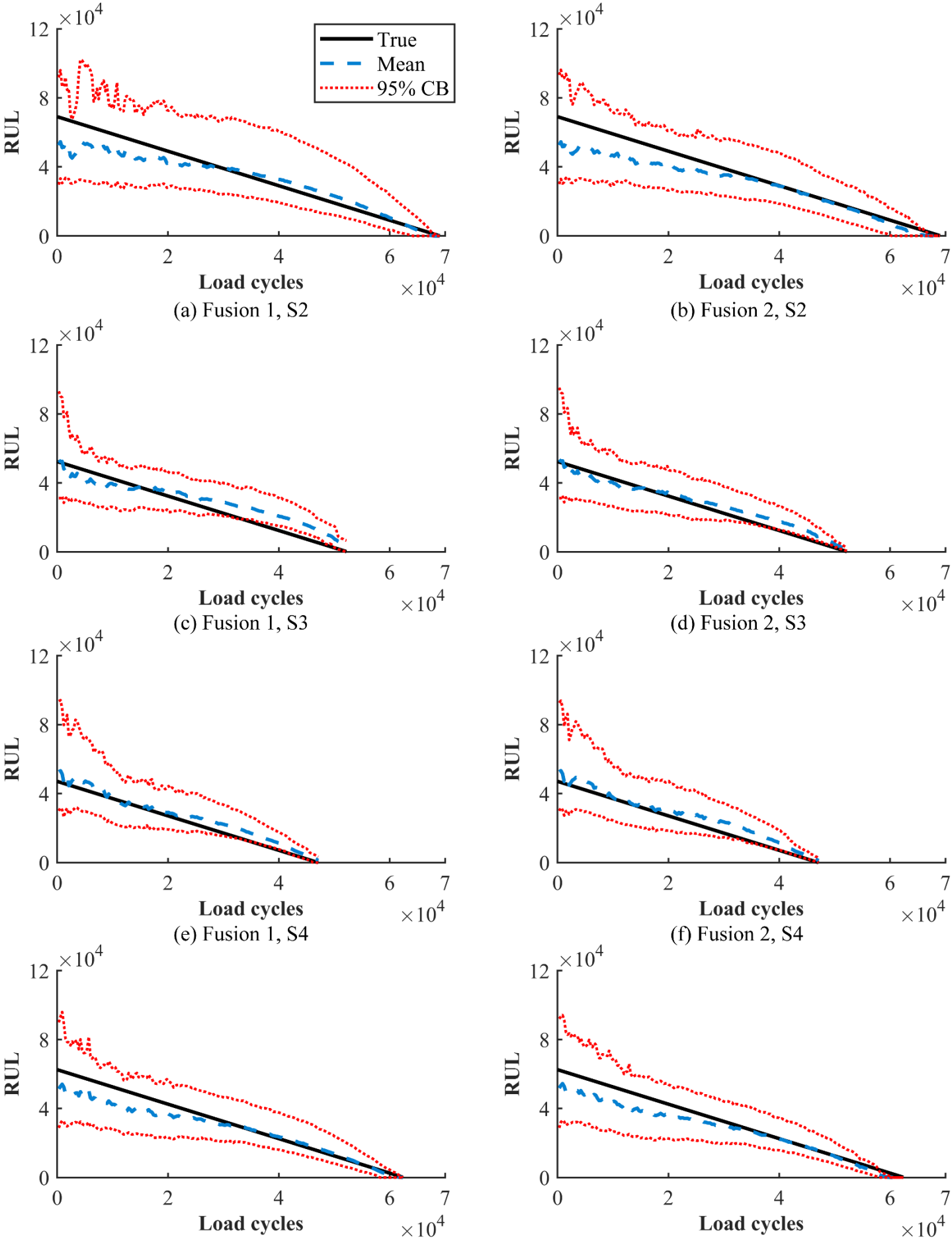

Figure 12 RUL predictions from new method for specimens S2 ~ S5.
Note: 'CB' means the confidence boundary.

5. Conclusions

Damage prognosis methods typically require a properly selected degradation model describing the damage growth with time or load cycle step. In order to provide more robust prognostic performance, this work has proposed a particle filter (PF)-based damage prognosis framework by fusing multiple degradation models.

The results of the traditional and new methods can lead to the following conclusions. When using the traditional method of relying on one degradation model, it is important to note that the best degradation model can differ among the five specimens and also vary depending on the performance metrics used. Simply combining the estimates from multiple models does not enhance the accuracies of crack length quantification and RUL prediction. In all of the five specimens evaluated, the new method, leveraging either the crossover or mutation operator, consistently outperforms the simple mixture mentioned above, attesting to its robustness.

Based on the results presented in this paper, it can be concluded that the proposed method offers a promising alternative to the traditional approach. While the proposed method may not always result in superior performance compared to the best model-based traditional approach, it addresses the uncertainty involved in determining the most effective model in advance. Furthermore, the proposed method provides a more comprehensive evaluation of the degradation behavior by considering multiple models, which can enhance the accuracy of damage quantification and RUL prediction.

In a more practical application scenario where tens of or hundreds of available degradation models are available, some of those models may consistently provide inaccurate crack length quantification and RUL prediction results, thereby compromising the performance of the proposed method if such models are included. Consequently, it is necessary to develop an offline or online scheme to select a list of ‘good’ degradation models or ‘good’ PF estimates. Moreover, the proposed method requires all the prognostic models share specific same state components like crack length, which may not always be possible, especially considering that some data-driven models only include some sort of data-driven health indicator. Necessary extension has been made towards the case of no shared state component. Finally, it should be noted that the proposed approach requires the use of multiple PFs, which can increase computational effort. However, this issue can be addressed by developing computationally efficient particle filters, which will enable the use of more models without significantly increasing computation time and enhance the practical applicability of the proposed method.

Appendix A.1

The estimation and prognostic results of the traditional method using each of the three damage degradation models for specimen S1 are shown in Figures A.1 ~ A.5, which are the crack length estimation, the crack growth parameter estimation (ln C and m), the bias estimation, the future state prediction, and the RUL prediction, respectively.

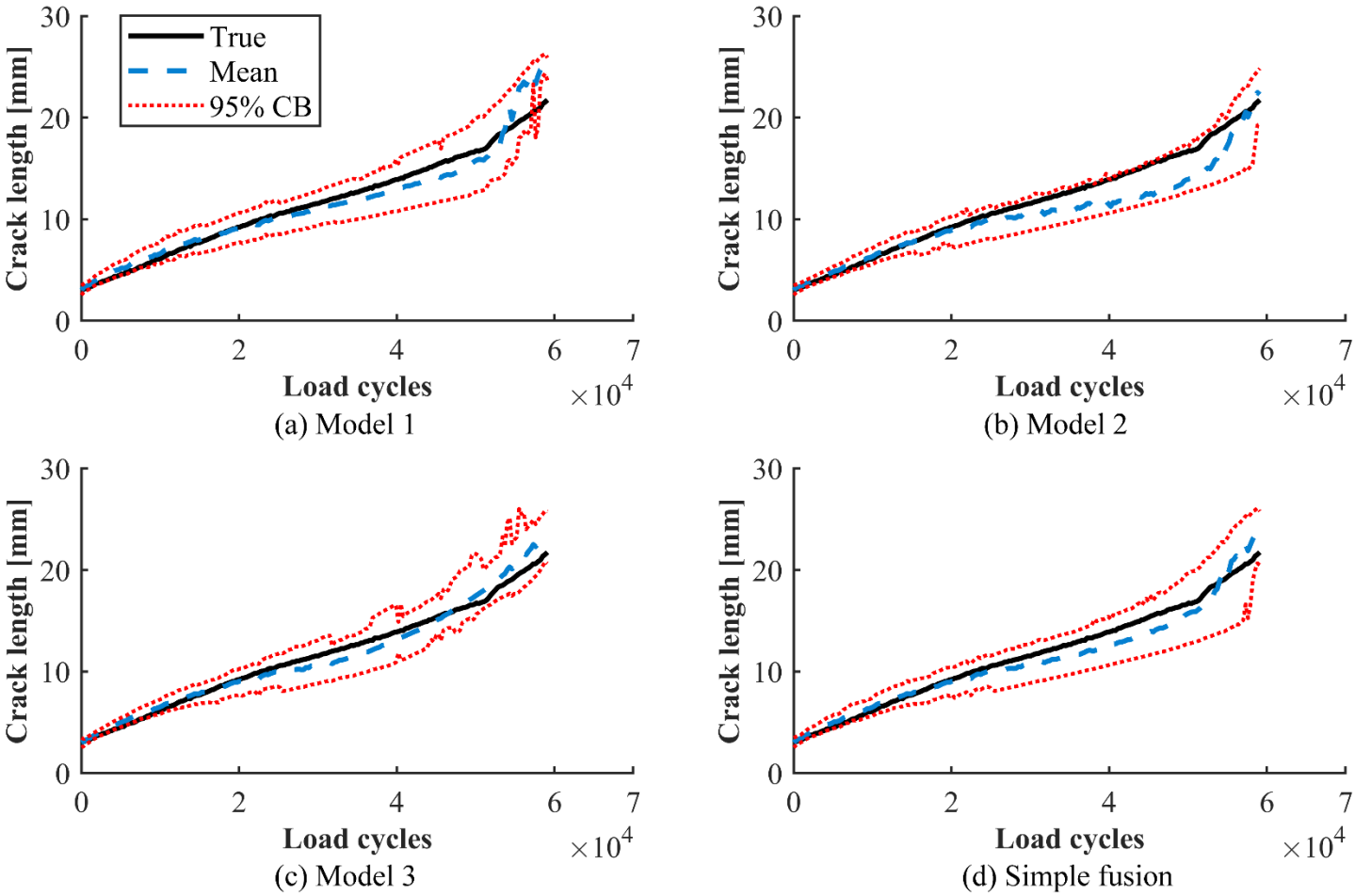

Figure A.1 Crack length estimation using traditional method resorting to one degradation model for specimen S1. Note: 'CB' means the confidence boundary. Same below.

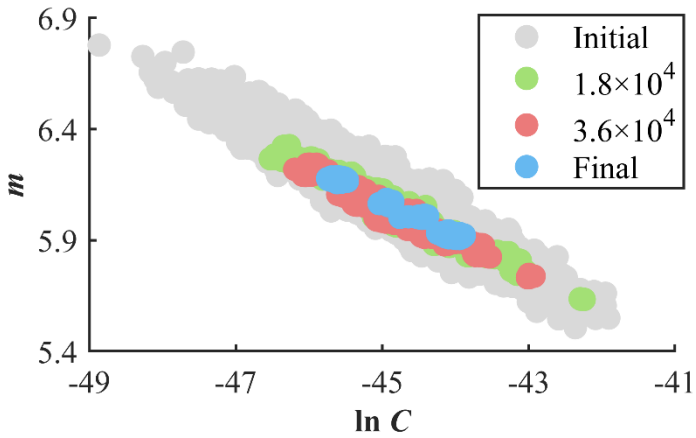

(a) Model 1, parameters ln C & m

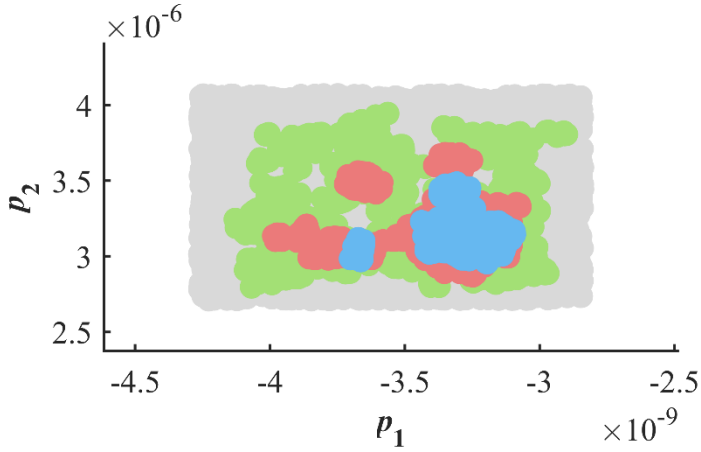

(b) Model 2, parameters p_1 & p_2

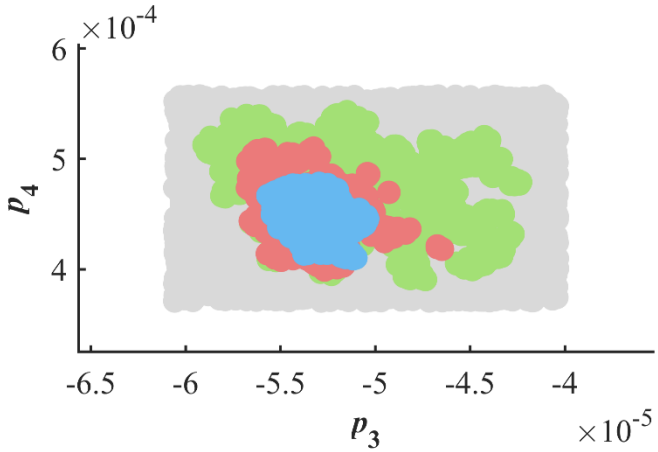

(c) Model 2, parameters p_3 & p_4

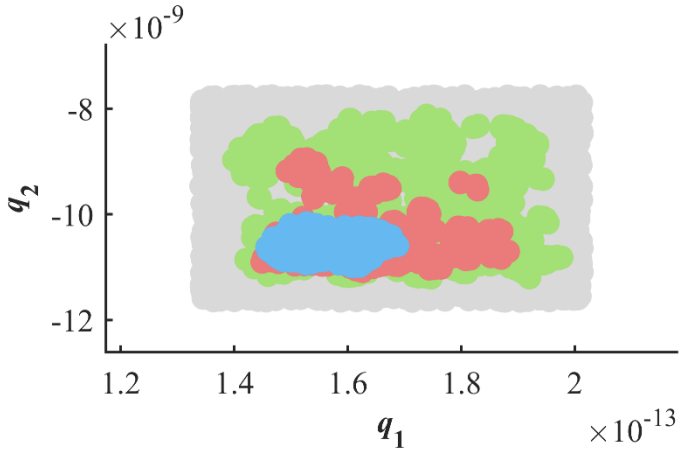

(d) Model 3, parameters q_1 & q_2

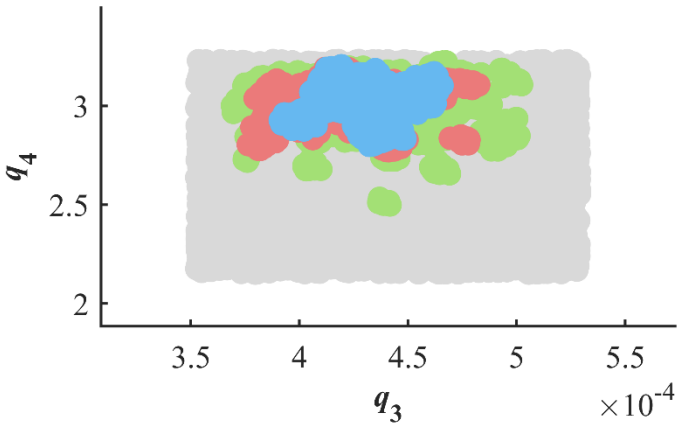

(e) Model 3, parameters q_3 & q_4

Figure A.2 Parameter estimation using traditional method resorting to one degradation model for specimen S1. Note that 'Initial', '1.8×10^4', '3.6×10^4', and 'Final' within the legend represent the samples of the three parameters at 0, 1.8×10^4, 3.6×10^4, and last load cycles, respectively.

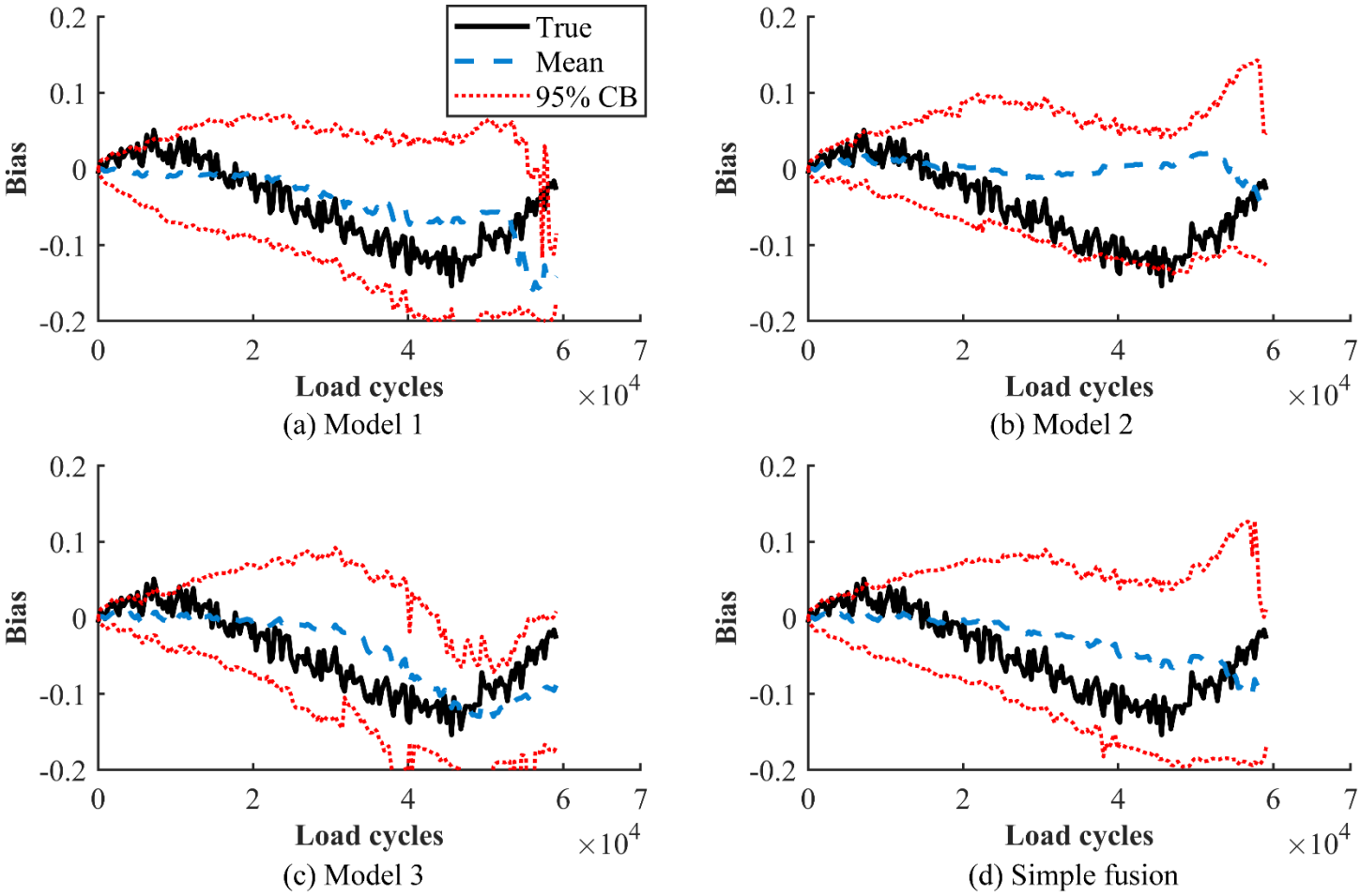

Figure A.3 Bias estimation using traditional method resorting to one degradation model for specimen S1.

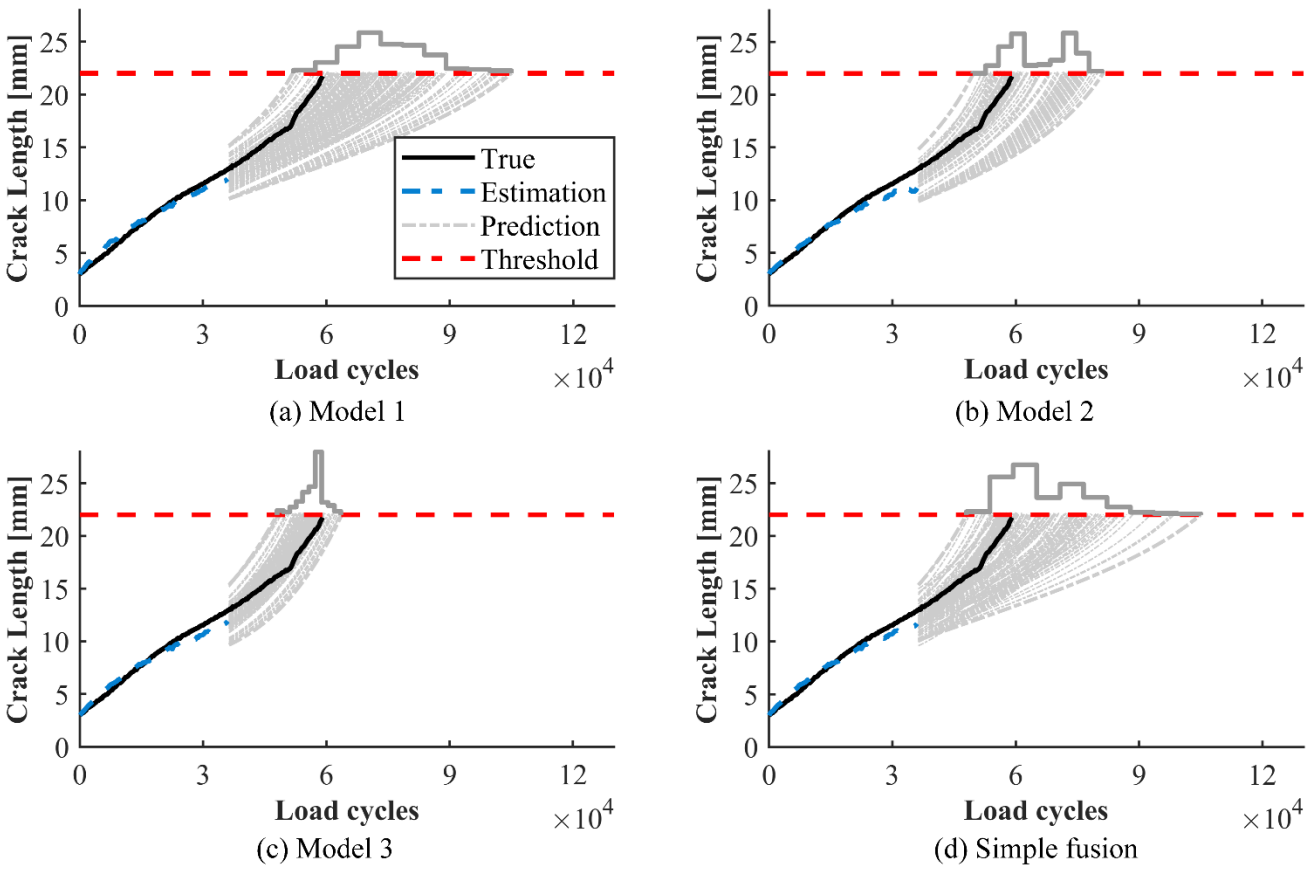

Figure A.4 Future state prediction at 3.6×10^4 load cycles using traditional method resorting to one degradation model for specimen S1.

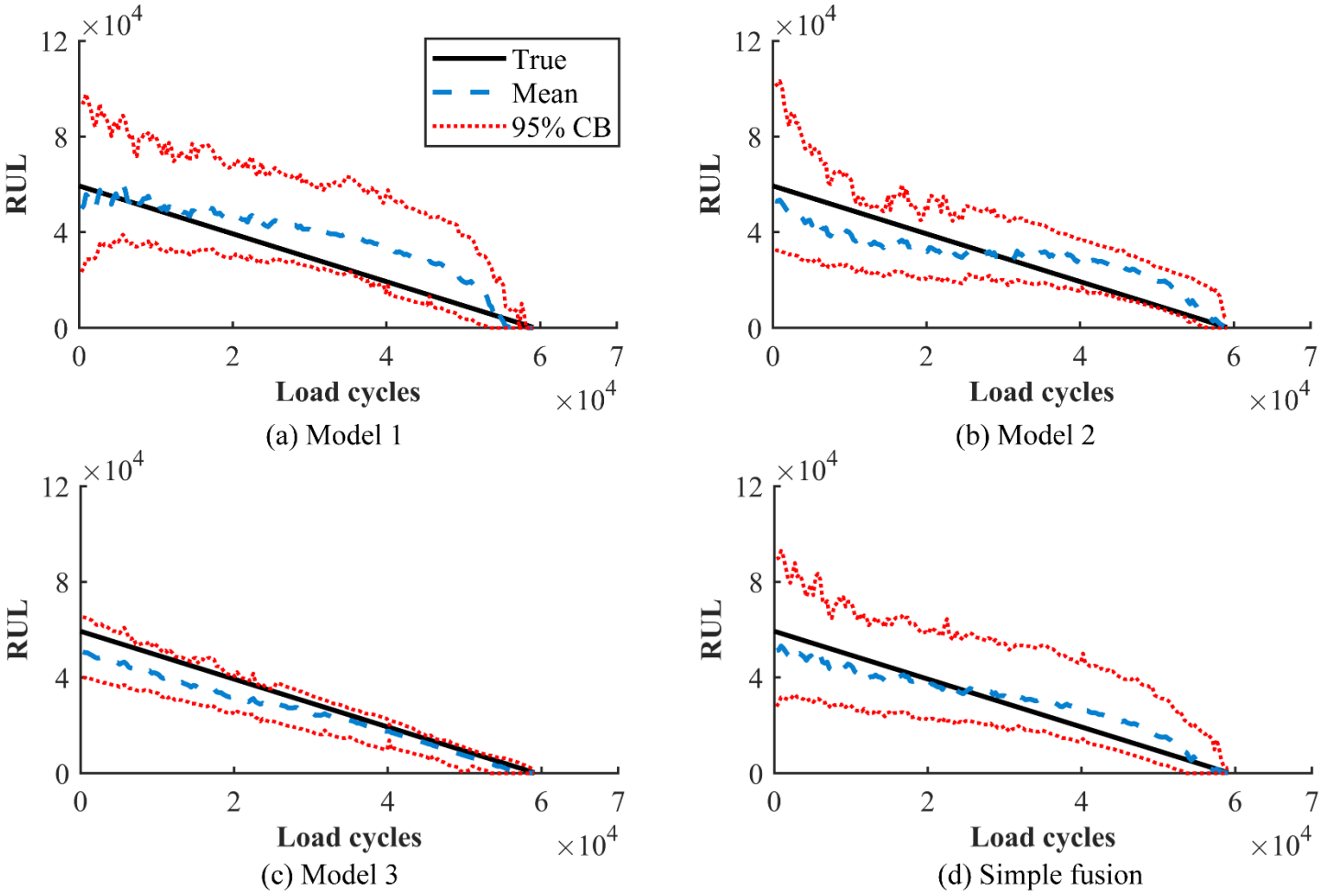

Figure A.5 RUL prediction using traditional method resorting to one degradation model for specimen S1.

Acknowledgments

This project has received funding from the European Union's Horizon 2020 research and innovation programme under the Marie Skłodowska-Curie grant agreement No. 859957.

References

[1] M. Chiachío, J. Chiachío, S. Sankararaman, K. Goebel, J. Andrews, A new algorithm for prognostics using Subset Simulation, Reliability Engineering & System Safety, 168 (2017) 189-199.

[2] T. Li, F. Cadini, M. Chiachío, J. Chiachío, C. Sbarufatti, Particle filter-based delamination shape prediction in composites subjected to fatigue loading, Structural Health Monitoring, (2022) 14759217221116041.

[3] C. Tao, C. Zhang, H. Ji, J. Qiu, Application of neural network to model stiffness degradation for composite laminates under cyclic loadings, Composites Science and Technology, 203 (2021) 108573.

[4] N. Yue, A. Broer, W. Briand, M. Rébillat, T. Loutas, D. Zarouchas, Assessing stiffness degradation of stiffened composite panels in post-buckling compression-compression fatigue using guided waves, Composite Structures, 293 (2022) 115751.

[5] T. Li, L. Lomazzi, F. Cadini, C. Sbarufatti, J. Chen, S. Yuan, Numerical simulation-aided particle filter-based damage prognosis using Lamb waves, Mechanical Systems and Signal Processing, 178 (2022) 109326.

[6] T. Li, C. Sbarufatti, F. Cadini, J. Chen, S. Yuan, Particle filter-based hybrid damage prognosis considering

measurement bias, Structural Control and Health Monitoring, n/a (2021) e2914.
[7] F. Cadini, C. Sbarufatti, M. Corbetta, F. Cancelliere, M. Giglio, Particle filtering-based adaptive training of neural networks for real-time structural damage diagnosis and prognosis, Structural Control and Health Monitoring, 26 (2019).
[8] F. Cadini, C. Sbarufatti, M. Corbetta, M. Giglio, A particle filter-based model selection algorithm for fatigue damage identification on aeronautical structures, Structural Control & Health Monitoring, (2017) e2002.
[9] X. Zhou, S. He, L. Dong, S.N. Atluri, Real-Time Prediction of Probabilistic Crack Growth with a Helicopter Component Digital Twin, AIAA Journal, 60 (2022) 2555-2567.
[10] M. Moradi, A. Broer, J. Chiachío, R. Benedictus, T.H. Loutas, D. Zarouchas, Intelligent health indicator construction for prognostics of composite structures utilizing a semi-supervised deep neural network and SHM data, Engineering Applications of Artificial Intelligence, 117 (2023) 105502.
[11] N. Eleftheroglou, D. Zarouchas, R. Benedictus, An adaptive probabilistic data-driven methodology for prognosis of the fatigue life of composite structures, Composite Structures, 245 (2020) 112386.
[12] X. Liu, Y. Lei, N. Li, X. Si, X. Li, RUL prediction of machinery using convolutional-vector fusion network through multi-feature dynamic weighting, Mechanical Systems and Signal Processing, 185 (2023) 109788.
[13] G. Galanopoulos, N. Eleftheroglou, D. Milanoski, A. Broer, D. Zarouchas, T. Loutas, A novel strain-based health indicator for the remaining useful life estimation of degrading composite structures, Composite Structures, 306 (2023) 116579.
[14] F. Zhao, X. Zhou, C. Wang, L. Dong, S.N. Atluri, Setting Adaptive Inspection Intervals in Helicopter Components, Based on a Digital Twin, AIAA Journal, (2023) 1-14.
[15] Y. Lei, N. Li, L. Guo, N. Li, T. Yan, J. Lin, Machinery health prognostics: A systematic review from data acquisition to RUL prediction, Mechanical Systems and Signal Processing, 104 (2018) 799-834.
[16] P. Baraldi, F. Mangili, E. Zio, Investigation of uncertainty treatment capability of model-based and data-driven prognostic methods using simulated data, Reliability Engineering & System Safety, 112 (2013) 94-108.
[17] I. Lopez, N. Sarigul-Klijn, A review of uncertainty in flight vehicle structural damage monitoring, diagnosis and control: Challenges and opportunities, Progress in Aerospace Sciences, 46 (2010) 247-273.
[18] X. Guan, R. Jha, Y. Liu, Model selection, updating, and averaging for probabilistic fatigue damage prognosis, Structural Safety, 33 (2011) 242-249.
[19] A. Guha, A. Patra, State of Health Estimation of Lithium-Ion Batteries Using Capacity Fade and Internal Resistance Growth Models, IEEE Transactions on Transportation Electrification, 4 (2018) 135-146.
[20] X. Su, S. Wang, M. Pecht, L. Zhao, Z. Ye, Interacting multiple model particle filter for prognostics of lithium-ion batteries, Microelectronics Reliability, 70 (2017) 59-69.
[21] M.S. Arulampalam, S. Maskell, N. Gordon, T. Clapp, A tutorial on particle filters for online nonlinear/non-Gaussian Bayesian tracking, IEEE Transactions on Signal Processing, 50 (2002) 174-188.
[22] S. Yin, X. Zhu, Intelligent Particle Filter and Its Application to Fault Detection of Nonlinear System, IEEE Transactions on Industrial Electronics, 62 (2015) 3852-3861.
[23] S. Yin, X. Zhu, J. Qiu, H. Gao, State Estimation in Nonlinear System Using Sequential Evolutionary Filter, IEEE Transactions on Industrial Electronics, 63 (2016) 3786-3794.
[24] X. Wang, T. Li, S. Sun, J.M. Corchado, A Survey of Recent Advances in Particle Filters and Remaining Challenges for Multitarget Tracking, Sensors, 2017.
[25] T. Li, S. Sun, T.P. Sattar, J.M. Corchado, Fight sample degeneracy and impoverishment in particle filters: A review of intelligent approaches, Expert Systems with Applications, (2014).
[26] J. Chen, S. Yuan, H. Wang, On-line updating Gaussian process measurement model for crack prognosis using the particle filter, Mechanical Systems and Signal Processing, 140 (2020) 106646.
[27] L. Qiu, S. Yuan, X. Shi, T. Huang, Design of piezoelectric transducer layer with electromagnetic

shielding and high connection reliability, Smart Materials and Structures, 21 (2012) 075032.
[28] S. Buchaiah, P. Shakya, Bearing fault diagnosis and prognosis using data fusion based feature extraction and feature selection, Measurement, 188 (2022) 110506.
[29] M. Corbetta, C. Sbarufatti, M. Giglio, M.D. Todd, Optimization of nonlinear, non-Gaussian Bayesian filtering for diagnosis and prognosis of monotonic degradation processes, Mechanical Systems and Signal Processing, 104 (2018) 305-322.
[30] J. Liu, M. West, Combined parameter and state estimation in simulation-based filtering, Sequential Monte Carlo methods in practice, Springer, 2001, pp. 197-223.
[31] A. Saxena, J. Celaya, E. Balaban, K. Goebel, B. Saha, S. Saha, M. Schwabacher, Metrics for evaluating performance of prognostic techniques, 2008 International Conference on Prognostics and Health Management, 2008, pp. 1-17.

CHAPTER 4

DAMAGE QUANTIFICATION

Chapter 4 illustrates the use of indirect *damage quantification* in prognostic investigations. The latter can lead to the three fundamental questions, namely uncertainties, insufficient experimental damage data, and feature fusion and selection, which correspond to three contributions in this chapter.

First, a bias-based prognostic model is proposed to account for those uncertainties. Additionally, some numerically simulated Lamb waves are used to build the damage quantification model. Finally, a method for online fusing multiple features and selecting the best one for prognosis is proposed. All three contributions are tested by the same aluminum fatigue test with Lamb wave monitoring.

Check for updates

Received: 22 July 2021 | Revised: 18 October 2021 | Accepted: 28 November 2021

DOI: 10.1002/stc.2914

RESEARCH ARTICLE

WILEY

Particle filter-based hybrid damage prognosis considering measurement bias

Tianzhi Li[1] | **Claudio Sbarufatti**[1] | **Francesco Cadini**[1] | **Jian Chen**[2] | **Shenfang Yuan**[2]

[1]Department of Mechanical Engineering, Politecnico di Milano, Milano, via La Masa 1, 20156, Italy

[2]Research Center of Structural Health Monitoring and Prognosis, State Key Laboratory of Mechanics and Control of Mechanical Structures, Nanjing University of Aeronautics and Astronautics, Nanjing, China

Correspondence
Claudio Sbarufatti, Department of Mechanics, Polytechnic University of Milan, Milan, Italy.
Email: claudio.sbarufatti@polimi.it

Funding information
H2020 Marie Skłodowska-Curie Actions, Grant/Award Number: 859957; Horizon 2020

Summary

Hybrid methods combining physical knowledge and data-driven techniques have shown great potential for damage prognosis in structural health monitoring (SHM). Current practices consider the physics-based process and data-driven measurement equations to describe the damage evolution and the mapping between the damage state and the measurement, respectively. However, the bias between the measurements predicted by the data-driven equation and the sensor-based measurements obtained from any SHM system, arising from uncertainties like damage geometries and sensor placement or noise, can lead to inaccurate prognosis results. To improve the prognosis performance in case of bias, this paper adopts a methodology typically applied in sensor fault diagnosis and develops a new hybrid prognostic model with a bias parameter included in the measurement equation and the state vector. Particle filter (PF) serves as the estimation technique to identify the state and parameters relating to the damage as well as the bias parameter, and the remaining useful life (RUL) can be predicted by the physics-based process equation, with PF posterior estimates of the related parameters and state variables as an input. The experimental study of an aluminum lug structure subject to fatigue crack growth and equipped with a Lamb wave monitoring system demonstrates the improved estimation and prediction performances of the new prognostic model.

KEYWORDS

fault prognosis, hybrid model, Lamb wave, measurement bias, measurement equation, particle filter

1 | INTRODUCTION

Structural degradation is a phenomenon affecting the majority of engineering structures, which may lead to the occurrence of structural damage and eventually structural failure if not properly addressed. Regular inspection and maintenance should be carried out during the service life of a structure to ensure the structural safety, however often

This is an open access article under the terms of the Creative Commons Attribution-NonCommercial-NoDerivs License, which permits use and distribution in any medium, provided the original work is properly cited, the use is non-commercial and no modifications or adaptations are made.
© 2021 The Authors. Structural Control and Health Monitoring published by John Wiley & Sons Ltd.

incurring in high operative costs. In a predictive maintenance scenario, to simultaneously guarantee the safety at a reduced cost, inspection can be scheduled sufficiently before the structural damage reaches a critical level that may hamper the structural performance, which requires advanced prognostic techniques to predict the remaining useful life (RUL).

In the last decades, a great variety of damage prognosis techniques have been developed, depending on the availability of physics knowledge and data. From the perspective of how the prognostic models are formulated, they can be classified into physics-based,[1–3] data-driven,[4–6] and hybrid methods.[7–11] Physics-based methods utilize specific mechanistic knowledge and theories to formulate pure physics-based models, which describe the structural degradation phenomena and the links between the damage states and the SHM measurements. Data-driven methods, resorting to data-driven modeling techniques such as neural networks[4,6] and Markov chains,[5] attempt to use a large amount of data to build the relationship between the internal degradation behavior and the external observations. Hybrid methods, taken as a combination of the two above, usually consider the physics-based process and data-driven measurement equations to describe the damage evolution and the mapping between the damage state and the measurement, respectively.

The proper method (or model) is case-specific, as each type of method has its pros and cons.[12–14] A common belief is that, given the uncertainties arising from complex structural degradations, the environmental effects, and the sensor health conditions,[15,16] either the physics-based or the data-driven methods with sole deterministic models cannot provide an accurate prognostic result. A well-acknowledged strategy for both the physics-based[1–3] and data-driven methods[4–6] to improve their prognostic performance is to set the model parameters as unknown variables to be updated by a state estimation technique, such as the particle filter (PF) given its versatility for nonlinear and non-Gaussian problems. However, this strategy is not fully exploited in hybrid methods,[8,9,17] where the physics-based process equation is updated by setting its parameters as unknown variables to be estimated by PF, while the data-driven measurement equation is typically fixed.

Focusing on the latter, the relationship between the damage state and the measurement should probably vary in different specimens of the same structure[7] due to the uncertainties mentioned above. In practice, if the measurement equation describing the above relationship is built using both a data-driven modeling technique and the data from some specimens, then the bias between the measurements from a test specimen and those predicted by the measurement equation is unavoidable. In this context, the measurement equation that fails to be online updated or to take the bias into account will lead to inaccurate damage estimation[18] and prognosis[7] in case of large-level bias. Such a problem is investigated only in a few hybrid damage prognosis studies,[7,11,19] where either (i) the true damage state obtained by an additional measurement system is adopted to update the measurement equation at prescribed time instants[7,11] or (ii) all the parameters of both the process and measurement equations are set as unknown components to be estimated online,[19] strongly enhancing the algorithm adaptability to system deviations. However, on one hand, it is rarely possible to provide additional system observations of the true damage state, and on the other hand, it is always desired to limit to a minimum the parameters to be updated online for a robust algorithm convergence and to guarantee the state space full observability.

We anticipated that the bias between the sensor-based and the predicted measurements can be regarded as a typical sensor fault, which can be detected, localized, and identified by adding a bias parameter in both the measurement and process equations for estimation.[20,21] Moreover, leveraging on the little effect this bias can have on the estimation of other state components when accurately estimated by a state estimation technique, it has also been used for physics-based damage prognosis in An et al.,[22] where the bias is an error caused by the measurement system and is considered as a fixed parameter, but never in the hybrid damage prognosis framework so far, where the bias originating from multiple uncertainties can hardly be avoided and it is generally time varying.

This paper develops a new hybrid prognosis model that combines the approaches from sensor fault diagnosis and hybrid prognosis. The hybrid prognostic framework is based on a PF and it consists of three main steps. First, the measurement equation is built by a data-driven technique (i.e., polynomial fitting regression) with a bias parameter included to consider time variable discrepancies in consecutive tests, while the process equation considers the physical law describing damage evolution, and its state vector is augmented to include the damage state, the degradation law parameters, and the measurement bias. Then, the PF is used to estimate the damage state and model parameters. Finally, the future states and the RUL are estimated resorting to the process equation and the estimated damage state and parameters. The proposed prognostic framework is validated by an experimental activity, consisting of a fatigue crack growth in an aluminum structure, equipped with a Lamb wave measurement system.

The rest of this paper is organized as follows: Section 2 introduces the traditional and new models as well as the prognostic framework. The experimental validation is discussed in Section 3. Finally, Section 4 concludes this paper with a view toward future activities.

2 | DAMAGE PROGNOSIS FRAMEWORK

PF-based damage prognosis generally includes three main steps, namely, (i) formulating the prognostic model in a state space, (ii) estimating the unknown state variables using PF, and (iii) calculating the future state and RUL by taking the posterior PF estimates and the process equation into account. The hybrid damage prognosis framework taking the unknown bias into consideration is schematized in Figure 1, while details will be provided in the following paragraphs, where the differences with respect to the traditional version[8,9] are highlighted. Note: the variables b, $\boldsymbol{\theta}$, x, y, and the function $g(\cdot)$ will be introduced in Section 2.1.

2.1 | New prognostic model

Assume a discrete form of damage evolution model can be described as

$$x_k = f(x_{k-1}, \boldsymbol{\theta}), \tag{1}$$

where x is the damage state, $\boldsymbol{\theta}$ is a vector including the parameters governing the damage evolution, the subscript k is the discrete time step, and the function $f(\cdot)$ is usually a physical or semi-empirical law. The parameters $\boldsymbol{\theta}$ can vary in different specimens of the same structure due to the uncertainties in the damage evolution process; a deterministic evolution model may hardly provide accurate prognosis results. To overcome this problem, according to the common practices in PF-based prognosis, the parameters in $\boldsymbol{\theta}$ should also be taken as unknown variables to be online updated within the process equation:[8,17]

$$\boldsymbol{z}_k = \begin{bmatrix} \boldsymbol{\theta}_k \\ x_k \end{bmatrix} = \begin{bmatrix} \boldsymbol{\theta}_{k-1} + \boldsymbol{\omega}_{\theta,k} \\ f(x_{k-1}, \boldsymbol{\theta}_k, \omega_k) \end{bmatrix}, \tag{2}$$

where $\boldsymbol{z}$ is the state vector with both the damage state x and the model parameters $\boldsymbol{\theta}$ included, ω and $\boldsymbol{\omega}_\theta$ are the process noises for the damage state and the parameters, respectively.

Given the difficulties in directly measuring the damage state, many PF-based damage prognosis investigations[8,17] have the unknown damage state inferred from indirect observations y, related each other through a measurement equation $g(\cdot)$. The traditional state space model in hybrid damage prognosis can be formulated as follows.[8,17]

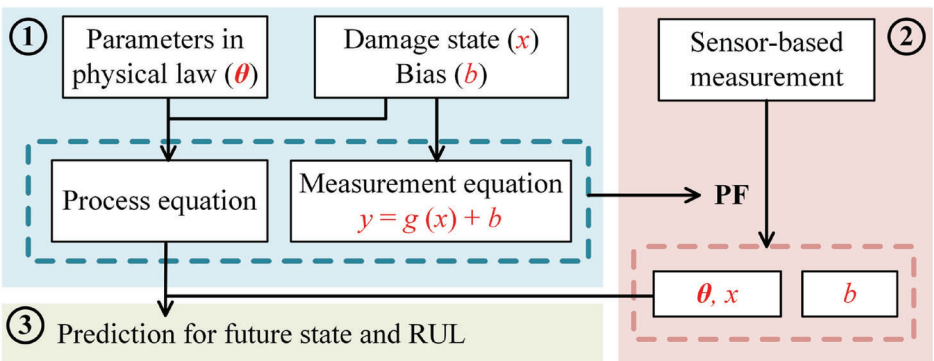

FIGURE 1 Hybrid damage prognosis framework

$$\begin{cases} \boldsymbol{z}_k = \begin{bmatrix} \boldsymbol{\theta}_k \\ x_k \end{bmatrix} = \begin{bmatrix} \boldsymbol{\theta}_{k-1} + \boldsymbol{\omega}_{\theta,k} \\ f(x_{k-1}, \boldsymbol{\theta}_k, \omega_k) \end{bmatrix}, \\ y_k = g(x_k) + \nu_k \end{cases} \tag{3}$$

where the data-driven function $g(\cdot)$ describes the relationship between the damage state x and the measurement y (i.e., a feature extracted from Lamb wave signals in this study), respectively, and ν is the measurement noise, which is assumed zero-mean Gaussian hereafter.

One main step of the PF routine, and in general of methods for Bayesian inference leveraging on Monte-Carlo sampling, is the drawing of the posterior distribution of the unknown variables, which, in turn, is based on the prior knowledge and the assignment of a score based on the likelihood with respect to the sensor observations. While the selection of the latter is arbitrary (a Gaussian likelihood function is used in this study without any loss of generality), it always entails a comparison between the measurements predicted through the function $g(\cdot)$ and the sensor measurements at discrete time k. However, it rarely happens that the function $g(\cdot)$, calibrated on a set of reference specimens, will properly fit the sensor observations from a different set of specimens, due to the inevitable uncertainties, such as different specimen and damage geometries, sensor errors, etc. Sufficiently large bias between the sensor-based and the predicted measurements will induce inaccurate estimation[18] and prognosis.[7]

This measurement bias can be considered as a typical sensor fault, which can be estimated including a bias parameter in the measurement equation $g(\cdot)$.[20,21] It will have limited effect on the estimation for the other state components when being accurately identified.[22] Therefore, by combing the methods from sensor fault diagnosis and hybrid damage prognosis,[8,17] a new hybrid prognosis model with the bias parameter b included is proposed to improve damage state and parameter estimation in presence of a measurement bias:

$$\begin{cases} \boldsymbol{z}_k = \begin{bmatrix} \boldsymbol{\theta}_k \\ x_k \\ b_k \end{bmatrix} = \begin{bmatrix} \boldsymbol{\theta}_{k-1} + \boldsymbol{\omega}_{\theta,k} \\ f(x_{k-1}, \boldsymbol{\theta}_k, \omega_k) \\ b_{k-1} + \omega_{b,k} \end{bmatrix}, \\ y_k = g(x_k) + b_k + \nu_k \end{cases} \tag{4}$$

where ω_b is the process noise for the parameter b. Note that Equations 3 and 4 are usually nonlinear and non-Gaussian, due to the nonlinear functions $f(\cdot)$ and $g(\cdot)$ and the non-Gaussian noise, respectively, as will be further detailed in Section 3.2.

2.2 | Particle filter

In a Bayesian framework, the unknown state vector at kth step $\boldsymbol{z}_k$ is inferred based on a sequence of sensor observations as follows:

$$p(\boldsymbol{z}_k|\boldsymbol{y}_{1:k-1}) = \int p(\boldsymbol{z}_k|\boldsymbol{z}_{k-1}) p(\boldsymbol{z}_{k-1}|\boldsymbol{y}_{1:k-1}) d\boldsymbol{z}_{k-1}, \tag{5}$$

$$p(\boldsymbol{z}_k|\boldsymbol{y}_{1:k}) \propto p(y_k|\boldsymbol{z}_k) p(\boldsymbol{z}_k|\boldsymbol{y}_{1:k-1}), \tag{6}$$

where $\boldsymbol{y}_{1:k}$ are the measurements collected from time step 1 to k, the transition distribution $p(\boldsymbol{z}_k|\boldsymbol{z}_{k-1})$ and the likelihood function $p(y_k|\boldsymbol{z}_k)$ are obtained from the process and measurement equations, respectively, $p(\boldsymbol{z}_k|\boldsymbol{y}_{1:k-1})$ and $p(\boldsymbol{z}_k|\boldsymbol{y}_{1:k})$ are the prior and the posterior probability distribution functions (PDF) of the variables in the state vector, respectively, and $\propto$ denotes the proportionality.

Equations 5 and 6 form the basis for the optimal Bayesian solution, which is however difficult to be analytically calculated in a nonlinear and non-Gaussian system as it happens in many problems of practical interest. Therefore, the sampling importance resampling (SIR) PF[23] is used in this study to provide an approximated solution for $p(\boldsymbol{z}_k|\boldsymbol{y}_{1:k})$. Figure 2 presents the four steps in SIR PF,[24] i.e.,

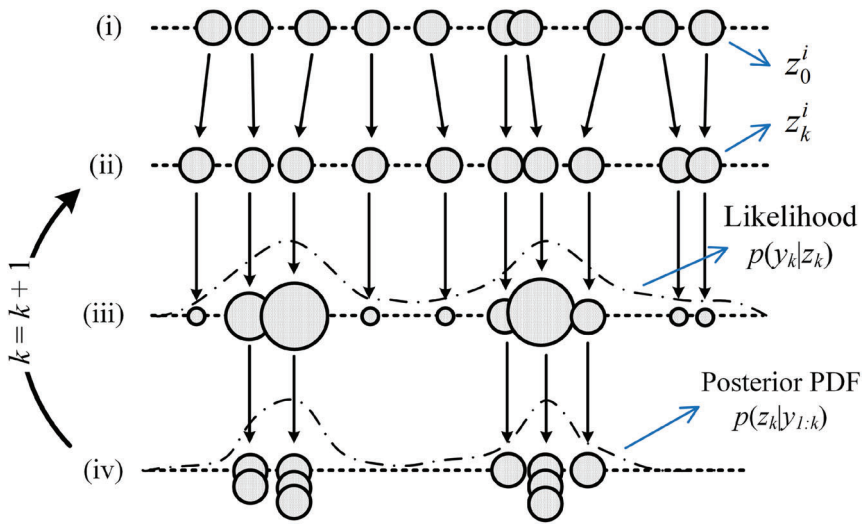

FIGURE 2 Sampling importance resampling (SIR) particle filter[24]

i. **Initialization**: draw N_p particles $\{\boldsymbol{z}_0^i : i = 1, 2, ..., N_p\}$ from the initial distribution $p(\boldsymbol{z}_0)$,

For $k = 1, 2, ...$

ii. **Prediction:** draw N_p particles $\{\boldsymbol{z}_k^i : i = 1, 2, ..., N_p\}$ by the transition distribution $p(\boldsymbol{z}_k|\boldsymbol{z}_{k-1})$,

iii. **Updating:** calculate the weight w_k^i by the likelihood function $p(y_k|\boldsymbol{z}_k^i)$ as

$$w_k^i \propto p(y_k|\boldsymbol{z}_k^i), \tag{7}$$

and assign its normalized form $\widetilde{w}_k^i$ to the particle $\boldsymbol{z}_k^i$,

iv. **Resampling** for $\{\boldsymbol{z}_k^i : i = 1, 2, ..., N_p\}$ using the normalized weights and then assign equal weight to each particle. Systematic resampling is adopted hereafter.

2.3 | Prediction for future state and RUL

The target of many health monitoring applications is that of providing a residual lifetime statistical estimate based on the updated knowledge of the current health state. Thus, by combining the damage evolution model Equation 1 and the kth posterior PDF of damage state $p(x_k|\boldsymbol{y}_{1:k})$, the prognostic step enables predicting the qth step ahead posterior PDF of damage state as follows:[25]

$$p(x_{k+q}|\boldsymbol{y}_{1:k}) = \int \cdots \int \prod_{j=k+1}^{k+q} p(x_j|x_{j-1}) p(x_k|\boldsymbol{y}_{1:k}) \prod_{j=k}^{k+q-1} d(x_j), \tag{8}$$

where $p(x_j|x_{j-1})$ is another form of Equation 1.

Given the impossibility to solve Equation 8 for problems of practical interest, one alternative within a PF framework is to use the particles and their weights to approximate the q-step ahead state PDF as follows:[26]

$$p\left(x_{k+q}|\boldsymbol{y}_{1:k}\right) = \sum_{i=1}^{N_p} \widetilde{w}_{k+q-1}^{i} p\left(x_{k+q}|x_{k+q-1}^{i}\right), \tag{9}$$

where $\widetilde{w}_{k+q-1}^{i}$ is the weight of the ith particle at time step $k+q-1$, considered independent from q and equal to $1/N_p$ if particle q-step ahead projection is done after resampling at each iteration. $p\left(x_{k+q}|x_{k+q-1}^{i}\right)$ is computed through Equation 1 and the PF estimates at kth step. Finally, RUL definition requires a damage state threshold to be set l_{th}, thus declaring structural failure when the future damage state calculated by Equation 9 overcomes l_{th}.

Table 1 summarizes the pseudo code for the calculation of the future states and the RUL. The future state evolution of each particle is iteratively calculated through the damage evolution model Equation 1 at each time step k, until the calculated state reaches the threshold l_{th}. The multiplication of the load cycle range (ΔN) and the number of prediction steps ahead is taken as the RUL of each state particle at current time step.

3 | APPLICATION

3.1 | Experimental setup and data

Fatigue tests of a lug joint aluminum specimen, as given in Figure 3, are used to experimentally validate the method. The experimental setup is briefly introduced hereafter and more details can be found in previous studies.[7,17,27] The thickness of the specimen T_s and the diameter of the through-thickness hole D_h are 5 and 25 mm, respectively. A 2-mm notch is machined at the edge of the hole to initiate the fatigue crack growth. The MTS810 electro-hydraulic testing apparatus applies a sinusoidal fatigue load, with maximum load $L_{max} = 18$ kN, corresponding to 25% of the fracture load, load ratio $R = 0.1$ and loading frequency 10 Hz.

A digital microscope is adopted to observe the crack, while 1-mm equally spaced scale lines on the specimen surface allow for target dimension estimate, as presented in Figure 3c. A 1-mm crack length increase is considered each time the crack passes a new line. For better visualization, the fatigue loading is occasionally paused during the test, and an 18-kN static tensile load is applied to the structure to open the crack.

Two piezoelectric transducers are bonded to the surface of the structure for ultrasonics crack monitoring. One serves as the actuator providing an excitation to the structure, while the other is the sensor collecting the Lamb wave signal. During the monitoring process, the crack growth will induce changes in the Lamb wave signals, manifesting as signal delays and peak amplitude modifications, thus also varying the features extracted from the Lamb wave signals and used for crack length assessment.

Five specimens were tested, and their relative crack growths are shown in Figure 4 for specimens labeled S1–S5. It is clear that a deterministic damage evolution model can hardly provide an accurate prognostic result in presence of typical uncertainties related to the material properties, the specimen and test assembling, the external loading condition, etc. As a 1-mm fatigue pre-cracking is performed at the beginning of the fatigue test, the 3-mm crack (the notch

TABLE 1 Calculation of future state and RUL at time step k

Initialization: Set $\left\{x_k^{i,0} : i = 1,2,...,N_p\right\}$ as $\left\{x_k^{i} : i = 1,2,...,N_p\right\}$
For $i = 1$: N_p
    $q = 0$
    While $x_k^{i,q} < l_{th}$
        Calculate the future state $x_k^{i,q+1}$ by $x_k^{i,q+1} = f\left(x_k^{i,q}, \boldsymbol{\theta}_k^{i}\right)$
        $q = q + 1$
    End
    $RUL_k^{i} = q\Delta N$
End

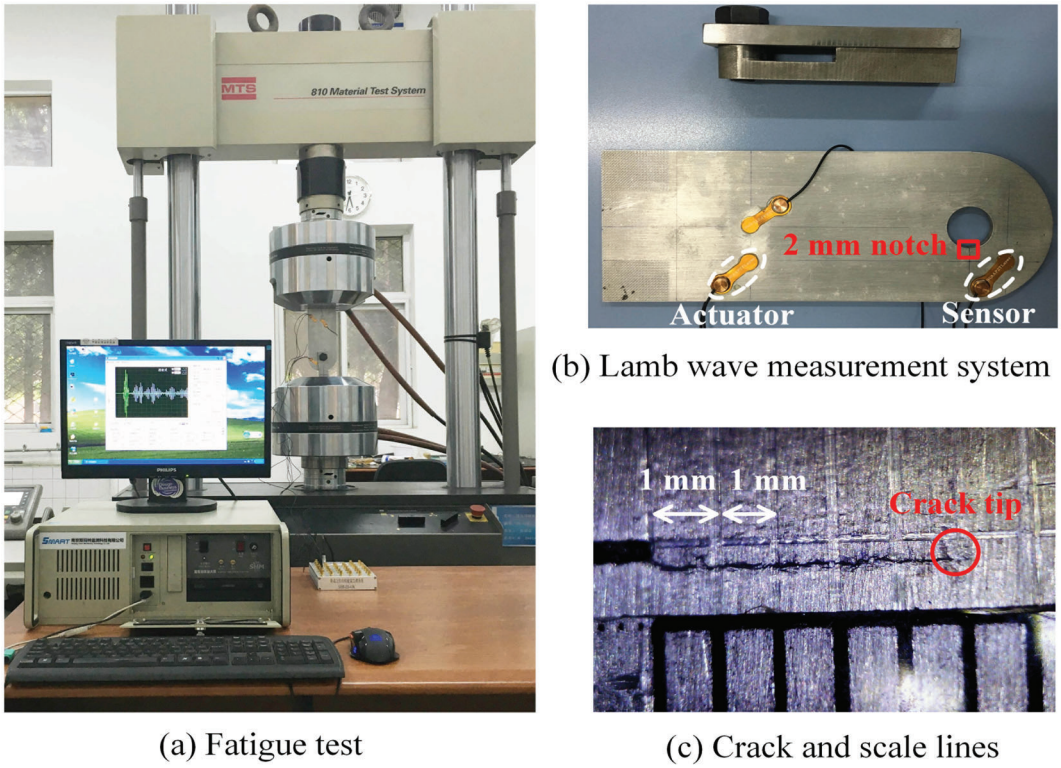

(a) Fatigue test (b) Lamb wave measurement system (c) Crack and scale lines

FIGURE 3 Experimental setup[7]

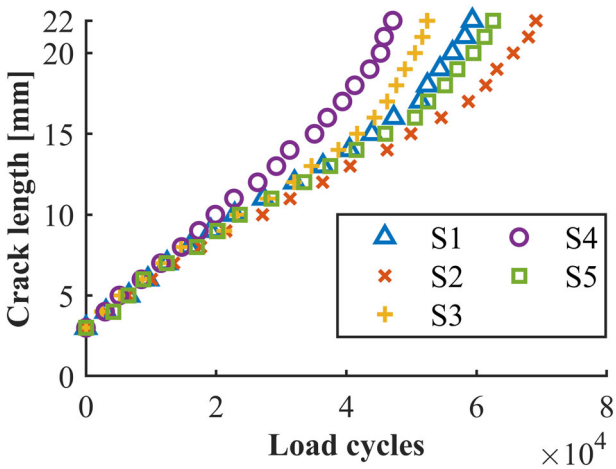

FIGURE 4 Crack growths from specimen S1–S5

length and the pre-cracking length) is taken as the initial crack length, while the threshold crack length for RUL prediction is arbitrarily set to 22 mm, however guaranteeing sufficient residual strength to the joint.

At each measured crack length, the actuator provides a 3-cycle Hanning–Windowed sine burst with central frequency of the excitation 160 kHz, and the sensor collects the Lamb wave signal with the sampling frequency 50 MHz for 2×10^{-4} s, as given in Figure 5. The first wave packet is a crosstalk caused by the electromagnetic induction between the circuits of the actuator and sensor, which carries no information about the crack growth. The signals between 6×10^{-5} and 8×10^{-5} s are taken as the S_0 mode contribution,[7] where the increasing crack length induces a monotonically decreasing amplitude of the signals and a delay of the wave packet as well. These phenomena are used for damage quantification after the feature extraction procedure described below is carried out.

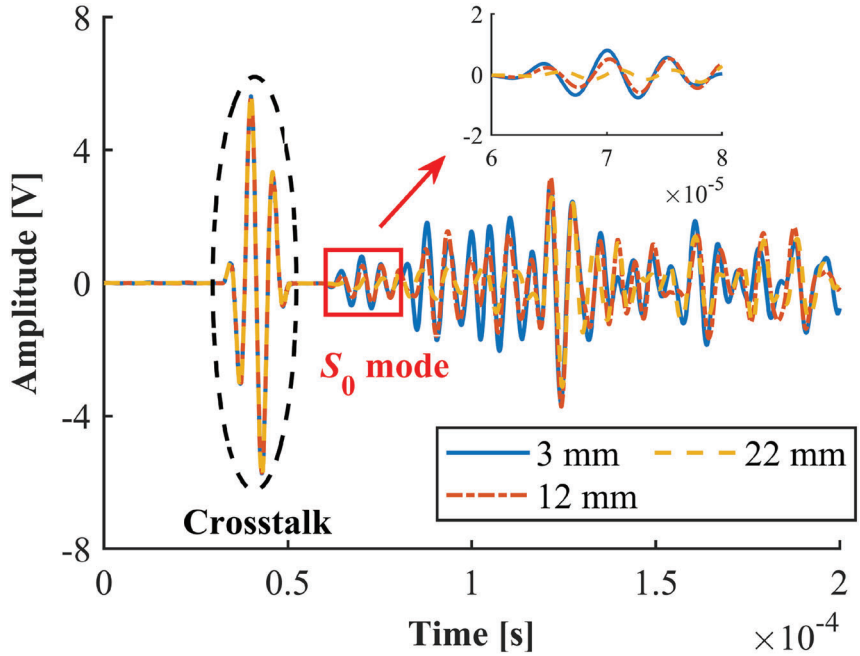

FIGURE 5 Lamb wave signals at three crack lengths from specimen S1

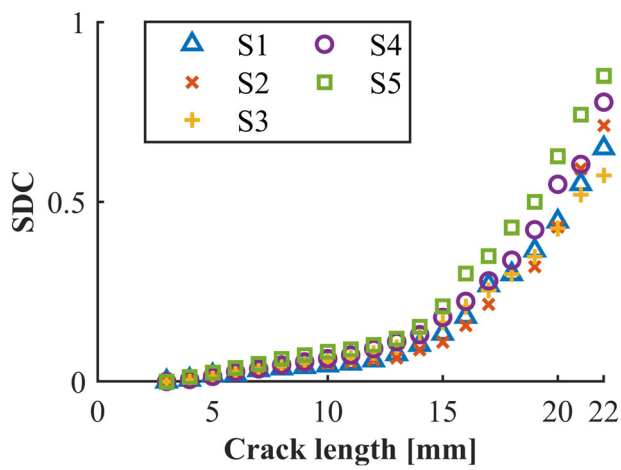

FIGURE 6 SDCs at different crack lengths from specimens S1–S5

The signal difference coefficient (SDC)[28] serves as the statistical feature extracted from the Lamb waves, i.e.:

$$SDC_l = 1 - \left| \frac{cov(f_l, f_b)}{std(f_l)std(f_b)} \right|, \tag{10}$$

where f_b and f_l are the selected S_0 mode signals at the reference crack length 3 mm and current crack length l mm, respectively, the functions "cov" and "std" are the covariance matrix of the two sets of signals and the standard deviation (STD) of one set of signals, respectively. Note that the SDC feature is considered as the available measurement from now on.

Figure 6 presents the monotonically increasing SDCs as a function of crack length for the specimens S1–S5, which confirms the relationship between the crack length and the measurement can vary in different specimens of the same structure. Data relative to specimens S2–S5 are used to fit the function $g(\cdot)$ in the measurement equation in Section 3.2, while specimen S1 will be used for testing the methodology and verify the capability of the algorithm in coping with the bias between the features read in S1 and the corresponding features in S2–S5.

3.2 | Model formulation

The crack growth in a metallic structure subject to fatigue loads is typically described by the Paris' law,

$$\frac{dx}{dN} = C(\Delta K)^m, \tag{11}$$

where x indicates the crack length, C and m are two empirical material parameters governing damage progression, ΔK is the stress intensity factor (SIF) range, calculated with Equation 12 by fitting a set of numerical simulations, as detailed in Appendix A,

$$\Delta K(x) = 0.0014x^3 + 0.5626x^2 - 13.50x + 497.8. \tag{12}$$

With sufficiently small load cycle increment ΔN, Equation 11 can be discretized as

$$x_k = x_{k-1} + C(\Delta K(x_{k-1}))^m \Delta N, \tag{13}$$

and it will be adopted to predict the future crack evolution. The intrinsic stochasticity of the crack growth can be described by adding an unbiased log-normally distributed noise e^{ω} to Equation 13 as in.[3]

$$x_k = x_{k-1} + e^{\omega_k} C(\Delta K(x_{k-1}))^m \Delta N, \tag{14}$$

where $\omega \sim \mathcal{N}\left(-\frac{\sigma^2}{2}, \sigma^2\right)$ is a Gaussian noise with STD σ.

Considering the different crack growth trajectories for the same structure in Figure 4, the future state can hardly be accurately predicted through Equation 13 by considering the parameters in Equation 13 as deterministic and known. One online model updating strategy is to set the parameters C and m as unknown variables and then to form the process equation with both the crack length and parameters included:[3]

$$\begin{bmatrix} \ln C_k \\ m_k \\ x_k \end{bmatrix} = \begin{bmatrix} \ln C_{k-1} + \omega_{1,k} \\ m_{k-1} + \omega_{2,k} \\ x_{k-1} + e^{\omega_k} C_k (\Delta K(x_{k-1}))^{m_k} \Delta N \end{bmatrix}, \tag{15}$$

where ω_1 and ω_2 are zero-mean Gaussian process noises, and $\ln(\cdot)$ is the natural logarithm for an easier sampling.

As the prediction accuracy depends on the state and parameter estimation, kernel smoothing[29] is adopted to improve the estimation performance for the parameters C and m, as already used in.[3,9]

$$\begin{cases} \ln C_k = \sqrt{1-h^2} \ln C_{k-1} + \left(1 - \sqrt{1-h^2}\right) \widehat{\ln C}_k + \omega_{1,k} \\ m_k = \sqrt{1-h^2} m_{k-1} + \left(1 - \sqrt{1-h^2}\right) \widehat{m}_{k-1} + \omega_{2,k} \end{cases}, \tag{16}$$

where $\widehat{\ln C}$ and $\widehat{m}$ denote the means of the samples for the parameters $\ln C$ and m, and $h \in [0\ 1]$ is the smoothing parameter, with a higher value of h meaning a larger shrinkage. The parameter h is set as 0.1, as recommended in Corbetta et al. and Cristiani et al.[3,9]

By combining a measurement equation with Equations 15 and 16, the traditional hybrid prognostic model can finally be formulated as in.[3]

$$\begin{cases} \begin{bmatrix} \ln C_k \\ m_k \\ x_k \end{bmatrix} = \begin{bmatrix} \sqrt{1-h^2} \ln C_{k-1} + \left(1 - \sqrt{1-h^2}\right) \widehat{\ln C}_k + \omega_{1,k} \\ \sqrt{1-h^2} m_{k-1} + \left(1 - \sqrt{1-h^2}\right) \widehat{m}_{k-1} + \omega_{2,k} \\ x_{k-1} + e^{\omega_k} C_k (\Delta K(x_{k-1}))^{m_k} \Delta N \end{bmatrix}, \\ y_k = g(x_k) + \nu_k \end{cases} \tag{17}$$

where the measurement y is the SDC feature obtained from the Lamb waves and the function $g(\cdot)$ describing the mapping between the crack length and the SDC is a fourth-order polynomial function as in.[17]

$$g(x_k) = a_0 {x_k}^4 + a_1 {x_k}^3 + a_2 {x_k}^2 + a_3 x_k + a_4, \tag{18}$$

where a_0, a_1, a_2, a_3, and a_4 are the coefficients obtained from specimens S2—S5 via two steps:

i. the crack lengths and the SDCs for each specimen are fitted by a fourth-order polynomial function to provide one set of coefficients a_0, a_1, a_2, a_3, and a_4 for each specimen;
ii. the averages of the coefficients from the four specimens serve as the corresponding coefficients in $g(\cdot)$.

The new hybrid framework with a bias parameter included for estimation is formulated as

$$\begin{cases} \begin{bmatrix} \ln C_k \\ m_k \\ x_k \\ b_k \end{bmatrix} = \begin{bmatrix} \sqrt{1-h^2}\ln C_{k-1} + \left(1-\sqrt{1-h^2}\right)\widehat{\ln C}_k + \omega_{1,k} \\ \sqrt{1-h^2} m_{k-1} + \left(1-\sqrt{1-h^2}\right)\widehat{m}_{k-1} + \omega_{2,k} \\ x_{k-1} + e^{\omega_k} C_k (\Delta K(x_{k-1}))^{m_k} \Delta N \\ b_{k-1} + \omega_{b,k} \end{bmatrix} \\ y_k = g(x_k) + b_k + \nu_k \end{cases}, \tag{19}$$

where b is the parameter representing the bias, and ω_b is its process noise. Equations 17 and 19 are nonlinear and non-Gaussian, justifying the adoption of the PF algorithm as an efficient state and parameter estimation technique.

3.3 | Target crack growth and SDC observations

The crack length and the Lamb wave feature observations have been experimentally collected at a long interval (i.e., every several thousand load cycles). In order to simulate an online SHM application where the crack length can be evaluated at a shorter interval, exploiting the monotonicity and trendability of the observed features, sequential observations of the target crack growth of specimen S1 have been artificially generated by the following:

i. linearly interpolate the crack length available for specimen S1, generating a new denser target where the crack lengths are available every 300 load cycles,
ii. corrupt the crack lengths by a white Gaussian noise with a signal-to-noise ratio SNR = 50 dB to simulate the uncertainty in crack growth,
iii. use linear interpolation to generate a new SDC at each crack length, and corrupt these SDCs by a white Gaussian noise with SNR = 30 dB to simulate sensor noise.

Figure 7a shows the resulting target crack growth, where a total number of $T = 197$ discrete time steps corresponds to 5.91×10^4 load cycles. Figure 7b shows the sensor-based SDCs and the SDCs predicted by the function $g(\cdot)$ at these crack lengths. A time-varying bias is noticeably existing between the two types of SDCs, potentially hampering the PF performance as shown later in Section 3.5.

3.4 | PF parameters

All the PF parameters used in this study are reported in Table 2. It is worth noting that the PF performance relies on a proper selection of these parameters. The criteria for their selection in this study are given below, while more details on sensitivity analyses can be found in literatures, including number of particles,[30–32] STD in likelihood function,[9] process noise,[30,33] and initial distribution or range.[30]

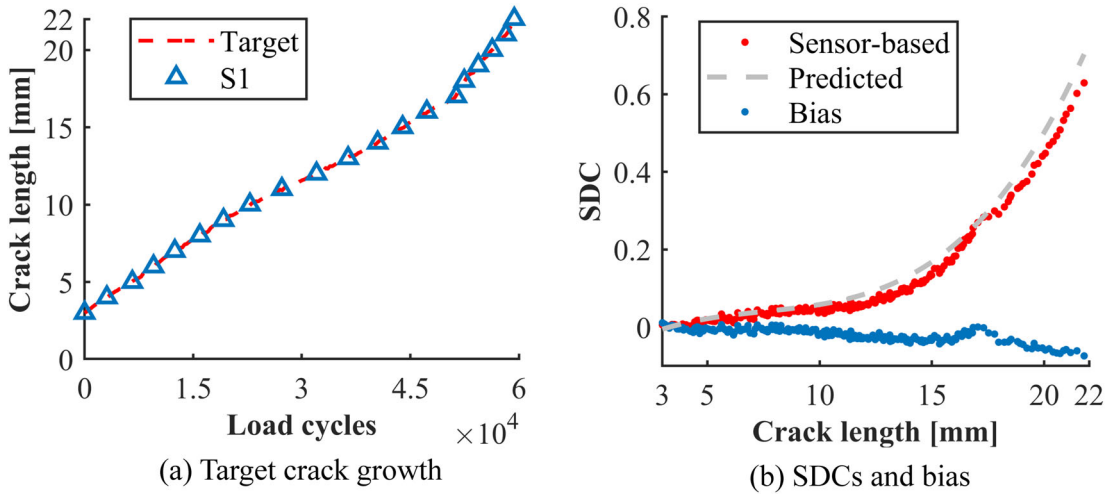

FIGURE 7 Target crack growth and sensor-based and predicted SDCs

TABLE 2 Particle filter parameters

Number of particles N_p **8,000**		**STD in likelihood function σ_y** **0.01**	
Initial distributions for ln C $[\ln\left(\frac{\text{mm}}{\text{cycle}\left(\text{MPa}\sqrt{\text{mm}}\right)^{-m}}\right)]$, m [−]		Initial range for x [mm]	Initial value for b [−]
$\begin{bmatrix}\ln C_0\\ m_0\end{bmatrix}\sim\mathcal{N}\left(\begin{bmatrix}-57.18\\ 8.101\end{bmatrix},\begin{bmatrix}0.9966 & -0.1764\\ -0.1764 & 0.0346\end{bmatrix}\right)$		$x_0\in(2.5, 3.5)$	$b_0=0$
Distributions of process noises $\{\omega, \omega_1, \omega_2, \omega_3\}$ for x, ln C, m, b			
x, ω [−]	ln C $\left[\ln\left(\frac{\text{mm}}{\text{cycle}\left(\text{MPa}\sqrt{\text{mm}}\right)^{-m}}\right)\right]$, ω_1 [−]	m, ω_2 [−]	b, ω_3 [−]
$\mathcal{N}\left(-\frac{0.01^2}{2},0.01^2\right)$	$\mathcal{N}(0,0.02^2)$	$\mathcal{N}(0,0.002^2)$	$\mathcal{N}(0,0.005^2)$

The number of particles N_p can be set as a trade-off between the accuracy and the computation cost,[34] since PF with more particles generally provides more satisfactory estimates but requires more computational effort.[30–32] A satisfactory number is usually determined through a convergence analysis, meaning particles are increased until no significant improvement is found on the result accuracy.[35–37] Eight thousand particles are sufficient to provide stable estimation results in this study.

The calculation of the particle weights essentially depends on the likelihood of each particle with respect to the actual observation. Given that the measurement noise is assumed zero-mean Gaussian in this study, the likelihood function can be formulated as

$$p\left(y_k|\boldsymbol{z}_k^i\right)=\frac{1}{\sqrt{2\pi}\sigma_y}\exp\left(-\frac{1}{2\sigma_y{}^2}\left(y_k-y_k^i\right)^2\right), \tag{20}$$

where y_k is the observation at kth discrete time step, y_k^i is the simulated observation for the state particle x_k^i, and σ_y can be set as the STD of the measurement noise. However, in different applications, σ_y can be either directly assigned,[5,18,38,39] empirically selected,[40,41] or calculated from the data.[8,42] A trial-and-error procedure is adopted to determine a proper value in this study.

The PF requires the definition of an initial range or distribution for initializing the particles. The initial distributions for ln C and m in a PF-based damage prognosis framework can be considered as multivariate Gaussian.[3] The means are determined through the fitting procedure in Appendix A, and the covariance matrix are initialized as in Corbetta et al. and Virkler et al.[3,43] All the initial samples of the parameter b are set as zero, as the bias is close to zero at initial step. The initial crack length is set as a range including the initial observed length.

A random term should be included in the process equation to describe the state evolution uncertainty. It does not have to be a physical noise, but it is often referred to as process noise (or system noise), where the "process" and "noise" denote the system evolution process as well as the stochastic and perturbative nature, respectively.[3,44] In implementing the PF, at each time step, N_p process noise samples will be sampled from the distributions in Table 2 and assigned to the N_p particles. The noise distributions in this study are determined from Corbetta et al. and Cristiani et al,[3,9,10] while the means and STDs are selected based on a trial-and-error procedure.

3.5 | Prognostic performances

Figures 8a,b present the crack length and parameter estimation results using the traditional approach without taking the measurement bias into consideration, respectively. Despite that the particles for ln C and m converge around fixed values during the sequential estimation, the estimated crack lengths are noticeably smaller than the true ones during the estimation process. The observed SDCs are smaller than the predicted ones as visible in Figure 7b, meaning those particles underestimating the crack length are assigned larger weights through the likelihood function, and they will be duplicated in the resampling step. The estimated crack lengths after about 5×10^4 load cycles are closer to the target, due to the lower proportion of the bias in the actual measurements. In fact, the ratio of the root mean square (RMS) of the bias with respect to the RMS value of the measurements is 0.11 after about 5×10^4 load cycles, compared to 0.25 before 5×10^4 load cycles. In conclusion, the traditional approach cannot provide an accurate state and parameter estimation, and its performance is highly related to (i) whether the actual measurements are above or below the predicted ones and (ii) the relative magnitude of bias compared to the measurements.

Figures 9a–c present the crack length, material parameters, and bias estimation results by the new approach, respectively. The estimated crack length is noticeably more accurate than that in Figure 8a, as the bias is correctly identified by the PF, and it is taken into consideration for the estimation for the other state components. Both the accurate crack length estimation and the convergence of parameters ln C and m show that the new model can provide more accurate state and parameter estimation results than the traditional model. As the use of one additional parameter in measurement equation introduces additional uncertainties, the confidence boundaries (CBs) for crack length result larger and the particles of the parameters C and m are more diversely distributed, as was also observed in Rabiei et al.[19]

The difficulty in estimating the time-varying bias, which leads to a small-level error in crack length estimation, might be alleviated by (i) adopting PF with an adaptive process noise,[45] which enhance the performance in estimating the time-varying parameter or (ii) collecting the true crack length to update the bias parameter at a limited number of load cycles.

Figures 10a,b present the prediction for future states at 3.6×10^4 load cycles using the traditional and new approaches, respectively. Each gray dotted line is the crack length trajectory predicted by Equation 13 for one posterior

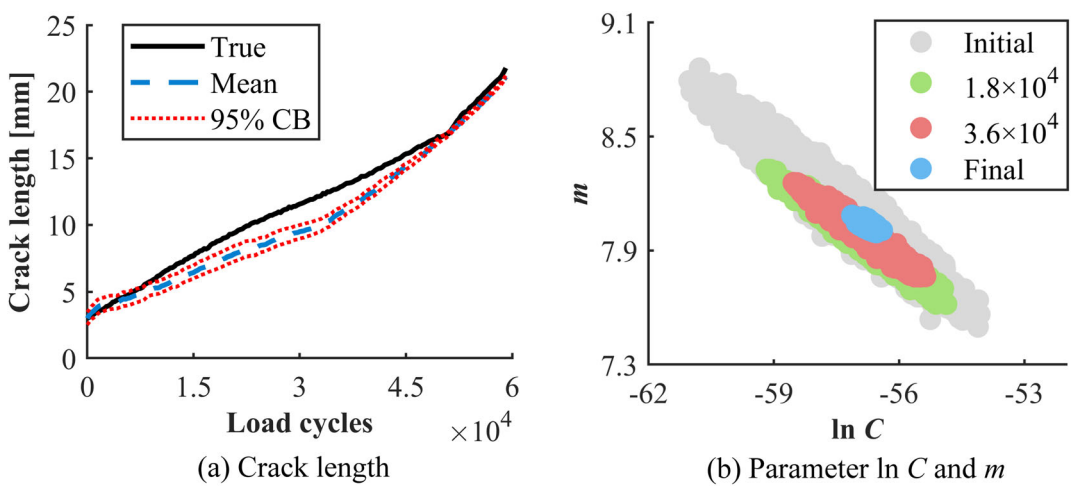

FIGURE 8 State and parameter estimation using traditional model

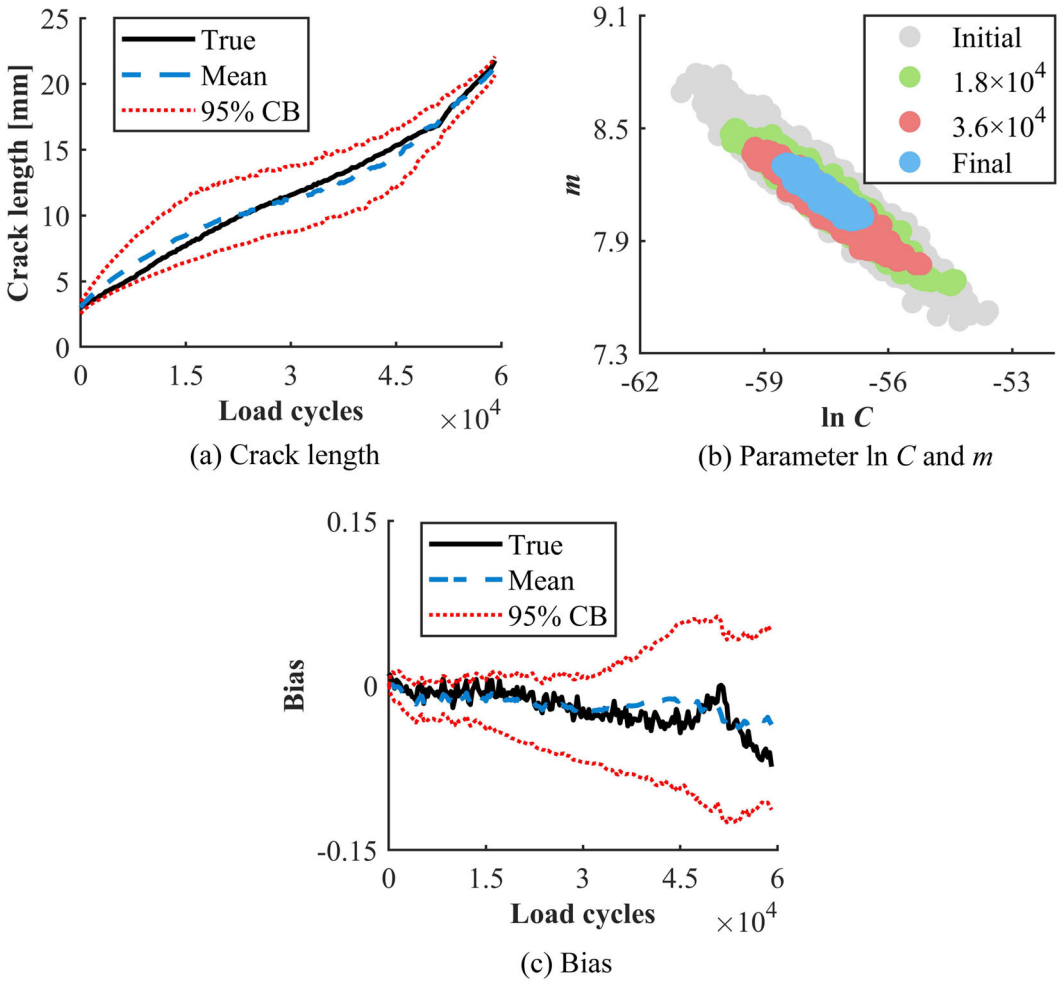

FIGURE 9 State and parameter estimation using new model

sample of the state vector. The gray histogram at the end of life (identified as the critical crack length 22 mm) is the RUL posterior PDF. Figures 11a,b show the RUL predictions using the traditional and new approaches, respectively, along with their 95% CBs. The predicted states and the RUL are noticeably improved by adding the bias as a parameter to be estimated in the state vector, which is strictly related to the improved accuracy of the state posterior estimates.

3.6 | Performances under different-magnitude biases

The performance of the two approaches (with and without taking the bias into consideration) is now tested under different-magnitude biases. Four sets of SDCs target observations are artificially created by

i. scaling the bias in Figure 7b (without measurement noise) by a set of scaling factors s_f {0, 0.5, 1.5, 2} to create four bias levels with the same morphology,
ii. adding these biases to the predicted SDCs in Figure 7b, and
iii. corrupting the artificially generated SDCs observations by a white Gaussian noise with SNR 30 dB.

The analysis in Section 3.5 is repeated with the four sets of SDCs. Performances are expressed in terms of the root mean square errors (RMSEs) metric for the crack length and bias, while the cumulative relative accuracy (CRA) metric is used for the RUL:

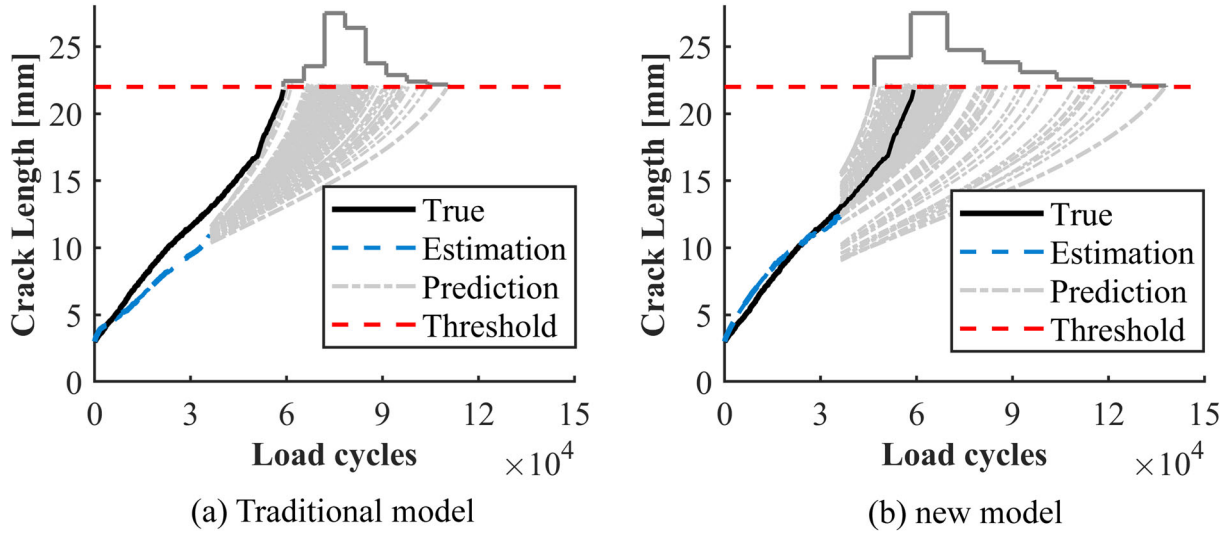

FIGURE 10 Predicted future states at 3.6×10^4 load cycles from traditional and new models

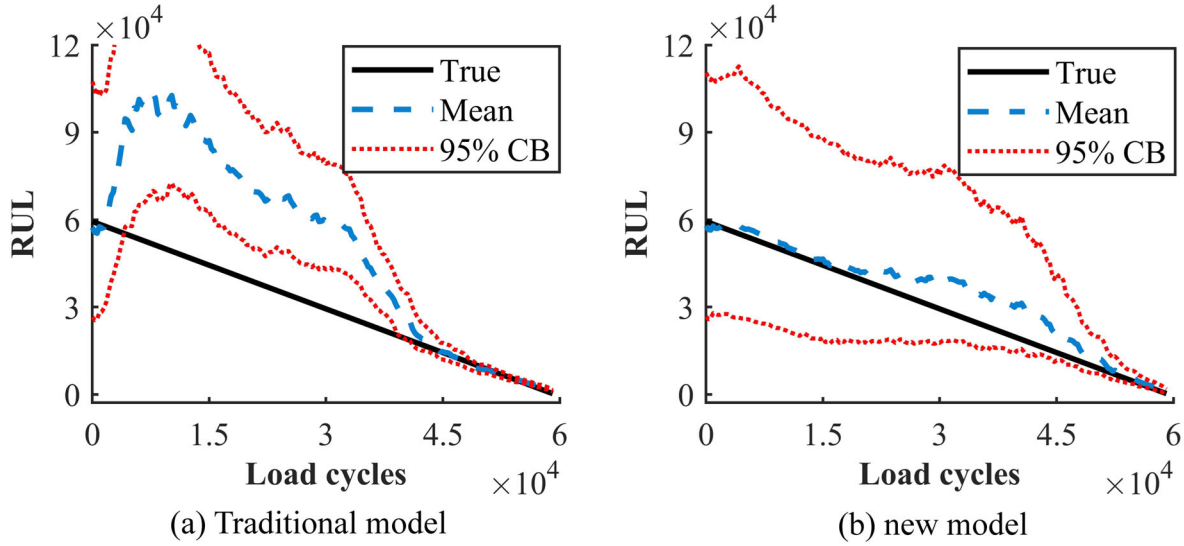

FIGURE 11 RUL predictions from traditional and new models

$$RMSE = \sqrt{\frac{1}{T}\sum_{k=1}^{T}\left(s_{mean,k} - s_{true,k}\right)^2}, \tag{21}$$

$$CRA = \sum_{k=1}^{T-1}\left(1 - \frac{\left|RUL_{mean,k} - RUL_{true,k}\right|}{RUL_{true,k}}\right), \tag{22}$$

where s is the generic state component to be evaluated, either the crack length or the bias, and $T = 197$ is the number of discrete time steps. Lower RMSE and higher CRA represent better estimation and prognosis performances, respectively.

Figures 12a–c present the RMSEs of crack length, the CRAs of RUL, and the RMSE of bias, respectively, as a function of the level of bias. Note that the results of the level-one magnitude have already been presented in Section 3.5. The traditional approach slightly outperforms the new approach under no bias, because the unnecessary bias

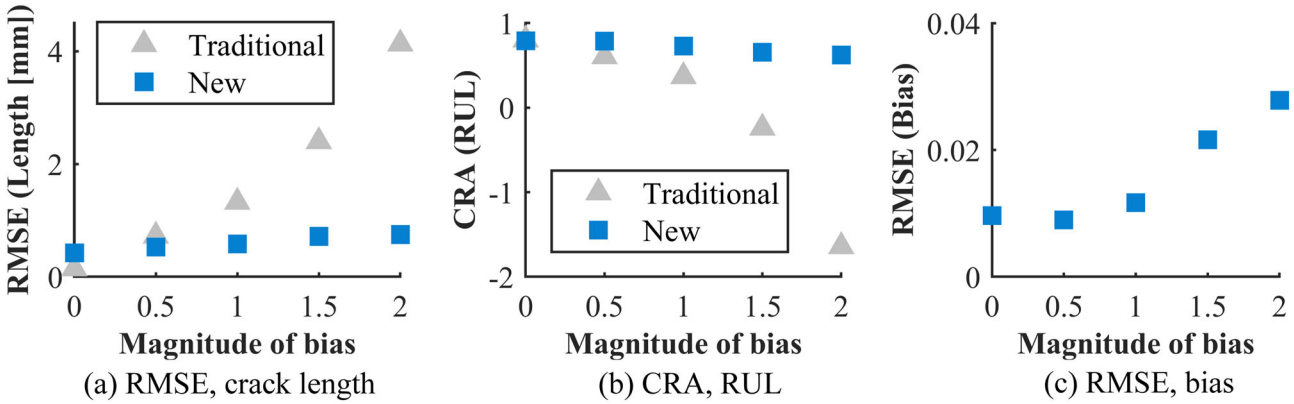

FIGURE 12 Performances of the traditional and new models under different-magnitude biases

estimation introduces more uncertainties. By increasing the bias level, the estimation and prognostic performances of the traditional model significantly decrease, compared with the slight decrease of new model. Meanwhile, the latter might be difficult to be avoided in practice, because the larger the bias level is, the less accurate its estimation will be, as given in Figure 12c, but this might be alleviated resorting to the two strategies mentioned Section 3.5, i.e., (i) adopting a more efficient state estimation technique, e.g., the adaptive PF,[45] to estimate the time-varying bias parameter, and (ii) collecting the true crack length to update the bias parameter at some load cycles.

4 | CONCLUSIONS

The bias between the sensor observation and its prediction by a measurement equation is unavoidable in hybrid prognostic investigations, leading to inaccurate state and parameter estimations and prognostic results. Inspired by sensor fault diagnosis and hybrid damage prognosis, this paper has proposed a new hybrid state space model that includes a bias parameter in the prognostic model for estimation. The experimental study, where an aluminum lug structure is subject to fatigue cracking and monitored by ultrasonic Lamb waves, has proven that the new model can provide accurate estimation and prognostic results provided that the bias is correctly estimated. Furthermore, the estimation and prognostic performances of the new approach have been shown to be noticeably more robust than those of the traditional model in presence of an increasing bias. The slight performance reduction by increasing the bias level might not be avoided even in the newly proposed approach, but can be alleviated by combining different features for damage quantification or by implementing an efficient state estimation technique for time-varying parameters.

The approach remains valid for more complex scenarios, although the acquisition of sufficient experimental or in-field data during the entire run-to-failure process might be infeasible, due to unconceivable costs. Thus, one may resort to simulated data, e.g. from a finite element model, for the definition of the measurement model and the process equation, surely affected by bias, thus justifying additional effort by the authors in present and future research. Moreover, with tens or hundreds of sensors installed on large structures, the measurement equation will become high-dimensional. Although most of the measurements will be unaffected by damage, due to its localized nature, this may lead to an inaccurate and time-consuming prognosis. Online selection of the most appropriate combination of observations is another promising field of research in this framework.

ACKNOWLEDGMENTS

This project has received funding from the European Union's Horizon 2020 research and innovation programme under the Marie Skłodowska-Curie grant agreement no. 859957.

DATA AVAILABILITY STATEMENT

The data that support the findings of this study are available on request from the corresponding author. The data are not publicly available due to privacy or ethical restrictions.

ORCID

Claudio Sbarufatti https://orcid.org/0000-0001-5511-8194
Francesco Cadini https://orcid.org/0000-0001-9235-396X

REFERENCES

1. Chiachío J, Chiachío M, Sankararaman S, Saxena A, Goebel K. Condition-based prediction of time-dependent reliability in composites. *Reliability Engineering & System Safety*. 2015;142:134-147.
2. Chiachío M, Chiachío J, Sankararaman S, Goebel K, Andrews J. A new algorithm for prognostics using Subset Simulation. *Reliability Engineering & System Safety*. 2017;168:189-199.
3. Corbetta M, Sbarufatti C, Giglio M, Todd MD. Optimization of nonlinear, non-Gaussian Bayesian filtering for diagnosis and prognosis of monotonic degradation processes. *Mechanical Systems and Signal Processing*. 2018;104:305-322.
4. Cadini F, Sbarufatti C, Corbetta M, Cancelliere F, Giglio M. Particle filtering-based adaptive training of neural networks for real-time structural damage diagnosis and prognosis. *Struct Control Health Monit*. 2019;26(12).
5. Chiachío J, Jalón ML, Chiachío M, Kolios A. A Markov chains prognostics framework for complex degradation processes. *Reliability Engineering & System Safety*. 2020;195:106621.
6. Guo L, Li N, Jia F, Lei Y, Lin J. A recurrent neural network based health indicator for remaining useful life prediction of bearings. *Neurocomputing*. 2017;240:98-109.
7. Chen J, Yuan S, Wang H. On-line updating Gaussian process measurement model for crack prognosis using the particle filter. *Mechanical Systems and Signal Processing*. 2020;140:106646.
8. Chen J, Yuan S, Jin X. On-line prognosis of fatigue cracking via a regularized particle filter and guided wave monitoring. *Mechanical Systems and Signal Processing*. 2019;131:1-17.
9. Cristiani D, Sbarufatti C, Giglio M. Damage diagnosis and prognosis in composite double cantilever beam coupons by particle filtering and surrogate modelling. *Structural Health Monitoring*. 2020;1475921720960067.
10. Cristiani D, Sbarufatti C, Cadini F, Giglio M. Fatigue damage diagnosis and prognosis of an aeronautical structure based on surrogate modelling and particle filter. *Structural Health Monitoring*. 2020;1475921720971551.
11. Orchard ME, Vachtsevanos GJ. A particle-filtering approach for on-line fault diagnosis and failure prognosis. *Transactions of the Institute of Measurement and Control*. 2009;31(3-4):221-246.
12. Peng Y, Dong M, Zuo MJ. Current status of machine prognostics in condition-based maintenance: a review. *The International Journal of Advanced Manufacturing Technology*. 2010;50(1-4):297-313.
13. Liao L, Köttig F. Review of hybrid prognostics approaches for remaining useful life prediction of engineered systems, and an application to battery life prediction. *IEEE Transactions on Reliability*. 2014;63(1):191-207.
14. Lei Y, Li N, Guo L, Li N, Yan T, Lin J. Machinery health prognostics: A systematic review from data acquisition to RUL prediction. *Mechanical Systems and Signal Processing*. 2018;104:799-834.
15. Lopez I, Sarigul-Klijn N. A review of uncertainty in flight vehicle structural damage monitoring, diagnosis and control: Challenges and opportunities. *Progress in Aerospace Sciences*. 2010;46(7):247-273.
16. Baraldi P, Mangili F, Zio E. Investigation of uncertainty treatment capability of model-based and data-driven prognostic methods using simulated data. *Reliability Engineering & System Safety*. 2013;112:94-108.
17. Yuan S, Chen J, Yang W, Qiu L. On-line crack prognosis in attachment lug using Lamb wave-deterministic resampling particle filter-based method. *Smart Materials and Structures*. 2017;26(8):085016.
18. Cadini F, Sbarufatti C, Corbetta M, Giglio M. A particle filter-based model selection algorithm for fatigue damage identification on aeronautical structures. *Structural Control & Health Monitoring*. 2017;24(11):e2002.
19. Rabiei E, Droguett EL, Modarres M. Fully adaptive particle filtering algorithm for damage diagnosis and prognosis. *Entropy*. 2018;20(2).
20. Giremus A, Tourneret J-Y, Calmettes V. A particle filtering approach for joint detection/estimation of multipath effects on GPS measurements. *IEEE Transactions on Signal Processing*. 2007;55(4):1275-1285.
21. Grauer JA. Real-Time Data-Compatibility Analysis Using Output-Error Parameter Estimation. *J Aircr*. 2015;52(3):940-947.
22. An D, Choi J-H, Kim NH. Identification of correlated damage parameters under noise and bias using Bayesian inference. *Structural Health Monitoring*. 2011;11:293-303.
23. Arulampalam MS, Maskell S, Gordon N, Clapp T. A tutorial on particle filters for online nonlinear/non-Gaussian Bayesian tracking. *IEEE Transactions on Signal Processing*. 2002;50(2):174-188.
24. Chatzi EN, Smyth AW. Particle filter scheme with mutation for the estimation of time-invariant parameters in structural health monitoring applications. *Structural Control & Health Monitoring*. 2013;20(7):1081-1095.
25. Doucet A, Godsill S, Andrieu C. On sequential Monte Carlo sampling methods for Bayesian filtering. *Statistics & Computing*. 2000;10(3):197-208.
26. Zio E, Peloni G. Particle filtering prognostic estimation of the remaining useful life of nonlinear components. *Reliability Engineering & System Safety*. 2011;96(3):403-409.
27. Chen J, Yuan S, Qiu L, Wang H, Yang W. On-line prognosis of fatigue crack propagation based on Gaussian weight-mixture proposal particle filter. *Ultrasonics*. 2017;82:134-144.
28. Qing XP, Chan H-L, Beard SJ, Kumar A. An active diagnostic system for structural health monitoring of rocket engines. *Journal of Intelligent Material Systems and Structures*. 2006;17(7):619-628.

29. Liu J, West M. Combined parameter and state estimation in simulation-based filtering, sequential Monte Carlo methods in practice. *Springer*. 2001;197-223.
30. Chatzi EN, Smyth AW. The unscented Kalman filter and particle filter methods for nonlinear structural system identification with non-collocated heterogeneous sensing. *Structural Control & Health Monitoring*. 2010;16:99-123.
31. Ubeda-Medina L, García-Fernández A, Grajal J. Sigma-point multiple particle filtering. *Signal Processing*. 2019;160:271-283.
32. Chavali P, Nehorai A. Hierarchical particle filtering for multi-modal data fusion with application to multiple-target tracking ☆. *Signal Processing*. 2014;97:207-220.
33. Yoo SJ, Jung DH, Kim JH, Lee JM. A comparative study of soft sensor design for lipid estimation of microalgal photobioreactor system with experimental validation. *Bioresour Technol*. 2015;179:275-283.
34. Li X, Yang X, Yang Y, Bennett I, Mba D. An intelligent diagnostic and prognostic framework for large-scale rotating machinery in the presence of scarce failure data. *Struct Health Moni*. 2019;5:1375-1390, 1475921719884019.
35. Nguyen LH, Goulet J-A. Real-time anomaly detection with Bayesian dynamic linear models. *Struct Control Health Monit*. 2019;26(9): e2404.
36. Ching J, Beck JL, Porter KA. Bayesian state and parameter estimation of uncertain dynamical systems. *Probabilistic Engineering Mechanics*. 2006;21(1):81-96.
37. Sen D, Erazo K, Nagarajaiah S. Bayesian estimation of acoustic emissions source in plate structures using particle-based stochastic filtering. *Struct Control Health Monit*. 2017;24(11):e2005.
38. Fan X, Liu Y. Use of monitored daily extreme stress data for performance prediction of steel bridges: Dynamic linear models and Gaussian mixed particle filter. *Mechanical Systems and Signal Processing*. 2019;121:841-855.
39. Cadini F, Zio E, Peloni G. Particle filtering for the detection of fault onset time in hybrid dynamic systems with autonomous transitions. *IEEE Transactions on Reliability*. 2012;61(1):130-139.
40. Chen C, Zhang B, Vachtsevanos G, Orchard M. Machine condition prediction based on adaptive neuro–fuzzy and high-order particle filtering. *IEEE Transactions on Industrial Electronics*. 2011;58(9):4353-4364.
41. Corbetta M, Sbarufatti C, Giglio M, Saxena A, Goebel K. A Bayesian framework for fatigue life prediction of composite laminates under co-existing matrix cracks and delamination. *Composite Structures*. 2018;187:58-70.
42. Sajeeb R, Manohar CS, Roy D. A conditionally linearized Monte Carlo filter in non-linear structural dynamics. *International Journal of Non-Linear Mechanics*. 2009;44(7):776-790.
43. Virkler DA, Hillberry BM, Goel PK. The statistical nature of fatigue crack propagation. *Journal of Engineering Materials and Technology*. 1979;101(2):148-153.
44. Svensson A, Schön TB, Lindsten F. Learning of state-space models with highly informative observations: a tempered sequential Monte Carlo solution. *Mechanical Systems and Signal Processing*. 2018;104:915-928.
45. Liu M, Zang S, Zhou D. Fast leak detection and location of gas pipelines based on an adaptive particle filter. *International Journal of Applied Mathematics & Computer Science*. 2005;15:541-550.

How to cite this article: Li T, Sbarufatti C, Cadini F, Chen J, Yuan S. Particle filter-based hybrid damage prognosis considering measurement bias. *Struct Control Health Monit*. 2021;e2914. doi:10.1002/stc.2914

APPENDIX A.

Given the analytical solution for the SIFs at different crack lengths is not available, numerical models of the lug structure are built by ABAQUS to provide the maximum SIFs K_{max} at several crack lengths under the maximum fatigue load, which are then used to establish the relationship between the SIF range ΔK and the crack length. The numerical model is plotted in Figure A1.

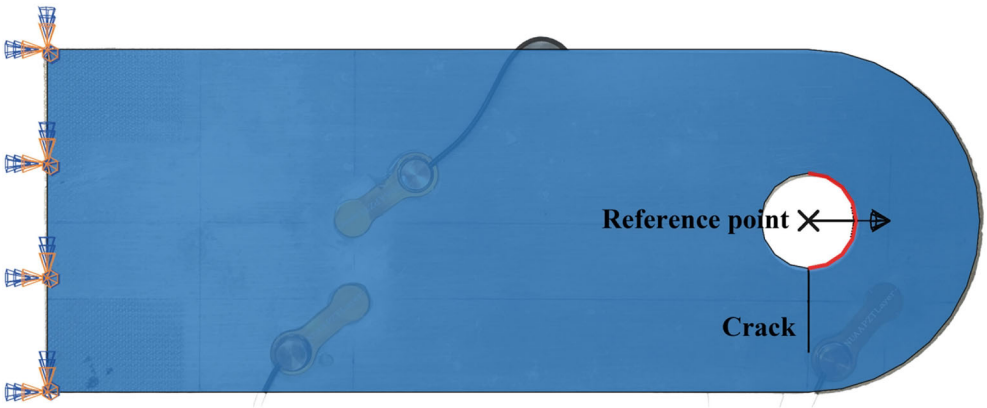

FIGURE A1 ABAQUS model of the experimental structure

The lug structure is modeled as a 2D shell, with Young's modulus, density and Poisson's ratio 72,000 MPa, 2,700 kg/dm^3, and 0.33, respectively. The left side of the structure is fixed. A reference point is located at the center of the circle hole, and it is coupling with the right side of the hole (plotted as red curve). The static analysis, where a concentrated force (maximum fatigue load, 18 kN) is horizontally applied to the reference point, is used to provide the SIF K_{max} at each crack length.

Table A1 lists the numerical SIFs at different crack lengths. Considering that no nonlinearity exists in this model, the SIF range ΔK at each crack length can be calculated by the K_{max} and the load ratio R. A third order polynomial regression is used to fit the relationship between the crack length x and SIF range ΔK. Specifically, Equation 13 can be transformed into its logarithmic form:

$$\underbrace{\ln\frac{x_k - x_{k-1}}{\Delta N}}_{Output} = \ln C + m\underbrace{\ln \Delta K(x_{k-1})}_{Input}, \tag{A1}$$

where $\ln C$ and m can be easily calculated by the input and output (with x_k and x_{k-1} being two observed consecutive crack lengths) from specimens S2–S5 through a first order polynomial fitting regression. They result -57.18 $\left[\ln\left(\frac{\text{mm}}{\text{cycle}\left(\text{MPa}\sqrt{\text{mm}}\right)^{-m}}\right)\right]$ and 8.101 [−], respectively, and are considered for the initialization of the multivariate Gaussian distribution for $\ln C$ and m.

TABLE A1 Polynomial regression using numerical SIF ranges at different crack lengths

Crack length x [mm]	3	5	8	10	12	15	18	20	22
K_{max} $[MPa \cdot \sqrt{mm}]$	514.4	493.3	473.2	467.4	466.7	475.0	494.3	514.7	543.5
ΔK $[MPa \cdot \sqrt{mm}]$	$K_{max}(1-R)$								
Third order polynomial regression: $\Delta K(x) = 0.0014x^3 + 0.5626x^2 - 13.50x + 497.8$									

Mechanical Systems and Signal Processing 178 (2022) 109326

Contents lists available at ScienceDirect

Mechanical Systems and Signal Processing

journal homepage: www.elsevier.com/locate/ymssp

Numerical simulation-aided particle filter-based damage prognosis using Lamb waves

Tianzhi Li [a], Luca Lomazzi [a], Francesco Cadini [a], Claudio Sbarufatti [a], Jian Chen [b], Shenfang Yuan [b]

[a] Dipartimento di Meccanica, Politecnico di Milano, Milan, Italy
[b] Research Center of Structural Health Monitoring and Prognosis, State Key Laboratory of Mechanics and Control of Mechanical Structures, Nanjing University of Aeronautics and Astronautics, Nanjing, China

ARTICLE INFO

Communicated by Wieslaw Ostachowicz

Keywords:
Structural health monitoring
Damage prognosis
Numerical simulation
Particle filter
Lamb wave

ABSTRACT

Damage prognosis generally resorts to a damage evolution model and the current damage state to predict the future state and the remaining useful life (RUL). As a properly defined damage-sensitive statistical feature extracted from the Lamb waves can be used to online quantify the damage state, it is here exploited within a particle filter (PF) scheme to perform damage prognosis in structural health monitoring. An accurate mapping between the damage state and this feature would require a sufficient set of experimental Lamb waves collected in correspondence of different damage levels occurring during the run-to-failure process, which, however, is not usually available in real practice due to the high costs and the complex logistics involved in such experimental campaigns. In order to deal with this issue, this paper develops a new numerical simulation-aided particle filter-based damage prognosis framework, where the process equation is still built on the basis of available physical knowledge about the degradation process, whereas the measurement equation is built by means of a data-driven modeling approach using the features extracted from the numerically simulated Lamb waves. The PF framework serves as the state estimation tool which allows to identify the damage state and the parameters in the two equations. The future damage states and the RUL can finally be predicted by projecting the PF estimates in the future using the process equation. The proposed framework is demonstrated with reference to experimental studies of fatigue crack growth in aluminum lug structures with online Lamb wave monitoring.

1. Introduction

Engineering structures have to withstand various mechanical and environmental loads during their service life, resulting in fatigue damage, e.g., a crack in a metallic structure or a delamination in a composite. The damage may usually evolve in time (or load cycles in structural fatigue problems), so that, eventually, the structure fails when the damage state reaches a pre-defined threshold, beyond which its functionality cannot be guaranteed any longer. In order to timely avoid this issue, usually inspections are carried out to evaluate the structural performance, often requiring quite high financial expenses, also due to unwanted system shutdowns. In order to simultaneously ensure structural safety and reduce maintenance costs, one possibility is to schedule the maintenance just before the damage state reaches the critical limit. In this context, an advanced damage prognosis technique is desired to estimate the time

E-mail address: francesco.cadini@polimi.it (F. Cadini).

https://doi.org/10.1016/j.ymssp.2022.109326
Received 10 November 2021; Received in revised form 24 February 2022; Accepted 17 May 2022
0888-3270/© 2022 The Authors. Published by Elsevier Ltd. This is an open access article under the CC BY license (http://creativecommons.org/licenses/by/4.0/).

required by the state to become not reach the threshold value, i.e., the structure remaining useful life (RUL).

As the damage evolution under a certain service condition may follow a specific pattern, the future state can be calculated by the current one by means of a proper model describing such a pattern. These damage evolution models in prognostic practices can be either physics-based [1–3] or data-driven [4–6], according to the type of information used for modeling the damage behavior, namely the physical knowledge or observed data, respectively. Physics-based models utilize the physical knowledge, such as Paris' law [1] and its extensions [2,3], to relate the damage state with the load cycles and external loading conditions, while data-driven models, e.g., neural network [4] and non-homogenous hidden semi Markov model [5,6], resort to sufficient monitoring data collected during the degradation process for depicting the above relationship. There are no universally best models, given that each type of model has its own advantages and disadvantages [7,8].

On the other hand, no matter which type of model is adopted, any deterministic form of a damage evolution model can hardly provide an accurate prognostic result, given the uncertainties arising from complex structural degradations [9], the environmental effects [10], and the sensor health conditions [10]. A common strategy for these models to improve their prognostic performances is to set the model parameters as unknown variables to be updated online by a state estimation technique, such as particle filter (PF), given its demonstrated performances in nonlinear and non-Gaussian problems.

Another issue in RUL prediction is the required quantification of the current damage state through a direct or indirect measurement system. The first approach, i.e., when the damage state can be directly measured, has already received plenty of investigations in this field, such as for example the case of the crack length in a metallic structure acquired by a caliper [1,4] or that of matrix cracking density and delamination length in composites measured by X-rays [2,3]. In case the damage state cannot be directly measured, one may refer to an indirect measurement system, such as fiber Bragg grating strain sensors [11] or Lamb wave-based monitoring systems [12–14], to infer the damage state through a measurement equation describing the relationship between the damage state and the measurement (either the directly measured signal or some statistical feature extracted from the signal). Such equation is usually built through a data-driven modeling technique, e.g., neural network [11], polynomial function [14], leave-one-out method [13] or Gaussian process regression [12].

Among the available sensing systems for SHM applications, those based on Lamb waves are probably the most promising, due to their capability for online operation and high sensitivity to damage [15]. Their efficiency in prognostic investigations has been well demonstrated in several works, e.g., [12–14], where an accurate mapping between the damage state and the feature extracted from the Lamb waves requires a sufficiently large database of signals during the run-to-failure process, which, unfortunately, rarely occurs, mainly due to too high costs. On the other hand, numerical Lamb wave simulations can capture the actual Lamb wave propagation, possibly leading to a satisfactory agreement between the features extracted from the numerical Lamb waves and those from the experimental signals. This allows adopting the numerical features taken at different damage state levels, e.g., crack lengths in metal [16,17] or delamination sizes in composite [18], to empirically build the measurement equation following the procedure indicated above. However, this method has not been used for damage prognosis so far, which might be because the unavoidable bias between the features predicted by the measurement equation and those obtained from the experimental Lamb waves [16,18] can lead to severely inaccurate online prognostic results, as already discussed in [14].

By combining the numerical simulation-aided damage quantification method [16–18] with a damage prognosis approach accounting for the measurement bias [14], this paper proposes a novel numerical simulation-aided particle filter-based damage prognosis framework, where the numerical Lamb waves are used to build the measurement equation. The proposed framework consists of four main steps. First, the numerical Lamb wave simulations of the monitored structure are developed to provide the statistical features of the Lamb waves at different damage levels (or extents). Second, the process equation is formulated using both a bias parameter and the physical law describing damage propagation, whereas the measurement equation representing the relationship between the damage state and the observed feature is built by resorting to a data-driven technique and the use of a bias parameter. Third, a PF is used to estimate the damage state, the damage parameters, and the bias. Finally, the future states and the RUL can be estimated by

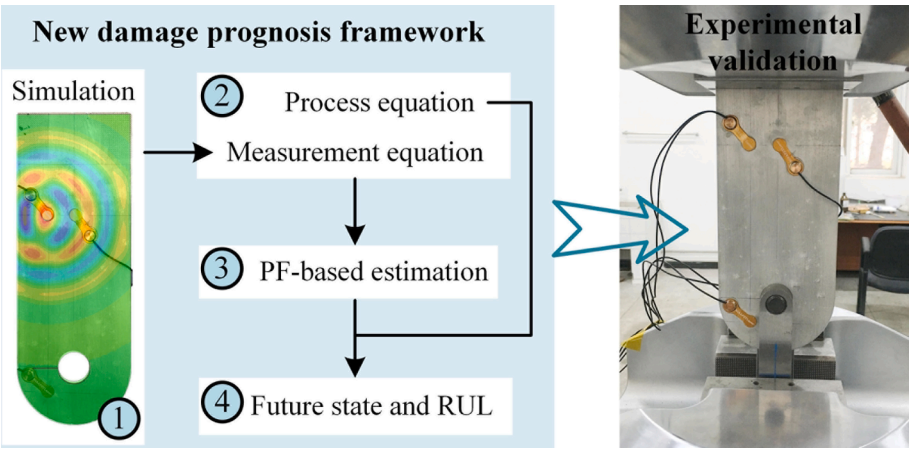

Fig. 1. Numerical simulation-aided PF-based damage prognosis framework.

projecting into the future the process equation starting from the current PF-based estimates of the damage state. The proposed prognosis framework is demonstrated by an experimental study, where an aluminum lug structure subject to fatigue crack growth (FCG) is monitored by a Lamb wave measurement system.

The rest of this paper is organized as follows: Section 2 introduces the four main steps in the prognosis framework. The numerical and experimental Lamb waves are discussed in Section 3, while the application of the proposed method to the experimental case study is provided in Section 4. Finally, Section 5 concludes this paper.

2. Novel damage prognosis framework

Fig. 1 presents the four main steps of the proposed damage prognosis framework, namely, (i) simulating the Lamb waves at different damage levels by means of the numerical model, (ii) formulating a state space model, (iii) estimating the damage state, its damage evolution model parameters, and the bias by PF, and (iv) projecting into the future by the process equation starting from the current PF estimates. The main novelty of the proposed prognosis framework compared to the state-of-the-art methods [12–14] is that numerical Lamb waves at different damage levels, instead of experimental signals, are used for formulating a measurement equation, so that the costs and efforts in conducting run-to-failure tests or collecting in-field data for model formulation can be avoided. The four steps of the proposed procedure are introduced below, and the experimental setup and validation will be discussed in Sections 3 and 4, respectively.

2.1. Lamb wave simulation

Depending on the type of excitation used in a numerical model, the Lamb wave simulations can be broadly divided into two categories, i.e., (i) those using voltage [18,19] and (ii) those using mechanical loads like force [16], pressure [20], or displacement [17]. The first ones are similar to how the actuator and sensor work in a real experiment. The actuator and sensor are modeled as elements with electro-mechanical and mechanical properties. The former can deform when receiving the voltage and consequently lead to the vibration of the monitored structure to which it is attached, while the latter one deforms with the vibration and consequently generates the voltages, which are taken as the numerical Lamb wave.

As to the second type of simulations, the modeling for the actuator and sensor is not mandatory. The excitation at the actuator location can be a mechanical load like force [16], pressure [20], or displacement [17], while the vibration responses at the sensor location, e.g., out-of-the plane displacement, are taken as the numerical Lamb wave. These simulations can provide three modes of Lamb waves, i.e., full mode, pure S mode, and pure A mode, corresponding to one single excitation, two symmetric excitations, and two anti-symmetric excitations. Note that many numerical models [16–19] will only have either S_0, A_0 or both two modes simulated by applying an excitation with a relatively small center frequency. High-order Lamb waves may not be frequently used in SHM practices.

As the two types of numerical simulations can capture the actual Lamb wave propagation, some statistical features calculated from numerical Lamb waves are in good agreement with those from experimental ones, which enables the feasibility of adopting the numerical features to formulate a measurement equation for damage quantification, as already performed in [16–18]. In this study, the Lamb wave simulations of the monitored structure are conducted to provide the features at different levels of damage, which will be then adopted to formulate a measurement equation, as will be introduced in Section 3.

2.2. Prognostic model

In general, upon proper discretization in time (or load cycle), the damage evolution can be described by:

$$x_k = f(x_{k-1}, \boldsymbol{\theta}) \tag{1}$$

where x is the damage state, $f(\cdot)$ is the evolution function, $\boldsymbol{\theta}$ is a model parameter vector, and the subscript k is the discrete time step index. Due to the uncertainties in the damage evolution process, the parameters $\boldsymbol{\theta}$ can vary in different specimens of the same structure. According to the common practice of PF-based diagnosis and prognosis, the unknown parameters are treated as stochastic variables (similarly to the damage state) that can be added to the state vector [13,14],

$$\begin{bmatrix} \boldsymbol{\theta}_k \\ x_k \end{bmatrix} = \begin{bmatrix} \boldsymbol{\theta}_{k-1} + \boldsymbol{\omega}_{\theta,k} \\ f(x_{k-1}, \boldsymbol{\theta}_k, \omega_k) \end{bmatrix} \tag{2}$$

where ω_k and $\boldsymbol{\omega}_\theta$ are the process noises for the damage state and the parameters, respectively, accounting for their stochasticity.

With a proper measurement y (i.e., a feature extracted from the Lamb waves in this study) for inferring the unknown damage state, the measurement equation in a PF-based damage prognosis can be formulated as:

$$y_k = g(x_k) + \nu_k \tag{3}$$

where the function $g(\cdot)$ describes the relationship between the damage state and the measurement, ν_k is the measurement noise assumed as zero-mean Gaussian distributed. Current PF and Lamb wave-based damage prognosis practices [13,14] usually resort to the Paris' law, or an extension thereof, and a data-driven model to describe the damage state process evolution $f(\cdot)$ and to approximate the relationship $g(\cdot)$, respectively, with the latter usually requiring the availability of a sufficiently large training dataset during the run-to-

failure process of a structure.

Given the difficulties and costs associated with the acquisition of sufficiently informative datasets in laboratory experiments or, even, in the field, some Lamb wave-based damage quantification investigations [16–18] have adopted the features from numerically simulated Lamb waves to build the function $g(\cdot)$. However, the unavoidable biases between the features predicted by $g(\cdot)$ and those extracted from experimental Lamb waves acquired on a testing specimen may not lead to satisfactory prognostic results, as already discussed in [14].

By combining the numerical simulation-aided damage quantification method in [16–18] with the approach to damage prognosis in presence of significant measurement bias [14], this paper develops a novel prognosis framework that resorts to the numerical Lamb waves for building the measurement equation, where the effect of the unavoidable bias can be alleviated by further augmenting the state space with a bias parameter for estimation. The prognostic framework finally reads,

$$\begin{cases} z_k = \begin{bmatrix} \boldsymbol{\theta}_k \\ x_k \\ b_k \end{bmatrix} = \begin{bmatrix} \boldsymbol{\theta}_{k-1} + \boldsymbol{\omega}_{\theta,k} \\ f(x_{k-1}, \boldsymbol{\theta}_k, \omega_k) \\ b_{k-1} + \omega_{b,k} \end{bmatrix} \\ y_k = g(x_k) + b_k + \nu_k \end{cases} \tag{4}$$

where b is the bias parameter and ω_b is its associated process noise, and z_k is a newly defined augmented state vector including both the state and the parameters to be estimated,

2.3. Particle filter

In a Bayesian approach, the unknown state vector at k-th step z_k can be inferred from the measurement as:

$$p(z_k|\boldsymbol{y}_{1:k-1}) = \int p(z_k|z_{k-1})p(z_{k-1}|\boldsymbol{y}_{1:k-1})dz_{k-1} \tag{5}$$

$$p(z_k|\boldsymbol{y}_{1:k}) \propto p(y_k|z_k)p(z_k|\boldsymbol{y}_{1:k-1}) \tag{6}$$

where $\boldsymbol{y}_{1:k}$ is the measurement vector collected from time step 1 to k, the symbol $\propto$ means 'proportional to', the transition distribution $p(z_k|z_{k-1})$ and the likelihood function $p(y_k|z_k)$ denote the process and measurement equations, respectively, $p(z_k|\boldsymbol{y}_{1:k-1})$ and $p(z_k|\boldsymbol{y}_{1:k})$ are the prior and posterior probability distribution function (PDF), respectively.

Eqs. (5) and (6) form the basis for the optimal Bayesian solution, which is, however, difficult to be analytically calculated in a nonlinear and non-Gaussian system like Eq. (4). Therefore, the sampling importance resampling (SIR) PF [21], as an efficient state estimation in this kind of problem, is used in this study. Table 1 lists the pseudo-code of the SIR PF.

2.4. Prediction for future state and RUL

Within the PF framework, by resorting to the damage evolution model of Eq. (1) and the k-th posterior PDF of damage state $p(x_k|\boldsymbol{y}_{1:k})$, the prognostic stage enables the prediction of the q-th step ahead posterior PDF of the damage state $p(x_{k+q}|\boldsymbol{y}_{1:k})$ as [22]:

$$p(x_{k+q}|\boldsymbol{y}_{1:k}) = \int \cdots \int \prod_{j=k+1}^{k+q} p(x_j|x_{j-1})p(x_k|\boldsymbol{y}_{1:k}) \prod_{j=k}^{k+q-1} dx_j \tag{7}$$

where $p(x_j|x_{j-1})$ is the so-called prior distribution, directly associated to the process equation.

Given the difficulty in analytically calculating the solution of Eq. (7), one alternative within a PF-based prognosis framework is to approximate the PDF by the particles and their weights as [23]:

Table 1
Sampling importance resampling particle filter.

Initialization: draw N_p particles $\{z_0^i : i = 1, 2, \cdots, N_p\}$ from the initial distribution$p(z_0)$
For $k = 1, 2, \ldots,$
Prediction in PF: draw N_p particles $\{z_k^i : i = 1, 2, \cdots, N_p\}$ by $z_k^i \sim p(z_k|z_{k-1}^i)$
Weight update: calculate the weight w_k^i by $w_k^i \propto p(y_k|z_k^i)$, and then assign its normalized form $\tilde{w}_k^i$ to each particle z_k^i
Resample for $\{z_k^i : i = 1, 2, \cdots, N_p\}$ using the particle weights $\{\tilde{w}_k^i : i = 1, 2, \cdots, N_p\}$
Approximate the estimate $\hat{z}_k$ from $\hat{z}_k = \frac{1}{N_p}\sum_{i=1}^{N_p} z_k^i$
End

$$p\left(x_{k+q}\middle|\mathbf{y}_{1:k}\right) = \sum_{i=1}^{N_p} \widetilde{w}_{k+q-1}^{i} p\left(x_{k+q}\middle|x_{k+q-1}^{i}\right) \tag{8}$$

where $\widetilde{w}_{k+q-1}^{i}$ is the weight of the i-th particle at time step k+q-1, considered independent from q and equal to $1/N_p$ as the q-step ahead particle projection is done after resampling at each iteration in this study, whereas $p\left(x_{k+q}|x_{k+q-1}^{i}\right)$ can be computed through Eq. (1) and the PF state estimates available at the k-th step.

Table 2 summarizes the calculation required to obtain the estimate of the posterior of the future state and the RUL. The RUL prediction generally requires the definition of an additional threshold value of the damage state l_{th}. The structure is considered to fail when the future state calculated through Eq. (1) reaches the threshold, so that the RUL turns out to be equal to the multiplication of the number of prediction steps and the number of load cycles ΔN in one step.

3. Experimental and numerical Lamb waves

The experimental setup and the physical behavior of the Lamb waves are briefly introduced in Sections 3.1 and 3.2, respectively. The numerical models of the Lamb waves generated and propagating within the experimental specimen are developed in Section 3.3. Section 3.4 compares the Lamb waves from the two studies, which are then adopted to provide some features for damage quantification in Section 3.5.

3.1. Experimental setup

Fatigue tests of the lug joint aluminum structure equipped with a Lamb wave-based monitoring system [13,24], as given in Fig. 2 (a) and (b), are used to validate the proposed method. The thickness of the specimen and the diameter of the through hole are 5 mm and 25 mm, respectively. One 2 mm long notch is machined at the edge of the hole to initiate the crack growth. The MTS810 electro-hydraulic servo material test system is employed to provide the sinusoidal tensile fatigue load. The maximum load L_{max}, load ratio R, and loading frequency are 18 kN, 0.1, and 10 Hz, respectively.

Fig. 2 (c) presents the crack and the scale lines on the surface observed by a digital microscope. These lines are equally spaced by 1 mm. The fatigue loading is occasionally paused during the test, and an 18 kN static tensile load is applied to the structure to open the crack for better visualization. The crack length is considered to increase by 1 mm once the crack tip reaches the next line. A pre-cracking step is performed at the beginning of the fatigue test until the crack length reaches 3 mm.

Fig. 3 shows the crack growths observed for the five specimens S1 ~ S5 under fatigue testing. Due to the uncertainties from the material property, specimen assembling, external loading condition, etc., an obvious dispersion can be noted among the propagation trajectories of these specimens, which confirms that a deterministic damage evolution model can hardly provide accurate prognostic results. Similarly to [12], a 3 mm crack is taken as the initial crack, and the maximum crack length 22 mm is set as the threshold for damage prognosis.

As shown in Fig. 2 (b), the two piezoelectric transducers for crack monitoring are bonded on the surface of the structure with epoxy resin, and they are working with d_{31} mode. At each measured crack length, i.e., when the 18 kN static tensile load is applied to the structure, one serves as the actuator providing a 3-cycles Hanning-windowed sine burst with the central frequency 160 kHz, and another one serves as the sensor collecting the Lamb wave with a sampling frequency of 50 MHz.

3.2. Experimental Lamb waves

By assuming that the Young modulus, density, and Poisson's ratio of the aluminum specimen used in this study are 72000 MPa, 2700 kg/m^3, and 0.33, respectively, the dispersion curves of the Lamb waves can be calculated by means of the Dispersion Calculator developed by the German Aerospace Center [25]. Since the central frequency 160 kHz is below the minimum frequencies for generating S_1 mode and A_1 mode Lamb waves, only S_0 and A_0 Lamb waves are observed in the experiment, and their group velocities at the frequency 160 kHz are 5.31×10^6mm/s and 3.13×10^6mm/s, respectively. The times of flight (ToFs) of S_0 and A_0 waves can then be calculated by the velocities and the distance between the sensor and the actuator (140 mm), yielding 2.637×10^{-5}s and $4.473 \times$

Table 2
Calculation of future state and RUL at time step k.

Initialization: set $\left\{x_k^{i,0} : i = 1, 2, \cdots, N_p\right\}$ as $\left\{x_k^{i} : i = 1, 2, \cdots, N_p\right\}$
For $i = 1$: N_p
  $j = 0$
  While $x_k^{i,j} < l_{th}$
    Calculate the future state $x_k^{i,j+1}$ by $x_k^{i,j+1} = f\left(x_k^{i,j}, \boldsymbol{\theta}_k^{i}\right)$
    $j = j + 1$
  End
  $RUL_k^{i} = j \times \Delta N$
End

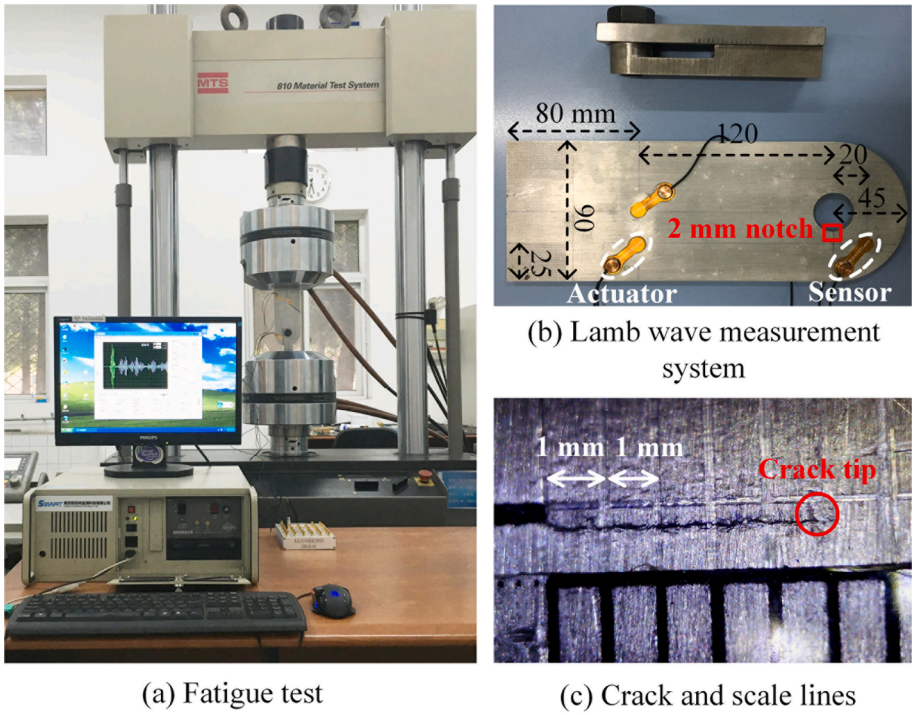

(a) Fatigue test (b) Lamb wave measurement system (c) Crack and scale lines

Fig. 2. Experimental setup.

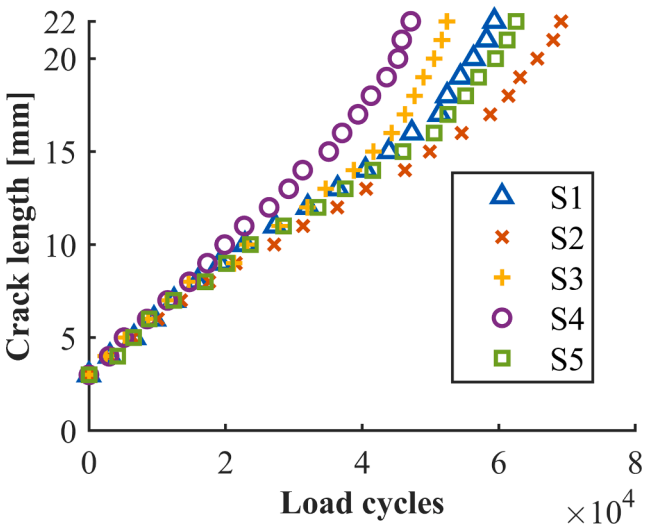

Fig. 3. Crack growths of specimens S1 ~ S5.

10^{-5}s, respectively.

Fig. 4 compares the analytical S_0 and A_0 arrivals with the experimental Lamb waves at three different crack lengths, over a time horizon of 1.2×10^{-4}s. The first wave package is a crosstalk caused by the electromagnetic induction between the circuits of the actuator and the sensor, so the start of the crosstalk (SoC) wave is approximately equivalent to the time at which the excitation from the actuator is applied to the structure [26]. The analytical arrivals of the S_0 and A_0 waves are approximately equal to the summation of the SoC and the S_0 wave ToF, and to that of the SoC and the A_0 ToF, respectively. A good match can be found between the calculated S_0 arrival and the start of the second wave package (i.e., the S_0 mode wave). The increasing crack lengths in general give rise to amplitude reductions of the S_0 waves, and consequently, to the variation of the feature extracted from these waves.

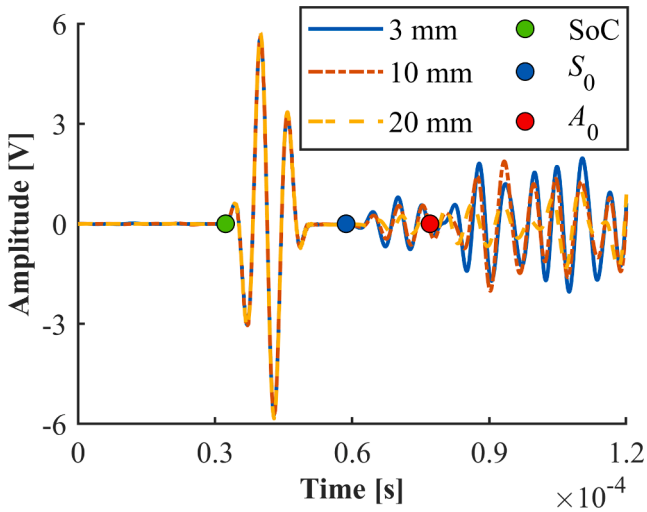

Fig. 4. Lamb wave signals at three crack lengths from specimen S1.Note: 'SoC' means 'start of crosstalk'.

3.3. Numerical Lamb waves

ABAQUS EXPLICIT is adopted to calculate the numerical S_0 Lamb waves of the aluminum lug structure at different crack lengths {3, 5, 8, 10, 12, 15, 18, 20, 22 mm}, as given in Fig. 5. Similarly to the case of Section 3.2, the Young's modulus, density, and Poisson's ratio of the aluminum used in this simulation are 72000 MPa, 2700 kg/m^3, and 0.33, respectively. The structure and crack are modeled as '3D solid' and 'seam', respectively. The left side of the plate and the right side of the hole are fixed. The actuator and sensor are not modeled to save computation time. Two symmetric out-of-plane pressures are applied within the 4 mm radius (size of the actuator) circles on the two sides of the plate, whose amplitudes are shaped according to the 3-cycles Hanning-windowed sine burst, i.e., the same as the excitation used in the experiment. The out-of-plane displacements at the center of the sensor location are taken as the numerical Lamb wave of reference.

The mesh size of the finite element in a Lamb wave simulation, s_e, should satisfy [27]:

$$s_e < \frac{\lambda_{min}}{20} = 1.69\text{mm} \tag{9}$$

where the smallest wavelength λ_{min} is the S_0 mode wavelength 33.87 mm. Thus a mesh size of 1 mm used in this study is sufficiently small. As recommended by the ABAQUS user manual, the time step Δt for a stable simulation is determined according to:

$$\Delta t < \frac{L_{min}}{c_d} = 1.59 \times 10^{-7}\text{s} \tag{10}$$

where the smallest element length L_{min} in the numerical model can be approximated as the mesh size (1 mm) and the longitudinal wave velocity is $c_d = 6.29 \times 10^6 \text{mm/s}$. A step $\Delta t = 5 \times 10^{-9}\text{s}$ is chosen in this study.

Fig. 6 shows the comparison between the initial times of the numerical S_0 mode Lamb waves at the three different crack lengths and the analytical S_0 arrival time. Similarly to the experimental Lamb waves in Fig. 4, the increasing crack lengths seem to give rise to a monotonic amplitude decrease of the numerical Lamb waves before $6 \times 10^{-5}s$.

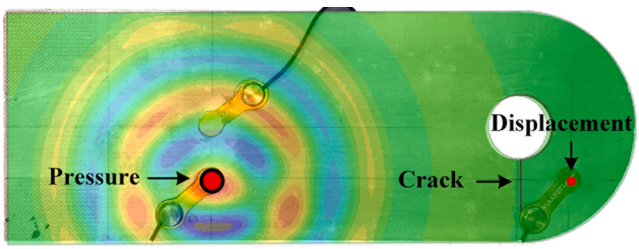

Fig. 5. Numerical setup.

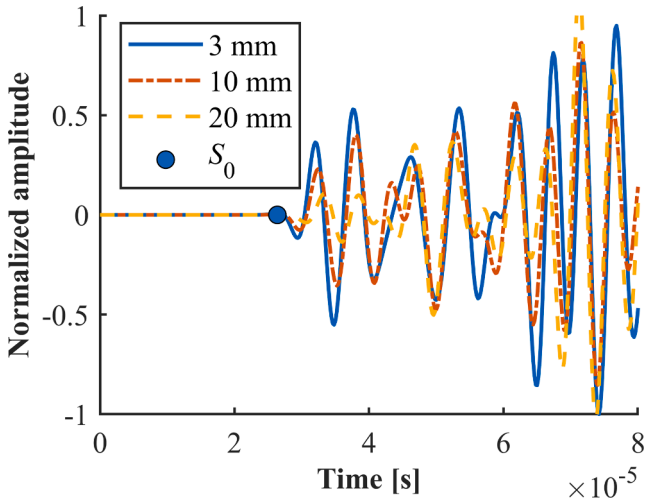

Fig. 6. Numerical S_0 mode Lamb waves and analytical S_0 arrival.

3.4. Comparison of numerical and experimental Lamb waves

Fig. 7 (a) and (b) show the comparisons of the numerical and experimental (specimen S1) Lamb waves at crack length 3 mm and 20 mm, respectively. The crosstalk of the experimental signal is replaced by zero values for simplicity. The numerical S_0 Lamb waves satisfactorily agree with the experimental ones before 4×10^{-5}s, similarly to the comparison of numerical and experimental Lamb waves shown in [16]. The differences showing up after the time 4×10^{-5}s might be due to multiple causes, for example, the differences between the simulated and the actual cracks, and those between the simulated and the actual excitation. An even more obvious difference can be noted after the A_0 arrival, as only the S_0 wave is numerically simulated, whereas both the S_0 and A_0 waves might co-exist in the experimental signals after the A_0 arrival.

3.5. Feature extraction

As already performed in [12,14], only the portion of the Lamb wave signals falling within a properly set time window are chosen for further processing, i.e., for extracting the statistical features for the estimation of the crack length. The window is defined to start at the S_0 arrival and with a width equal to 10^{-5}s.

The signal difference coefficient (SDC) [28] is chosen as the damage-sensitive statistical feature to be extracted from the Lamb waves, given its demonstrated performances in prognostic investigations [12,14]. It is defined as:

$$SDC_l = 1 - \left| \frac{cov(f_l, f_r)}{std(f_l)std(f_r)} \right| \tag{11}$$

where f_r and f_l are the windowed numerical Lamb waves at the initial crack length 3 mm and another generic crack length l mm, respectively, the function '*cov*' is the covariance of the Lamb waves f_r and f_l, and the function '*std*' is the standard deviation of an

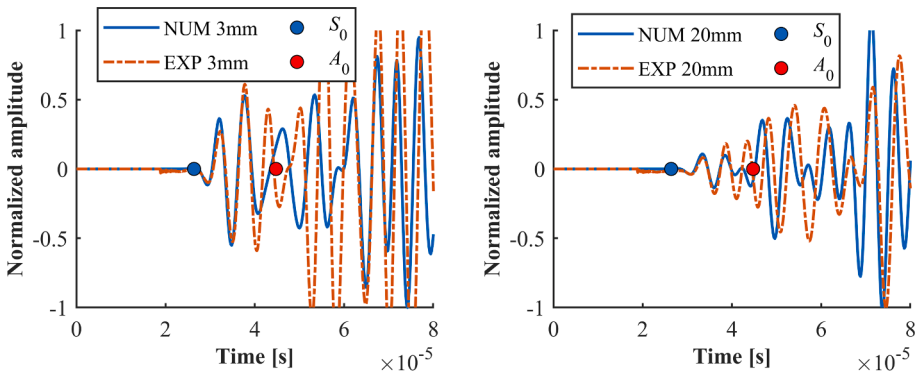

(a) 3 mm crack length. (b) 20 mm crack length.

Fig. 7. Numerical and experimental (specimen S1) Lamb waves at two crack lengths.

individual set of signals. The same procedure is also carried out for the experimental Lamb waves from each of the available specimens.

The SDCs at different crack lengths from the numerical and experimental Lamb waves are given in Fig. 8, where a satisfactory match can be found between the two types of SDCs. The numerical SDCs at the nine crack lengths are used to build a 4-th order polynomial fitting regression function $g(\cdot)$ as:

$$g(x) = -2.3086 \times 10^{-5}x^4 + 1.2296 \times 10^{-3}x^3 - 0.0192x^2 + 0.1258x - 0.2477 \tag{12}$$

The crack growth data and the SDCs from specimen S1 will be processed in Section 4.2 for demonstrating the proposed framework, whereas the validation results using specimen S1 and the other specimens are given in Sections 4.3 and 4.4, respectively.

4. Validation of the proposed framework

Section 4.1 presents the state space model and the PF parameters. Section 4.2 illustrates the creation of a target crack growth and of the SDCs using the data of specimen S1. The feasibility and robustness of the proposed method are discussed in Sections 4.3 and 4.4, respectively.

4.1. State space model and PF parameters

The discretized Paris's law is adopted to describe the crack propagation as:

$$x_k = x_{k-1} + C(\Delta K(x_{k-1}))^m \Delta N \tag{13}$$

where x is the crack length, ΔN is the number of load cycles included in a discretization step, the two parameters C and m are the empirical values governing the crack growth, and ΔK is the stress intensity factor range as determined in the numerical simulations performed by some of the same authors in [14]:

$$\Delta K(x) = 0.0014x^3 + 0.5626x^2 - 13.50x + 497.8 \tag{14}$$

This strategy remains valid for more complex structures, where structural complexity may introduce more uncertainties like the unknown initial crack location or curved crack propagation. In this case, the ΔK may depend on multiple damage states, e.g., crack length, location, and shape, thus its calculation is similar to that in [14], but with more damage states involved.

The generic prognostic model of Eq. (4) can then be specified as:

$$\begin{cases} z_k = \begin{bmatrix} \ln C_k \\ m_k \\ x_k \\ b_k \end{bmatrix} = \begin{bmatrix} \ln C_{k-1} + \omega_{1,k} \\ m_{k-1} + +\omega_{2,k} \\ x_{k-1} + e^{\omega_k} C_k (\Delta K(x_{k-1}))^{m_k} \Delta N \\ b_{k-1} + \omega_{b,k} \end{bmatrix} \\ y_k = g(x_k) + b_k + \nu_k \end{cases} \tag{15}$$

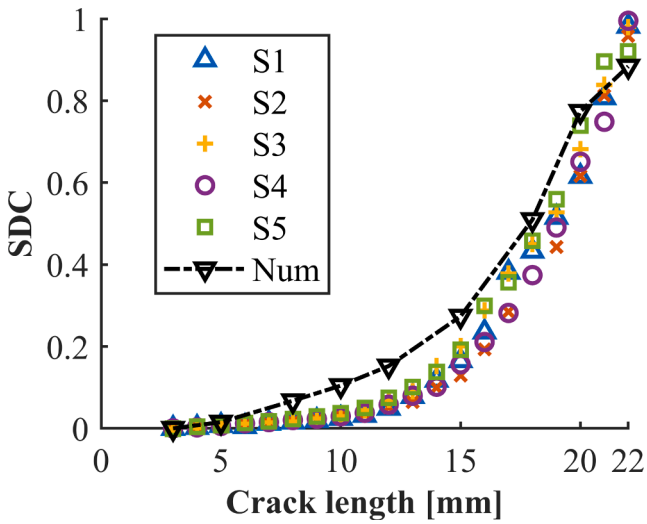

Fig. 8. SDCs at different crack lengths from numerical and experimental studies.

where $\omega \sim \mathcal{N}\left(-\frac{\sigma^2}{2}, \sigma^2\right)$ is the unbiased Gaussian process noise with standard deviation σ [1], ω_1, ω_2 and ω_b are zero-mean Gaussian process noises and the measurement y is the feature SDC. Thus, Eq. (15) turns out to be a nonlinear and non-Gaussian model, due to the non-linearities of the Paris' law and the function $g(\cdot)$, and the non-Gaussian noise e^{ω}, respectively.

As the prognosis accuracy highly depends on the state estimation accuracy, one can resort to kernel smoothing [29] to improve the accuracy of estimating the time-invariant parameters ln C and m,

$$\begin{cases} \ln C_k = \sqrt{1-h^2}\ln C_{k-1} + \left(1-\sqrt{1-h^2}\right)\widehat{\ln C}_{k-1} + \omega_{1,k} \\ m_k = \sqrt{1-h^2}\, m_{k-1} + \left(1-\sqrt{1-h^2}\right)\widehat{m}_{k-1} + \omega_{2,k} \end{cases} \tag{16}$$

where $h \in [0\ \ 1]$ is the smoothing parameter, and $\widehat{\ln C}$ and $\widehat{m}$ are the means of the samples for the parameters ln C and m, respectively.

Table 3 shows the values of the PF parameters used in this study, which are determined from [14] and by a trial-and-error procedure. The effects of these parameters on the PF performances can be found in [30] (number of particles), [11] (standard deviation of the measurement noise - likelihood function), [30] (process noise), and [30] (initial distribution or range).

4.2. Target crack growth and SDCs

The crack lengths and the Lamb waves in the experiment have been collected over a long-time interval (i.e., every several thousand load cycles). In order to simulate a realistic online SHM application scenario, where the Lamb waves can be collected at quite high frequencies (or, equivalently, at shorter load cycle intervals) for feature extraction, and consequently for crack length quantification, the crack growth and the SDCs from specimen S1 are used to create the target crack lengths and the corresponding experimental SDCs according to the following procedure [14]:

(i) Linearly interpolate the crack lengths from specimen S1 to generate a new target with more datapoints, where the crack lengths are available to measurements every 300 load cycles,
(ii) Corrupt the crack lengths by white Gaussian noise with the signal-to-noise ratio (SNR) 50 dB to simulate stochasticity in the crack growth process,
(iii) Use linear interpolation to generate a new SDC at each target crack length, and corrupt these SDCs by white Gaussian noise with SNR 30 dB to simulate the measurement noise.

Fig. 9 (a) shows the resulting target crack growth, where the number of load cycles is $N = 5.91 \times 10^4$. Fig. 9 (b) shows the target experimental SDCs (red dots) and the SDCs predicted by the function $g(\cdot)$ (dashed, grey line). A time-varying bias (blue dots) can be observed between the two types of SDCs, whose effects on the estimation of the crack length and the parameters ln C and m can be alleviated by adding a bias parameter into the state-space model for estimation as shown in Eq. (4) [14].

4.3. Estimation and prediction results

Fig. 10 (a) (b) and (c) present the estimates of the crack length, the parameters ln C and m, and the bias parameter b, respectively. As the bias between the measurements predicted by the function $g(\cdot)$ and the target measurements is satisfactorily identified, both the estimates of the posterior PDF of the crack length remain close to the target values, and the samples (particles) associated with the parameters ln C and m keep reducing their spread during the simulation and accumulate around some final values. On the other hand, the estimated bias turns out to be larger than the true one over the load cycle range between 3×10^4 and 5×10^4, thus giving rise to estimated crack lengths smaller than the target ones in correspondence of the same load cycles (the opposite behavior can be observed after 5×10^4 load cycles).

The predicted future states at 3.6×10^4 load cycles are given in Fig. 11 (a), showing the estimated crack length (blue, dashed line), the crack length prediction trajectory (grey, dotted line), and the RUL posterior PDF (grey histogram). The predicted future states are well distributed around the true crack lengths due to the satisfactory estimation performances for the damage state and its propagation

Table 3
Particle filter parameters.

Number of particles N_p	h in kernel smoothing	Standard deviation in likelihood function
8000	0.1	0.01
Initial distributions for ln C [$\ln\frac{\text{mm}}{\text{cycle}(\text{MPa}\sqrt{\text{mm}})^{-m}}$], m [-]	Initial range for x [mm]	Initial value for b [-]
$\begin{bmatrix}\ln C_0 \\ m_0\end{bmatrix} \sim \mathcal{N}\left(\begin{bmatrix}-57.18 \\ 8.101\end{bmatrix}, \begin{bmatrix}0.9966 & -0.1764 \\ -0.1764 & 0.0346\end{bmatrix}\right)$	$x_0 \in (2.5, 3.5)$	$b_0 = 0$
Distributions of process noises $\{\omega, \omega_1, \omega_2, \omega_b\}$ for x, ln C, m, b		
$\omega \sim \mathcal{N}\left(-\frac{0.01^2}{2}, 0.01^2\right)$	$\omega_1 \sim \mathcal{N}(0, 0.02^2)$	$\omega_2 \sim \mathcal{N}(0, 0.002^2)$ $\omega_b \sim \mathcal{N}(0, 0.01^2)$

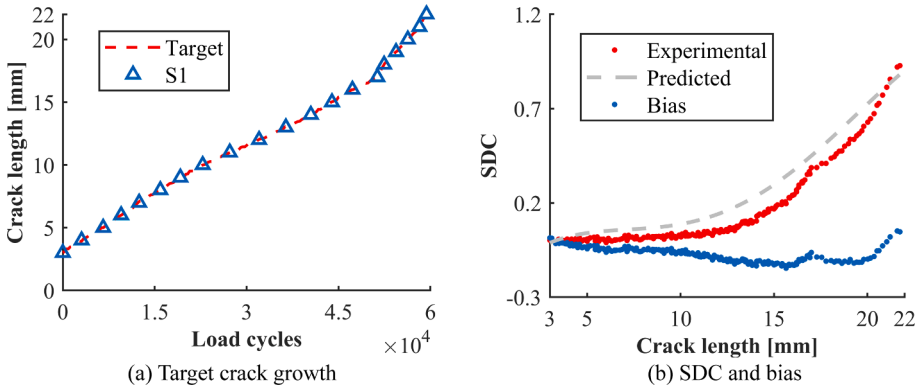

(a) Target crack growth (b) SDC and bias

Fig. 9. Target crack growth, SDCs and bias.

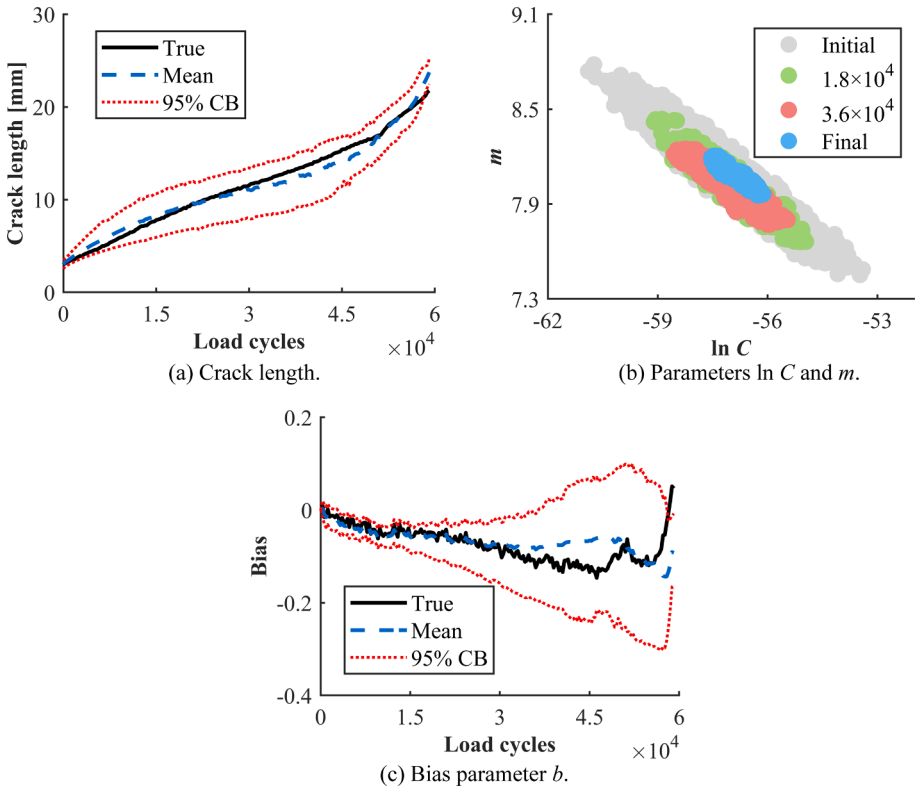

(a) Crack length. (b) Parameters ln C and m.

(c) Bias parameter b.

Fig. 10. Estimation for crack length, parameters ln C and m, and bias from specimen S1. Note: 'CB' means the confidence boundary.

parameters. This is also evident in the RUL prediction of Fig. 11 (b), where the predicted RUL is close to the target RUL, with confidence boundaries shrinking as the load cycles increase.

4.4. Validation with all specimens

The robustness of the proposed framework is now tested with the specimens S2 ~ S5. The procedure for creating the target crack growth and its corresponding SDCs for each specimen is the same as that for specimen S1. The analysis in Section 4.3 is repeated with the same PF parameters. Their crack length estimation and RUL prediction results are presented in Figs. 12 and 13, respectively, which can still yield the conclusions drawn from Fig. 10 (a) and 11(b), demonstrating the feasibility of the proposed method over different specimens. In fact, the method allows taking the uncertainties of both the damage evolution and the measurement models into account by simultaneously and online updating the damage evolution and the bias parameters. On the other hand, the performance of this method for each specimen is noted slightly different, which can hardly be avoided due to several reasons like the stochasticity in crack

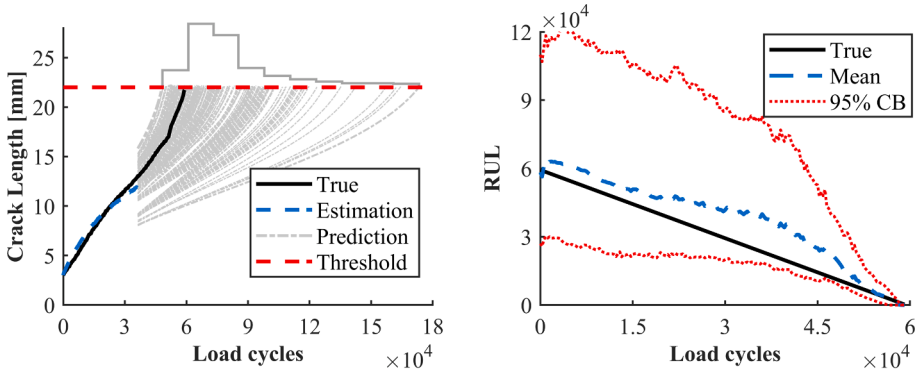

(a) Predicted future state at 3.6×104 load cycles. (b) RUL prediction.

Fig. 11. Prediction for future crack length and RUL from specimen S1.

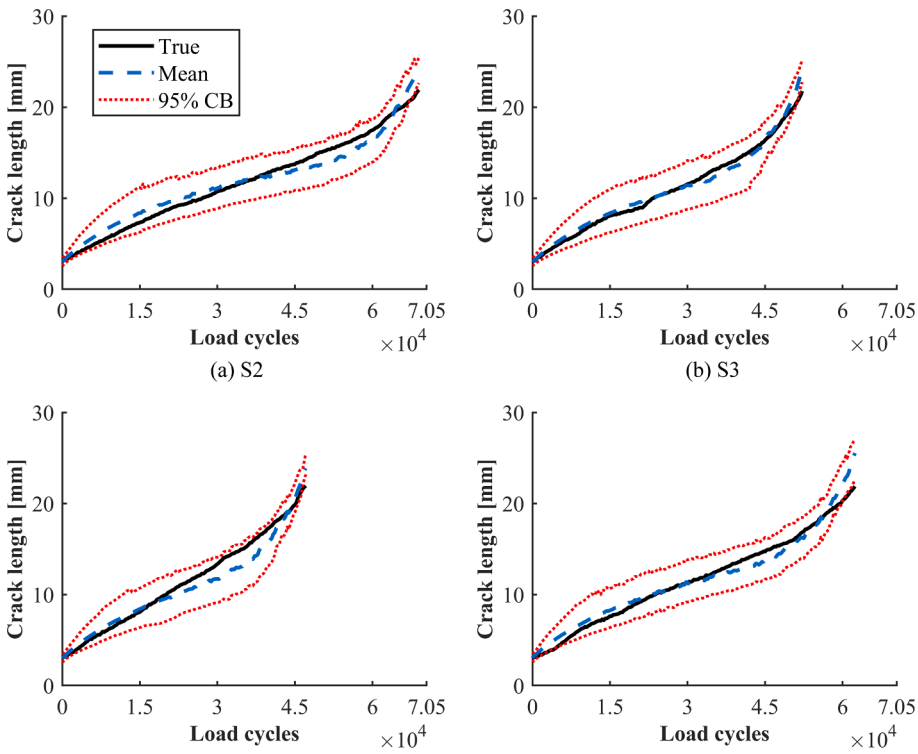

(a) S2 (b) S3 (c) S4 (d) S5

Fig. 12. Crack length estimation results from specimens S2 ∼ S5.

growth and the magnitude of measurement bias.

The root-mean-square error (RMSE) of the crack length estimate, the cumulative relative accuracy (CRA) of the RUL, and the prognostic horizon (PH) of the RUL serve as the three metrics to evaluate the performances of the proposed method, i.e.:

$$RMSE = \sqrt{\frac{1}{T}\sum_{k=1}^{T}\left(\overline{x}_k - x_{true,k}\right)^2} \tag{17}$$

$$CRA = \frac{1}{T-1}\sum_{k=1}^{T-1}\left(1 - \frac{\left|\overline{RUL}_k - RUL_{true,k}\right|}{RUL_{true,k}}\right) \tag{18}$$

where $\overline{x}$ and $\overline{RUL}$ denote the posterior estimates of the crack length and of the RUL, respectively, the subscript '*true*' means the true

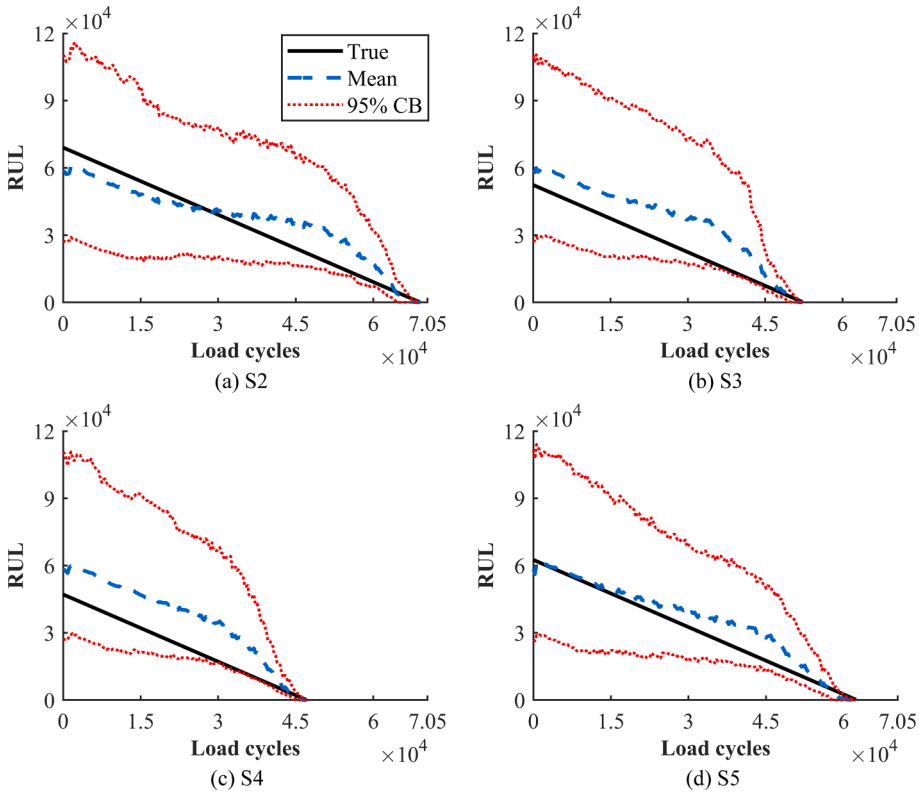

Fig. 13. RUL prediction results from specimens S2 ~ S5.

Table 4
Estimation and prognostic performances from all five specimens.

	S1	S2	S3	S4	S5
RMSE [mm]	0.709	0.911	0.578	1.039	0.866
CRA	0.628	0.678	0.486	0.365	0.727
PH [Load cycles]	9900	8400	7800	6300	11,400

crack length or RUL, T is the number of discrete load cycle steps required by the PF until failure is reached. Lower RMSE and higher CRA represent better estimation and prognosis performances, respectively.

PH is the difference between the current load cycle step and the end-of-prediction utilizing data accumulated up to the current step, provided the prediction meets desired specifications [31]. The end-of-prediction is the end of the test, i.e., the number of load cycles N, and the PH is the number of load cycles when 60% of the RUL distribution first falls within the range 'true RUL $\pm$ 10%N' [1].

Table 4 presents the RMSEs, CRAs, and PHs from all specimens, where the different performances of the proposed method over different specimens are more apparent. In order to further improve its robustness, one may refer to either (i) a PF with an adaptive process noise which enhances the performance in estimating the time-varying parameter [32], or (ii) the usage of multiple damage-sensitive features from Lamb waves to infer the unknown crack length [12].

5. Conclusions

Lamb wave-based damage prognosis methods typically require a data-driven measurement equation to describe the relationship between the damage state and some properly chosen damage-sensitive features of Lamb waves. The formulation of such a model generally requires sufficiently experimental or in-field datasets collected during the run-to-failure process, which, however, may not be available due to some causes like the high costs.

By combining a numerical simulation-aided damage quantification method with a damage prognosis framework accounting for the unavoidable measurement bias, this work has proposed a new particle filter-based damage prognosis framework, which only requires numerically simulated Lamb waves for building the measurement equation. The proposed framework has three advantages, i.e.,

- The costs and efforts in conducting run-to-failure tests and collecting experimental or in-field data for model formulation can be avoided.

- The numerical database developed in this work only consists of nine Lamb wave propagation simulations, each of which requires few computation efforts, i.e., about four minutes on an AMD Ryzen 9 3950X 16-Core Processor.
- The proposed method is robust, as validated by the results from the five specimens, because it takes the uncertainties from both the damage evolution and measurement models into account by online updating their parameters.

In a more realistic application scenario, where tens of or hundreds of sensors are installed for monitoring, the measurement vector in this method can be high-dimensional and most of the measurements far away from the damage can be damage-insensitive, which should possibly lead to an inaccurate and time-consuming prognosis. In order to deal with this problem, one may refer to a proper measurement partitioning strategy by online selecting limited-amount damage-sensitive measurements for estimation.

Declaration of Competing Interest

The authors declare that they have no known competing financial interests or personal relationships that could have appeared to influence the work reported in this paper.

Acknowledgments

This project has received funding from the European Union's Horizon 2020 research and innovation programme under the Marie Skłodowska-Curie grant agreement No. 859957.

References

[1] M. Corbetta, C. Sbarufatti, M. Giglio, M.D. Todd, Optimization of nonlinear, non-Gaussian Bayesian filtering for diagnosis and prognosis of monotonic degradation processes, Mech. Syst. Sig. Process. 104 (2018) 305–322.
[2] M. Corbetta, C. Sbarufatti, M. Giglio, A. Saxena, K. Goebel, A Bayesian framework for fatigue life prediction of composite laminates under co-existing matrix cracks and delamination, Compos. Struct. 187 (2018) 58–70.
[3] M. Chiachío, J. Chiachío, S. Sankararaman, K. Goebel, J. Andrews, A new algorithm for prognostics using Subset Simulation, Reliab. Eng. Syst. Saf. 168 (2017) 189–199.
[4] F. Cadini, C. Sbarufatti, M. Corbetta, F. Cancelliere, M. Giglio, Particle filtering-based adaptive training of neural networks for real-time structural damage diagnosis and prognosis, Struct. Control Health Monit. 26 (12) (2019).
[5] N. Eleftheroglou, T. Loutas, Fatigue damage diagnostics and prognostics of composites utilizing structural health monitoring data and stochastic processes, Struct. Health Monit. 15 (2016) 473–488.
[6] N. Eleftheroglou, D. Zarouchas, T. Loutas, R. Alderliesten, R. Benedictus, Structural health monitoring data fusion for in-situ life prognosis of composite structures, Reliab. Eng. Syst. Saf. 178 (2018) 40–54.
[7] Y. Peng, M. Dong, M.J. Zuo, Current status of machine prognostics in condition-based maintenance: a review, Int. J. Adv. Manuf. Technol. 50 (1-4) (2010) 297–313.
[8] L. Liao, F. Köttig, Review of Hybrid Prognostics Approaches for Remaining Useful Life Prediction of Engineered Systems, and an Application to Battery Life Prediction, IEEE Trans. Reliab. 63 (2014) 191–207.
[9] P. Baraldi, F. Mangili, E. Zio, Investigation of uncertainty treatment capability of model-based and data-driven prognostic methods using simulated data, Reliab. Eng. Syst. Saf. 112 (2013) 94–108.
[10] I. Lopez, N. Sarigul-Klijn, A review of uncertainty in flight vehicle structural damage monitoring, diagnosis and control: Challenges and opportunities, Prog. Aerosp. Sci. 46 (7) (2010) 247–273.
[11] D. Cristiani, C. Sbarufatti, M. Giglio, Damage diagnosis and prognosis in composite double cantilever beam coupons by particle filtering and surrogate modelling, Struct. Health Monit. 1475921720960067 (2020).
[12] J. Chen, S. Yuan, H. Wang, On-line updating Gaussian process measurement model for crack prognosis using the particle filter, Mech. Syst. Sig. Process. 140 (2020), 106646.
[13] J. Chen, S. Yuan, X. Jin, On-line prognosis of fatigue cracking via a regularized particle filter and guided wave monitoring, Mech. Syst. Sig. Process. 131 (2019) 1–17.
[14] T. Li, C. Sbarufatti, F. Cadini, J. Chen, S. Yuan, Particle filter-based hybrid damage prognosis considering measurement bias, Strct. Control Health Monit. 29 (4) (2022) e2914.
[15] T. Stepinski, M. Mańka, A. Martowicz, Interdigital lamb wave transducers for applications in structural health monitoring, NDT E Int. 86 (2017) 199–210.
[16] C. Sbarufatti, G. Manson, K. Worden, A numerically-enhanced machine learning approach to damage diagnosis using a Lamb wave sensing network, J. Sound Vib. 333 (2014) 4499–4525.
[17] J. He, Y. Ran, B. Liu, J. Yang, X. Guan, A fatigue crack size evaluation method based on lamb wave simulation and limited experimental data, Sensors 17 (2017) 2097.
[18] T. Peng, A. Saxena, K. Goebel, Y. Xiang, Y. Liu, Integrated experimental and numerical investigation for fatigue damage diagnosis in composite plates, Struct. Health Monit. 13 (2014) 537–547.
[19] Y. Wu, X. Shen, D. Li, Numerical and experimental research on damage shape recognition of aluminum alloy plate based on Lamb wave, J. Intell. Mater. Syst. Struct. (2021), 1045389X21990885.
[20] C.T. Ng, M. Veidt, A Lamb-wave-based technique for damage detection in composite laminates, Smart Mater. Struct. 18 (2009), 074006.
[21] M.S. Arulampalam, S. Maskell, N. Gordon, T. Clapp, A tutorial on particle filters for online nonlinear/non-Gaussian Bayesian tracking, IEEE Trans. Signal Process. 50 (2002) 174–188.
[22] A. Doucet, S. Godsill, C. Andrieu, On sequential Monte Carlo sampling methods for Bayesian filtering, Stat. Comput. 10 (2000) 197–208.
[23] E. Zio, G. Peloni, Particle filtering prognostic estimation of the remaining useful life of nonlinear components, Reliab. Eng. Syst. Saf. 96 (2011) 403–409.
[24] J. Chen, S. Yuan, L. Qiu, H. Wang, W. Yang, On-line prognosis of fatigue crack propagation based on Gaussian weight-mixture proposal particle filter, Ultrasonics 82 (2018) 134–144.
[25] https://www.dlr.de/zlp/en/desktopdefault.aspx/tabid-14332/24874%7B/_%7Dread-61142/%7B/24874_read-61142/.
[26] L. Qiu, S. Yuan, X. Shi, T. Huang, Design of piezoelectric transducer layer with electromagnetic shielding and high connection reliability, Smart Mater. Struct. 21 (2012), 075032.
[27] F. Moser, L.J. Jacobs, J. Qu, Modeling elastic wave propagation in waveguides with the finite element method, NDT E Int. 32 (1999) 225–234.
[28] X.P. Qing, H.-L. Chan, S.J. Beard, A. Kumar, An Active Diagnostic System for Structural Health Monitoring of Rocket Engines, J. Intell. Mater. Syst. Struct. 17 (2006) 619–628.

[29] J. Liu, M. West, Combined parameter and state estimation in simulation-based filtering, Sequential Monte Carlo methods in practice, in: A. Doucet, N. Freitas, N. Gordon (Eds.), Sequential Monte Carlo Methods in Practice, Springer New York, New York, NY, 2001, pp. 197–223.
[30] E.N. Chatzi, A.W. Smyth, The unscented Kalman filter and particle filter methods for nonlinear structural system identification with non-collocated heterogeneous sensing, Struct. Control Health Monit. 16 (2010) 99–123.
[31] A. Saxena, J. Celaya, E. Balaban, K. Goebel, B. Saha, S. Saha, M. Schwabacher, Metrics for evaluating performance of prognostic techniques, in: International Conference on Prognostics and Health Management, 2008, pp. 1–17.
[32] M. Liu, S. Zang, D. Zhou, Fast leak detection and location of gas pipelines based on an adaptive particle filter, Int. J. Appl. Math. Comput. Sci. 15 (2005) 541–550.

Particle filter-based damage prognosis using online feature fusion and selection

Tianzhi Li[1], Jian Chen[2], Shenfang Yuan[2], Francesco Cadini[1], Claudio Sbarufatti[1, *]

[1]*Dipartimento di Meccanica, Politecnico di Milano, Milan, Italy*

[2]*Research Center of Structural Health Monitoring and Prognosis, State Key Laboratory of Mechanics and Control of Mechanical Structures, Nanjing University of Aeronautics and Astronautics, Nanjing, China*

**claudio.sbarufatti@polimi.it*

Abstract

Damage prognosis generally resorts to damage quantification functions and evolution models to quantify the current damage state and to predict the future states and the remaining useful life (RUL). The former typically consists of a function describing the relationship between the damage state and a statistical feature extracted from the measured signals, thus the prognostic performance will strongly depend on the selection of a proper feature. Given the best feature may vary for different specimens or even at each time instant for the same specimen during damage progression, such selection is a challenging task but has received little investigation so far. In this context, this paper proposes a particle filter-based damage prognosis framework, which involves a scheme for online fusing multiple features and selecting the best one. A prognostic model is considered for each feature, with a multivariate process equation, formulated using both a damage degradation function and a bias parameter, and a measurement equation linking the damage state and that feature considering a data-driven model and the bias. One PF is used to estimate the damage state, its evolution parameters, and the bias for each model. Then, at each step, the feature with the smallest estimated bias is selected as the best feature providing the most likely state vectors and is used to select the most likely samples of the damage state and growth parameters for predicting the RUL and for calculating the prior at the next step. The proposed prognostic framework is demonstrated by an experimental study, where an aluminum lug structure subject to fatigue crack growth is monitored by a Lamb wave measurement system.

Keywords: structural health monitoring, damage prognosis, feature fusion and selection, particle filter, Lamb wave

1. Introduction

Degradation is an inevitable phenomenon in structures, where damage can evolve over time or with the number of load cycles. Eventually, safety may no longer be guaranteed when the damage state reaches a predefined threshold. Regular inspections should be carried out to evaluate functionality but they require high financial expenses and unwanted system shutdowns. One possibility for simultaneously ensuring structural safety and reducing maintenance costs is to schedule maintenance just before the damage state reaches the critical limit. In this context, the structure's remaining useful life (RUL), i.e., the time required by the component or structure to reach its operative limit, is desired to be estimated online by an advanced damage prognosis technique.

Structural degradation can be defined through either (i) a physics-based damage state, e.g. including matrix crack density [1], delamination length [2], delamination shape [3], or stiffness reduction [4, 5] for composites, and crack length [6-9] or shape [10] in metals, or (ii) some sort of data-driven health indicators [11-13] extracted from online measurements like acoustic emission and strain. Provided that degradation can follow a certain pattern under a specific input load condition, the future damage condition can be projected by the current state through a model. Depending on the type of information used for degradation modeling, namely physical knowledge or experimental and in-field data, damage evolution models can be classified either as physics-based [1, 2, 6-10] or data-driven [3, 5, 11, 14]. The former generally falls into the scope of Paris' law or its extensions, where the rate of damage evolution, e.g., strain energy release rate or stress intensity factor, is either analytically calculated [1, 2, 8] or fitted from numerical simulations through a data-driven modeling strategy such as polynomial fitting [6, 7], support vector regression [10], or neural networks [9]. On the other hand, pure data-driven approaches, including polynomial fitting [3], neural networks [5, 14], or Markov models [11], are usually built through sufficient damage data or health indicators measured during the experimental or in-field degradation process.

However, given the uncertainties related to complex structural degradations [15], environmental effects [16] and sensor health conditions [16], a deterministic damage evolution model itself can hardly yield an accurate prognostic result, even in different replica of the same structure or specimen. One possibility is to set some model parameters as unknown variables to be online updated by a state estimation technique, such as particle filter (PF), widely implemented for non-linear and non-Gaussian problems [17, 18]. This, on the other hand, implies a direct or indirect damage quantification scheme. The former implies the direct measure of a damage feature, e.g., measuring the matrix crack density and delamination area through X-ray [1, 19] then extracting some residual strength indicators from the online measured signals [20-22]. The latter

resorts to measurement of a physical feature which must then be correlated to damage features through a measurement equation. Typical examples includes sensor networks based on fiber Bragg grating strain sensors [2, 23], Lamb wave-based monitoring systems [6, 24, 25], or accelerometers [26, 27]. Such measurement equation, linking the damage state with some damage-sensitive features obtained from measurements, can be physical or, in most of the cases, it is fitted by a data-driven technique, e.g., neural network [2, 23], polynomial function [6], leave-one-out method [24] or Gaussian process regression [28]. However, the implementation of this measurement equation poses some challenges.

First, the relationship between the damage state and the observed feature(s) can vary in different replica of the same structure due to the uncertainties mentioned above, inevitably inducing a bias between the observed features and those predicted by the measurement equation, eventually deteriorating the prognostic performance if not properly considered [3, 6]. Few prognostic studies [3, 6, 29] aimed to alleviate the effect of such bias, where one or more bias parameters are included in the measurement equation and are online estimated for error compensation.

Second, one feature is typically used for building the measurement equation in [3, 6, 29]. When more features are embedded into the measurement equation, each one potentially affected by a bias, multiple bias parameters should be included in the state space for identification and error compensation, possibly suffering from the curse of dimensionality, and eventually leading to an inaccurate state and parameter estimation. As a result, the prognostic performance will strictly depend on the selection of a proper feature, which is not a trivial task, especially considering the best feature may vary in different replica of the same structure, or even, at different time instants during damage progression on the same structure or specimen. This naturally calls for an integrated framework to fuse multiple features (feature fusion) and to online select the best ones (feature selection) for identifying the current damage state, which, however, has received little attention in current practices.

Feature fusion and selection have been investigated in some pure data-driven RUL prediction studies [21, 22], where three main steps are typically included, i.e., (i) extracting some statistical features from the measured signals, then (ii) fusing multiple features or selecting the best ones through a proposed metric or criterion for building the health indicator (HI), finally (iii) calculating the RUL through a model describing the relationship between the RUL and the HI. While processing some preliminary features into one more sophisticated (i.e., the HI), no physics-based damage state is considered. On the other hand, feature fusion and selection have also been applied to damage quantification in [30, 31], where, due to the lack of a metric for online feature selection, an offline selection scheme was adopted.

In this context, combining the prognostic model for measurement bias identification proposed by

the authors in [6] with the general idea of feature selection, this paper proposes a novel online feature fusion and selection scheme based on the identification of the measurement bias within a prognostic framework based on a particle filter. A general principle arising from [6] is that, among multiple features observed on the same specimen, the more one feature is associated with the smallest bias (i.e., being the best feature), the best overall prognostic performance it should provide. Stemming from this concept, the method proposed hereafter consists of the following steps. First, a prognostic state space model is considered for each feature, with a multivariate process equation, formulated using both a damage degradation function and a bias parameter, and a measurement equation linking the damage state and that feature considering a data-driven model and the same bias. One PF is used to predict the damage state, the evolution parameters, and the bias, separately for each feature, thus resulting in multiple groups of resampled particles. Then, at each step, the feature with the smallest estimated bias is selected as the best feature providing the best state vector samples, where the relative best samples of the damage state and damage growth parameters are used for predicting the RUL, and the best damage state samples are substituted to all the other less performing features. The proposed prognostic framework is demonstrated by an experimental study, where an aluminum lug structure subject to fatigue crack growth (FCG) is monitored by a Lamb wave measurement system.

The rest of this paper is organized as follows: Section 2 defines the novel prognostic framework. The application setup is shown in Section 3, while the results of the proposed method for the experimental case study are provided in Section 4. Finally, Section 5 concludes this paper.

2. Novel damage prognosis framework

Figure 1 presents the four main steps of the proposed damage prognosis framework, namely, (i) formulate some independent prognostic models, each with one associated observed feature [6, 7], (ii) estimate the damage state, the damage evolution model parameters, and the bias by the PF for each prognostic model, (iii) select the feature with the smallest estimated bias as the best and substitute the damage state samples for each prognostic model by those from the prognostic model with the best associated feature, and (iv) project damage state into the future by the process equation starting from the damage state samples associated with the best feature. Compared to the traditional method [6, 7], where PF is only applied to one prognostic model to provide the samples for predicting the future state and RUL, the main novelty of the proposed method is that a fusion and selection scheme is online implemented to identify the best feature at each step, then adopting its samples for the health state and RUL calculations.

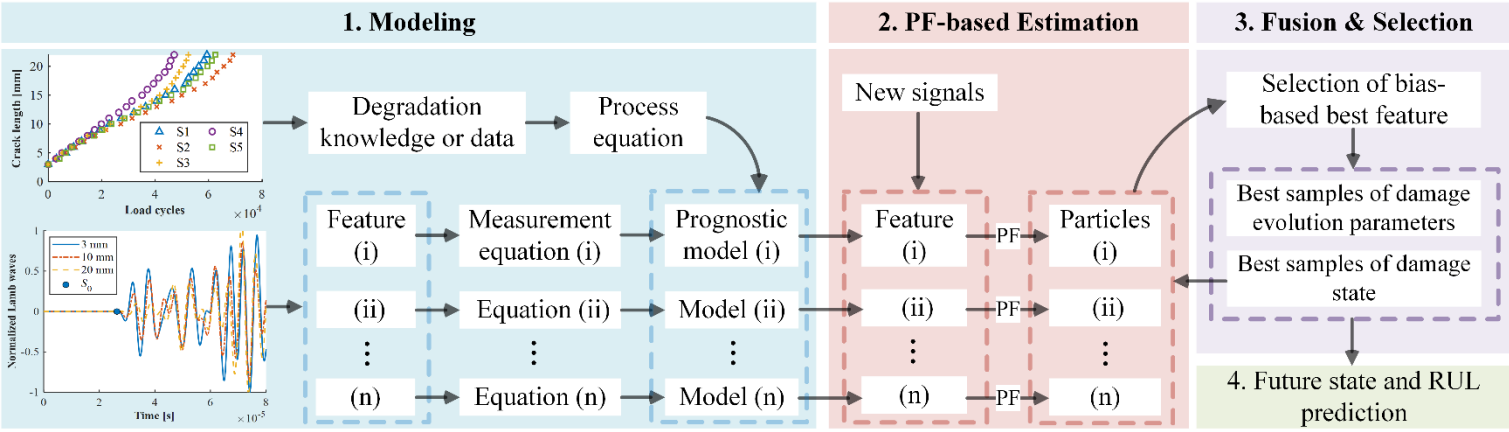

Figure 1 Novel particle filter (PF)-based damage prognosis framework with embedded feature fusion and selection.

2.1 State space modeling

The damage evolution with time or the number of load cycles is usually discretized as

$$x_k = f(x_{k-1}, \boldsymbol{\theta}) \tag{1}$$

where x is the damage state, $f(\cdot)$ is the evolution function that is derived from either physical knowledge or damage data, $\boldsymbol{\theta}$ is a vector of damage evolution parameters, and the subscript k denotes the k-th time step. Then, the parameters $\boldsymbol{\theta}$ are usually treated as some unknown variables in the state vector to be updated [6, 24],

$$\begin{bmatrix} \boldsymbol{\theta}_k \\ x_k \end{bmatrix} = \begin{bmatrix} \boldsymbol{\theta}_{k-1} + \boldsymbol{\omega}_{\theta,k} \\ f(x_{k-1}, \boldsymbol{\theta}_k, \omega_k) \end{bmatrix} \tag{2}$$

where ω_k and $\boldsymbol{\omega}_\theta$ are the process noises for the damage state and model parameters, respectively.

When some indirect online measurement systems like Lamb wave are applied, some sort of statistical feature is usually extracted from the measured signals for damage quantification. With a proper measurement y_l (i.e., the l-th feature extracted from those signals) for inferring the unknown damage state, the measurement equation in a PF-based damage prognosis can be formulated as:

$$y_{l,k} = g_l(x_k) + v_k \tag{3}$$

where $g_l(\cdot)$ is usually a data-driven function describing the relationship between the damage state and the l-th feature, v_k is the measurement noise. Given the unavoidable bias between the observed and predicted (from the function g_l) measurements, the prognostic model based on the l-th feature can be formulated as

[3, 6]:

$$\begin{cases} \boldsymbol{z}_{l,k} = \begin{bmatrix} \boldsymbol{\theta}_k \\ x_k \\ b_{l,k} \end{bmatrix} = \begin{bmatrix} \boldsymbol{\theta}_{k-1} + \boldsymbol{\omega}_{\theta,k} \\ f(x_{k-1}, \boldsymbol{\theta}_k, \omega_k) \\ b_{l,k-1} + \omega_{l,b,k} \end{bmatrix} \\ y_{l,k} = g_l(x_k) + b_{l,k} + v_{l,k} \end{cases} \tag{4}$$

where b is the bias parameter, variable with time, ω_b is its corresponding process noise, and $\boldsymbol{z}_k$ is a newly defined augmented state vector. Note the number of models built in this study is equal to the number (L) of available features $l = 1, \dots, L$.

2.2 Particle filter-based estimation

When a Bayesian approach is applied to the l-th prognostic model, the unknown state vector $\boldsymbol{z}_{l,k}$ can be inferred from the measurement as:

$$p\left(\boldsymbol{z}_{l,k} \middle| \boldsymbol{y}_{l,1:k-1}\right) = \int p(\boldsymbol{z}_{l,k} | \boldsymbol{z}_{l,k-1}) p(\boldsymbol{z}_{l,k-1} | \boldsymbol{y}_{l,1:k-1}) d\boldsymbol{z}_{l,k-1} \tag{5}$$

$$p\left(\boldsymbol{z}_{l,k} \middle| \boldsymbol{y}_{l,1:k}\right) \propto p\left(y_{l,k} \middle| \boldsymbol{z}_{l,k}\right) p\left(\boldsymbol{z}_{l,k} \middle| \boldsymbol{y}_{l,1:k-1}\right) \tag{6}$$

where $\boldsymbol{y}_{l,1:k}$ is the measurement vector collected from time step 1 to k, the symbol $\propto$ indicates proportionality, the transition distribution $p(\boldsymbol{z}_{l,k} | \boldsymbol{z}_{l,k-1})$ and the likelihood function $p\left(y_{l,k} \middle| \boldsymbol{z}_{l,k}\right)$ denote the process and measurement equations, respectively, $p\left(\boldsymbol{z}_{l,k} \middle| \boldsymbol{y}_{l,1:k-1}\right)$ and $p\left(\boldsymbol{z}_{l,k} \middle| \boldsymbol{y}_{l,1:k}\right)$ are the prior and posterior-updated probability distribution function (PDF) of the augmented state vector, respectively.

Eqs. (5) and (6) form the basis of the optimal Bayesian solution, which is, however, difficult to be analytically calculated in a nonlinear and non-Gaussian system like Eq. (4). Therefore, an efficient state estimation algorithm, i.e., the sampling importance resampling (SIR) PF [32], is used in this study. Table 1 lists the pseudo-code of the SIR PF.

Table 1 Sampling importance resampling particle filter

Initialization: draw N_p particles $\{\boldsymbol{z}_{l,0}^i : i = 1,2, \dots, N_p\}$ from the initial distribution $p(\boldsymbol{z}_{l,0})$
For k = 1, 2, …,
Prediction in PF: draw N_p particles $\{\boldsymbol{z}_{l,k}^i : i = 1,2, \dots, N_p\}$ by $\boldsymbol{z}_{l,k}^i \sim p(\boldsymbol{z}_{l,k} \| \boldsymbol{z}_{l,k-1}^i)$
Weight update: calculate the weight w_k^i by $w_k^i \propto p(\boldsymbol{y}_{l,k} \| \boldsymbol{z}_{l,k}^i)$, and assign its normalized form $\widetilde{w}_k^i$ to each particle $\boldsymbol{z}_{l,k}^i$

Resample for $\{\boldsymbol{z}_{l,k}^{i}: i = 1,2,\dots,N_p\}$ using the particle weights $\{\widetilde{w}_k^i: i = 1,2,\dots,N_p\}$

End

2.3 Online fusion and selection

Consider multiple prognostic models based on different features are applied to the same specimen. As a smaller bias between the predicted and observed feature induces a minor effect on the damage state quantification, the feature (or the prognostic model) having the smallest bias at one step is deemed the best at that step. As a consequence, the strategy of maximizing the use of the best features (defined as those associated with the smallest bias) can enhance the damage quantification accuracy and, consequently, contribute to a more robust RUL prediction.

Provided that all prognostic models share a damage state variable, one possibility is to substitute the damage state samples obtained by the prognostic model with the best feature into the others for the one-step-ahead prior calculation. As, in real applications, the direct measurement of damage is not always available, thus impeding the calculation of the true bias, one alternative is to approximate the bias by PF and subsequently use that for selecting the best feature. The online fusion and selection procedure involves the following steps:

(i) calculating the root-mean-square (RMS) value of bias samples for each measurement model in Eq. (4) at the previous step,

(ii) defining the feature with the smallest RMS as the best feature for that step,

(iii) setting the particles from that feature as the best particles, and relative samples of crack length and growth parameters (x and $\boldsymbol{\theta}$) are used for calculating the future state and RUL, and the crack length samples (x) to replace samples associated to the other less performing features.

Note that the $\boldsymbol{\theta}$ -samples from the best feature are not involved in such substitution. We assume the bias only has a direct relationship with the damage state arising from the measurement equation, and not with parameters governing the damage growth process. Table 2 lists the pseudo-code of the above procedure.

Table 2 Proposed feature fusion and selection scheme

Provided with resampled particles at k-th step from each PF

For $l = 1,2,\dots,L$

Select the bias samples $\{b_{l,k}^{i}: i = 1,2,\dots,N_p\}$ from the particles $\{\boldsymbol{z}_{l,k}^{i}: i = 1,2,\dots,N_p\}$

Calculate the root-mean-square (RMS) value of the bias samples

End

Define the feature with the smallest bias RMS value as the best, and its particles as $\{\boldsymbol{z}_{best,k}^{i}: i = 1,2,\dots,N_p\}$

For $l = 1,2,\dots,L$

Replace the samples of damage state within $\{\boldsymbol{z}_{l,k}^{i}: i = 1,2,\dots,N_p\}$ by those within $\{\boldsymbol{z}_{best,k}^{i}: i = 1,2,\dots,N_p\}$

End

2.4 Calculation of future state and RUL

Within a PF-based prognostic framework, the prognostic step enables the prediction of future damage states through the degradation model Eq. (1) and based on the particles filtered by the best feature. The prediction for each particle stops when the future state reaches a pre-defined threshold value of the damage state l_{th}. Then, the RUL is deemed to be equal to the multiplication of the number of prediction steps by the number of load cycles ΔN in one step. The procedure is outlined by the pseudo-code in Table 3.

Table 3 Calculation of future state and RUL at time step k

Initialization: define samples of the damage state and evolution parameters from $\{\boldsymbol{z}_{best,k}^{i}: i = 1,2,\dots,N_p\}$ as $\{x_k^{i,0}: i = 1,2,\dots,N_p\}$ and $\{\boldsymbol{\theta}_{best,k}^{i}: i = 1,2,\dots,N_p\}$, respectively

For $i = 1{:}N_p$

$j = 0$

While $x_k^{i,j} < l_{th}$

Calculate the future state $x_k^{i,j+1}$ by $x_k^{i,j+1} = f(x_k^{i,j}, \boldsymbol{\theta}_{best,k}^{i})$

$j = j + 1$

End

$\mathrm{RUL}_k^{i} = j \times \Delta N$

End

3. Application setup

This section introduces the experimental and numerical application setups. More specifically, the fatigue tests of five aluminum lug structures and the Lamb wave monitoring system are briefly introduced in Section 3.1; Section 3.2 presents the numerical simulations of the Lamb waves at different crack lengths [7]; the Lamb waves from both the experimental and numerical studies are processed to provide four different statistical features for damage quantification in Section 3.3; Section 3.4 presents the formulation of Paris'

law-based process equation and feature-based measurement equation, and the PF hyperparameters applied to each prognostic model; finally Section 3.5 illustrates the target crack growths and their corresponding features using all the experimental specimens.

3.1 Experimental study

Figures 2 (a) and (b) show the fatigue tests of the lug joint aluminum structure and a Lamb wave-based monitoring system [28], respectively. The thickness of the specimen and the diameter of the through hole are 5 mm and 25 mm, respectively. One 2 mm long notch is created at the edge of the hole to initiate the crack growth. The MTS810 electro-hydraulic servo material test system is employed to provide the sinusoidal tensile fatigue load, whose maximum value, load ratio, and frequency are 18 kN, 0.1 and 10 Hz, respectively.

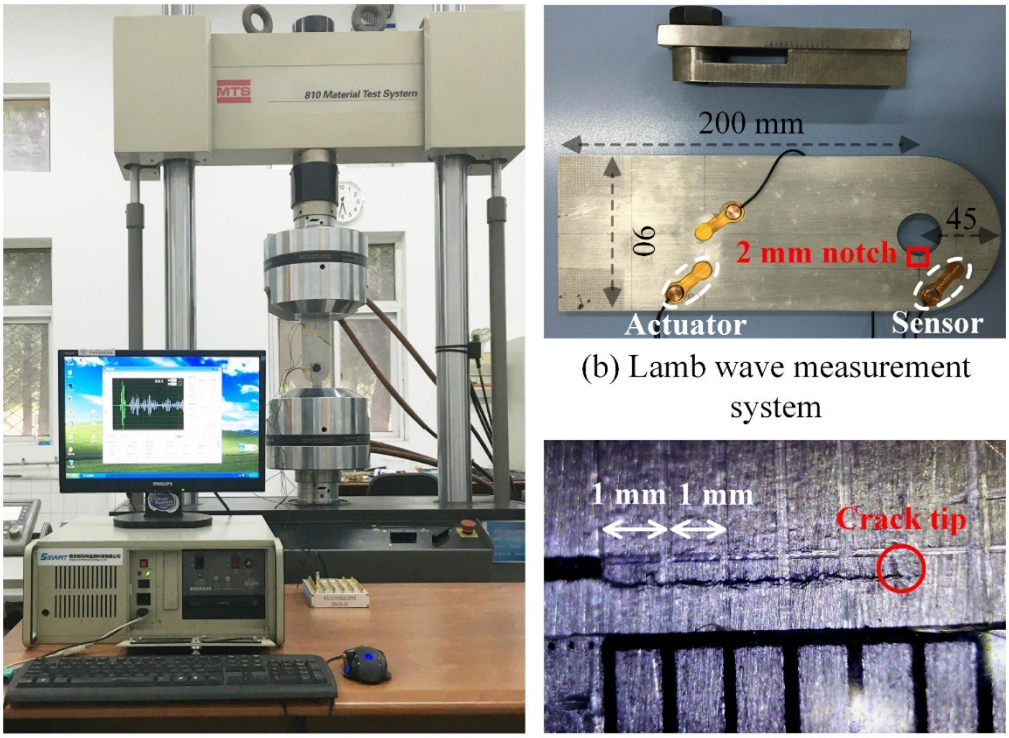

(a) Fatigue test

(b) Lamb wave measurement system

(c) Crack and scale lines

Figure 2 Experimental setup.

Figure 2 (c) presents the crack on the specimen surface observed by a digital microscope. The scale lines are equally spaced by 1 mm. A pre-cracking step is performed at the beginning of the fatigue test until the crack length reaches 3 mm. The fatigue loading is occasionally paused during the test, and 18 kN static tensile load is applied to the structure to open the crack for better visualization. The crack length is considered to increase by 1 mm once the crack tip reaches the next line.

Figure 3 shows the fatigue crack growth trajectories of the five specimens S1 ~ S5. Their differences

are mainly caused by the uncertainties arising from the material property, specimen assembling, external loading condition, etc., which confirms that a deterministic damage evolution model can hardly provide accurate prognostic results. The crack lengths of $3\ \mathrm{mm}$ and $22\ \mathrm{mm}$ are taken as the initial crack and the threshold for RUL calculation, respectively.

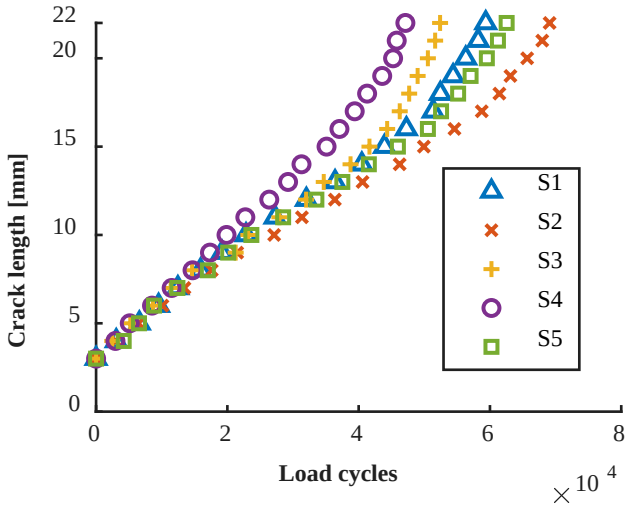

Figure 3 Crack growths of specimens S1 ~ S5.

Figure 2 (b) shows the piezoelectric transducers used as actuator and sensor in this study. At each measured crack length, the actuator provides a 3-cycle Hanning-windowed sine burst with a central frequency of $160\ \mathrm{kHz}$, and the sensor collects the Lamb wave with a sampling frequency of $50\ \mathrm{MHz}$.

Figure 4 compares the experimental Lamb waves at three different crack lengths over a time window of 1.2×10^{-4} s, where the green, blue, and red dots represent the start of crosstalk (SoC), the analytical S_0 and A_0 arrivals, respectively. The first (fictitious) wave packet is a crosstalk arising from the electromagnetic induction between the actuator and sensor circuits, so the start of the crosstalk (SoC) is approximately equivalent to the time at which the excitation from the actuator is applied to the structure [26]. The analytical S_0 arrival is approximated by the summation of the SoC and its wave time-of-flight, and so is the analytical A_0 arrival. The interested reader may refer to [7] for more details. The second wave package is the S_0 mode wave. A good match can be found between the calculated and actual S_0 arrivals. The increasing crack lengths induce amplitude reductions of the S_0 waves, and consequently, the variation of the statistical feature extracted from those signals.

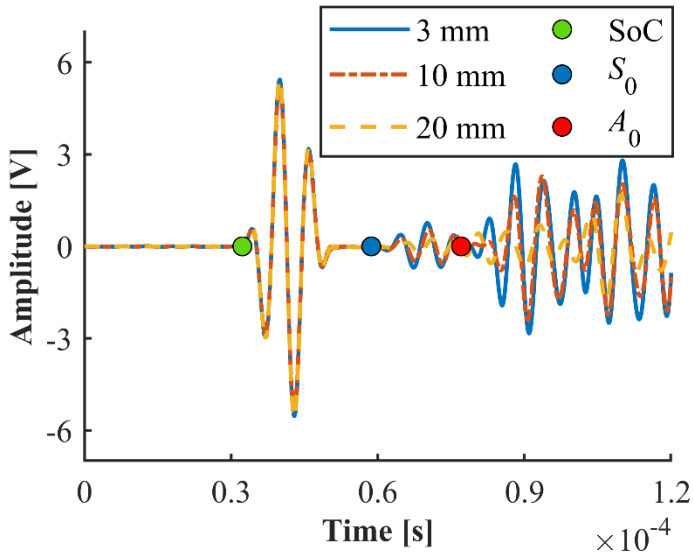

Figure 4 Lamb wave signals at three crack lengths from specimen S5.
Note: 'SoC' means 'start of crosstalk'.

3.2 Numerical study

The numerical simulations of Lamb waves under different crack lengths [7] are introduced here, and they will be processed to provide some statistical features for modeling the measurement equation later. The interested reader may refer to [7] for more details of the simulations. Figure 5 shows the results of an ABAQUS EXPLICIT simulation providing the numerical S_0 Lamb waves of the aluminum lug structure at nine crack lengths, i.e., $\{3, 5, 8, 10, 12, 15, 18, 20, 22\ \text{mm}\}$. Two symmetric out-of-plane pressures are applied within the $4\ \text{mm}$ radius circles (shape of the actuator) on the two sides of the plate, whose amplitudes are the same as the excitation used in the experiment. The out-of-plane displacements at the center of the sensor location are taken as the numerical Lamb wave of reference.

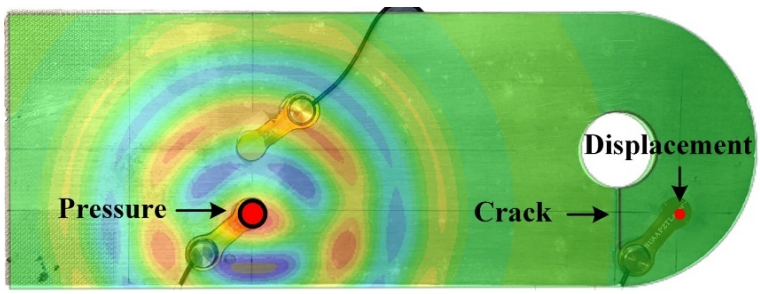

Figure 5 Numerical setup.

Figures 6 (a) and (b) show the comparisons of the numerical and experimental (specimen S5) Lamb waves at crack lengths of $3\ \text{mm}$ and $20\ \text{mm}$, respectively. The crosstalk of the experimental signal is replaced by zero values for simplicity. The numerical S_0 Lamb waves satisfactorily agree with the experimental ones before $4 \times 10^{-5}\ \text{s}$, while the increasing differences after $4 \times 10^{-5}\ \text{s}$ is related to

multiple sources of uncertainty, e.g., the differences between the simulated and the actual cracks, and those between the wave modes of simulated (*S* mode only) and experimental (*S* and *A* modes) signal, as well as diverse boundary reflections.

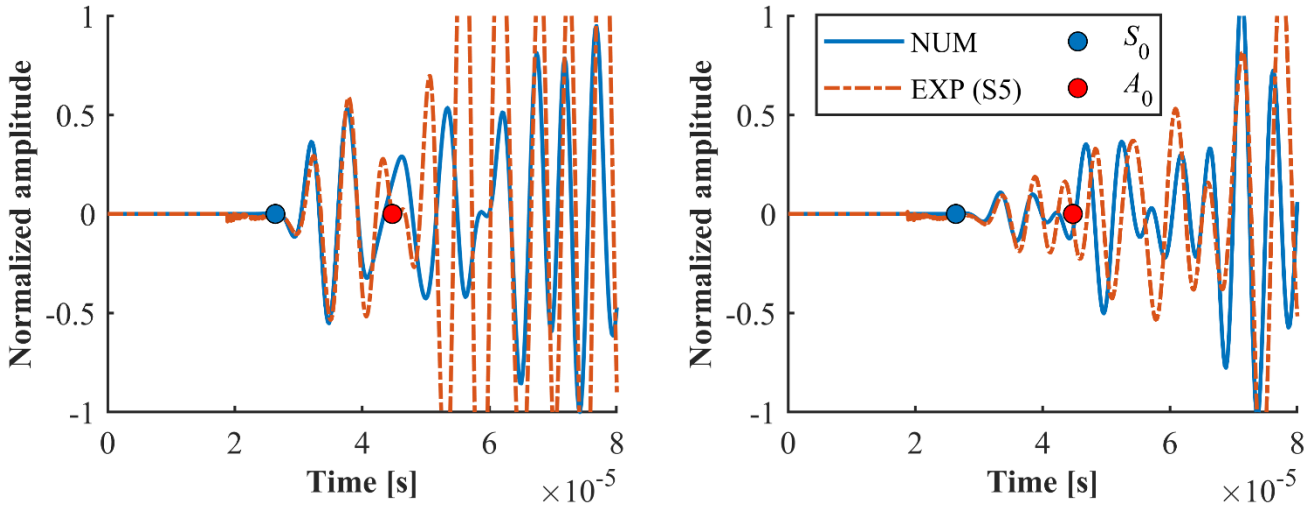

(a) 3 mm crack length (b) 20 mm crack length

Figure 6 Numerical and experimental (specimen S5) Lamb waves at two crack lengths.

3.3 Feature extraction

As already performed in [7], some damage-sensitive statistical features are extracted from the Lamb waves within a certain window, whose start and width are the S_0 arrival and 10^{-5} s, respectively. Table 4 shows the four features used in this study, and their performances for damage prognosis are demonstrated in [7, 22, 28]. Note that f_r and f_d are the windowed Lamb waves at the initial reference crack length of 3 mm and another crack length d, respectively, t means the time instant, the function '*cov*' is the covariance of the Lamb waves f_r and f_d, and the functions '*std*', '*max*', '*rms*' are the standard deviation, peak value, and root-mean-square value of an individual set of signals, respectively.

Table 4 Four damage-sensitive statistical features used in this study.

Signal energy-based feature [33]	$F_{1,d} = 1 - \left\lvert \frac{cov(f_d, f_r)}{std(f_d)std(f_r)} \right\rvert$
Signal energy-based feature [34]	$F_{2,d} = \frac{\int (f_d(t), f_r(t))^2 dt}{\int (f_r(t))^2 dt}$
Peak-based feature	$F_{3,d} = 1 - \frac{max(f_d)}{max(f_r)}$
Root-mean-square (RMS) value-based feature	$F_{4,d} = 1 - \frac{rms(f_d)}{rms(f_r)}$

The above feature extraction is carried out for the numerical and the experimental Lamb waves from

each of the five specimens, as shown in Figure 7. First, the monotonic upward trend between crack length and the features demonstrates that all four features are sensitive to crack growth. The satisfactory match between the numerical and experimental features allows the adoption of the numerical data for modeling the measurement equation, however, as mentioned above, the unavoidable bias (though small) might hamper a satisfactory prognosis. The features from experimental specimens S1 ~ S5 will be processed in Section 3.5 for validating the proposed framework.

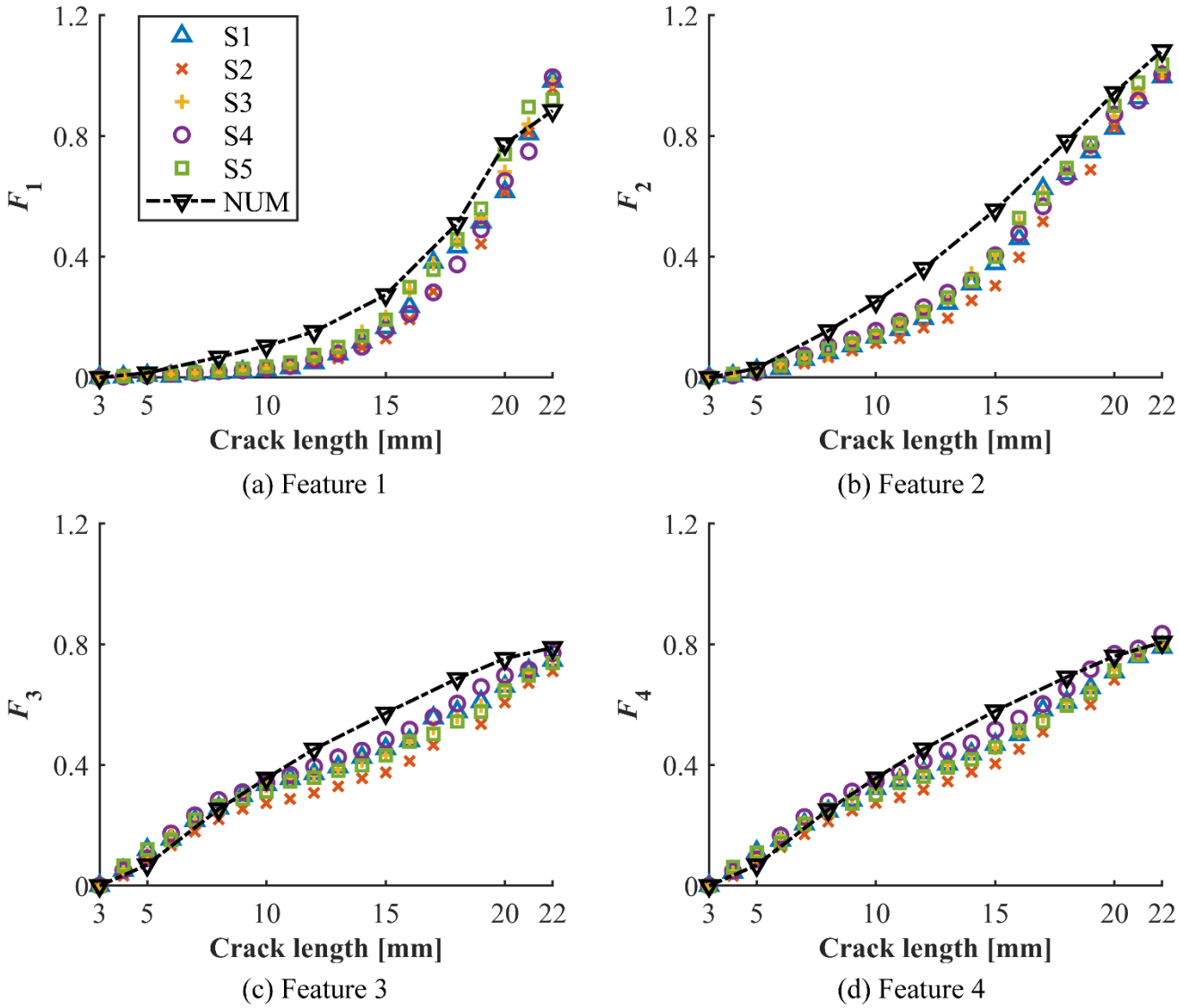

Figure 7 Four damage-sensitive features at different crack lengths from numerical and experimental studies.

3.4 State space modeling and PF parameters

The crack propagation is described by the discrete form of Paris's law,

$$x_k = x_{k-1} + C\left(\Delta K(x_{k-1})\right)^m \Delta N \tag{7}$$

where x is the crack length, ΔN is the number of load cycles included at one time step, C and m are two empirical parameters governing the crack growth, and the relationship between the stress intensity factor range ΔK and crack length is fitted through some numerical data calculated by the same authors in [6]:

$$\Delta K(x) = 0.0014x^3 + 0.5626x^2 - 13.50x + 497.8 \tag{8}$$

Then, the prognostic model for the l-th feature can be written as [6]:

$$\begin{cases} \boldsymbol{z}_{l,k} = \begin{bmatrix} \ln C_k \\ m_k \\ x_k \\ b_{l,k} \end{bmatrix} = \begin{bmatrix} \ln C_{k-1} + \omega_{1,k} \\ m_{k-1} + +\omega_{2,k} \\ x_{k-1} + e^{\omega_k} C_k (\Delta K(x_{k-1}))^{m_k} \Delta N \\ b_{l,k-1} + \omega_{l,b,k} \end{bmatrix} \\ y_{l,k} = g_l(x_k) + b_{l,k} + v_{l,k} \end{cases} \tag{9}$$

where $\omega \sim \mathcal{N}\left(-\frac{\sigma^2}{2}, \sigma^2\right)$ is the unbiased Gaussian process noise with standard deviation σ [17], ω_1, ω_2 and ω_b are zero-mean Gaussian process noises, and the observed signal feature y can be one of those in Table 4.

The function $g_l(\cdot)$ is taken as a 4-th order polynomial fitting regression:

$$g_l(x) = p_1 x^4 + p_2 x^3 + p_3 x^2 + p_4 x + p_5 \tag{10}$$

There can be four independent prognostic models in this study, each sharing the same form of Eq. (9) but having its polynomial coefficients for $g_l(x)$ in Eq. (10). More specifically, coefficients $p_1, \ldots, p_5$ are fitted based on numerically simulated features (as a function of crack length), and they are given in Table 5.

Table 5 Coefficients of the 4-th order polynomial function for each feature fitted from numerical study.

		p_1 [$\times 10^{-5}$]	p_2 [$\times 10^{-3}$]	p_3 [$\times 10^{-2}$]	p_4 [$\times 10^{-1}$]	p_5
Model (i)	Feature 1	-2.309	1.230	-1.922	1.258	-0.248
Model (ii)	Feature 2	-0.181	0.022	0.266	0.008	-0.031
Model (iii)	Feature 3	0.571	-0.336	0.584	0.139	-0.092
Model (iv)	Feature 4	0.742	-0.420	0.727	0.044	-0.074

Notice that Eq. (9) is taken as a nonlinear and non-Gaussian model, due to the non-linearities of

Paris' law and the function $g(\cdot)$, and the non-Gaussian noise e^{ω}, respectively. Kernel smoothing [35] is adopted to improve the accuracy of estimating the time-invariant parameters ln *C* and *m*, through Eq. (11)

$$\begin{cases} \ln C_k = \sqrt{1-h^2}\ln C_{k-1} + \left(1-\sqrt{1-h^2}\right)\widehat{\ln C}_{k-1} + \omega_{1,k} \\ m_k = \sqrt{1-h^2}m_{k-1} + \left(1-\sqrt{1-h^2}\right)\widehat{m}_{k-1} + \omega_{2,k} \end{cases} \tag{11}$$

where the smoothing parameter *h* is a value within a range of $[0 \quad 1]$, and $\widehat{\ln C}$ and $\widehat{m}$ are the means of the samples for the parameters ln*C* and *m*, respectively.

Table 6 shows the values of the PF parameters used in this study, most of which are determined based on the previous experiences of the same authors [6, 7]. The four models above share the same PF parameters. The effects of these parameters on PF performances can be found in literature [2, 36], thus is not discussed hereafter for simplicity.

Table 6 Particle filter parameters.

Number of particles N_p	h in kernel smoothing	Standard deviation in likelihood function	
6000	0.1	0.02	
Initial distributions for $\ln C$ $\left[\ln \frac{\text{mm}}{\text{cycle}(\text{MPa}\sqrt{\text{mm}})^{-m}}\right]$, m [-]		Initial range for x [mm]	Initial value for b [-]
$\begin{bmatrix} \ln C_0 \\ m_0 \end{bmatrix} \sim \mathcal{N}\left(\begin{bmatrix} -57.18 \\ 8.101 \end{bmatrix}, \begin{bmatrix} 0.9966 & -0.1764 \\ -0.1764 & 0.0346 \end{bmatrix}\right)$		$x_0 \sim \mathrm{U}(2.5, 3.5)$	$b_0 = 0$
Distributions of process noises $\{\omega, \omega_1, \omega_2, \omega_b\}$ for x, $\ln C$, m, b			
$\omega \sim \mathcal{N}\left(-\frac{0.01^2}{2}, 0.01^2\right)$	$\omega_1 \sim \mathcal{N}(0, 0.01^2)$	$\omega_2 \sim \mathcal{N}(0, 0.001^2)$	$\omega_b \sim \mathcal{N}(0, 0.005^2)$

3.5 Target crack growth and features

The available experimental crack lengths and the Lamb wave signals have been off-line collected over a long-time interval (i.e., every several thousand load cycles), resulting in few observations and preventing an efficient convergence of the PF, which inevitably demands for a minimum number of observation for an efficient state vector identification. To simulate an online SHM application scenario, where the Lamb waves can be collected at a higher frequency (or, equivalently, at shorter load cycle intervals) for crack length quantification, the crack growth and the features from each of the five experimental specimens are used to create the target crack lengths and the corresponding features through the procedure below [6, 7]:

(i) Linearly interpolate the crack lengths from each specimen to create the target lengths every 300

load cycles, and corrupt the crack lengths by white Gaussian noise with a signal-to-noise ratio (SNR) of $50\ \mathrm{dB}$ to simulate stochasticity in the crack growth process. Notice that, for these crack growth trajectories, we consider that no direct measurement has been applied during the degradation process, which represents the realistic situation in which the crack length can hardly be directly measured.

(ii) For each specimen, use linear interpolation to assign the four features at each created crack length, and corrupt these features by white Gaussian noise with a SNR of $30\ \mathrm{dB}$ to simulate the measurement noise.

Figure 8 shows the target experimental and predicted (by the function $g_l(\cdot)$) feature measurements from specimen S5, confirming that the bias from any feature is time-varying and different. Note that, in this study, the true bias at one step is taken as the smallest absolute value of bias at that step and the feature with the smallest true bias is taken as the target best feature. Table 7 lists the number of time steps each feature results the best in tracking each specimen degradation. Here we remark the best feature for one specimen is not guaranteed to be the most performing for another one, indicating that the traditional method resorting to one feature may result in different prognostic performances for different specimens. Moreover, each of the four features can be the best only at specific steps for the same specimen (and not during the entire degradation process), which proves the need for an integrated framework for online fusing and selecting the best feature.

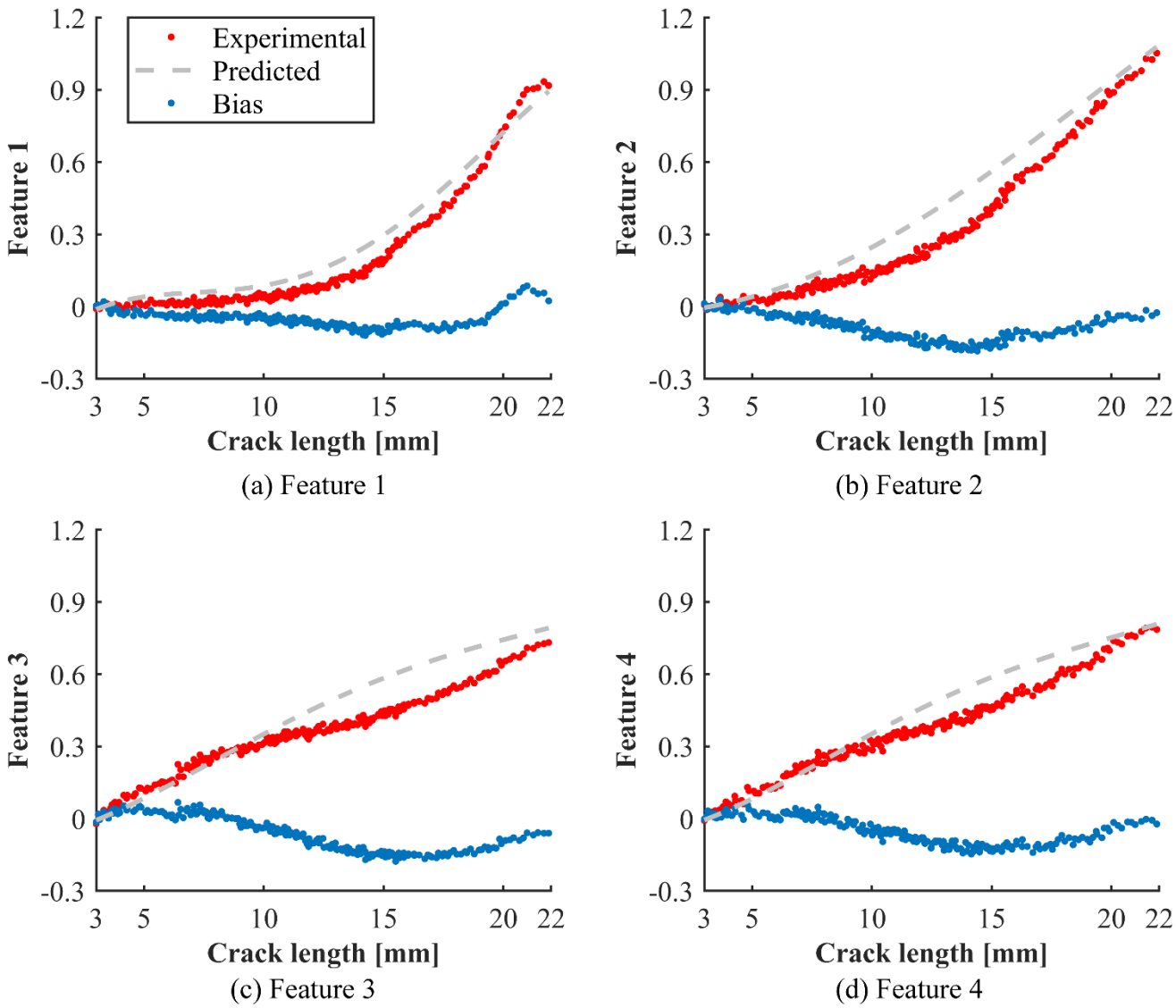

Figure 8 Experimental and predicted features and bias at each crack length from specimen S5.

Table 7 Number of time steps of each feature being the best feature.

	Total number of time steps	Feature 1	Feature 2	Feature 3	Feature 4
Specimen S1	197	19	15	53	110
Specimen S2	230	109	5	47	69
Specimen S3	175	56	10	46	62
Specimen S4	157	6	19	34	98
Specimen S5	208	111	14	34	49

Note: the largest step number of one feature being the best for each specimen is highlighted in grey.

4. Application results

Results by the new approach based on feature fusion are described hereafter, applied to all five experimental specimens and compared to those from the traditional approach based on a single feature. Section 4.1 and

4.2 present the results by the traditional method separately resorting to each of the four features and by the new approach with feature fusion and selection, respectively, focused on specimen S5. The performances of the two methods on all the other specimens are synthetised in Section 4.3.

4.1 Application of traditional method (specimen S5)

For the traditional method, four particle filter (PF) routines are independently applied to the four prognostic models, each based on a single observed feature, thus resulting in four estimates of crack lengths, of parameters ln*C* and *m*, and of the measurement bias, as plotted in Figures A.1, A.2, and A.3, respectively. In general, given the rather satisfactory bias estimation, the posterior PDF of the crack length based on each feature has its means remaining close to the target values, and also the samples corresponding to the parameters ln*C* and *m* are reducing their spread while more observations are processed and finally accumulate around some target values. However, their error, though apparently small, will result in a non-robust prognostic performance, as visible in Figure A.5.

The predicted future states at 3.6×10^4 load cycles are given in Figure A.4, where the predicted future states are distributed around the true crack lengths. This is also apparent in the RUL prediction of Figure A.5, where the mean of RUL is close to the target RUL, and the confidence boundaries shrink with the increasing load cycle steps. The above observations are the same as those in [3, 6]. However, due to the different bias levels among the four features, their overall performances are noted different, especially in RUL assessment, thus calling for a strategy of maximizing the use of best features to enhance the prognostic accuracy.

To explore the relation between the bias level and the diagnostic/prognostic performances, the results are processed by three metrics, i.e., the root-mean-square error (RMSE) of the crack length estimate, Eq. (12), the cumulative relative accuracy (CRA) of the RUL, Eq. (13), and the prognostic horizon (PH), i.e.,

$$RMSE = \sqrt{\frac{1}{T}\sum_{k=1}^{T}\left(\bar{x}_k - x_{true,k}\right)^2} \tag{12}$$

$$CRA = \frac{1}{T-1}\sum_{k=1}^{T-1}\left(1 - \frac{\left|\overline{RUL}_k - RUL_{true,k}\right|}{RUL_{true,k}}\right) \tag{13}$$

where $\bar{x}$ and $\overline{RUL}$ denote the posterior estimates of the crack length and of the RUL, respectively, the subscript '$true$' means the true crack length or RUL, and T is the number of discrete load cycle steps required by the PF until failure is reached.

PH is defined as the difference between the load cycle step at which the prediction meets desired

criteria [37] and the end-of-life. The end-of-life is considered as the end of the test, i.e., the number of load cycles N, and the PH is the distance between the number of load cycles when 60% of the RUL distribution falls within a range of 'true RUL $\pm$ 10%N' [17] and the end-of-life. Lower RMSE, higher CRA, and larger PH indicate better performances.

Table 8 presents the RMSEs, CRAs, and PHs from all specimens, where, despite the use of online estimation for compensating the measurement bias, the four features still yield different performances for the same specimen. In general, the feature being the best for the largest number of steps (i.e., the one having the smallest true bias) can provide the best prognostic performance. Any of the four features can be the best at specific time steps, justifying the effort in developing a scheme to maximise the adoption of the best features.

Table 8 Estimation and prognostic performances using one feature (traditional method) for specimen S5.

		Traditional method using one feature			
Selected feature		1	2	3	4
Performance metric	RMSE [mm]	0.863	1.289	0.906	1.091
	PH [Load cycles]	13800	10200	4800	6000
	CRA	0.631	0.413	0.644	0.602
Number of steps of each feature being the best / Number of total steps		111/208	14/208	34/208	49/208

Note: (i) the largest step number of one feature being the best feature is highlighted in grey; (ii) the smallest RMSE, largest PH, or highest CRA means the 'best' performance, and they are highlighted in green.

4.2 Application of feature fusion and selection (specimen S5)

The newly proposed PF scheme combines the four prognostic models, each with a different observed feature. At each step, the best feature is defined as the one with the smallest estimated bias, and then the PF routine applies the best samples of crack length and its growth parameters for RUL prediction, and those of crack length for the one-step-ahead prediction by each prognostic model. Results are provided in Figures 9 and 10 and Table 9. A separate PF routine is also considered for reference in Table 9, where the best feature is selected according to the true bias (not available in a real application but useful herein to assess the algorithm performance), instead of the predicted bias approximated by the PF.

Figure 9 shows the bias estimates based on the fused features and the best estimates of crack length and its growth parameters, while Figure 10 presents the relative future states and RUL predictions. The conclusions about the mean values are similar to those arising from the figures in Appendix A.1, thus not

repeated here. On the other hand, given that each feature can be the best one at specific time steps, the best samples of crack length have been selected among those of different features. As the range of those samples that have gone through four features should be smaller than that for one feature, the proposed method naturally brings to the narrower CBs of crack length and, consequently, RUL and bias, compared with those from the traditional method.

Table 9 compares the performances of traditional and new methods. By adopting the true bias to select the best feature at each time step (note that this can hardly happen in reality and is just used as a reference for comparison), the new method always behaves better than the traditional one, confirming that the use of the bias-based best feature can improve the prognostic performance. There are still some estimation and prognostic errors because the true bias is not taken as a known constant in the state space model. When the estimated bias is used to define the best feature, a selection accuracy of 54.8% (114/208) is obtained, i.e., the proposed feature selection criterion is capable of finding the target best feature at 114 out of 208 time steps. However, the RMSE, PH, and CRA of the proposed method are still more accurate than those of the traditional method using any of the four features.

One may be confused that Feature 1 has the most steps being the target best feature (111/208), and the performance of the traditional method resorting to that feature is much less accurate than that of the new method. A sudden bias variation from one feature like that of Feature 1 after 6×10^4 load cycles can hardly be accurately estimated, thus deteriorating the damage quantification performance, as shown in Figure A.3. On the other hand, the new method always relies on different features providing the crack length samples for prior calculation at different steps, thus being less sensitive to such variation.

Table 9 Estimation and prognostic performances by adopting one feature (traditional method) and by combining multiple features (new method) for specimen S5.

		Traditional method using one feature				New method using four features	
Selected feature		1	2	3	4	Use **true** bias to define best feature	Use **estimated** bias to define best feature
Performance metric	RMSE [mm]	0.863	1.289	0.906	1.091	0.604	0.727
	PH [Load cycles]	13800	10200	4800	6000	36300	45900
	CRA	0.631	0.413	0.644	0.602	0.837	0.835
Number of steps of each feature being the best / Number of total steps		111/208	14/208	34/208	49/208	-	-
Accuracy of using estimated bias to find the target best feature		-				-	114/208 (54.8%)

Note: (i) the largest step number of one feature being the best feature is highlighted in grey; (ii) the smallest RMSE, largest PH,

or highest CRA means the 'best' performance, and they are highlighted in green; and (iii) the result from new method is highlighted in blue if it is more accurate than that from the traditional method. Same below.

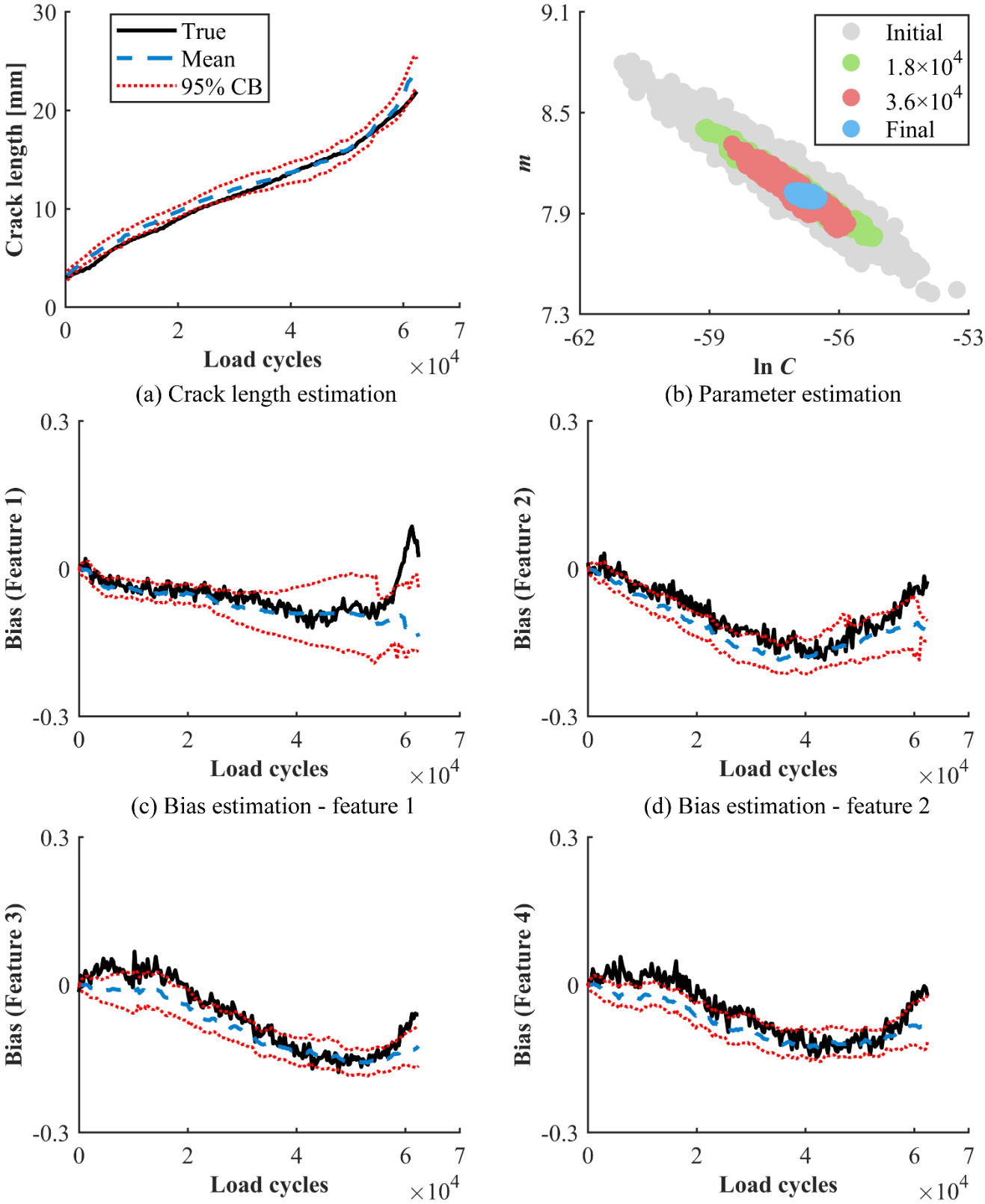

(a) Crack length estimation (b) Parameter estimation

(c) Bias estimation - feature 1 (d) Bias estimation - feature 2

(e) Bias estimation - feature 3 (f) Bias estimation - feature 4

Figure 9 Estimation results using new method from specimen S5.

Note: (i) Figures (a), (c), (d), (e) and (f) share the same legend, (ii) 'CB' means the confidence boundary; (iii) 'Initial', '1.8×10^4', '3.6×10^4', and 'Final' represent the samples of the three parameters at 0, 1.8×10^4, 3.6×10^4, and last load cycles, respectively.

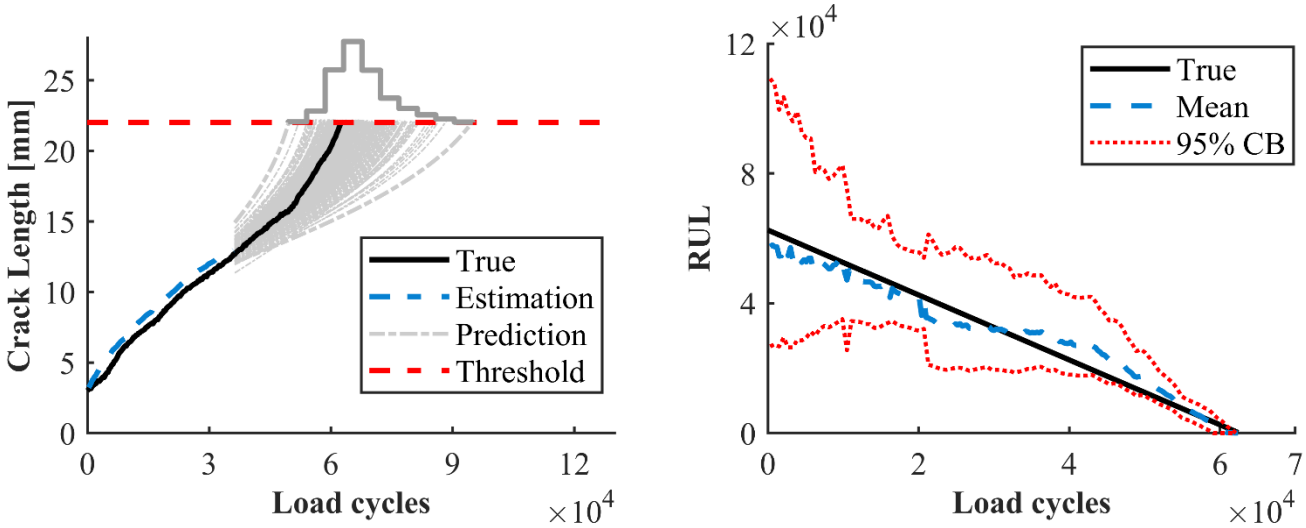

(a) Future state prediction (b) RUL prediction

Figure 10 Future state prediction at 3.6×10^4 load cycles and RUL prediction using the new method from specimen S5.

4.3 Results from all the other specimens

The robustness of the proposed framework is tested with the specimens S1 ~ S4. The analyses in Sections 4.1 and 4.2 are repeated with the same PF parameters given in Section 3.4. The crack length estimation and RUL prediction results using the new method are presented in Figures 11 and 12, respectively, which lead to the same conclusions drawn from Figures 9 and 10 relatively to Specimen S5, demonstrating the robustness of the proposed method over different specimens.

Tables 10 ~ 13 show the damage quantification and RUL prediction performances for specimens S1 ~ S4, respectively. Similar conclusions from Sections 4.1 and 4.2 can be drawn here. One exception is for specimen S4, where the new method has the best crack length estimation but less satisfactory RUL prediction, possibly because of the unsatisfactory estimation of the parameters ln C and m, which calls for some sort of strategy for fast and robust parameter estimation and also a better initialization of those parameters.

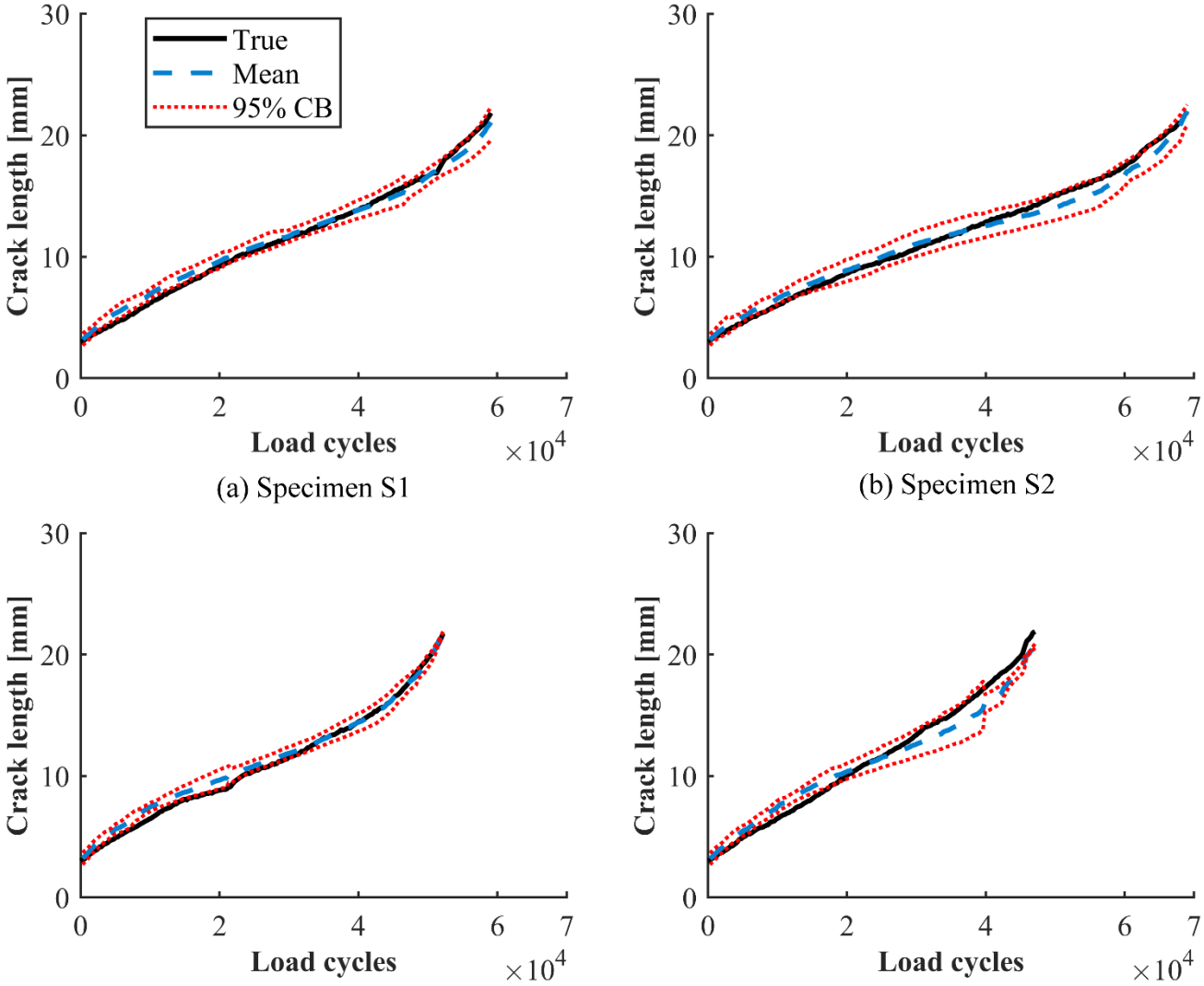

(a) Specimen S1 (b) Specimen S2

(c) Specimen S3 (d) Specimen S4

Figure 11 Crack length estimations from the new method for specimens S1 ~ S4.

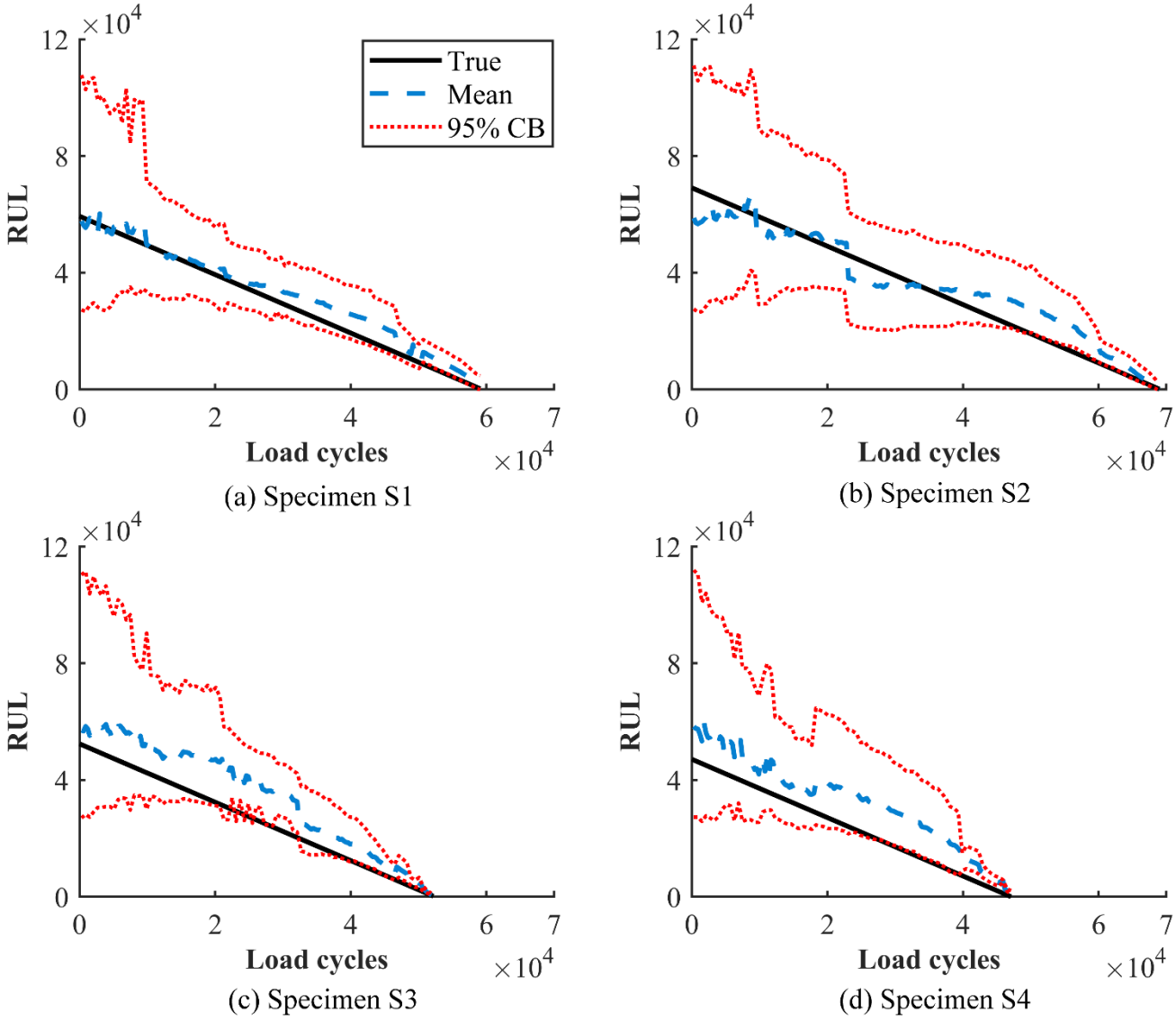

Figure 12 RUL predictions from the new method for specimens S1 ~ S4.

Table 9 Estimation and prognostic performances by adopting one feature (traditional method) and by combining multiple features (new method) for specimen S1.

		Traditional method using one feature				New method using four features	
Which feature to be used		1	2	3	4	Use **true** bias to define best feature	Use **estimated** bias to define best feature
Performance metric	RMSE [mm]	0.903	1.582	1.011	0.890	0.276	0.505
	PH [Load cycles]	9900	8400	3900	4800	33000	41400
	CRA	0.556	0.112	0.479	0.594	0.798	0.747
Number of steps of each feature being the best one / Number of total steps		19/197	15/197	53/197	110/197	-	-
Accuracy of using estimated bias to find the target best feature		-				-	110/197 (55.8%)

Note: (i) the largest step number of one feature being the best feature is highlighted in grey; (ii) the smallest RMSE, largest PH, or highest CRA means the 'best' performance, and they are highlighted in green; and (iii) the result from new method is highlighted in blue if it is more accurate than that from the traditional method. Same below.

Table 11 Estimation and prognostic performances by adopting one feature (traditional method) and by combining multiple features (new method) for specimen S2.

		Traditional method using one feature				New method using four features	
Which feature to be used		1	2	3	4	Use **true** bias to define best feature	Use **estimated** bias to define best feature
Performance metric	RMSE [mm]	0.962	1.744	1.401	1.773	0.853	0.568
	PH [Load cycles]	7500	10500	1800	4800	44700	35700
	CRA	0.606	0.206	0.275	0.289	0.802	0.752
Number of steps of each feature being the best one / Number of total steps		109/230	5/230	47/230	69/230	-	-
Accuracy of using estimated bias to find the target best feature		-				-	176/230 (76.5%)

Table 12 Estimation and prognostic performances by adopting one feature (traditional method) and by combining multiple features (new method) for specimen S3.

		Traditional method using one feature				New method using four features	
Which feature to be used		1	2	3	4	Use **true** bias to define best feature	Use **estimated** bias to define best feature
Performance metric	RMSE [mm]	0.597	1.466	1.204	0.973	0.523	0.514
	PH [Load cycles]	6600	600	1200	2100	29400	9300
	CRA	0.267	-0.301	0.043	0.282	0.782	0.605
Number of steps of each feature being the best one / Number of total steps		56/174	10/174	46/174	62/174	-	-
Accuracy of using estimated bias to find the target best feature		-				-	104/174 (59.8%)

Table 13 Estimation and prognostic performances by adopting one feature (traditional method) and by combining multiple features (new method) for specimen S4.

		Traditional method using one feature				New method using four features	
Which feature to be used		1	2	3	4	Use **true** bias to define best feature	Use **estimated** bias to define best feature
Performance metric	RMSE [mm]	1.298	1.500	1.349	1.107	0.888	0.934
	PH [Load cycles]	6300	6000	300	3900	4500	4500
	CRA	0.192	0.021	0.054	0.434	0.497	0.361
Number of steps of each feature being the best one / Number of total steps		6/157	19/157	34/157	98/157	-	-
Accuracy of using estimated bias to		-				-	75/157 (47.8%)

find the target best feature		

5. Conclusions

Damage prognosis methods typically require a data-driven measurement equation to describe the relationship between the damage state and some properly chosen damage-sensitive statistical features. As the best feature can vary for different specimens, or even, at different time steps for the same specimen, the selection of such a feature can hardly be a trivial task but has received little attention in current practices. By combining a novel online feature fusion and selection scheme with multiple prognostic models considering measurement bias, this work has proposed a new particle filter-based damage prognosis framework, where, at each step, the feature with the smallest estimated bias is taken as the best feature providing the best estimates at that step.

The results of the new method have been compared with the traditional approach, where the prognostic model resorting to one feature has been processed through one PF for damage quantification and RUL prediction. The traditional method has shown performance dependance from the feature choice. The smaller bias one feature has, the better performance it can provide, as a smaller bias can be more accurately estimated, having less effect on the estimation of the crack length. Any feature can be the best feature at specific steps, and the proposed method maximizes the use of the best features, thus yielding more accurate estimation and prognostic performances.

To move towards a more practical and robust application, one may consider three potential paths, from the perspectives of degradation modeling, sensor fusion, and feature selection.

- This method only relies on Paris's law for degradation modeling. The fusion of multiple degradation models, like those arising from physical knowledge and data-driven approaches, deserves more investigation.
- This method only resorts to the bias parameter for selecting the best feature at each step. The performance of PF-based estimation can be evaluated by other coefficients like the *effective sample size*, which could be also exploited for selecting the best feature. Furthermore, rather than always resorting to the estimates from the best feature, different groups of estimates can be weighted by the above coefficients and then applied to prior calculation, improving the particle diversity and possibly yielding a more robust prognostic performance.
- This method is only validated in a case study where features can only be extracted from Lamb wave signals, specifically by the same piezoelectrical transducer. Given that multiple transducers and different types of sensors, like strain gauges and accelerometers, are often

installed for monitoring, the fusion of those sensor signals remains a challenge.

Appendix A.1

The damage estimation and prognostic results for the traditional method (by using each of the four features separately) applied to specimen S5 are shown in Figures A.1 ~ A.5, specifically for crack length estimation, crack growth parameter estimation (ln*C* and *m*), bias estimation, future state prediction and the RUL prediction, respectively.

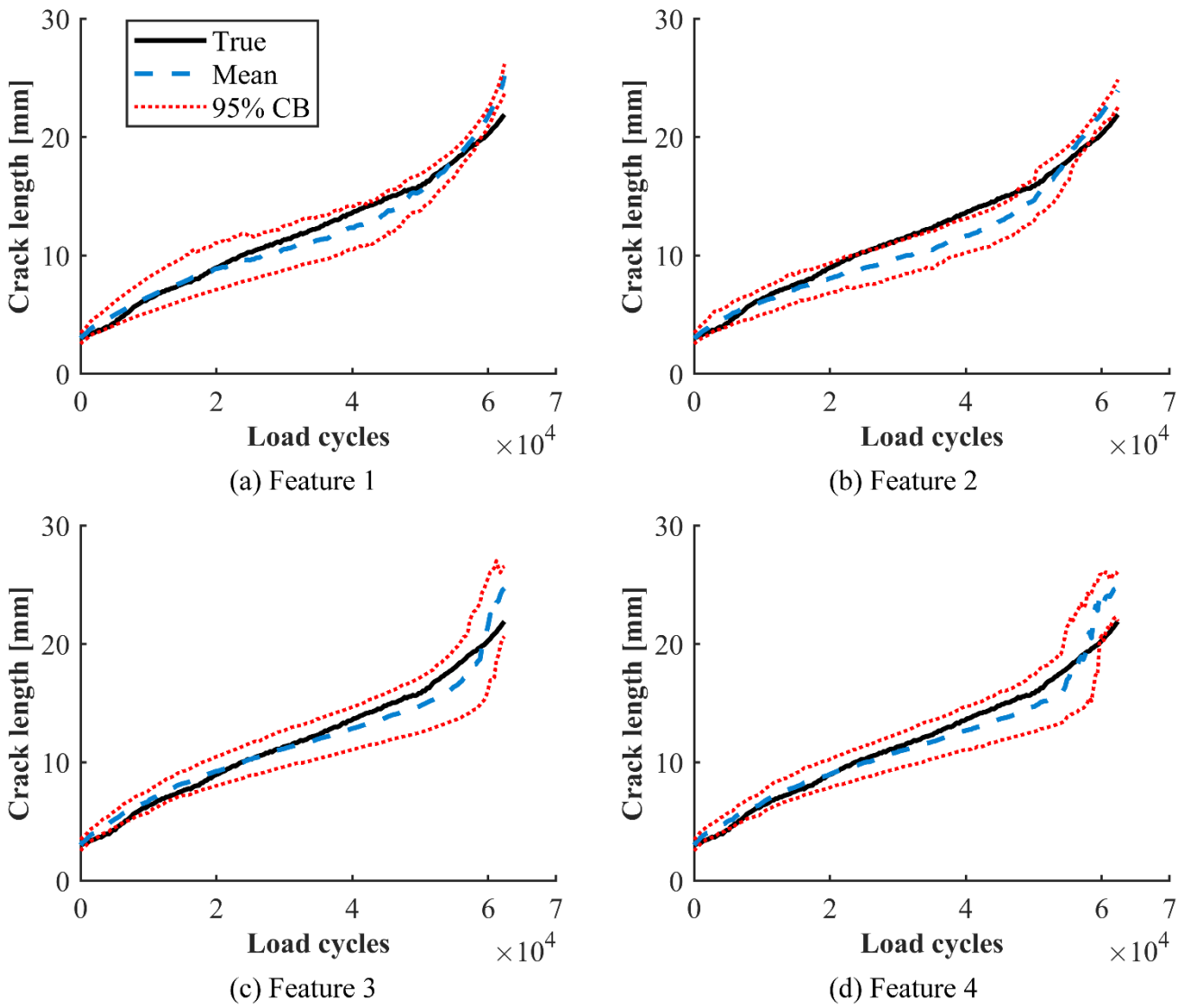

Figure A.1 Crack length estimation using traditional method resorting to one feature for specimen S5. Note: 'CB' means the confidence boundary.

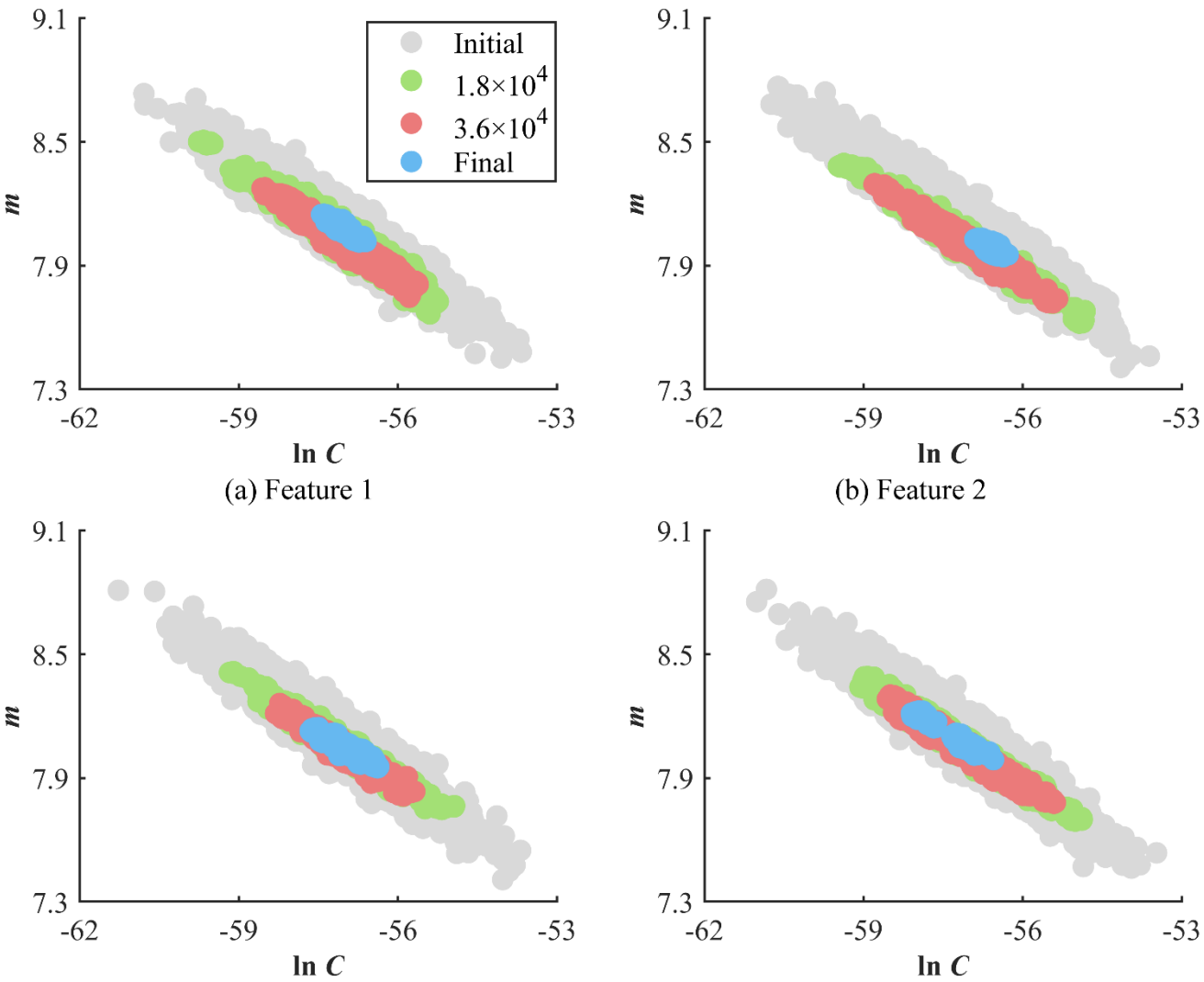

(a) Feature 1 (b) Feature 2

(c) Feature 3 (d) Feature 4

Figure A.2 Parameter estimation using traditional method resorting to one feature for specimen S5. Note that 'Initial', '1.8×10^4', '3.6×10^4', and 'Final' represent the samples of the three parameters at 0, 1.8×10^4, 3.6×10^4, and last load cycles, respectively.

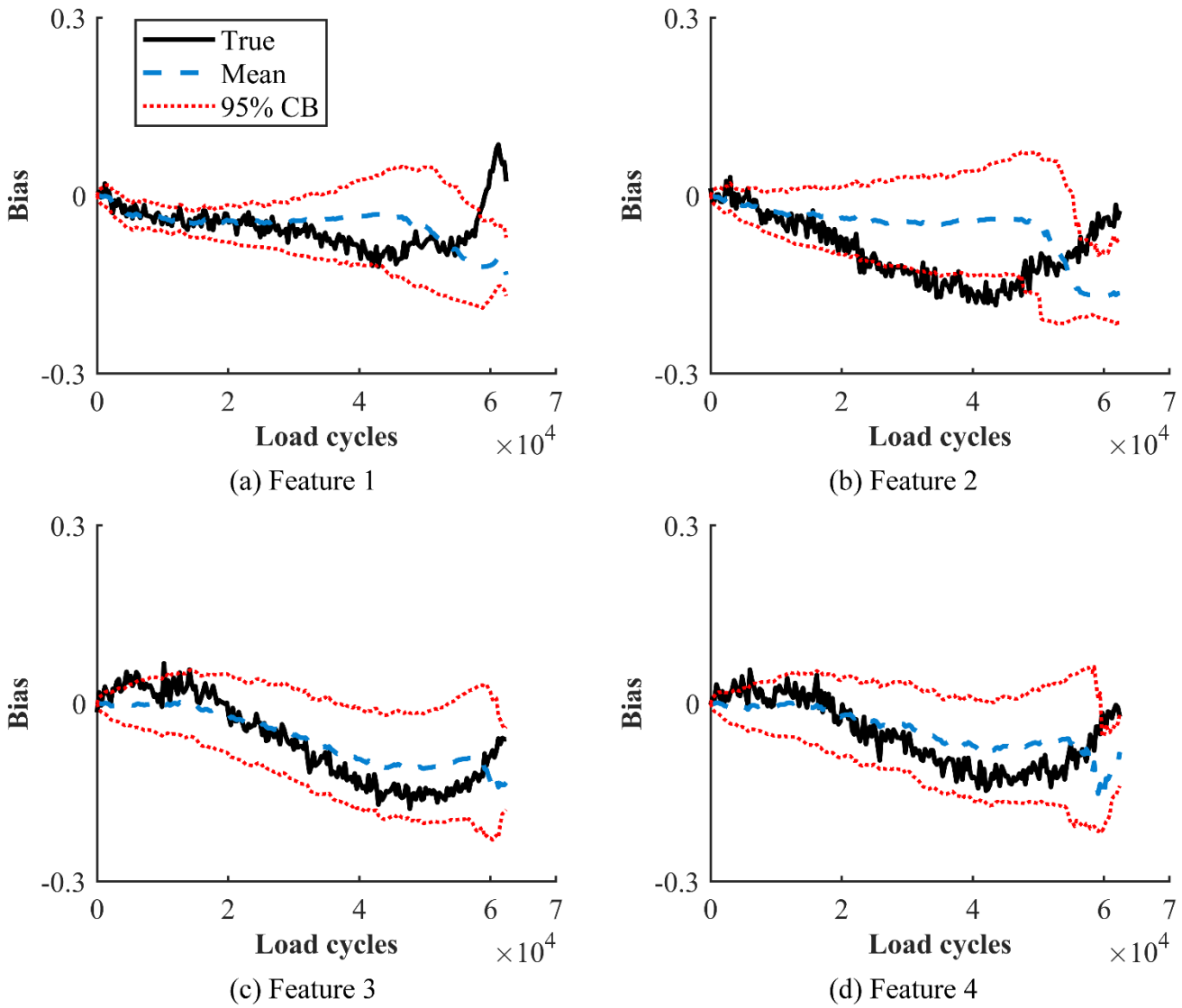

(a) Feature 1 (b) Feature 2

(c) Feature 3 (d) Feature 4

Figure A.3 Bias estimation using traditional method resorting to one feature for specimen S5.

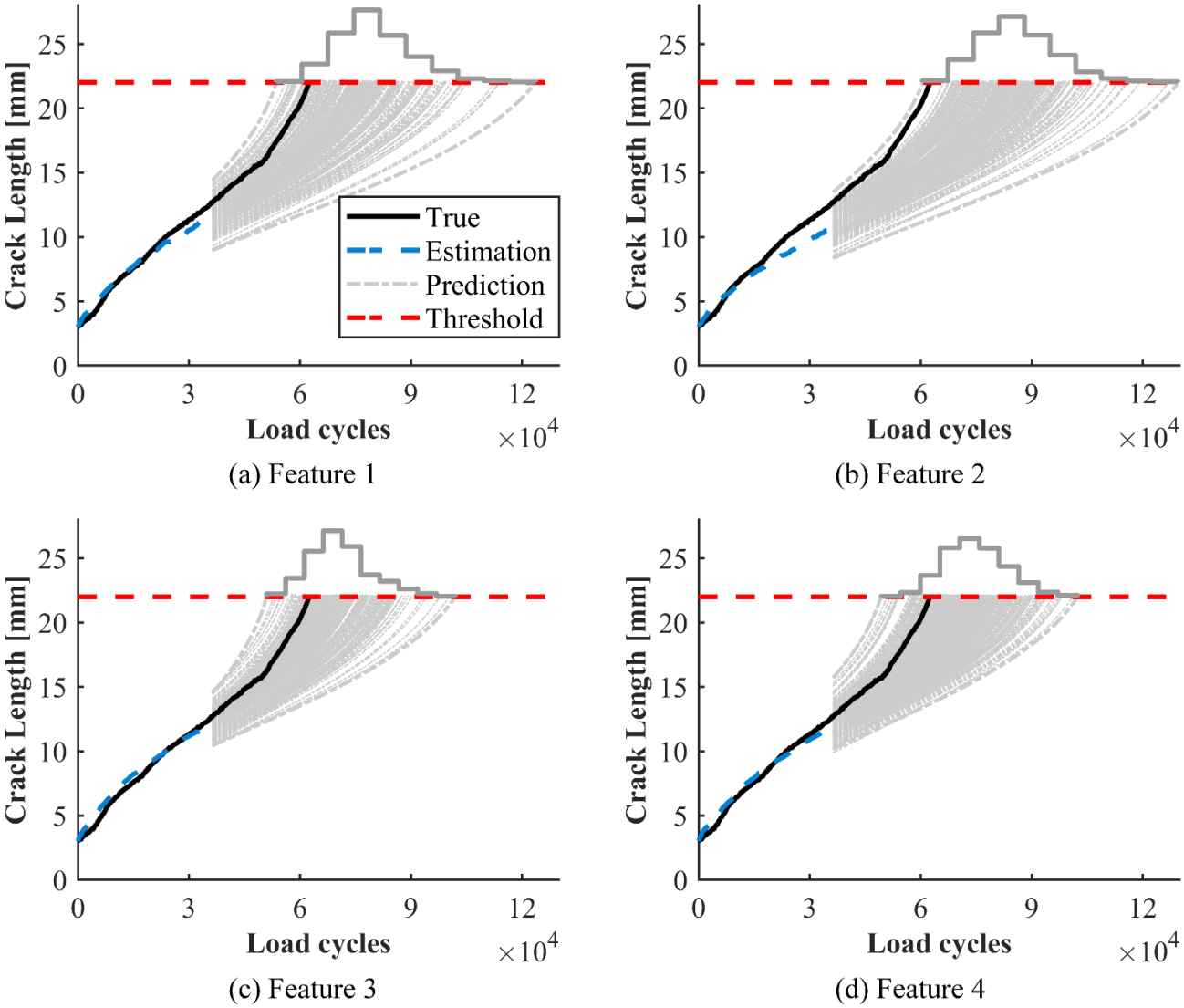

Figure A.4 Future state prediction at 3.6×10^4 load cycles using traditional method resorting to one feature for specimen S5.

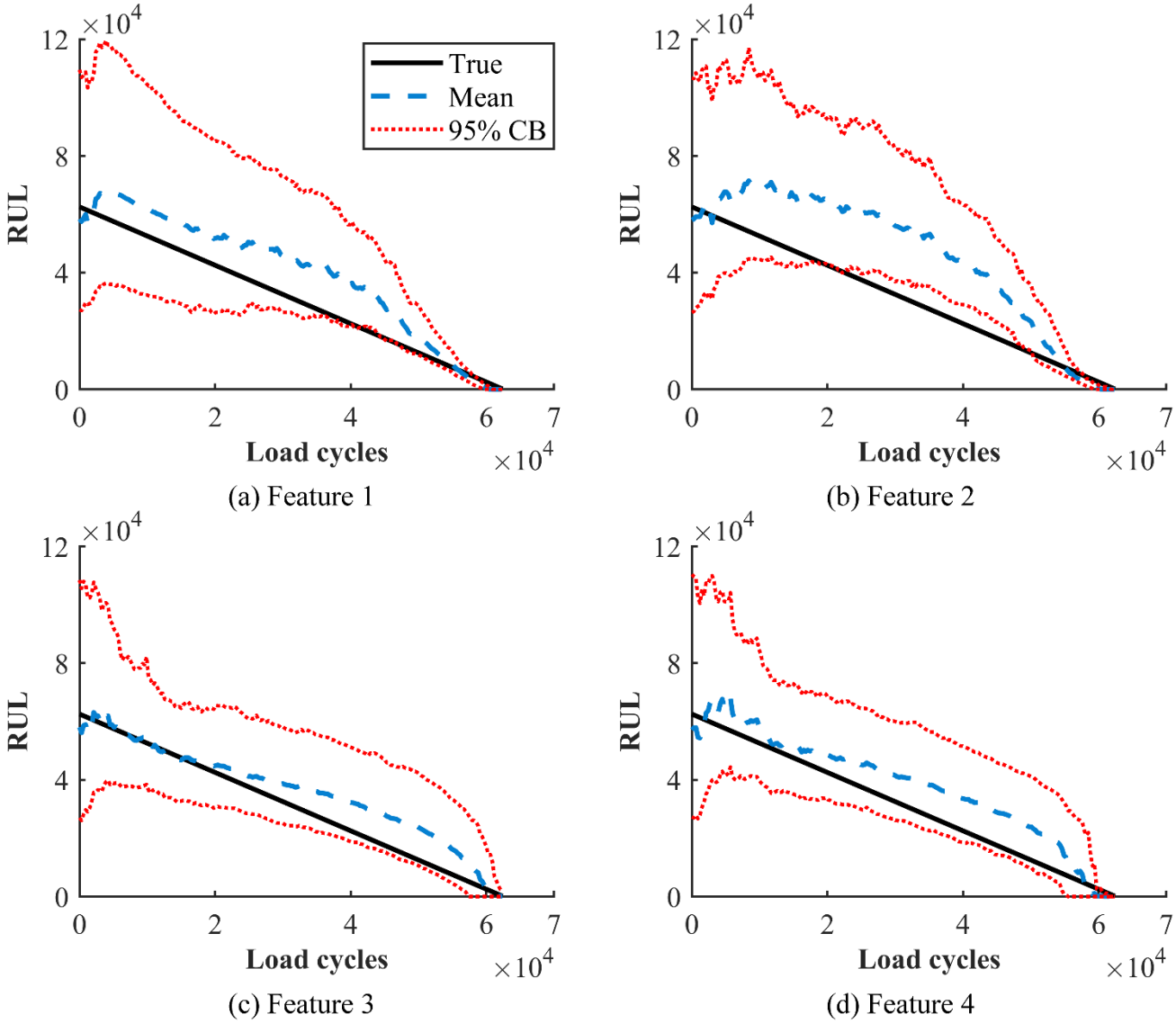

Figure A.5 RUL prediction using traditional method resorting to one feature for specimen S5.

Acknowledgments

This project has received funding from the European Union's Horizon 2020 research and innovation programme under the Marie Skłodowska-Curie grant agreement No. 859957.

References

[1] M. Chiachío, J. Chiachío, S. Sankararaman, K. Goebel, J. Andrews, A new algorithm for prognostics using Subset Simulation, Reliability Engineering & System Safety, 168 (2017) 189-199.

[2] D. Cristiani, C. Sbarufatti, M. Giglio, Damage diagnosis and prognosis in composite double cantilever beam coupons by particle filtering and surrogate modelling, Structural Health Monitoring, (2020) 1475921720960067.

[3] T. Li, F. Cadini, M. Chiachío, J. Chiachío, C. Sbarufatti, Particle filter-based delamination shape prediction in composites subjected to fatigue loading, Structural Health Monitoring, (2022) 14759217221116041.

[4] N. Yue, A. Broer, W. Briand, M. Rébillat, T. Loutas, D. Zarouchas, Assessing stiffness degradation of stiffened composite panels in post-buckling compression-compression fatigue using guided waves, Composite Structures, 293 (2022) 115751.

[5] C. Tao, C. Zhang, H. Ji, J. Qiu, Application of neural network to model stiffness degradation for composite laminates under cyclic loadings, Composites Science and Technology, 203 (2021) 108573.
[6] T. Li, C. Sbarufatti, F. Cadini, J. Chen, S. Yuan, Particle filter-based hybrid damage prognosis considering measurement bias, Strctural Control and Health Monitoring, n/a (2021) e2914.
[7] T. Li, L. Lomazzi, F. Cadini, C. Sbarufatti, J. Chen, S. Yuan, Numerical simulation-aided particle filter-based damage prognosis using Lamb waves, Mechanical Systems and Signal Processing, 178 (2022) 109326.
[8] J. Chen, S. Yuan, C. Sbarufatti, X. Jin, Dual crack growth prognosis by using a mixture proposal particle filter and on-line crack monitoring, Reliability Engineering & System Safety, 215 (2021) 107758.
[9] F. Zhao, X. Zhou, C. Wang, L. Dong, S.N. Atluri, Setting Adaptive Inspection Intervals in Helicopter Components, Based on a Digital Twin, AIAA Journal, (2023) 1-14.
[10] X. Zhou, S. He, L. Dong, S.N. Atluri, Real-Time Prediction of Probabilistic Crack Growth with a Helicopter Component Digital Twin, AIAA Journal, 60 (2022) 2555-2567.
[11] N. Eleftheroglou, D. Zarouchas, R. Benedictus, An adaptive probabilistic data-driven methodology for prognosis of the fatigue life of composite structures, Composite Structures, 245 (2020) 112386.
[12] M. Moradi, A. Broer, J. Chiachío, R. Benedictus, T.H. Loutas, D. Zarouchas, Intelligent health indicator construction for prognostics of composite structures utilizing a semi-supervised deep neural network and SHM data, Engineering Applications of Artificial Intelligence, 117 (2023) 105502.
[13] G. Galanopoulos, N. Eleftheroglou, D. Milanoski, A. Broer, D. Zarouchas, T. Loutas, A novel strain-based health indicator for the remaining useful life estimation of degrading composite structures, Composite Structures, 306 (2023) 116579.
[14] J. Fernández, M. Chiachío, J. Chiachío, R. Muñoz, F. Herrera, Uncertainty quantification in Neural Networks by Approximate Bayesian Computation: Application to fatigue in composite materials, Engineering Applications of Artificial Intelligence, 107 (2022) 104511.
[15] P. Baraldi, F. Mangili, E. Zio, Investigation of uncertainty treatment capability of model-based and data-driven prognostic methods using simulated data, Reliability Engineering & System Safety, 112 (2013) 94-108.
[16] I. Lopez, N. Sarigul-Klijn, A review of uncertainty in flight vehicle structural damage monitoring, diagnosis and control: Challenges and opportunities, Progress in Aerospace Sciences, 46 (2010) 247-273.
[17] M. Corbetta, C. Sbarufatti, M. Giglio, M.D. Todd, Optimization of nonlinear, non-Gaussian Bayesian filtering for diagnosis and prognosis of monotonic degradation processes, Mechanical Systems and Signal Processing, 104 (2018) 305-322.
[18] F. Cadini, L. Lomazzi, M. Ferrater Roca, C. Sbarufatti, M. Giglio, Neutralization of temperature effects in damage diagnosis of MDOF systems by combinations of autoencoders and particle filters, Mechanical Systems and Signal Processing, 162 (2022) 108048.
[19] M. Corbetta, C. Sbarufatti, M. Giglio, A. Saxena, K. Goebel, A Bayesian framework for fatigue life prediction of composite laminates under co-existing matrix cracks and delamination, Composite Structures, 187 (2018) 58-70.
[20] T. Loutas, N. Eleftheroglou, D. Zarouchas, A data-driven probabilistic framework towards the in-situ prognostics of fatigue life of composites based on acoustic emission data, Composite Structures, 161 (2017) 522-529.
[21] X. Liu, Y. Lei, N. Li, X. Si, X. Li, RUL prediction of machinery using convolutional-vector fusion network through multi-feature dynamic weighting, Mechanical Systems and Signal Processing, 185 (2023) 109788.
[22] S. Buchaiah, P. Shakya, Bearing fault diagnosis and prognosis using data fusion based feature extraction and feature selection, Measurement, 188 (2022) 110506.
[23] D. Cristiani, C. Sbarufatti, F. Cadini, M. Giglio, Fatigue damage diagnosis and prognosis of an aeronautical structure based on surrogate modelling and particle filter, Structural Health Monitoring, 0 1475921720971551.

[24] J. Chen, S. Yuan, X. Jin, On-line prognosis of fatigue cracking via a regularized particle filter and guided wave monitoring, Mechanical Systems and Signal Processing, 131 (2019) 1-17.
[25] W. Wu, M.K. Malik, S. Cantero-Chinchilla, T. Lawrie, W.J. Yan, G. Tanner, R. Remenyte-Prescott, D. Chronopoulos, Guided waves-based damage identification in plates through an inverse Bayesian process, Ultrasonics, 125 (2022) 106773.
[26] D. Yang, H.R. Karimi, K. Sun, Residual wide-kernel deep convolutional auto-encoder for intelligent rotating machinery fault diagnosis with limited samples, Neural Networks, 141 (2021) 133-144.
[27] J. Tian, D. Han, M. Li, P. Shi, A multi-source information transfer learning method with subdomain adaptation for cross-domain fault diagnosis, Knowledge-Based Systems, 243 (2022) 108466.
[28] J. Chen, S. Yuan, H. Wang, On-line updating Gaussian process measurement model for crack prognosis using the particle filter, Mechanical Systems and Signal Processing, 140 (2020) 106646.
[29] E. Rabiei, E.L. Droguett, M. Modarres, Fully Adaptive Particle Filtering Algorithm for Damage Diagnosis and Prognosis, Entropy, 20 (2018).
[30] D. Song, F. Xu, T. Ma, Crack damage monitoring for compressor blades based on acoustic emission with novel feature and hybridized feature selection, Structural Health Monitoring, (2022) 14759217211068107.
[31] A. Broer, G. Galanopoulos, R. Benedictus, T. Loutas, D. Zarouchas, Fusion-based damage diagnostics for stiffened composite panels, Structural Health Monitoring, 21 (2021) 613-639.
[32] M.S. Arulampalam, S. Maskell, N. Gordon, T. Clapp, A tutorial on particle filters for online nonlinear/non-Gaussian Bayesian tracking, IEEE Transactions on Signal Processing, 50 (2002) 174-188.
[33] S. Torkamani, S. Roy, M.E. Barkey, E. Sazonov, S. Burkett, S. Kotru, A novel damage index for damage identification using guided waves with application in laminated composites, Smart Materials and Structures, 23 (2014) 095015.
[34] X.P. Qing, H.-L. Chan, S.J. Beard, A. Kumar, An Active Diagnostic System for Structural Health Monitoring of Rocket Engines, Journal of Intelligent Material Systems and Structures, 17 (2006) 619-628.
[35] J. Liu, M. West, Combined parameter and state estimation in simulation-based filtering, Sequential Monte Carlo methods in practice, Springer, 2001, pp. 197-223.
[36] E.N. Chatzi, A.W. Smyth, The unscented Kalman filter and particle filter methods for nonlinear structural system identification with non-collocated heterogeneous sensing, Structural Control & Health Monitoring, 16 (2010) 99-123.
[37] A. Saxena, J. Celaya, E. Balaban, K. Goebel, B. Saha, S. Saha, M. Schwabacher, Metrics for evaluating performance of prognostic techniques, 2008 International Conference on Prognostics and Health Management, 2008, pp. 1-17.

CHAPTER 5

HIGH-DIMENSIONAL PARTICLE FILTER

In Chapter 5, targeting the curse of dimensionality, the author proposes a new particle filter method that can simplify a high-dimensional identification into multiple lower-dimensional identifications, whose robustness is tested by a toy example and a numerical simulation of twenty-story Bouc-wen frame structure under seismic excitation.

Multiple local particle filter for high-dimensional structural system identification

*Tianzhi Li, Claudio Sbarufatti, Francesco Cadini**

Dipartimento di Meccanica, Politecnico di Milano, Milan, Italy

*Corresponding author, *Email: francesco.cadini@polimi.it*

Abstract

Various time-domain state estimation algorithms have been developed for nonlinear system identification in structural health monitoring (SHM). Particle filter (PF) is one of the successful applications, but it suffers from the curse of dimensionality and behaves poorly in high-dimensional structural dynamic systems. The idea of state and measurement partitioning has been used in many PF algorithms to simplify high-dimensional identification problems into the identification of several lower-dimensional subgroups, but with very few applications to SHM problems. In this context, by combining multiple particle filters (MPF) with the decay of correlations property, this paper develops a novel multiple local particle filter (MLPF) for high-dimensional structural identification problems. One state vector with the components from multiple degrees of freedom (DOFs) is partitioned into several state subgroups, each consisting of the component from one DOF and then estimated by one PF through a novel likelihood including the local state and measurement vectors. The feasibility and efficiency of the proposed method are tested through a benchmark toy example and a case study of a twenty-story Bouc-Wen frame structure under ground motion.

Keywords: structural health monitoring, system identification, particle filter, curse of dimensionality, decay of correlations.

1. Introduction

Structural health monitoring (SHM) has seen a lot of research in the field of structural system identification, utilizing various time-domain techniques such as the least square method [1], the extended Kalman filter [2, 3], the unscented Kalman filter [4, 5], and the particle filter (PF) [5-8]. These methods use a state-space models to describe the dynamic behavior of a monitored structure, where the parameters such as stiffness or damping, and the state variables such as velocity and displacement are combined to form an augmented state vector and coupled in both the process and measurement equations, leading to nonlinear identification problems [5].

Particle filter (PF) has been demonstrated successful for nonlinear system identification in SHM. However, it suffers from the curse of dimensionality, i.e., as more components (i.e., parameters and variables) are added into the state vector for estimation, the number of particles will be exponentially increased with the vector dimension, consequently leading to tremendous, or sometimes unaffordable, computation efforts [9, 10]. On the other hand, the SHM system typically has tens or hundreds of sensors installed for inferring the unknown structural parameters and states at multiple locations, possibly resulting in a high-dimensional problem. Very few PF modifications [6, 7] are proposed in SHM practices to alleviate the effect of the curse of dimensionality on high-dimensional identification. They consist in partitioning the state vector into the two-state subgroups, namely linear and nonlinear ones, and then combining PF with the marginalization approach for estimation. However, the dimensions of either one subgroup or both of them could still be quite large in a high-dimensional system, limiting the usage of those methods.

The curse of dimensionality is a well-known issue when using PF in engineering applications beyond SHM, such as multiple target tracking [11], where a whole state vector always consists of the unknown components (e.g., the location coordinates) from multiple targets. A common modification in the these applications is to partition the whole state vector into several state subgroups, each having the components of one target and then estimated through one PF, based on the assumptions of the independent posterior distribution and state evolution between the subgroups. By simplifying a problem of high-dimensional identification into that of multiple lower-dimensional identifications, this idea has led to the development of successful high-dimensional PF algorithms, including multiple particle filter (MPF) [13, 14] and its extensions [11, 15], and independent partition particle filter [12] and its extensions [16, 17].

On one hand, state space models commonly used in structural health monitoring (SHM) practices can not always satisfy the assumption of independent state evolution. Specifically, when adopting a state partitioning strategy from multiple target tracking [13, 14], a state vector containing multiple degrees of freedom (DOFs) can be partitioned into several subgroups, each consisting of components (e.g., velocity and displacement) from a single DOF. However, it is possible that one subgroup has to evolve with the state components from itself and another subgroup, for example, in the case of calculating the hysteretic displacement of top story in a multiple-story Bouc-Wen frame using the velocities from that story and its lower story. This violates the aforementioned assumption and restricts the applicability of existing algorithms for structural system identification.

On the other hand, the likelihood calculation in a high-dimensional problem can impose a significant computation burden [18], as seen in the PF algorithms mentioned above, where calculating the likelihood of

one subgroup involves either all state and measurement components [11, 13-15] or partial state components and all measurements [12, 16, 17]. To improve the computation efficiency, a modified likelihood with fewer state and measurement components involved is always desirable. The decay of correlations property indicates that, as a high-dimensional system is spatially distributed over relatively large distances, the conditional distribution of one state subgroup should significantly depend on the collected measurements at its nearby location [19]. This allows for estimating the posterior distribution of each subgroup with its nearby measurements. Fewer measurements in posterior estimation bring to fewer state and measurement components in likelihood, as shown in the use of PF in the application of target tracking [20, 21], providing a mechanism to reduce the computational cost.

In this study, we propose two contributions for high-dimensional structural identification. First, we extend the concept of state partitioning to account for dependent state evolution. Specifically, we partition one state vector into several state subgroups, each containing the state components of one degree of freedom (DOF) and evolving with itself and additional state components. Next, we develop a novel multiple local particle filter (MLPF) by combining the decay of correlations property and the idea of state partitioning. The MLPF utilizes a novel likelihood function that includes fewer state and measurement components, resulting in computational savings. The feasibility of the extension is tested through a numerical simulation of a twenty-story Bouc-Wen frame structure under the ground motion, and the efficiency of the proposed MLPF over PF and MPF is validated by a toy example from [9] and the above numerical study.

The remainder of this paper is organized as follows: Section 2 describes the particle filter, multiple particle filter, the extension about dependent state evolution, and the novel multiple local particle filter. The performances of the three algorithms are compared by the toy example in Section 3 and the numerical simulation of a twenty-story Bouc-Wen frame structure in Section 4. Finally, Section 5 concludes the paper with some topics for further work.

2. Particle filter algorithms

In this Section, we first review some fundamental concepts related to the particle filter (PF) method, including the state space model, analytical calculation of posterior probability density function (PDF), Monte Carlo sampling, sequential importance sampling, and standard PF. Then, we introduce the multiple particle filter (MPF), which is designed for multiple target tracking, and propose an extension of dependent state evolution for MPF. We then develop the multiple local particle filter (MLPF) by introducing a new likelihood into the MPF. Finally, we propose a definition of local state and measurement vectors for MLPF and explain why

MLPF can be more computationally efficient than MPF.

2.1 Particle filter

The state space model for the system identification problem can be formulated as

$$\boldsymbol{X}_k = f\left(\boldsymbol{X}_{k-1}, \boldsymbol{u}_{k-1}, \boldsymbol{\omega}_{k-1}\right) \tag{1}$$

$$\boldsymbol{Y}_k = h\left(\boldsymbol{X}_k, \boldsymbol{u}_k, \boldsymbol{\eta}_k\right) \tag{2}$$

where the subscript k is the time step, $\boldsymbol{X}$, $\boldsymbol{u}$, and $\boldsymbol{Y}$ represent the state, input, and measurement vectors, $\boldsymbol{\omega}$ and $\boldsymbol{\eta}$ are the process and measurement noise vectors, whose distributions are assumed as zero-mean Gaussian in this study, $f(\cdot)$ and $h(\cdot)$ are the process and measurement functions describing the system state evolution and the relationship between the states and the measurements, respectively.

From a Bayesian perspective, the problem of estimating the state vector $\boldsymbol{X}_k$ based on a sequence of the available measurements up to time step k $\boldsymbol{Y}_{1:k}$ is to recursively build the posterior probability density function (PDF) $p\left(\boldsymbol{X}_k \mid \boldsymbol{Y}_{1:k}\right)$ as:

$$p\left(\boldsymbol{X}_k \mid \boldsymbol{Y}_{1:k-1}\right) = \int p(\boldsymbol{X}_k \mid \boldsymbol{X}_{k-1}) p(\boldsymbol{X}_{k-1} \mid \boldsymbol{Y}_{1:k-1}) d\boldsymbol{X}_{k-1} \tag{3}$$

$$p\left(\boldsymbol{X}_k \mid \boldsymbol{Y}_{1:k}\right) \propto p\left(\boldsymbol{Y}_k \mid \boldsymbol{X}_k\right) p\left(\boldsymbol{X}_k \mid \boldsymbol{Y}_{1:k-1}\right) \tag{4}$$

where $\boldsymbol{Y}_{1:k}$ are the measurements collected from time step 1 to k, $\propto$ denotes proportionality, and $p(\boldsymbol{X}_k \mid \boldsymbol{X}_{k-1})$, $p\left(\boldsymbol{X}_k \mid \boldsymbol{Y}_{1:k-1}\right)$, and $p\left(\boldsymbol{X}_k \mid \boldsymbol{Y}_{1:k}\right)$ are the transition distribution, prior PDF, and likelihood function, respectively.

Obtaining an analytical solution of Eqs. (3) and (4) is rare in a nonlinear and non-Gaussian problem. As a result, Monte Carlo sampling is often used to approximate the posterior PDF with N particles $\left\{\boldsymbol{X}_k^i : i = 1, 2, \ldots, N\right\}$ as

$$p\left(\boldsymbol{X}_k \mid \boldsymbol{Y}_{1:k}\right) \approx \frac{1}{N} \sum_{i=1}^{N} \delta\left(\boldsymbol{X}_k - \boldsymbol{X}_k^i\right) \tag{5}$$

where $\delta(\cdot)$ is a Dirac-delta function.

Given the difficulty in sampling from the true posterior PDF, an alternative is to apply importance sampling to draw N samples from a properly chosen importance density $q(\boldsymbol{X})$ like $q\left(\boldsymbol{X}_k \mid \boldsymbol{Y}_{1:k}\right)$ for building

the PDF $p\left(\boldsymbol{X}_k \mid \boldsymbol{Y}_{1:k}\right)$ as

$$p\left(\boldsymbol{X}_k \mid \boldsymbol{Y}_{1:k}\right) \approx \sum_{i=1}^{N} \tilde{w}_k^i \delta\left(\boldsymbol{X}_k - \boldsymbol{X}_k^i\right) \tag{6}$$

where the weight $\tilde{w}_k^i$ corresponding to the *i*-th particle $\boldsymbol{X}_k^i$ denotes the normalized form of the weight w_k^i calculated as:

$$w_k^i \propto \frac{p\left(\boldsymbol{X}_k^i \mid \boldsymbol{Y}_{1:k}\right)}{q\left(\boldsymbol{X}_k^i \mid \boldsymbol{Y}_{1:k}\right)} \tag{7}$$

The computation effort of Eq. (7) will increase over time, as more measurements will be included in the vector $\boldsymbol{Y}_{1:k}$.

In order to improve the efficiency of computing the particle weight, the PDF $p\left(\boldsymbol{X}_{0:k} \mid \boldsymbol{Y}_{1:k}\right)$ should be built with *N* particles $\left\{\boldsymbol{X}_{0:k}^i : i = 1, 2, \ldots, N\right\}$ from the density $q\left(\boldsymbol{X}_{0:k} \mid \boldsymbol{Y}_{1:k}\right)$ as

$$p\left(\boldsymbol{X}_{0:k} \mid \boldsymbol{Y}_{1:k}\right) \approx \sum_{i=1}^{N} \tilde{w}_k^i \delta\left(\boldsymbol{X}_{0:k} - \boldsymbol{X}_{0:k}^i\right) \tag{8}$$

then we have

$$\begin{aligned} w_k^i &\propto \frac{p\left(\boldsymbol{X}_{0:k}^i \mid \boldsymbol{Y}_{1:k}\right)}{q\left(\boldsymbol{X}_{0:k}^i \mid \boldsymbol{Y}_{1:k}\right)} \\ &\propto \frac{p\left(\boldsymbol{X}_{0:k-1}^i \mid \boldsymbol{Y}_{1:k-1}\right) p\left(\boldsymbol{X}_k^i \mid \boldsymbol{X}_{k-1}^i\right) p\left(\boldsymbol{Y}_k \mid \boldsymbol{X}_k^i\right)}{q\left(\boldsymbol{X}_{0:k-1}^i \mid \boldsymbol{Y}_{1:k-1}\right) q\left(\boldsymbol{X}_k^i \mid \boldsymbol{X}_{0:k-1}^i, \boldsymbol{Y}_{1:k}\right)} \\ &\propto \tilde{w}_{k-1}^i \frac{p\left(\boldsymbol{Y}_k \mid \boldsymbol{X}_k^i\right) p\left(\boldsymbol{X}_k^i \mid \boldsymbol{X}_{k-1}^i\right)}{q\left(\boldsymbol{X}_k^i \mid \boldsymbol{X}_{k-1}^i, \boldsymbol{Y}_k\right)} \end{aligned} \tag{9}$$

It is often convenient to choose the density $q\left(\boldsymbol{X}_k \mid \boldsymbol{X}_{k-1}, \boldsymbol{Y}_k\right)$ to be the transition distribution,

$$q\left(\boldsymbol{X}_k \mid \boldsymbol{X}_{k-1}, \boldsymbol{Y}_k\right) = p\left(\boldsymbol{X}_k \mid \boldsymbol{X}_{k-1}\right) \tag{10}$$

which yields

$$w_k^i \propto \tilde{w}_{k-1}^i p\left(\boldsymbol{Y}_k \mid \boldsymbol{X}_k^i\right) \tag{11}$$

Finally, we can obtain the posterior PDF by [22, 23]

$$
\begin{aligned}
p\left(\boldsymbol{X}_k \mid \boldsymbol{Y}_{1:k}\right) &= \int p\left(\boldsymbol{X}_{0:k} \mid \boldsymbol{Y}_{1:k}\right) d\boldsymbol{X}_{0:k-1} \\
&\approx \int \sum_{i=1}^{N} \tilde{w}_k^i \delta\left(\boldsymbol{X}_k - \boldsymbol{X}_k^i, \boldsymbol{X}_{0:k-1} - \boldsymbol{X}_{0:k-1}^i\right) d\boldsymbol{X}_{0:k-1} \\
&= \int \sum_{i=1}^{N} \tilde{w}_k^i \delta\left(\boldsymbol{X}_k - \boldsymbol{X}_k^i\right) \delta\left(\boldsymbol{X}_{0:k-1} - \boldsymbol{X}_{0:k-1}^i\right) d\boldsymbol{X}_{0:k-1} \\
&= \sum_{i=1}^{N} \tilde{w}_k^i \delta\left(\boldsymbol{X}_k - \boldsymbol{X}_k^i\right)
\end{aligned}
\tag{12}
$$

Eqs. (8) ~ (12) give rise to the universally known sequential importance sampling (SIS) algorithm, which, however, is shown to suffer from particle degeneracy, i.e., most particles are assigned with a trivial weight after a few time steps. This phenomenon can be evaluated by the effective sample size N_{eff} as

$$
N_{eff,k} = \frac{1}{\sum_{i=1}^{N} \left(\tilde{w}_k^i\right)^2} \tag{13}
$$

Once N_{eff} falls below a predefined threshold N_T, a resampling technique is adopted to eliminate the small-weight particles and duplicate the large-weight particles. A standard PF typically has a resampling step inserted into an SIS scheme [24, 25], and its pseudo-code is given in Table 1.

Table 1 Pseudo-code of particle filter

For k=0

Initialization: draw N particles $\left\{\boldsymbol{X}_k^i : i = 1, 2, \ldots, N\right\}$ from the known $p(\boldsymbol{X}_0)$.

For k=1, 2, …

Prediction: draw N particles $\left\{\boldsymbol{X}_k^i : i = 1, 2, \ldots, N\right\}$ from $p(\boldsymbol{X}_k \mid \boldsymbol{X}_{k-1})$.

Weight update: calculate the particle weight and the effective sample size $N_{eff,k}$ by Eqs. (11) and (13), respectively.

If $N_{eff,k} / N$ is below the threshold N_T

Resample for $\left\{\boldsymbol{X}_k^i : i = 1, 2, \ldots, N\right\}$ based on the normalized weights $\left\{\tilde{w}_k^i : i = 1, 2, \ldots, N\right\}$ and then define each weight as 1/N.

Approximate the mean $\hat{\boldsymbol{X}}_k$ by $\hat{\boldsymbol{X}}_k = \sum_{i=1}^{N} \tilde{w}_k^i \boldsymbol{X}_k^i$.

The PF algorithm is widely recognized as an efficient approach for many nonlinear and non-Gaussian engineering problems. However, its practical application is often limited to low-dimensional state spaces due

to the curse of dimensionality, which requires the number of particles to increase exponentially with the dimension of the state vector [9]. To overcome this challenge, one possible solution is to partition the state vector into several subgroups and then use a separate PF for each subgroup, such as that performed in multiple particle filter (MPF) [13, 14].

2.2 Multiple particle filter

MPF was first proposed in [13, 14] for multiple object tracking and then detailed in [11]. First, a whole state vector $\boldsymbol{X}_k$ can be partitioned into *b* state subgroups as

$$\boldsymbol{X}_k = \begin{bmatrix} \boldsymbol{x}_k^1 & \boldsymbol{x}_k^2 & \dots & \boldsymbol{x}_k^b \end{bmatrix}^T \tag{14}$$

where $\boldsymbol{x}_k^j$ denotes the *j*-th subgroup, i.e., a vector of state components from the *j*-th target. Each subgroup has the same state component as the others.

MPF always assumes each state subgroup to independently evolve from the rest, i.e.,

$$\boldsymbol{x}_k^j \sim p\left(\boldsymbol{x}_k^j \mid \boldsymbol{x}_{k-1}^j\right) \tag{15}$$

Then, by resorting to the assumption of posterior independence between each subgroup, it is possible to write:

$$\begin{aligned} p\left(\boldsymbol{X}_k \mid \boldsymbol{Y}_{1:k}\right) &= p\left(\boldsymbol{x}_k^1 \mid \boldsymbol{Y}_{1:k}, \boldsymbol{x}_k^2, \dots, \boldsymbol{x}_k^b\right) p\left(\boldsymbol{x}_k^2, \boldsymbol{x}_k^3, \dots, \boldsymbol{x}_k^b \mid \boldsymbol{Y}_{1:k}\right) \\ &= p\left(\boldsymbol{x}_k^1 \mid \boldsymbol{Y}_{1:k}\right) p\left(\boldsymbol{x}_k^2, \boldsymbol{x}_k^3, \dots, \boldsymbol{x}_k^b \mid \boldsymbol{Y}_{1:k}\right) \\ &= \prod_{j=1}^{b} p\left(\boldsymbol{x}_k^j \mid \boldsymbol{Y}_{1:k}\right) \end{aligned} \tag{16}$$

It should be noted that, although the posterior probability density function (PDF) of each subgroup is not generally independent due to the correlations arising from the measurement equation, this assumption has been shown to be beneficial in high-dimensional particle filters [11]. Therefore, we adopt this assumption in this section, as well as in the subsequent analyses.

The estimation of the posterior PDF for a whole state vector can be consequently simplified into that for multiple subgroups. Take the *j*-th subgroup as a reference example. Let us define:

$$\boldsymbol{X}_k^{-j} = \begin{bmatrix} \boldsymbol{x}_k^1 & \cdots & \boldsymbol{x}_k^{j-1} & \boldsymbol{x}_k^{j+1} & \cdots & \boldsymbol{x}_k^b \end{bmatrix}^T \tag{17}$$

The posterior PDF $p\left(\boldsymbol{x}_k^j \mid \boldsymbol{Y}_{1:k}\right)$ can be obtained through a Bayesian approach as

$$
\begin{aligned}
p\left(\boldsymbol{x}_k^j \mid \boldsymbol{Y}_{1:k}\right) &= \int p\left(\boldsymbol{X}_k \mid \boldsymbol{Y}_{1:k}\right) d\boldsymbol{X}_k^{-j} \\
&\propto \int p\left(\boldsymbol{Y}_k \mid \boldsymbol{X}_k\right) p\left(\boldsymbol{X}_k^{-j} \mid \boldsymbol{Y}_{1:k-1}\right) p\left(\boldsymbol{x}_k^j \mid \boldsymbol{X}_k^{-j}, \boldsymbol{Y}_{1:k-1}\right) d\boldsymbol{X}_k^{-j} \\
&= p\left(\boldsymbol{x}_k^j \mid \boldsymbol{Y}_{1:k-1}\right) \int p\left(\boldsymbol{Y}_k \mid \boldsymbol{X}_k\right) p\left(\boldsymbol{X}_k^{-j} \mid \boldsymbol{Y}_{1:k-1}\right) d\boldsymbol{X}_k^{-j}
\end{aligned} \tag{18}
$$

where

$$
p\left(\boldsymbol{X}_k^{-j} \mid \boldsymbol{Y}_{1:k-1}\right) = \int p\left(\boldsymbol{X}_k^{-j} \mid \boldsymbol{X}_{k-1}^{-j}\right) p\left(\boldsymbol{X}_{k-1}^{-j} \mid \boldsymbol{Y}_{1:k-1}\right) d\boldsymbol{X}_{k-1}^{-j} \tag{19}
$$

Eqs. (18) and (19) are difficult to be analytically calculated in a nonlinear and non-Gaussian problem. Thus, similarly to what is performed for PF, the sequential importance sampling is used to estimate the posterior PDF $p\left(\boldsymbol{x}_{0:k}^j \mid \boldsymbol{Y}_{1:k}\right)$ through N particles drawn from the importance density $q\left(\boldsymbol{x}_{0:k}^j \mid \boldsymbol{Y}_{1:k}\right)$, i.e.,

$$
p\left(\boldsymbol{x}_{0:k}^j \mid \boldsymbol{Y}_{1:k}\right) \approx \sum_{i=1}^{N} \tilde{w}_k^{j,i} \delta\left(\boldsymbol{x}_{0:k}^j - \boldsymbol{x}_{0:k}^{j,i}\right) \tag{20}
$$

where $\tilde{w}_k^{j,i}$ is the normalized form of particle weight $\tilde{w}_k^{j,i}$ corresponding to the *i*-th particle for the *j*-th state subgroup.

The sequential calculation of the particle weights $\tilde{w}_k^{j,i}$ is demonstrated as follows. First, we have

$$
\begin{aligned}
p\left(\boldsymbol{x}_{0:k}^j \mid \boldsymbol{Y}_{1:k}\right) &= \int p\left(\boldsymbol{X}_{0:k} \mid \boldsymbol{Y}_{1:k}\right) d\boldsymbol{X}_{0:k}^{-j} \\
&\propto \int p\left(\boldsymbol{Y}_k \mid \boldsymbol{X}_k\right) p\left(\boldsymbol{X}_{0:k} \mid \boldsymbol{Y}_{1:k-1}\right) d\boldsymbol{X}_{0:k}^{-j} \\
&= \int p\left(\boldsymbol{Y}_k \mid \boldsymbol{X}_k\right) p\left(\boldsymbol{x}_{0:k}^j \mid \boldsymbol{X}_{0:k}^{-j}, \boldsymbol{Y}_{1:k-1}\right) p\left(\boldsymbol{X}_{0:k}^{-j} \mid \boldsymbol{Y}_{1:k-1}\right) d\boldsymbol{X}_{0:k}^{-j}
\end{aligned} \tag{21}
$$

With the assumption of independent state evolution and posterior distribution between each subgroup, we can have:

$$
p\left(\boldsymbol{x}_{0:k}^j \mid \boldsymbol{X}_{0:k}^{-j}, \boldsymbol{Y}_{1:k-1}\right) = p\left(\boldsymbol{x}_{0:k}^j \mid \boldsymbol{Y}_{1:k-1}\right) \tag{22}
$$

Eq. (21) then becomes:

$$
\begin{aligned}
p\left(\boldsymbol{x}_{0:k}^j \mid \boldsymbol{Y}_{1:k}\right) &\propto p\left(\boldsymbol{x}_{0:k}^j \mid \boldsymbol{Y}_{1:k-1}\right) \int p\left(\boldsymbol{Y}_k \mid \boldsymbol{X}_k\right) p\left(\boldsymbol{X}_{0:k}^{-j} \mid \boldsymbol{Y}_{1:k-1}\right) d\boldsymbol{X}_{0:k}^{-j} \\
&= p\left(\boldsymbol{x}_k^j \mid \boldsymbol{x}_{k-1}^j\right) p\left(\boldsymbol{x}_{0:k-1}^j \mid \boldsymbol{Y}_{1:k-1}\right) \int p\left(\boldsymbol{Y}_k \mid \boldsymbol{X}_k\right) \int p\left(\boldsymbol{X}_{0:k-1}^{-j}, \boldsymbol{X}_k^{-j} \mid \boldsymbol{Y}_{1:k-1}\right) d\boldsymbol{X}_{0:k-1}^{-j} d\boldsymbol{X}_k^{-j} \\
&= p\left(\boldsymbol{x}_k^j \mid \boldsymbol{x}_{k-1}^j\right) p\left(\boldsymbol{x}_{0:k-1}^j \mid \boldsymbol{Y}_{1:k-1}\right) \int p\left(\boldsymbol{Y}_k \mid \boldsymbol{X}_k\right) p\left(\boldsymbol{X}_k^{-j} \mid \boldsymbol{Y}_{1:k-1}\right) d\boldsymbol{X}_k^{-j}
\end{aligned} \tag{23}
$$

The prior PDF $p\left(\boldsymbol{X}_k^{-j} \mid \boldsymbol{Y}_{1:k-1}\right)$ can be defined through the Dirac function as

$$
p\left(\boldsymbol{X}_k^{-j} \mid \boldsymbol{Y}_{1:k-1}\right) \approx \delta\left(\boldsymbol{X}_k^{-j} - \hat{\boldsymbol{X}}_k^{-j}\right) \tag{24}
$$

where

$$
\hat{\boldsymbol{X}}_k^{-j} = \begin{bmatrix} \hat{\boldsymbol{x}}_k^1 & \cdots & \hat{\boldsymbol{x}}_k^{j-1} & \hat{\boldsymbol{x}}_k^{j+1} & \cdots & \hat{\boldsymbol{x}}_k^b \end{bmatrix}^T \tag{25}
$$

and

$$\hat{\boldsymbol{x}}_k^j = \sum_{i=1}^{N} \tilde{w}_{k-1}^{j,i} \boldsymbol{x}_k^{j,i} \tag{26}$$

Eq. (23) can then be written as

$$p\left(\boldsymbol{x}_{0:k}^j \mid \boldsymbol{Y}_{1:k}\right) \propto p\left(\boldsymbol{x}_{0:k-1}^j \mid \boldsymbol{Y}_{1:k-1}\right) p\left(\boldsymbol{x}_k^j \mid \boldsymbol{x}_{k-1}^j\right) p\left(\boldsymbol{Y}_k \mid \boldsymbol{x}_k^j, \hat{\boldsymbol{X}}_k^{-j}\right) \tag{27}$$

which yields

$$\begin{aligned} w_k^{j,i} &\propto \frac{p\left(\boldsymbol{x}_{0:k}^{j,i} \mid \boldsymbol{Y}_{1:k}\right)}{q\left(\boldsymbol{x}_{0:k}^{j,i} \mid \boldsymbol{Y}_{1:k}\right)} \\ &\propto \frac{p\left(\boldsymbol{x}_{0:k\text{-}1}^{j,i} \mid \boldsymbol{Y}_{1:k-1}\right) p\left(\boldsymbol{x}_k^{j,i} \mid \boldsymbol{x}_{k\text{-}1}^{j,i}\right) p\left(\boldsymbol{Y}_k \mid \boldsymbol{x}_k^{j,i}, \hat{\boldsymbol{X}}_k^{-j}\right)}{q\left(\boldsymbol{x}_{0:k\text{-}1}^{j,i} \mid \boldsymbol{Y}_{1:k\text{-}1}\right) q\left(\boldsymbol{x}_k^{j,i} \mid \boldsymbol{x}_{0:k\text{-}1}^{j,i}, \boldsymbol{Y}_{1:k}\right)} \\ &\propto \tilde{w}_{k-1}^{j,i} \frac{p\left(\boldsymbol{Y}_k \mid \boldsymbol{x}_k^{j,i}, \hat{\boldsymbol{X}}_k^{-j}\right) p\left(\boldsymbol{x}_k^{j,i} \mid \boldsymbol{x}_{k-1}^{j,i}\right)}{q\left(\boldsymbol{x}_k^{j,i} \mid \boldsymbol{x}_{k-1}^{j,i}, \boldsymbol{Y}_k\right)} \end{aligned} \tag{28}$$

With the importance density set as the prior distribution,

$$q\left(\boldsymbol{x}_k^j \mid \boldsymbol{x}_{k-1}^j, \boldsymbol{Y}_k\right) = p\left(\boldsymbol{x}_k^j \mid \boldsymbol{x}_{k-1}^j\right) \tag{29}$$

the particle weight for each subgroup can be sequentially calculated as

$$w_k^{j,i} \propto \tilde{w}_{k-1}^{j,i} p\left(\boldsymbol{Y}_k \mid \boldsymbol{x}_k^{j,i}, \hat{\boldsymbol{X}}_k^{-j}\right) \tag{30}$$

Finally, the posterior PDF $p\left(\boldsymbol{x}_k^j \mid \boldsymbol{Y}_{1:k}\right)$ can be similarly obtained through Eq. (12). One resampling step is implemented for each subgroup. The above summarizes the standard MPF algorithm [13, 14].

Table 2 Pseudo-code of multiple particle filter

For k = 0

Initialization: same as that in PF.

For k = 1, 2, …

For each subgroup, independently **do**

Prediction: draw N particles $\left\{\boldsymbol{x}_k^{j,i} : i = 1, 2, \ldots, N\right\}$ by Eq. (15).

Mean calculation: $\hat{\boldsymbol{x}}_k^j = \sum_{i=1}^{N} \tilde{w}_{k-1}^{j,i} \boldsymbol{x}_k^{j,i}$.

For each subgroup**,** independently **do**

Weight update: calculate the particle weight and the effective sample size $N_{eff,k}^j$ by Eqs. (30) and (13), respectively.

Resample for $\left\{ \boldsymbol{x}_k^{j,i} : i = 1, 2, \ldots, N \right\}$: same as that in PF.

Approximate the mean $\hat{\boldsymbol{x}}_k^j$ by $\hat{\boldsymbol{x}}_k^j = \sum_{i=1}^{N} \tilde{w}_k^{j,i} \boldsymbol{x}_k^{j,i}$.

The effectiveness of MPF compared to PF has been demonstrated in multiple object tracking, as it simplifies the identification of the whole state vector into several lower-dimensional subgroups. However, this algorithm has two limitations.

First, the assumption of independent state evolution cannot always be satisfied, especially in the application of structural system identification. Let us consider an application case of estimating the hysteretic displacement, velocity, and stiffness in a multiple-story Bouc-Wen frame. When following the state partitioning strategy from MPF [13, 14], a state vector containing multiple degrees of freedom (DOFs) can be partitioned into several subgroups, each consisting of components (i.e., stiffness, velocity, and displacement) from a single DOF. The displacement of each story (except the first story) has to be calculated by the velocity from that story and its lower story, violating the assumption of independent state evolution. Second, the likelihood for each state subgroup is calculated using all state and measurement components, as shown in Eq. (30), which can be computationally expensive [18] and requires modifying the likelihood function to include fewer state and measurement components to improve efficiency.

2.3 Extension about dependent state evolution

This study proposes an extension for the idea of state partitioning for the case of dependent state evolution, i.e., the *N* particles at the prediction step can also be sampled from:

$$\boldsymbol{x}_k^j \sim p\left(\boldsymbol{x}_k^j \mid \boldsymbol{x}_{k-1}^j, \hat{\boldsymbol{t}}_{k-1}^j \right) \tag{31}$$

where $\boldsymbol{t}^j$ is a vector of state components required for the state evolution of the *j*-th subgroup, i.e.,

$$\boldsymbol{x}_k^j = f^j\left(\boldsymbol{x}_{k-1}^j, \boldsymbol{t}_{k-1}^j, \boldsymbol{u}_{k-1}, \boldsymbol{\omega}_{k-1}^j \right) \tag{32}$$

The selection of these components will be further elaborated by a numerical example in Section 4.3.

MPF with Eq. (31) is given below. Provided that each state subgroup in a high-dimensional system may have a limited dependence on the rest, Eq. (22) can be considered sound. The prior PDF $p\left(\boldsymbol{x}_{0:k}^j \mid \boldsymbol{Y}_{1:k-1} \right)$ can be obtained by,

$$
\begin{aligned}
p\left(\boldsymbol{x}_{0:k}^{j} \mid \boldsymbol{Y}_{1:k-1}\right) &= \int p\left(\boldsymbol{x}_{k}^{j}, \boldsymbol{x}_{0:k-1}^{j}, \boldsymbol{t}_{k-1}^{j} \mid \boldsymbol{Y}_{1:k-1}\right) d\boldsymbol{t}_{k-1}^{j} \\
&= \int p\left(\boldsymbol{x}_{k}^{j} \mid \boldsymbol{Y}_{1:k-1}, \boldsymbol{t}_{k-1}^{j}, \boldsymbol{x}_{0:k-1}^{j}\right) p\left(\boldsymbol{x}_{0:k-1}^{j}, \boldsymbol{t}_{k-1}^{j} \mid \boldsymbol{Y}_{1:k-1}\right) d\boldsymbol{t}_{k-1}^{j} \\
&= \int p\left(\boldsymbol{x}_{k}^{j} \mid \boldsymbol{t}_{k-1}^{j}, \boldsymbol{x}_{k-1}^{j}\right) p\left(\boldsymbol{t}_{k-1}^{j} \mid \boldsymbol{x}_{0:k-1}^{j}, \boldsymbol{Y}_{1:k-1}\right) p\left(\boldsymbol{x}_{0:k-1}^{j} \mid \boldsymbol{Y}_{1:k-1}\right) d\boldsymbol{t}_{k-1}^{j} \\
&= p\left(\boldsymbol{x}_{0:k-1}^{j} \mid \boldsymbol{Y}_{1:k-1}\right) \int p\left(\boldsymbol{x}_{k}^{j} \mid \boldsymbol{t}_{k-1}^{j}, \boldsymbol{x}_{k-1}^{j}\right) \delta\left(\boldsymbol{t}_{k-1}^{j} - \hat{\boldsymbol{t}}_{k-1}^{j}\right) d\boldsymbol{t}_{k-1}^{j} \\
&= p\left(\boldsymbol{x}_{0:k-1}^{j} \mid \boldsymbol{Y}_{1:k-1}\right) p\left(\boldsymbol{x}_{k}^{j} \mid \hat{\boldsymbol{t}}_{k-1}^{j}, \boldsymbol{x}_{k-1}^{j}\right)
\end{aligned}
\tag{33}
$$

Provided with Eqs. (22) and (33), Eq. (21) then becomes,

$$
\begin{aligned}
p\left(\boldsymbol{x}_{0:k}^{j} \mid \boldsymbol{Y}_{1:k}\right) &\propto p\left(\boldsymbol{x}_{0:k-1}^{j} \mid \boldsymbol{Y}_{1:k-1}\right) p\left(\boldsymbol{x}_{k}^{j} \mid \hat{\boldsymbol{t}}_{k-1}^{j}, \boldsymbol{x}_{k-1}^{j}\right) \int p\left(\boldsymbol{Y}_{k} \mid \boldsymbol{X}_{k}\right) p\left(\boldsymbol{X}_{0:k}^{-j} \mid \boldsymbol{Y}_{1:k-1}\right) d\boldsymbol{X}_{0:k}^{-j} \\
&= p\left(\boldsymbol{x}_{0:k-1}^{j} \mid \boldsymbol{Y}_{1:k-1}\right) p\left(\boldsymbol{x}_{k}^{j} \mid \hat{\boldsymbol{t}}_{k-1}^{j}, \boldsymbol{x}_{k-1}^{j}\right) p\left(\boldsymbol{Y}_{k} \mid \boldsymbol{x}_{k}^{j}, \hat{\boldsymbol{X}}_{k}^{-j}\right)
\end{aligned}
\tag{34}
$$

Following Eqs. (28) ~ (30), the particle weight can be sequentially calculated as

$$
\begin{aligned}
w_{k}^{j,i} &\propto \frac{p\left(\boldsymbol{x}_{0:k}^{j,i} \mid \boldsymbol{Y}_{1:k}\right)}{q\left(\boldsymbol{x}_{0:k}^{j,i} \mid \boldsymbol{Y}_{1:k}\right)} \\
&\propto \tilde{w}_{k-1}^{j,i} \frac{p\left(\boldsymbol{Y}_{k} \mid \boldsymbol{x}_{k}^{j,i}, \hat{\boldsymbol{X}}_{k}^{-j}\right) p\left(\boldsymbol{x}_{k}^{j,i} \mid \boldsymbol{x}_{k-1}^{j,i}, \hat{\boldsymbol{t}}_{k-1}^{j}\right)}{q\left(\boldsymbol{x}_{k}^{j,i} \mid \boldsymbol{x}_{k-1}^{j,i}, \boldsymbol{Y}_{k}\right)} \\
&= \tilde{w}_{k-1}^{j,i} p\left(\boldsymbol{Y}_{k} \mid \boldsymbol{x}_{k}^{j,i}, \hat{\boldsymbol{X}}_{k}^{-j}\right)
\end{aligned}
\tag{35}
$$

where the importance density $q\left(\boldsymbol{x}_{k}^{j,i} \mid \boldsymbol{x}_{k-1}^{j,i}, \boldsymbol{Y}_{k}\right)$ is set as $p\left(\boldsymbol{x}_{k}^{j,i} \mid \boldsymbol{x}_{k-1}^{j,i}, \hat{\boldsymbol{t}}_{k-1}^{j}\right)$.

2.4 Novel multiple local particle filter

This Section presents the proposed multiple local particle filter (MLPF), which maintains the state partitioning approach and all the assumptions from the MPF. The decay of correlations property indicates that, as a high-dimensional system like a multiple-DOF structure is spatially distributed over relatively large distances, the conditional distribution of one state subgroup should be highly correlated to the measurements collected at its nearby location [19]. Let us define a vector of the measurements in nearby locations of the *j*-th state subgroup as $\boldsymbol{y}_{k}^{j}$. Then, Eq. (16) is modified accordingly,

$$
p\left(\boldsymbol{X}_{k} \mid \boldsymbol{Y}_{1:k}\right) = \prod_{j=1}^{b} p\left(\boldsymbol{x}_{k}^{j} \mid \boldsymbol{Y}_{1:k-1}, \boldsymbol{y}_{k}^{j}\right) \tag{36}
$$

The posterior PDF of the *j*-th state subgroup $p\left(\boldsymbol{x}_{k}^{j} \mid \boldsymbol{Y}_{1:k-1}, \boldsymbol{y}_{k}^{j}\right)$ can be described as

$$
\begin{aligned}
p\left(\boldsymbol{x}_{k}^{j} \mid \boldsymbol{Y}_{1:k-1}, \boldsymbol{y}_{k}^{j}\right) &= \int p\left(\boldsymbol{x}_{k}^{j}, \boldsymbol{q}_{k}^{j} \mid \boldsymbol{Y}_{1:k-1}, \boldsymbol{y}_{k}^{j}\right) d\boldsymbol{q}_{k}^{j} \\
&\propto p\left(\boldsymbol{x}_{k}^{j} \mid \boldsymbol{Y}_{1:k-1}\right) \int p\left(\boldsymbol{y}_{k}^{j} \mid \boldsymbol{x}_{k}^{j}, \boldsymbol{q}_{k}^{j}\right) p\left(\boldsymbol{q}_{k}^{j} \mid \boldsymbol{Y}_{1:k-1}\right) d\boldsymbol{q}_{k}^{j}
\end{aligned}
\tag{37}
$$

where

$$p\left(\boldsymbol{q}_k^j \mid \boldsymbol{Y}_{1:k-1}\right)=\int p\left(\boldsymbol{q}_k^j \mid \boldsymbol{q}_{k-1}^j\right) p\left(\boldsymbol{q}_{k-1}^j \mid \boldsymbol{Y}_{1:k-1}\right) d\boldsymbol{q}_k^j \tag{38}$$

and $\boldsymbol{q}_k^j$ is a vector of state components required for calculating the likelihood $p\left(\boldsymbol{y}_k^j \mid \boldsymbol{x}_k^j, \boldsymbol{q}_k^j\right)$. For the *j*-th state subgroup $\boldsymbol{x}_k^j$, the vectors $\boldsymbol{q}_k^j$ and $\boldsymbol{y}_k^j$ are defined as its local state and measurement vectors, respectively. The criterion for selecting such vectors will be explained later in Sections 2.4 and 3.3.

Just like the cases of PF and MPF recalled above, the analytical solution of Eq. (37) can hardly be obtained. The sequential importance sampling is therefore used to estimate the posterior PDF $p\left(\boldsymbol{x}_{0:k}^j \mid \boldsymbol{Y}_{1:k-1}, \boldsymbol{y}_k^j\right)$ as

$$p\left(\boldsymbol{x}_{0:k}^j \mid \boldsymbol{Y}_{1:k-1}, \boldsymbol{y}_k^j\right) \approx \sum_{i=1}^{N} \tilde{w}^{j,i} \delta\left(\boldsymbol{x}_{0:k}^j - \boldsymbol{x}_{0:k}^{j,i}\right) \tag{39}$$

Following the similar assumptions and procedures in Eqs. (21) ~ (27), we have

$$\begin{aligned}
p\left(\boldsymbol{x}_{0:k}^j \mid \boldsymbol{Y}_{1:k-1}, \boldsymbol{y}_k^j\right) &= \int p\left(\boldsymbol{x}_{0:k}^j, \boldsymbol{q}_{0:k}^j \mid \boldsymbol{Y}_{1:k-1}, \boldsymbol{y}_k^j\right) d\boldsymbol{q}_{0:k}^j \\
&\propto \int p\left(\boldsymbol{y}_k^j \mid \boldsymbol{x}_k^j, \boldsymbol{q}_k^j\right) p\left(\boldsymbol{x}_{0:k}^j, \boldsymbol{q}_{0:k}^j \mid \boldsymbol{Y}_{1:k-1}\right) d\boldsymbol{q}_{0:k}^j \\
&= p\left(\boldsymbol{x}_{0:k}^j \mid \boldsymbol{Y}_{1:k-1}\right) \int p\left(\boldsymbol{y}_k^j \mid \boldsymbol{x}_k^j, \boldsymbol{q}_k^j\right) p\left(\boldsymbol{q}_{0:k}^j \mid \boldsymbol{Y}_{1:k-1}\right) d\boldsymbol{q}_{0:k}^j \\
&= p\left(\boldsymbol{x}_{0:k}^j \mid \boldsymbol{Y}_{1:k-1}\right) \int p\left(\boldsymbol{y}_k^j \mid \boldsymbol{x}_k^j, \boldsymbol{q}_k^j\right) \int p\left(\boldsymbol{q}_{0:k-1}^j, \boldsymbol{q}_k^j \mid \boldsymbol{Y}_{1:k-1}\right) d\boldsymbol{q}_{0:k-1}^j d\boldsymbol{q}_k^j \\
&= p\left(\boldsymbol{x}_k^j \mid \boldsymbol{x}_{k-1}^j\right) p\left(\boldsymbol{x}_{0:k-1}^j \mid \boldsymbol{Y}_{1:k-1}\right) \int p\left(\boldsymbol{y}_k^j \mid \boldsymbol{x}_k^j, \boldsymbol{q}_k^j\right) p\left(\boldsymbol{q}_k^j \mid \boldsymbol{Y}_{1:k-1}\right) d\boldsymbol{q}_k^j \\
&= p\left(\boldsymbol{x}_k^j \mid \boldsymbol{x}_{k-1}^j\right) p\left(\boldsymbol{x}_{0:k-1}^j \mid \boldsymbol{Y}_{1:k-2}, \boldsymbol{y}_{k-1}^j\right) \int p\left(\boldsymbol{y}_k^j \mid \boldsymbol{x}_k^j, \boldsymbol{q}_k^j\right) \delta\left(\boldsymbol{q}_k^j - \hat{\boldsymbol{q}}_k^j\right) d\boldsymbol{q}_k^j \\
&= p\left(\boldsymbol{x}_k^j \mid \boldsymbol{x}_{k-1}^j\right) p\left(\boldsymbol{x}_{0:k-1}^j \mid \boldsymbol{Y}_{1:k-2}, \boldsymbol{y}_{k-1}^j\right) p\left(\boldsymbol{y}_k^j \mid \boldsymbol{x}_k^j, \hat{\boldsymbol{q}}_k^j\right)
\end{aligned} \tag{40}$$

Similarly to Eqs. (28) ~ (30), the particle weight can be sequentially calculated as

$$\begin{aligned}
w_k^{j,i} &\propto \frac{p\left(\boldsymbol{x}_{0:k}^{j,i} \mid \boldsymbol{Y}_{1:k-1}, \boldsymbol{y}_k^j\right)}{q\left(\boldsymbol{x}_{0:k}^{j,i} \mid \boldsymbol{Y}_{1:k-1}, \boldsymbol{y}_k^j\right)} \\
&\propto \frac{p\left(\boldsymbol{x}_{0:k-1}^{j,i} \mid \boldsymbol{Y}_{1:k-2}, \boldsymbol{y}_{k-1}^j\right) p\left(\boldsymbol{x}_k^{j,i} \mid \boldsymbol{x}_{k-1}^{j,i}\right) p\left(\boldsymbol{y}_k^j \mid \boldsymbol{x}_k^{j,i}, \hat{\boldsymbol{q}}_k^j\right)}{q\left(\boldsymbol{x}_{0:k-1}^{j,i} \mid \boldsymbol{Y}_{1:k-1}, \boldsymbol{y}_k^j\right) q\left(\boldsymbol{x}_k^{j,i} \mid \boldsymbol{x}_{0:k-1}^{j,i}, \boldsymbol{Y}_{1:k-1}, \boldsymbol{y}_k^j\right)} \\
&= \frac{p\left(\boldsymbol{x}_{0:k-1}^{j,i} \mid \boldsymbol{Y}_{1:k-2}, \boldsymbol{y}_{k-1}^j\right) p\left(\boldsymbol{x}_k^{j,i} \mid \boldsymbol{x}_{k-1}^{j,i}\right) p\left(\boldsymbol{y}_k^j \mid \boldsymbol{x}_k^{j,i}, \hat{\boldsymbol{q}}_k^j\right)}{q\left(\boldsymbol{x}_{0:k-1}^{j,i} \mid \boldsymbol{Y}_{1:k-2}, \boldsymbol{y}_{k-1}^j\right) q\left(\boldsymbol{x}_k^{j,i} \mid \boldsymbol{x}_{k-1}^{j,i}, \boldsymbol{y}_k^j\right)} \\
&= w_{k-1}^{j,i} \frac{p\left(\boldsymbol{x}_k^{j,i} \mid \boldsymbol{x}_{k-1}^{j,i}\right) p\left(\boldsymbol{y}_k^j \mid \boldsymbol{x}_k^{j,i}, \hat{\boldsymbol{q}}_k^j\right)}{q\left(\boldsymbol{x}_k^{j,i} \mid \boldsymbol{x}_{k-1}^{j,i}, \boldsymbol{y}_k^j\right)} \\
&\propto \tilde{w}_{k-1}^{j,i} p\left(\boldsymbol{y}_k^j \mid \boldsymbol{x}_k^{j,i}, \hat{\boldsymbol{q}}_k^j\right)
\end{aligned} \tag{41}$$

The posterior PDF $p\left(\boldsymbol{x}_k^j \mid \boldsymbol{Y}_{1:k-1}, \boldsymbol{y}_k^j\right)$ can finally be obtained by Eq. (12), the same as already performed for PF and MPF. In the case where the independent state evolution, i.e., Eq. (15), cannot be satisfied, one can

resort to Eq. (31) for calculating the prior, which similar to what has been performed for MPF, thus not detailed here.

By embedding a novel likelihood $p\left(\boldsymbol{y}_k^j \mid \boldsymbol{x}_k^{j,i}, \hat{\boldsymbol{q}}_k^j\right)$ into the MPF scheme, multiple local particle filter (MLPF) can be presented as outlined in Table 3. The difference between MPF and MLPF is that the latter uses a reduced number of components in its likelihood, resulting in superior computation efficiency.

Table 3 Pseudo-code of novel multiple local particle filter

For k = 0

Initialization: same as that in PF.

For k = 1, 2, …

For each subgroup, independently **do**

Prediction and **Mean calculation**: same as that in MPF.

For each subgroup**,** independently **do**

Weight update: calculate the weight and the effective sample size $N_{eff,k}^j$ by Eqs. (41) and (13), respectively.

Resample and **Approximate**: same as that in MPF.

2.5 Definition of local state and measurement vectors

The criterion for selecting the local measurement and state vectors for each state subgroup is presented here. Considering that the measurement $\boldsymbol{Y}$ is a d-dimensional vector as

$$\boldsymbol{Y}_k = \begin{bmatrix} y_{1,k} & y_{2,k} & \cdots & y_{d,k} \end{bmatrix}^T \tag{42}$$

the measurement equation Eq. (2) can be then partitioned into d equations as

$$\begin{cases} y_{1,k} = h_1\left(\boldsymbol{p}_{1,k}, \boldsymbol{u}_k, \eta_{1,k}\right) \\ y_{2,k} = h_2\left(\boldsymbol{p}_{2,k}, \boldsymbol{u}_k, \eta_{2,k}\right) \\ \quad\vdots \\ y_{d,k} = h_d\left(\boldsymbol{p}_{d,k}, \boldsymbol{u}_k, \eta_{d,k}\right) \end{cases} \tag{43}$$

where $\boldsymbol{p}_{l,k}$ is a vector of state components required for modeling the l-th equation.

The components of the state subgroup $\boldsymbol{x}_k^j$ exist in one or some rows of Eq. (43), all of which are selected to re-formulate a local measurement equation,

$$\boldsymbol{y}_k^j = h^j\left(\boldsymbol{x}_k^j, \boldsymbol{q}_k^j, \boldsymbol{u}_k, \boldsymbol{\eta}_k^j\right) \tag{44}$$

where $\boldsymbol{q}_k^j$ and $\boldsymbol{y}_k^j$ are the local state and measurement vectors for that subgroup. For example, let us consider the components of the first subgroup $\boldsymbol{x}_k^1$ exist in the first three rows of Eq. (43), i.e.,

$$\begin{cases} y_{1,k} = h_1\left(\boldsymbol{p}_{1,k}, \boldsymbol{u}_k, \eta_{1,k}\right) \\ y_{2,k} = h_2\left(\boldsymbol{p}_{2,k}, \boldsymbol{u}_k, \eta_{2,k}\right) \\ y_{3,k} = h_3\left(\boldsymbol{p}_{3,k}, \boldsymbol{u}_k, \eta_{3,k}\right) \end{cases} \tag{45}$$

Thus, the local measurement vector $\boldsymbol{y}_k^1$ of the first state subgroup consists of the first three measurements. All the state components from the three vectors $\boldsymbol{p}_{1,k}$, $\boldsymbol{p}_{2,k}$, and $\boldsymbol{p}_{3,k}$ can be used to build a new vector, which can be then divided in two vectors $\boldsymbol{x}_k^j$ and $\boldsymbol{q}_k^j$. This will be explained by a numerical example in Section 4.3.

When calculating the particle weights for one subgroup, MPF employs a likelihood function that requires the samples from that subgroup and the mean values of the samples from some additional state components. As a result, the formers are expected to have a significant contribution to the distribution of normalized weight compared to the latter. Same observation can be drawn for MLPF, despite using a reduced number of components in its likelihood. This indicates that MLPF can provide estimates that are nearly as precise as MPF, but with significantly reduced computational efforts.

3. Toy example

A toy example taken from [9] is adopted for comparing the performances of the three algorithms, i.e., PF, MPF and the proposed MLPF, in terms of accuracy and computational time. Its state space model is given as follows,

$$\boldsymbol{X}_k \sim \mathcal{N}\left(0, \mathrm{I}\right) \tag{46}$$

$$\boldsymbol{Y}_k = \boldsymbol{X}_k + \boldsymbol{\eta}_k \tag{47}$$

where $\mathcal{N}\left(0, \mathrm{I}\right)$ denotes the zero-mean Gaussian distribution with an identity matrix I serving as the covariance, and the measurement noise $\boldsymbol{\eta}_k$ is also sampled from the distribution $\mathcal{N}\left(0, \mathrm{I}\right)$. The state and measurement with a duration of two hundred steps are created through Eqs. (46) and (47). The size of the matrix I is increased from 10 to 90 with step 10, thus resulting in nine sets of target states and measurements for estimation.

Similarly to what has been performed in [9], the importance density for PF, MPF, or MLPF is set as

$\mathcal{N}(0,\mathrm{I})$ and no resampling procedure is applied. The root-mean-square error (RMSE) of the state estimates is taken as the performance metric to evaluate the estimation accuracy,

$$RMSE = \sqrt{\frac{1}{T}\sum_{k=1}^{T}\frac{1}{D_s}\sum_{l=1}^{D_s}\left(\hat{X}_{l,k} - X_{l,k,true}\right)^2} \tag{48}$$

where X_l denotes the *l*-th state component of the state vector, and *T* is the number of total time steps. A lower RMSE means a more accurate estimation.

Similarly with that performed in [9], the number of particles used for each algorithm is determined by

$$\begin{cases} N_{PF} = 10\times 2^a \\ N_{MPF} = a+1 \\ N_{MLPF} = a+1 \end{cases} \tag{49}$$

where the number *a* is increased from 0 with a step of 1, until the estimates obtained from PF, MPF, or MLPF are no worse than those simply relying on the measurements alone, i.e., the RMSE of the estimates is lower than that of the measurements,

$$\sqrt{\frac{1}{T}\sum_{k=1}^{T}\frac{1}{D_s}\sum_{l=1}^{D_s}\left(\hat{X}_{l,k} - X_{l,k,true}\right)^2} \le \sqrt{\frac{1}{T}\sum_{k=1}^{T}\frac{1}{D_s}\sum_{l=1}^{D_s}\left(Y_{l,k} - X_{l,k,true}\right)^2} \tag{50}$$

where Y_l denotes the *l*-th component of the measurement vector.

Both MPF and MLPF use the same state partitioning, where the state vector is divided into several subgroups, each containing an equal number of components. In this analysis, we examine the performance of MPF and MLPF under three different subgroup sizes, consisting of two, five, and ten components each. Notably, the assumption of independent state evolution for each subgroup is inherently met in this example. Furthermore, there is no need to define the local state vector in MLPF, because the likelihood function for each subgroup only involves the state components of that subgroup.

Figure 1 plots the numbers of particles and computational times at increasing state dimensions required by PF, averaged from twenty-five independent runs, and they can be formulated as

$$\begin{cases} \log_{10} N_{PF} = 0.053D_s + 0.698 \\ \log_{10} T_{c,PF} = 0.058D_s - 2.593 \end{cases} \tag{51}$$

which leads to the same conclusion from [9], i.e., the required number of particles and computation time appear to exponentially increase with the state dimension.

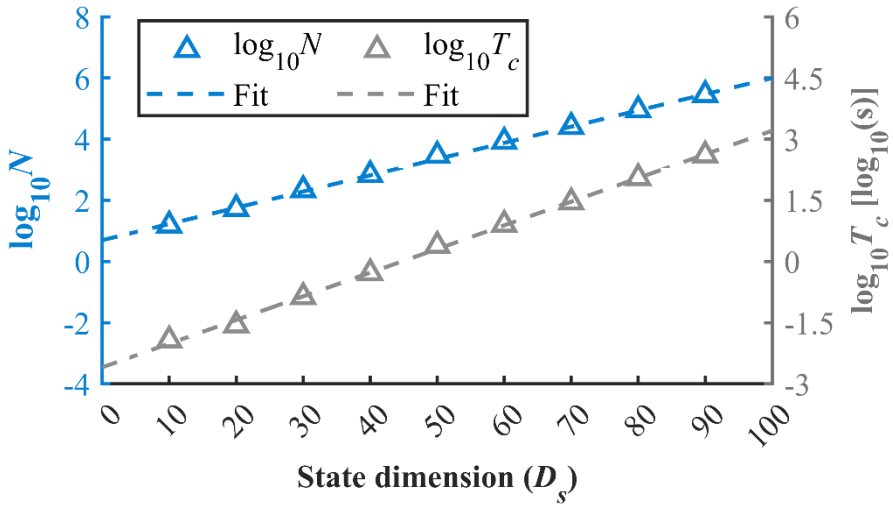

Figure 1 Numbers of particles and computation times required by PF for satisfying the criterion at increasing state dimensions

Figure 2 plots the numbers of particles at increasing state dimensions required by MPF and MLPF, averaged from twenty-five independent runs. The values in the brackets, i.e., 2, 5, and 10, indicate the number of state components in each state subgroup. By using state partitioning, both MPF and MLPF require significantly fewer particles than PF. Furthermore, the number of particles remains stable as state dimensions increase, demonstrating the potential of MPF and MLPF for mitigating the curse of dimensionality. Notably, the fewer components a state subgroup possesses, the fewer particles that MPF and MLPF require.

At the same time, the performances of MPF and MLPF in terms of accuracy are quite similar, i.e., they can provide similarly accurate estimates with the same number of particles. The reason has been given in Section 2.4 and again explained here. The main difference between MPF and MLPF is that the former requires more components for likelihood calculation. The additional components required by the MPF are some measurements and the means of specific state components, resulting in limited effect on the weight distribution after the normalization procedure, thus ensuring MLPF can provide nearly as precise estimates as MPF.

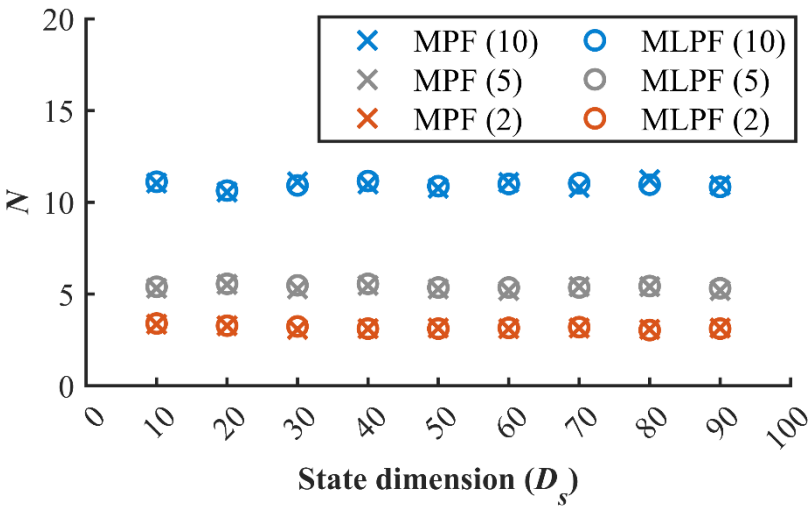

Figure 2 Numbers of particles required by MPF and MLPF for satisfying the criterion at

increasing state dimensions.
Note: the numbers ‘2’, ‘5’, and ‘10’ within the brackets denote the number of state components at each state subgroup.

Figure 3 depicts the average computation times required by the MPF and the MLPF at increasing state dimensions, computed from twenty-five independent runs. The values in brackets indicate the number of state components in each state subgroup. It is observed that the computation time for both the MPF and the MLPF increases with the dimension of the entire state vector, but always remains less than that required by PF. Additionally, when the subgroup size is two, the MPF and the MLPF require more computation time compared to the other cases, because of the increasing number of PFs used at each step. These results suggest that reducing the subgroup size can improve computation efficiency until the subgroup size becomes too small.

Although both the MPF and the MLPF require almost the same number of particles to produce similarly accurate estimates, as expected the MLPF exhibits faster computation time than the MPF due to its fewer components in likelihood. By taking the example of defining the subgroup size as 10, the computation time as a function of state dimension can be formulated as,

$$\begin{cases} T_{c,MPF} = 1.570\times10^{-5} D_s^{\,2} - 4.874\times10^{-6} D_s + 6.095\times10^{-3} \\ T_{c,MLPF} = 5.755\times10^{-4} D_s + 6.944\times10^{-4} \end{cases} \tag{52}$$

which suggests that the advantage of the MLPF over the MPF becomes more evident in a higher-dimensional system. This is due to the fact that the number of components required for likelihood calculation in MPF increases with the state dimension in this example, whereas the MLPF does not experience such a limitation.

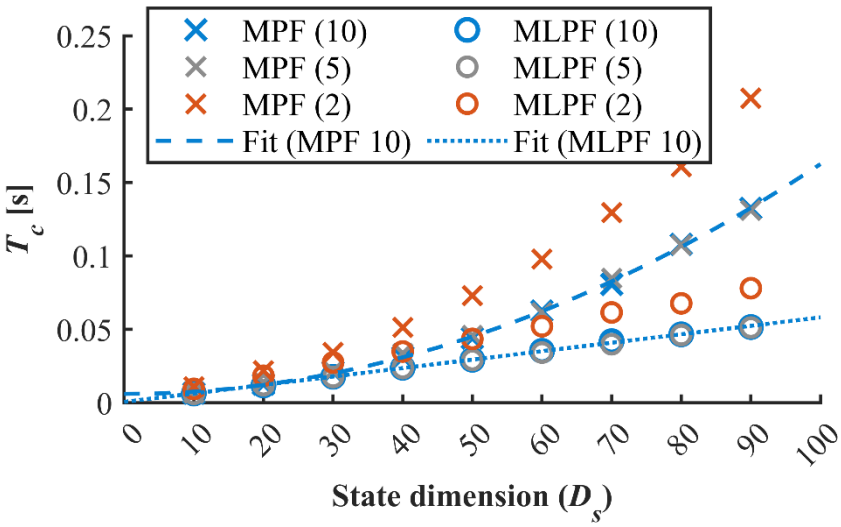

Figure 3 Computation times required by the MPF and the MLPF for satisfying the criterion at increasing state dimensions
Note: the numbers ‘2’, ‘5’, and ‘10’ within the brackets denote the number of state components at each state subgroup

4. Case study of a twenty-story frame structure

Sections 4.1 and 4.2 provide details on the development of dynamic responses for a twenty-story Bouc-Wen frame under the ground motion and state space modeling, respectively. Section 4.3 explains the process of partitioning the state into some subgroups and defining their corresponding local state and measurement vectors. In Section 4.4, the accuracy of estimation and computation efforts of the PF, the MPF, and the MLPF are compared. Additionally, Section 4.5 presents their performance with a limited number of measurements.

4.1 Data generation

A twenty-story Bouc-Wen frame structure under the ground motion serves as the numerical example for comparing the performances of the three PF algorithms, and its structural dynamic equation can be built as

$$\begin{bmatrix} m_1 & & & \\ & m_2 & & \\ & & \ddots & \\ & & & m_{20} \end{bmatrix} \begin{bmatrix} a_1 \\ a_2 \\ \vdots \\ a_{20} \end{bmatrix} + \begin{bmatrix} c_1+c_2 & -c_2 & & \\ -c_2 & c_2+c_3 & -c_3 & \\ & & \ddots & \\ & & -c_{20} & c_{20} \end{bmatrix} \begin{bmatrix} v_1 \\ v_2 \\ \vdots \\ v_{20} \end{bmatrix} + \begin{bmatrix} s_1+s_2 & -s_2 & & \\ -s_2 & s_2+s_3 & -s_3 & \\ & & \ddots & \\ & & -s_{20} & s_{20} \end{bmatrix} \begin{bmatrix} z_1 \\ z_2 \\ \vdots \\ z_{20} \end{bmatrix} = -\begin{bmatrix} m_1 \\ m_2 \\ \vdots \\ m_{20} \end{bmatrix} a_g \tag{53}$$

where the subscript l denotes the l-th story, a_g means the ground motion, a, v, c, m, and s mean the acceleration, velocity, damping, mass, and stiffness, respectively, and the hysteretic displacement z can be obtained from

$$\dot{z}_l = \left(v_l - v_{l\text{-}1}\right) - \beta \left|v_l - v_{l\text{-}1}\right| \left|z_l\right|^{n-1} z_l - \gamma \left(v_l - v_{l\text{-}1}\right) \left|z_l\right|^n \tag{54}$$

where β, γ, and n are the Bouc-Wen parameters.

For simulating the dynamic responses, the mass, damping, and stiffness for each story are 1 kg, 0.25 $\mathrm{Ns/m}$, and 9 $\mathrm{N/m}$, respectively [5], and the parameters β, γ, and n are 800 m^{-2}, 400 m^{-2}, and 2, respectively [26]. The first five-second El-Centro NS earthquake signal serves as the ground motion a_g $[\mathrm{m/s}^2]$. The structural dynamic responses are calculated at 400 Hz sampling frequency by the MATLAB ordinary differential equation solver 'ode45'. Both the acceleration of each story and the ground motion are assumed to be measured, and they are corrupted by zero-mean Gaussian noises with standard deviations (STDs) equal to 1% of the root-mean-square (RMS) value of the acceleration of that story and 1% of the RMS value of the ground motion, respectively.

4.2 State space modeling

With the stiffness, velocity, and hysteretic displacement of each story to be estimated, the state space model can be formulated as

$$\boldsymbol{X}_k = \begin{bmatrix} s_{1,k} \\ \vdots \\ v_{1,k} \\ \vdots \\ z_{1,k} \\ z_{2,k} \\ \vdots \end{bmatrix} = \begin{bmatrix} s_{1,k-1} \\ \vdots \\ v_{1,k-1} \\ \vdots \\ z_{1,k-1} \\ z_{2,k-1} \\ \vdots \end{bmatrix} + \begin{bmatrix} \omega_{1,k-1} \\ \vdots \\ a_{1,k-1}\Delta t + \omega_{21,k-1} \\ \vdots \\ \Delta t\left(v_{1,k-1} - \beta\left|v_{1,k-1}\right|\left|z_{1,k-1}\right|^{n-1} z_{1,k-1} - \gamma v_{1,k-1}\left|z_{1,k-1}\right|^{n}\right) + \omega_{41,k} \\ \Delta t\left(\left(v_{2,k-1} - v_{1,k-1}\right) - \beta\left|v_{2,k-1} - v_{1,k-1}\right|\left|z_{1,k-1}\right|^{n-1} z_{1,k-1} - \gamma\left(v_{2,k-1} - v_{1,k-1}\right)\left|z_{1,k-1}\right|^{n}\right) + \omega_{42,k} \\ \vdots \end{bmatrix} \quad (55)$$

$$\boldsymbol{Y}_k = \begin{bmatrix} a_{1,k} \\ \vdots \\ a_{20,k} \end{bmatrix} = -\begin{bmatrix} a_{g,k} \\ \vdots \\ a_{g,k} \end{bmatrix} - \begin{bmatrix} \frac{1}{m_1} & & \\ & \ddots & \\ & & \frac{1}{m_{20}} \end{bmatrix} \left(\begin{bmatrix} c_1 + c_2 & -c_2 & \\ & \ddots & \\ & -c_{20} & c_{20} \end{bmatrix} \begin{bmatrix} v_{1,k} \\ \vdots \\ v_{20,k} \end{bmatrix} + \begin{bmatrix} s_{1,k} + s_{2,k} & -s_{2,k} & \\ & \ddots & \\ & -s_{20,k} & s_{20,k} \end{bmatrix} \begin{bmatrix} z_{1,k} \\ \vdots \\ z_{20,k} \end{bmatrix} \right) + \begin{bmatrix} \eta_{1,k} \\ \vdots \\ \eta_{20,k} \end{bmatrix} \quad (56)$$

where Δt is the time interval, $\{\omega_i : i = 1, 2, \ldots, 60\}$ and $\{\eta_i : i = 1, 2, \ldots, 20\}$ are the zero-mean Gaussian process and measurement noises, respectively. The Bouc-Wen components and the multiplication of the unknown stiffness parameter and the displacement result in the nonlinearity of this model [5, 6], and the sixty unknown state components to be estimated account for the high dimensionality.

The numbers of particles for the PF, the MPF, and the MLPF are 80000, 800, and 800, respectively. Their other parameters are the same as defined as follows. The threshold N_T for systematic resampling is 0.5. The samples for initial stiffnesses are randomly selected within the same uniform distribution, i.e., $\{s_{1,0}, s_{2,0}, ..., s_{20,0}\} \sim \mathrm{U}(4,12)$. The initial velocity and displacement are zero. The displacement and velocity are calculated by trapezoidal integration from the measured acceleration. The STDs of process noises for velocity, displacement, and stiffness are 0.01 % of root-mean-square (RMS) values of the calculated velocity and displacement, and 0.001, respectively. The STD for each story in the likelihood is taken as 10% of the RMS value of the acceleration of that story.

4.3 Definition of state subgroup and local vectors

The application of multiple target tracking considers the state components from one target as one state subgroup. This also applies for a multiple-DOF structure. Specifically, the state components from one DOF, e.g., stiffness and displacement from one story, can be taken as one subgroup. Thus, for both the MPF and the MLPF, this numerical example has twenty state subgroups,

$$\begin{cases} \boldsymbol{x}_k^1 = \begin{bmatrix} s_{1,k} & v_{1,k} & z_{1,k} \end{bmatrix}^T \\ \boldsymbol{x}_k^2 = \begin{bmatrix} s_{2,k} & v_{2,k} & z_{2,k} \end{bmatrix}^T \\ \quad \vdots \\ \boldsymbol{x}_k^{20} = \begin{bmatrix} s_{20,k} & v_{20,k} & z_{20,k} \end{bmatrix}^T \end{cases} \tag{57}$$

As shown by the process equation Eq. (55), the first state subgroup can independently evolve, while the other subgroup needs to evolve by resorting to itself and one extra state component t^j. Let us take the second state subgroup as the reference example. The partial process equation for that subgroup can be selected from Eq. (55) as

$$\boldsymbol{x}_k^2 = \begin{bmatrix} s_{2,k} \\ v_{2,k} \\ z_{2,k} \end{bmatrix} = \begin{bmatrix} s_{2,k-1} \\ v_{2,k-1} \\ z_{2,k-1} \end{bmatrix} + \begin{bmatrix} \omega_{2,k-1} \\ a_{2,k-1}\Delta t + \omega_{22,k-1} \\ \Delta t\left(\left(v_{2,k-1} - v_{1,k\text{-}1}\right) - \beta\left|v_{2,k-1} - v_{1,k\text{-}1}\right|\left|z_{1,k-1}\right|^{n-1} z_{1,k-1} - \gamma\left(v_{2,k-1} - v_{1,k\text{-}1}\right)\left|z_{1,k-1}\right|^{n}\right) + \omega_{42,k} \end{bmatrix} \tag{58}$$

where the evolution of that subgroup has to resort to itself and one additional component v_1. Same procedure can be applied to the other state subgroup, and the extra component for the *j*-th subgroup can be defined as

$$t^j = v_{j-1} \tag{59}$$

The selection of the local state and measurement vectors for each subgroup in MLPF is explained by taking the first two state subgroups $\boldsymbol{x}_k^1$ and $\boldsymbol{x}_k^2$ as the reference example. The measurement equation Eq. (56) can be reformulated as

$$
\begin{cases}
a_{1,k} = \dfrac{-a_{g,k} - \begin{bmatrix} c_1 + c_2 & -c_2 \end{bmatrix} \begin{bmatrix} v_{1,k} \\ v_{2,k} \end{bmatrix} - \begin{bmatrix} s_{1,k} + s_{2,k} & -s_{2,k} \end{bmatrix} \begin{bmatrix} z_{1,k} \\ z_{2,k} \end{bmatrix}}{m_1} + \eta_{1,k} \\
a_{2,k} = \dfrac{-a_{g,k} - \begin{bmatrix} -c_2 & c_2 + c_3 & -c_3 \end{bmatrix} \begin{bmatrix} v_{1,k} \\ v_{2,k} \\ v_{3,k} \end{bmatrix} - \begin{bmatrix} -s_{2,k} & s_{2,k} + s_{3,k} & -s_{3,k} \end{bmatrix} \begin{bmatrix} z_{1,k} \\ z_{2,k} \\ z_{3,k} \end{bmatrix}}{m_2} + \eta_{2,k} \\
\vdots \\
a_{20,k} = \dfrac{-a_{g,k} - \begin{bmatrix} -c_{20} & c_{20} \end{bmatrix} \begin{bmatrix} v_{19,k} \\ v_{20,k} \end{bmatrix} - \begin{bmatrix} -s_{20,k} & s_{20,k} \end{bmatrix} \begin{bmatrix} z_{19,k} \\ z_{20,k} \end{bmatrix}}{m_{20}} + \eta_{20,k}
\end{cases}
\tag{60}
$$

where the three state components of the subgroup $\boldsymbol{x}_k^1$ exist in the first and second rows only. Thus, the local measurement equation for that subgroup can be obtained as

$$
\boldsymbol{y}_k^1 = \begin{bmatrix} a_{1,k} \\ a_{2,k} \end{bmatrix} = \begin{bmatrix}
\dfrac{-a_{g,k} - \begin{bmatrix} c_1 + c_2 & -c_2 \end{bmatrix} \begin{bmatrix} v_{1,k} \\ v_{2,k} \end{bmatrix} - \begin{bmatrix} s_{1,k} + s_{2,k} & -s_{2,k} \end{bmatrix} \begin{bmatrix} z_{1,k} \\ z_{2,k} \end{bmatrix}}{m_1} + \eta_{1,k} \\
\dfrac{-a_{g,k} - \begin{bmatrix} -c_2 & c_2 + c_3 & -c_3 \end{bmatrix} \begin{bmatrix} v_{1,k} \\ v_{2,k} \\ v_{3,k} \end{bmatrix} - \begin{bmatrix} -s_{2,k} & s_{2,k} + s_{3,k} & -s_{3,k} \end{bmatrix} \begin{bmatrix} z_{1,k} \\ z_{2,k} \\ z_{3,k} \end{bmatrix}}{m_2} + \eta_{2,k}
\end{bmatrix}
\tag{61}
$$

and its local state and measurement vectors can then be determined as

$$
\begin{cases}
\boldsymbol{y}_k^1 = \begin{bmatrix} a_{1,k} & a_{2,k} \end{bmatrix}^T \\
\boldsymbol{q}_k^1 = \begin{bmatrix} s_{2,k} & v_{2,k} & z_{2,k} & s_{3,k} & v_{3,k} & z_{3,k} \end{bmatrix}^T
\end{cases}
\tag{62}
$$

The same selection procedure applies to the subgroup $\boldsymbol{x}_k^2$ to determine its local state and measurement vectors,

$$
\begin{cases}
\boldsymbol{y}_k^2 = \begin{bmatrix} a_{1,k} & a_{2,k} & a_{3,k} \end{bmatrix}^T \\
\boldsymbol{q}_k^2 = \begin{bmatrix} s_{1,k} & v_{1,k} & z_{1,k} & s_{3,k} & v_{3,k} & z_{3,k} & s_{4,k} & v_{4,k} & z_{4,k} \end{bmatrix}^T
\end{cases}
\tag{63}
$$

4.4 Comparison of PF, MPF, and MLPF

In Figure 4, typical runs for stiffness estimations using the three algorithms are shown, and it can be observed that the three selected stiffness parameters, namely s_2, s_9, and s_{18}, converge in about three seconds but with different rates. Additionally, due to the initial acceleration of the higher story remaining close to zero for a

longer time, the measurement calculated by its stiffness weakly contributes to the likelihood at initial time steps, resulting in a slower convergence for the stiffness of the higher story compared to the lower story.

In the case of PF, the resampling procedure eliminates the samples of the two stiffness s_9 and s_{18} at initial steps, with little concern about whether their distributions are around the true values or not, resulting in an inaccurate estimation as shown in Figures 4 (b) and (c). However, by partitioning one state vector into several state subgroups, both MPF and MLPF algorithms keep the initial diversities of samples for the two parameters better, resulting in more accurate estimates than the PF, as shown in Figures 4 (e), (f), (h), and (i). Additionally, the accuracy of estimations from the MPF and the MLPF is quite similar. This is because the additional components in the likelihood of MPF have a limited effect on the distribution of normalized weight, leading to similar estimation results between the two algorithms.

Finally, the velocity and displacement estimations in Figures 5 and 6, respectively, yield the same conclusions as drawn from Figure 4, demonstrating the robustness of both the MPF and the MLPF.

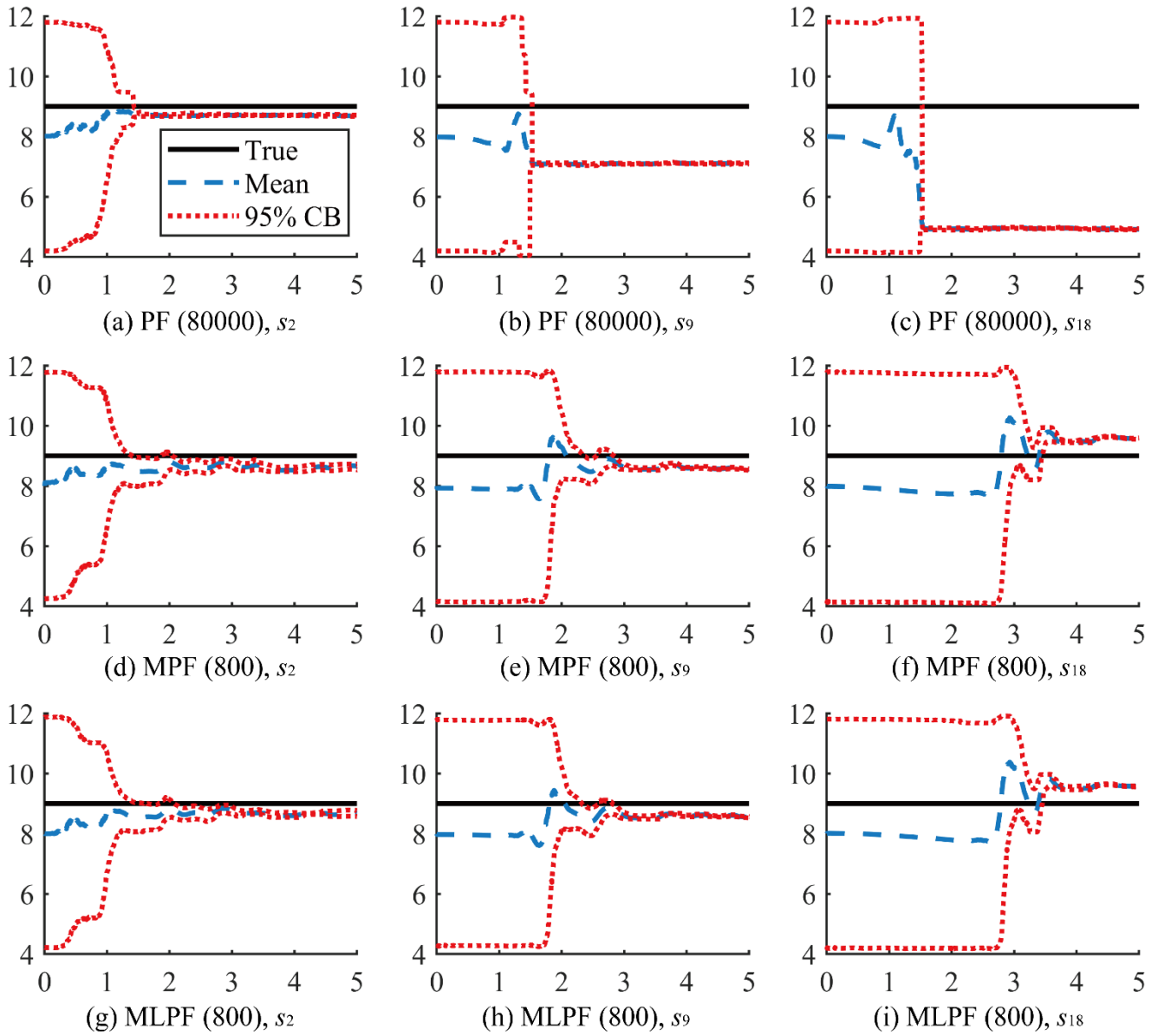

Figure 4 Stiffness estimations from the three algorithms

Note: (i) the *x* and *y* labels are 'time [s]' and 'stiffness [N/m]', respectively; (ii) the number within the bracket and 'CB' means the number of particles used in one run and confidence boundary, respectively.

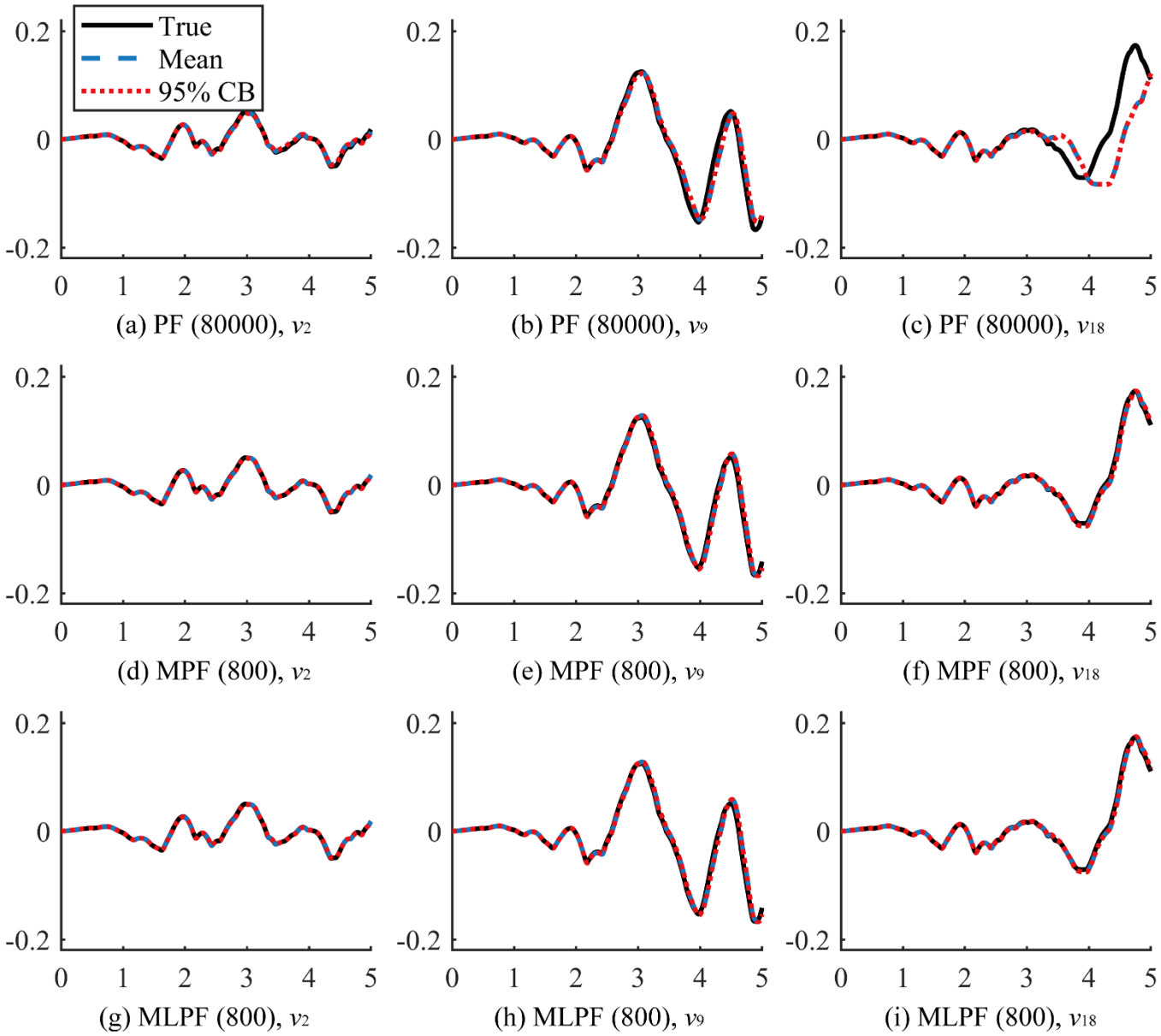

Figure 5 Velocity estimations from the three algorithms

Note: (i) the *x* and *y* labels are 'time [s]' and 'velocity [m/s]', respectively; (ii) the number within the bracket and 'CB' means the number of particles used in one run and confidence boundary, respectively.

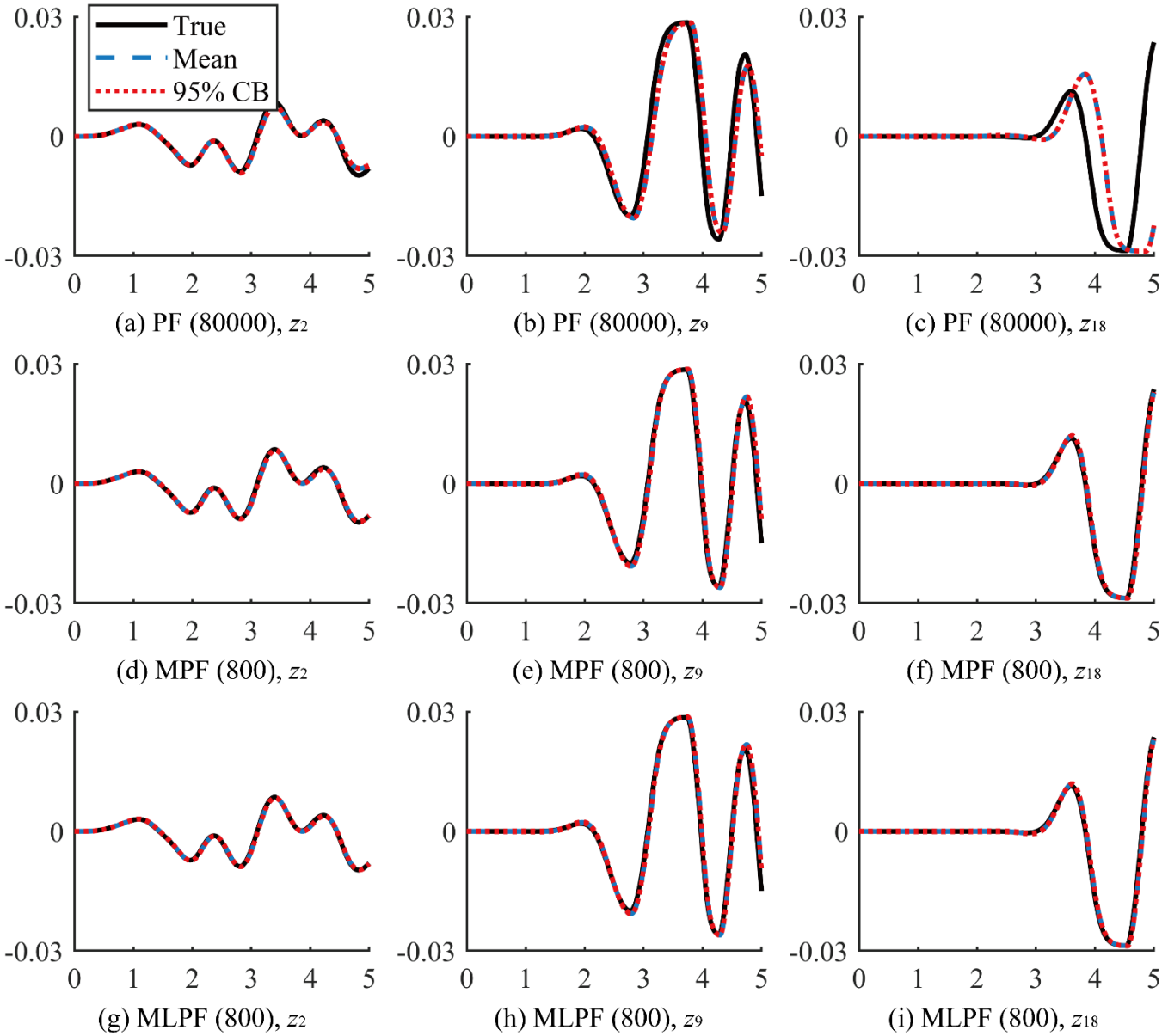

Figure 6 Displacement estimations from the three algorithms

Note: (i) the *x* and *y* labels are 'time [s]' and 'displacement [m]', respectively; (ii) the number within the bracket and 'CB' means the number of particles used in one run and confidence boundary, respectively.

To provide a more comprehensive comparison of stiffness estimations from the three algorithms, each algorithm is implemented 25 independent times to provide 25 sets of estimates. The Root-mean-square error (RMSE) and relative error (RE) serve as the performance metrics to evaluate the estimation accuracy of each run,

$$RMSE = \sqrt{\frac{1}{T}\sum_{k=1}^{T}\left(\hat{s}_k - s_{true,k}\right)^2} \tag{64}$$

$$RE = \frac{\left|\hat{s}_T - s_{true,T}\right|}{s_{true,T}} \tag{65}$$

where T is the number of time steps in PF implementation. Note that a lower RMSE or RE indicates a more

accurate estimation. Figure 7 presents the RMSE and RE averaged from 25 runs for each algorithm, highlighting the observations made in Figures 4-6.

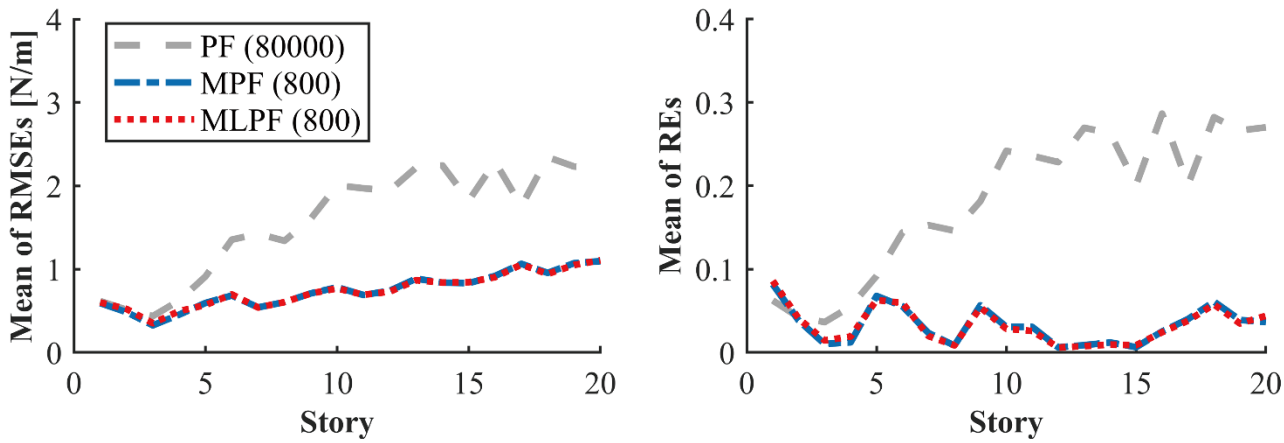

(a) Root-mean-square error (b) relative error

Figure 7 RMSE and RE averaged from the 25 runs of each algorithm

Note: the number within the bracket means the number of particles used for one run.

Table 4 presents the average computation time of one run for each algorithm on an AMD Ryzen 9 3950X 16-Core Processor. Similar to the observations made in Section 3, both MPF and MLPF require significantly less computation time than PF while still providing more accurate estimates. Additionally, it is worth noting that MLPF is more computationally efficient than MPF, as the former requires fewer state and measurement components for the likelihood calculation.

Table 4 Average computation time of one run for each algorithm

	PF	PF	MPF	MLPF
Number of particles	800	80000	800	800
Computation time [s]	13.7	1354.7	162.1	71.7

4.5 Identification with limited measurements

The accelerations of all stories were gathered for system identification in the above numerical study. However, in-field applications may only have a limited number of sensors installed for monitoring. Some Kalman filter algorithms have been adapted to perform system identification with limited measurements [27, 28], while there have been few attempts to do the same with PF. Nevertheless, PF algorithms can still function in such scenarios, albeit with a modified likelihood calculation.

The state space model, state and measurement partitioning, and PF initialization for the three

algorithms remain unchanged, but the likelihood is calculated using only the collected accelerations. It is important to note that, after the resampling step, the accelerations from all stories must be calculated using the measurement equation and then used for state evolution.

Let us consider only accelerations of the 1st, 3rd, 5th, ..., and 19th stories to be measured. The stiffness estimations from one typical run are given in Figure 8, and the RMSE and RE averaged from the 25 runs are presented in Figure 9. All the estimates converge in about three seconds, the same as Figure 4. On the other hand, the estimation accuracies from all three PFs decrease with fewer measurements, especially for the stiffnesses at higher stories, thus justifying the importance of sufficient sensors in the SHM system.

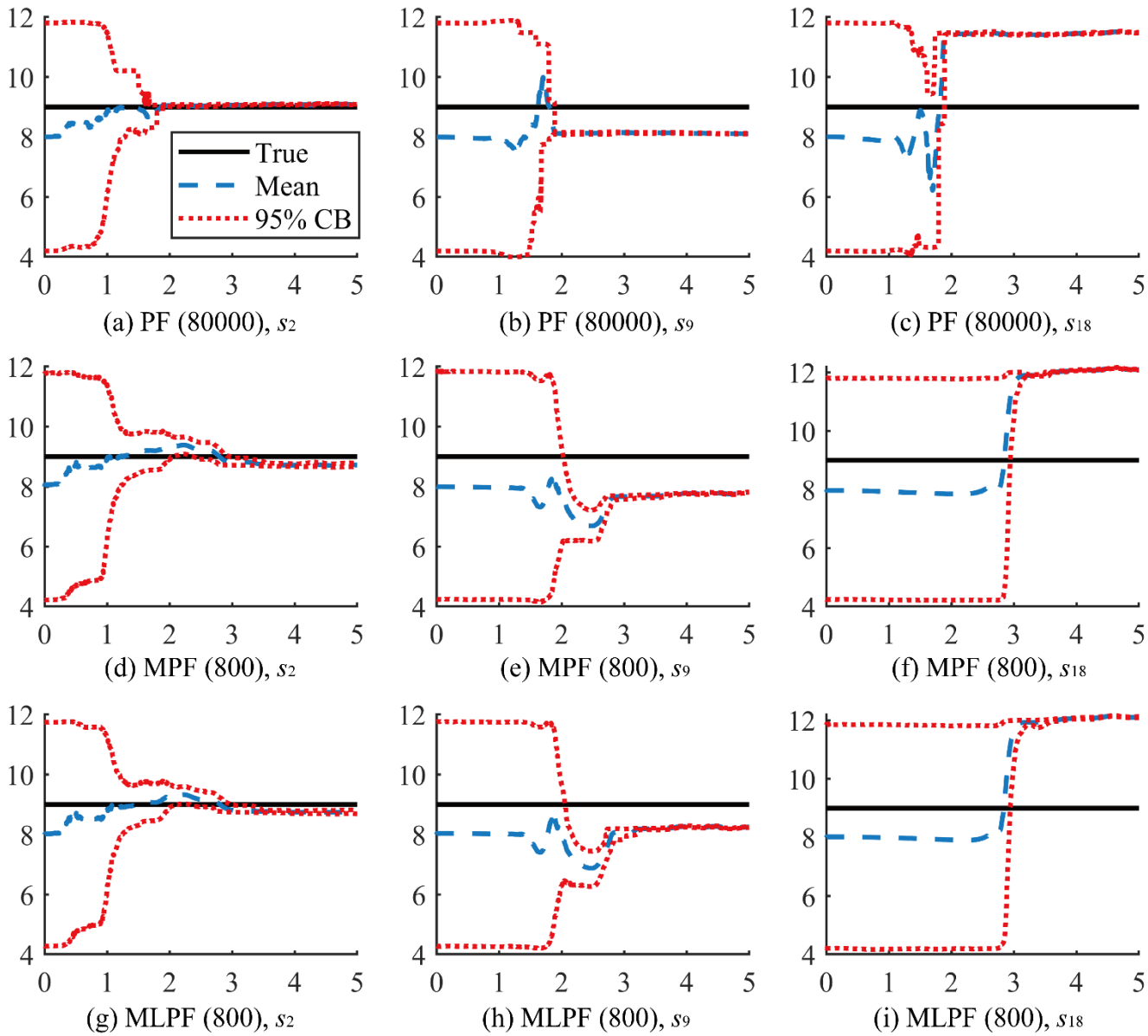

Figure 8 Stiffness estimations from the three algorithms with limited measurements

Note: (i) the *x* and *y* labels are 'time [s]' and 'stiffness [m/s]', respectively; (ii) the number within the bracket and 'CB' means the number of particles used in one run and confidence boundary, respectively.

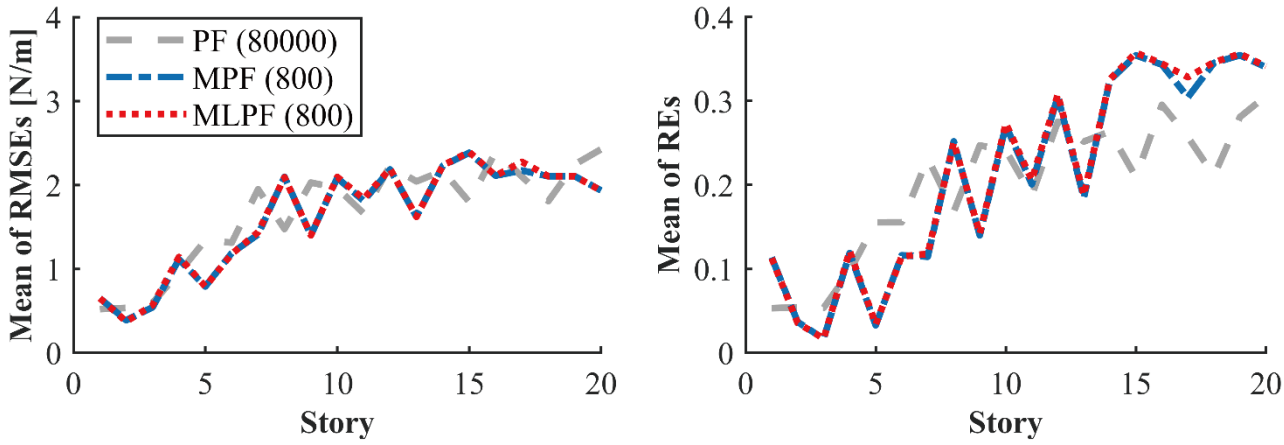

(a) Root-mean-square error (b) relative error

Figure 9 RMSE and RE averaged from the 25 runs of each algorithm with limited measurements
Note: the number within the bracket means the number of particles used for one run.

5. Conclusion

The application of particle filter in a high-dimensional system is limited due to the curse of dimensionality. By combining multiple particle filter (MPF) and the decay of correlations property, this paper has developed a novel multiple local particle filter (MLPF) for structural system identification. One state vector is partitioned into several state subgroups, each containing the components from one DOF and then estimated by one PF. The superior performances of the MLPF over the MPF and the PF with respect to computation effort and estimation accuracy have been proved by the identification results of the toy example and the numerical twenty-story Bouc-Wen frame structure under the ground motion.

The number of particles required by the PF will exponentially increase with the state dimension, while the number of particles required by the MPF or the MLPF will remain relatively stable. This proves the abilities of the MPF and the MLPF in alleviating the curse of dimensionality. the MLPF can provide similarly accurate estimations as the MPF under the same number of particles but requires less computation time due to fewer components involved in the likelihood. This advantage of the MLPF over the MPF will be even more apparent in a higher-dimensional system, where the number of components within the likelihood of the MPF will increase with a higher state dimension, while the number of components for the MLPF may not increase as much.

For the system identification of the twenty-story frame structure, it has been found that the stiffness of the story closer to the ground motion shows faster convergence, possibly due to its higher contribution to the likelihood calculation at the initial steps. Furthermore, PF algorithms can work with partial acceleration measurements but provide less accurate estimates. This justifies the importance of sufficient sensors for the SHM system and also calls for an advanced system identification method with a limited number of

measurements.

The state partitioning process for the structural dynamic model used in this study has been found to be straightforward. However, it may not be as simple for the other SHM applications, especially those using data-driven state space models. To address this challenge, it is recommended that a sensitivity analysis should be conducted to determine the appropriate state subgroups and their corresponding local vectors. Alternatively, an adaptive state partitioning approach could be developed to more fully explore the potential of this strategy for high-dimensional problems. By taking these steps, researchers can better tailor their SHM models to specific applications and ensure the most effective use of available data.

Acknowledgment

This project has received funding from the European Union's Horizon 2020 research and innovation programme under the Marie Skłodowska-Curie grant agreement No. 859957.

References

[1] S.S. Law, K. Zhang, Z.D. Duan, Structural damage detection from coupling forces between substructures under support excitation, Engineering Structures, 32 (2010) 2221-2228.
[2] S. Pan, D. Xiao, S. Xing, S.S. Law, P. Du, Y. Li, A general extended Kalman filter for simultaneous estimation of system and unknown inputs, Engineering Structures, 109 (2016) 85-98.
[3] J. He, Y.L. Xu, S. Zhan, Q. Huang, Structural control and health monitoring of building structures with unknown ground excitations: Experimental investigation, Journal of Sound & Vibration, 390 (2017) 23-38.
[4] Y. Ding, B.Y. Zhao, B. Wu, X.C. Zhang, L.N. Guo, Simultaneous Identification of Structural Parameter and External Excitation with an Improved Unscented Kalman Filter, Advances in Structural Engineering, 18 (2015) 1981-1998.
[5] E.N. Chatzi, A.W. Smyth, The unscented Kalman filter and particle filter methods for nonlinear structural system identification with non-collocated heterogeneous sensing, Structural Control & Health Monitoring, 16 (2009) 99-123.
[6] A. Olivier, A.W. Smyth, Particle filtering and marginalization for parameter identification in structural systems, Structural Control and Health Monitoring, 24 (2017) e1874.
[7] R. Sajeeb, C.S. Manohar, D. Roy, A conditionally linearized Monte Carlo filter in non-linear structural dynamics, International Journal of Non-Linear Mechanics, 44 (2009) 776-790.
[8] F. Cadini, L. Lomazzi, M. Ferrater Roca, C. Sbarufatti, M. Giglio, Neutralization of temperature effects in damage diagnosis of MDOF systems by combinations of autoencoders and particle filters, Mechanical Systems and Signal Processing, 162 (2022) 108048.
[9] C. Snyder, T. Bengtsson, P. Bickel, J. Anderson, Obstacles to high-dimensional particle filtering, Monthly Weather Review, 136 (2008) 4629-4640.
[10] C. Snyder, Particle filters, the "optimal" proposal and high-dimensional systems, Proceedings of the ECMWF Seminar on Data Assimilation for atmosphere and ocean, 2011, pp. 1-10.
[11] L. Úbeda-Medina, J. Grajal, Sigma-point multiple particle filtering, Signal Processing, 160 (2019) 271-283.

[12] M. Orton, W. Fitzgerald, A Bayesian approach to tracking multiple targets using sensor arrays and particle filters, IEEE Transactions on Signal Processing, 50 (2002) 216-223.
[13] M.F. Bugallo, T. Lu, P.M. Djuric, Target tracking by multiple particle filtering, 2007 IEEE aerospace conference, IEEE, 2007, pp. 1-7.
[14] P.M. Djuric, T. Lu, M.F. Bugallo, Multiple Particle Filtering, 2007 IEEE International Conference on Acoustics, Speech and Signal Processing - ICASSP '07, 2007, pp. III-1181-III-1184.
[15] P. Closas, M.F. Bugallo, Improving Accuracy by Iterated Multiple Particle Filtering, IEEE Signal Processing Letters, 19 (2012) 531-534.
[16] C. Kreucher, K. Kastella, A.O. Hero, Multitarget tracking using the joint multitarget probability density, IEEE Transactions on Aerospace and Electronic Systems, 41 (2005) 1396-1414.
[17] Y. Wei, M.R. Morelande, L. Kong, J. Yang, A Computationally Efficient Particle Filter for Multitarget Tracking Using an Independence Approximation, IEEE Transactions on Signal Processing, 61 (2013) 843-856.
[18] T. Li, S. Sun, J.M. Corchado, T.P. Sattar, S. Si, Numerical fitting-based likelihood calculation to speed up the particle filter, International Journal of Adaptive Control and Signal Processing, 30 (2016) 1583-1602.
[19] P. Rebeschini, R. Van Handel, Can local particle filters beat the curse of dimensionality?, The Annals of Applied Probability, 25 (2015) 2809-2866.
[20] P. Chavali, A. Nehorai, Hierarchical particle filtering for multi-modal data fusion with application to multiple-target tracking ☆, Signal Processing, 97 (2014) 207-220.
[21] J. MacCormick, M. Isard, Partitioned Sampling, Articulated Objects, and Interface-Quality Hand Tracking, Springer Berlin Heidelberg, Berlin, Heidelberg, 2000, pp. 3-19.
[22] L.A. Úbeda Medina, Robust techniques for multiple target tracking and fully adaptive radar= Técnicas robustas para seguimiento de múltiples blancos y radar adaptativo, Telecomunicacion, 2018.
[23] R.N. Bracewell, R.N. Bracewell, The Fourier transform and its applications, McGraw-hill New York, 1986.
[24] M.S. Arulampalam, S. Maskell, N. Gordon, T. Clapp, A tutorial on particle filters for online nonlinear/non-Gaussian Bayesian tracking, IEEE Transactions on Signal Processing, 50 (2002) 174-188.
[25] N.J. Gordon, D.J. Salmond, A.F.M. Smith, Novel approach to nonlinear/non-Gaussian Bayesian state estimation, IEE Proceedings F - Radar and Signal Processing, 140 (1993) 107-113.
[26] Y. Lei, D. Xia, K. Erazo, S. Nagarajaiah, A novel unscented Kalman filter for recursive state-input-system identification of nonlinear systems, Mechanical Systems and Signal Processing, 127 (2019) 120-135.
[27] Y. Lei, M. He, C. Liu, S.-Z. Lin, Identification of Tall Shear Buildings under Unknown Seismic Excitation with Limited Output Measurements, Advances in Structural Engineering, 16 (2013) 1839-1849.
[28] Y. Li, Y. Luo, H.-P. Wan, C.-B. Yun, Y. Shen, Identification of earthquake ground motion based on limited acceleration measurements of structure using Kalman filtering technique, Structural Control and Health Monitoring, 27 (2020) e2464.

CHAPTER 6

CONCLUSIONS AND FUTURE WORKS

6.1 Conclusions

In conclusion, this thesis has developed several robust and efficient methods for damage prognosis, with a focus on three main paths: *damage evolution modeling*, *damage quantification*, and *model updating algorithm*. The proposed methods have been evaluated through some experimental and numerical studies and have demonstrated their effectiveness in accurately predicting the remaining useful life (RUL) in structures.

The first contribution to *damage evolution modeling* has developed a novel PF-based delamination shape prediction method for composites by taking the delamination shape as a damage state for damage prognosis. By artificially defining some control lengths (CLs) to discretize the delamination contour, the shape prediction problem can be simplified into the predictions of these CLs, whose efficiency has been demonstrated concerning experimental tests of fatigue delamination growth in composite panels with ultrasonics C-scan monitoring during the entire run-to-failure process.

The second contribution proposed a numerical simulation-aided particle filter-based shape prediction framework that can save costs and efforts in conducting run-to-failure tests. This framework only requires numerically simulated delamination growth for building the function and then providing the PF initialization hyperparameters. This method is robust among three specimens and takes the model uncertainties into account by online updating their parameters.

The third contribution of this work focuses on the fusion of multiple degradation models for damage prognosis. The traditional method resorting to only one degradation model is not robust among different specimens, as the best degradation model can differ for each specimen. To address this, a new particle filter-based prognostic framework is proposed to fuse multiple degradation models by using the crossover or mutation operator. The new method consistently outperforms the traditional approach of simply combining estimates from multiple models, demonstrating its effectiveness and robustness.

As to *damage quantification*, this thesis has proposed a new prognostic model with a bias parameter included for estimation to account for the measurement uncertainties. The experimental study, where an aluminum lug structure is subject to fatigue cracking and monitored by ultrasonic Lamb waves, has proven that the new model can provide accurate estimation and prognostic results provided that the bias is correctly estimated.

As the formulation of such a model generally requires sufficiently experimental or in-field datasets collected during the run-to-failure process, which, however, may not be available due to some causes like the high costs. The author has proposed a new particle filter-based damage prognosis framework, which only requires numerically simulated Lamb waves for building the measurement equation.

Finally, as the best feature can vary for different specimens, or even, at different time steps for the same specimen, the selection of such a feature can hardly be a trivial task but has received little attention in current practices. By combining a novel online feature fusion and selection scheme with multiple prognostic models considering measurement bias, this work has proposed a new particle filter-based damage prognosis framework, where, at each step, the feature with the smallest estimated bias is taken as the best feature providing the best estimates at that step. The robustness of the proposed method has been demonstrated by the same test mentioned above.

In terms of *model updating algorithms*, the application of particle filter (PF) in a high-dimensional system is limited due to the curse of dimensionality. By combining multiple particle filter (MPF) and the decay of correlations property, this paper has developed a novel *multiple local particle filter* (MLPF) for high-dimensional identification. By partitioning one high-dimensional state vector into several lower-dimensional state subgroups, MLPF exhibits superior performance over MPF and PF concerning computation effort and estimation accuracy in the toy example and the numerical twenty-story Bouc-Wen frame structure under the ground motion.

6.2 Future works

To move towards a more practical and robust application, one can still consider the three paths mentioned above. Some possible questions that the author may continue to work on are listed in Table 6.

Table 6 Future works

Damage evolution modeling	• Coupling of multiple cracks in metal or multiple damage modes in composites • Fusion and selection of the ‘best’ degradation model
Damage quantification	• Robust feature fusion and selection • Sensor fusion
Model updating algorithm	• Auto-calibration particle filter
Others	• Uncertainties in failure threshold • Fusion of multiple prognostic methods

In terms of *damage evolution modeling*, it is very common to have multiple cracks in metal or multiple damage modes in composites, therefore it is of great importance to consider the coupling of multiple damages in the modeling process. Then, tens of or hundreds of available degradation models can be available in real practices, some of those models may

consistently provide inaccurate crack length quantification and RUL prediction results, thereby compromising the performance of the proposed method if such models are included. Consequently, it is necessary to develop an offline or online scheme to select a list of 'good' degradation models or 'good' PF estimates.

As to *damage quantification*, more coefficients should be fused for selecting a proper feature for more robust performance. Moreover, the proposed method is only validated in a case study where all the features can only be extracted from the Lamb waves from the same piezoelectrical transducer. Given that multiple transducers and different types of sensors like strain gauges and accelerometers are installed for monitoring, the fusion of those sensor signals remains a challenge.

Additionally, the estimation performance of particle filter (PF) is highly sensitive to the hyperparameters used, thus further research on developing an auto-calibration PF method may be considered.

Finally, the threshold of structural failure is usually deterministic in current practices, while its uncertainties deserve more investigation. Moreover, different categories of prognostic methods have been proposed, but separately validated. More attention should be paid to the fusion of all the prognostic methods for RUL prediction.

PUBLICATIONS

1. Tianzhi Li, Claudio Sbarufatti, Francesco Cadini, Jian Chen, and Shenfang Yuan. "Particle filter-based hybrid damage prognosis considering measurement bias." Structural Control and Health Monitoring 29, no. 4 (2022): e2914.

2. Tianzhi Li, Luca Lomazzi, Francesco Cadini, Claudio Sbarufatti, Jian Chen, and Shenfang Yuan. "Numerical simulation-aided particle filter-based damage prognosis using Lamb waves." Mechanical Systems and Signal Processing 178 (2022): 109326.

3. Tianzhi Li, Francesco Cadini, Manuel Chiachío, Juan Chiachío, and Claudio Sbarufatti. "Particle filter-based delamination shape prediction in composites subjected to fatigue loading." Structural Health Monitoring (2022): 14759217221116041.

4. Tianzhi Li, David Dumas, Olivier Pierard, Manuel Chiachío, Claudio Sbarufatti, and Francesco Cadini. "Numerical simulation-aided particle filter-based delamination shape prediction in composites." To be submitted.

5. Tianzhi Li, Jian Chen, Shenfang Yuan, Dimitrios Zarouchas, Claudio Sbarufatti, and Francesco Cadini. "Particle filter-based damage prognosis by fusing multiple degradation models." Under review by ‘Structural Health Monitoring’.

6. Tianzhi Li, Jian Chen, Shenfang Yuan, Francesco Cadini, and Claudio Sbarufatti. "Particle filter-based damage prognosis by online feature fusion and selection." Under review by ‘Mechanical Systems and Signal Processing’.

7. Tianzhi Li, Claudio Sbarufatti, and Francesco Cadini. "Multiple local particle filter for high-dimensional system identification." Under review by ‘Mechanical Systems and Signal Processing’.

8. Tianzhi Li (Presenter), Francesco Cadini, and Claudio Sbarufatti. "Particle filter-based hybrid damage prognosis considering bias." In 8th International Conference on Computational Methods in Structural Dynamics and Earthquake Engineering, 2021, Athens, Greece.

9. Tianzhi Li. "Multiple local particle filter for high-dimensional system identification." In 6th Edition of the Workshop on Nonlinear System Identification Benchmarks, 2022, Leuven, Belgium.

10. Tianzhi Li (Presenter), Francesco Cadini, Manuel Chiachío, Juan Chiachío, and Claudio Sbarufatti. "Particle filter-based delamination shape prediction in composites." In European Workshop on Structural Health Monitoring, 2022, Sicily, Italy.

BIOGRAPHY

Mr. Tianzhi Li was born in Wuhan, China, on 1995/02/13. He obtained the bachelor degree in Civil Engineering from Zhejiang University in 2016, and the master degree in Civil Engineering from Chongqing University in 2019.

Mr. Li was an early-stage-researcher funded by the ENHAnCE ITN project and also a Ph.D student at Politecnico di Milano from 2020/06/01 to 2023/05/31, under the supervisions of Prof. Claudio Sbarufatti, Prof. Francesco Cadini, and Ir. David Dumas.

ACKNOWLEDGEMENTS

As with the end of a performance, the actor takes a bow and says a few words of thanks to the attendance. I was always the latter but now become the former. It is my turn to conclude this three-year journey and express my gratitude.

Three years ago, I had been at home for a few months after my master graduation, struggling to find a PhD position. Despite I was rejected or on the way to being rejected, I seldom have the thought of giving up. At the end of that period, when it seemed unlikely my papers would be published due to many reasons, I accepted that I may have little chance of getting a position, and it was supposed to be the time for goodbye.

Almost at the same time, Claudio and Francesco sent me an email confirming my enrollment in a Marie-Curie project. Alright, it was still time to say goodbye, but to my parents and my home.

Then I moved to Milano and started pursuing my PhD. Everything went way more smoothly. Now the three-year journey comes to an end, at which I want to acknowledge all the people I have met.

A big thanks to Claudio and Francesco. You gave me the opportunity to start this journey. You were supporting me in past years. My memories about this journey may fade over time, but the feeling of being trusted, valued, and supported would never.

I thank my parents for their support in my life. I can always see your utmost confidence and trust in me. It has been more than two years I cannot make my return home possible. Your supports matter a lot during this period.

I would appreciate David and Olivier from Cenaero, and Dimitrios from Technical University of Delft. Thank you for hosting my secondments.

I would appreciate all the colleagues I have worked with, especially Max, Dayou, Luca, Alvaro, Alessandro, and Dario from our lab, and Manuel, Maria, Morteza, Aravind, and Wen from ENHAnCE project. I would also appreciate the secretaries at our department, Licia, Lucia, and Valentina, for their kind support before and during my PhD study.

Lastly, I would like to express my gratitude to myself three years ago for choosing this path. Starting was difficult for you, but ending it is much easier for me. Additionally, I would like to always remind myself to remember and appreciate all the people who have supported and helped me along the way.

李 天 之

2023/03/15, Milano